Functional and Responsive Nanoporous Silicon Nitride Membranes

THÈSE N^{O} 6203 (2014)

PRÉSENTÉE LE 6 JUIN 2014
À LA FACULTÉ DES SCIENCES ET TECHNIQUES DE L'INGÉNIEUR
LABORATOIRE DE MICROSYSTÈMES 4
PROGRAMME DOCTORAL EN MICROSYSTÈMES ET MICROÉLECTRONIQUE

ÉCOLE POLYTECHNIQUE FÉDÉRALE DE LAUSANNE

POUR L'OBTENTION DU GRADE DE DOCTEUR ÈS SCIENCES

PAR

Alexandre Zenon Ivan BOJKO

acceptée sur proposition du jury:

Prof. M. Gijs, président du jury
Prof. Ph. Renaud, Dr R. Pugin, directeurs de thèse
Prof. F. Montagne, rapporteur
Dr L. Nicu, rapporteur
Prof. L. G. Villanueva Torrijo, rapporteur

ÉCOLE POLYTECHNIQUE
FÉDÉRALE DE LAUSANNE
Suisse
2014

Acknowledgments

Acknowledgements

First, I would like to thank the members of the jury, Dr. Liviu Nicu, Prof. Guillermo Villanueva, Dr. Franck Montagne who kindly accepted to examine this manuscript and participate to the oral exam. Their comments, critics, and suggestions are more than welcome and I am sure they will lead to an interesting and constructive discussion during the exam. I would like to thank the president of the jury, Prof. Martinus Gijs who has accepted to supervise my oral exam.

I also would like to thank my thesis director Prof. Philippe Renaud for the interesting discussions during our meetings and also for his confidence in my research work which is a form of support much appreciated. Special thanks go to my thesis co-directors, Dr. Franck Montagne and Dr. Raphaël Pugin. Franck first started to supervise me at CSEM, putting me on the right tracks before he had to leave the company for another adventure at Roche Diagnostics. Then, Raphaël decided to take the lead and supervise the end of my thesis. His support and his critics helped me in finding the motivation to complete this thesis work. He also kindly accepted the difficult task of going through my manuscript. I am very grateful for his time, energy and experience, it was much appreciated.

Financial support from CSEM and the NanoTera program are gratefully acknowledged.

I also would like to thank my co-workers at CSEM with whom I had the greatest time, scientifically speaking, but also personally. Nico and Manu for the interesting discussions thanks to their knowledge and experience, and also for all the “contrat cactus” talks. My dear fellows from the CSEM Ph.D club, Bastien, Sher, Oswaldo. Angélique and Aurélie for their kindness and the technical support. Gaëlle for her comments on the manuscript. All the other people from division N for the moments shared during coffee time and Division outings. Massoud all our conversations and his expertise. Special thanks to Sophie and Patricia, the charming staff from Div-N. I also

would like to thank Harry, the head of our Div-N, with whom I always had interesting conversations.

I would like to thank people from EPFL who helped me in diverse ways during my thesis. First, Marie Halm, without her, Ph.D. students would be lost in the administrative labyrinth. Nicolas Xanthopoulos who helped me with the XPS measurements. All the CMi staff, especially Cyrille, Joffrey, Anthony, Didier and Boris.

On the personal side, I would like to thank Fabien, Guillaume, Toko, Maxime, Arnaud, Victor for our longtime friendship. Greg and Gilles, for their support, advices, St Martin and all the other moments to come. Charlie, Nuria, Katka, Olivia, Julius, Vinu, Deepta, Amalric for the fun times in Neuch and Lausanne. Camilla, for giving me the chance to travel the world. Special thanks go to my friends Philippe and Livio who I met in Tokyo for one of the most amazing experience I had during this thesis, these are things creating strong bonds that you never forget. I also would like to thank Margaux who had the difficult task to listen to my complaints every day during the writing, but most of all for her support. The basketball team of Val-de-Ruz, for the fun times during practice and the games which helped a lot to evacuate the pressure.

Finally I would like to thank my family. There are no words to express such gratitude. My parents and my sister, with their love, their support, made every day’s life easier, giving me the strength to rise from complicated situations, professional and personal. They will probably never read this thesis entirely, but at least they will read the acknowledgments section, this is why I want to say that I love them.

Abstract

Nanoporous membranes find many potential applications in biotechnology such as biomolecule separation, sample preparation for diagnostics, protein separation and purification and have therefore attracted the interest of many research groups. “Smart” sieving membranes are of special interest because of their double specificity allowing the size-based separation and the controlled release of molecules.

In this thesis work, efforts have been made to develop a robust and reliable process for the fabrication of ultrathin nanoporous silicon nitride membranes (NSiMs) at wafer-scale combining block copolymer lithography and standard microfabrication techniques. 200 nm thick nanoporous membranes with a mean pore size of 85 nm in diameter, nanopore density of $2.8x10^9$ nanopores/cm^2 and nanoporous areas ranging from 0.5 x 0.5 mm^2 up to 2.5 x 2.5 mm^2 were successfully fabricated. The final NSiMs were characterized in terms of pore opening and pore morphology using different techniques such as Atomic Force Microscopy (AFM), Scanning Electron Microscopy (SEM) and Transmission Electron Microscopy (TEM). The mechanical strength of the overall suspended nanoporous structure has also been evaluated using the bulge test method and 1 mm^2 NSiMs were able to withstand pressures as high as 700 mbar; demonstrating their potential ability to be integrated into pressure driven microfluidic devices.

A method for reducing the mean pore size of the NSiMs has been developed using Atomic Layer Deposition (ALD) technology. This approach allowed the fine tuning of the mean nanopore diameter from 85 nm down to 10 nm, modifying both the transport properties and the selectivity of NSiMs. Molecular transport experiments were conducted by integrating NSiMs into a specifically designed diffusion cell. The diffusion coefficient of fluorescein molecules across NSiMs with a mean pore diameter of 10 nm was found to be reduced by one order of magnitude compared to NSiMs with a mean pore diameter of 85 nm. Size-based separation experiments using FITC-Dextran molecules of different molecular weights were also conducted and a minimum cut-off value of 10 nm (diameter of the molecule) has been reached after pore size reduction.

Finally a thermo-responsive polymer, Poly(N-isopropylacrylamide) (PNIPAM) has been successfully grafted onto NSiMs. The grafting-to in melt approach allowed producing dense PNIPAM brush layers which configuration change upon temperature variation can be used for the pore opening and closing. Promising preliminary results demonstrated the ability of the PNIPAM functionalized NSiMs to act as “smart nano-valves” for the controlled diffusion of molecules. The ON-OFF behaviour of the PNIPAM functionalized NSiMs has been observed for the diffusion of molecules with a hydrodynamic radius superior to 3 nm.

Keywords: Nanoporous silicon nitride membrane, block copolymer lithography, poly(N-isopropylacrylamide), melt grafting, thermo-responsive nano-valve.

Résumé

Les membranes nanoporeuses sont utilisées dans le domaine de la biotechnologie et ce pour des applications comme la séparation de biomolécules, la préparation d'échantillons pour le diagnostic, la séparation de protéines, la purification et ont donc attiré l'intérêt de beaucoup de groupes de recherche. Les membranes de filtration dites « intelligentes » suscitent un intérêt tout particulier grâce à leur double spécificité permettant la séparation de molécules en fonction de leur taille et la distribution contrôlée de ces molécules.

Dans ce travail de thèse, des efforts particuliers ont été faits pour développer un procédé robuste et fiable pour la fabrication de membranes nanoporeuses ultrafines en nitrure de silicium (NSiMs) à l'échelle du wafer. Ce procédé combine la lithographie assistée par bloc copolymères et des techniques de micro-fabrication standards. Des membranes nanoporeuses d'une épaisseur de 200 nm, présentant une taille de pore moyenne de 85 nm, une densité de nanopores de $2.8x10^9$ nanopores/cm^2 avec des aires nanoporeuses allant de 0.5 x 0.5 mm^2 jusqu'à 2.5 x 2.5 mm^2 ont été fabriquées avec succès. L'ouverture totale des pores et la morphologie des NSiMs fabriquées ont été caractérisées en utilisant différentes techniques comme la microscopie à force atomique, la microscopie électronique à balayage et la microscopie électronique en trasnmission. La tenue mécanique de la structure nanoporeuse suspendue a été évaluée en utilisant la méthode de test par gonflement (bulge test). Avec ce test nous avons pu observer que les NSiMs de 1 mm^2 étaient capables de résister à des pressions jusqu'à 700 mbar, ceci démontrant la possibilité d'intégrer ces NSiMs dans des systèmes microfluidiques fonctionnant sous pression.

Une méthode pour réduire la taille de pore moyenne a été développée en utilisant la technologie de déposition par couche atomique. Cette approche a permis d'ajuster la taille moyenne des pores de 85 nm à 10 nm, modifiant les propriétés de transport des molécules et la sélectivité des NSiMs. Des expériences de transport moléculaire ont été menées en intégrant les NSiMs dans une cellule de diffusion spécifiquement conçue pour cet effet. Le coefficient de diffusion des molécules de fluorescéine au travers de NSiMs avec une taille de pore moyenne de 10 nm a été mesuré et se trouve être réduit d'un ordre de grandeur comparé à celui mesuré avec des NSiMs ayant une taille de pore moyenne de 85 nm. Des expériences de séparation de molécules en fonction de leur taille ont été menées en utilisant des Dextrans fluorescents de différents poids moléculaire. Une valeur limite de transport des molécules a été observée pour des molécules ayant un diamètre hydrodynamique de 10 nm lorsque des NSiMs avec une taille de pore minimum (après réduction de taille de pore) ont été utilisées.

Enfin, un polymère thermo responsif, le poly(N-isopropylacrylamide) (PNIPAM) a été greffé avec succès de manière covalente sur les NSiMs. L'approche du greffage sous fusion a permis de produire des brosses de PNIPAM denses observant un changement de conformation en fonction de la température. Ces brosses de PNIPAM greffées sur les NSiMs peuvent être utilisées pour fermer ou ouvrir physiquement les nanopores. Des résultats préliminaires prometteurs ont démontré la possibilité d'utiliser les NSiMs modifiées avec du PNIPAM comme des « nano-valves intelligentes » pour la diffusion contrôlée de molécules. Le comportement ON-OFF des NSiMs modifiées avec du PNIPAM a été observé pour la diffusion de molécules ayant un rayon hydrodynamique supérieur à 3 nm.

Mots-clés : Membrane nanoporeuse en nitrure de silicium, lithographie assistée par bloc copolymère, poly(N-isopropylacrylamide), greffage sous fusion, nano-valve thermoresponsive.

Contents

Chapter 1

Introduction

1.1. Suspended thin nanoporous membranes in biotechnology

A porous membrane is the interphase between two adjacent phases acting as a selective barrier, regulating the transport of substances between two compartments [1]. In general, porous materials are referred as nanoporous when the mean pore size is comprised between 1 and 100 nm [2]. Over the past half-century, with the emergence of new manufacturing techniques able to produce features down to the nanometer scale, manufacturing new synthetic thin nanoporous membranes have attracted interest of many research groups. Indeed, nanoporous membranes find numerous applications in biotechnology such as biomolecule and protein separation, sensing, sample preparation, sample purification and drug delivery [3,4]. Adiga et al. have used nanoporous membranes to control the diffusion kinetics of therapeutic agents [5]. Nanoporous membranes have also been used for the filtration of several molecules such as the rhinovirus 14 [6], bovine serum albumin, lysosome and myoglobin with controlled selectivity by modifying the electric potential applied to the conductive membrane [7]. Cell growth experiments with drug delivery through the nanoporous membranes to control the biochemical environment were demonstrated [8]. Long et al. integrated polycarbonate track etch nanoporous membranes in a microfluidic chip for sample preparation (pre-concentration of produced DNA from a PCR mixture) with electrophoretic separation [9].

Several key characteristics of nanoporous membranes such as the molecular cut-off, the selectivity, the throughput (high flux), chemical and mechanical stability are affecting the performance depending on the targeted application (Figure 1.1). In the case of size-based filtration, the mean diameter of the nanopores and their size distribution is important to reach precise control over molecular transport. In addition, a minimum thickness and a high porosity will enable high flux with low flow resistance across the membrane. But decreasing the thickness will also decrease the mechanical strength of the suspended nanoporous membrane. Therefore, a compromise should be found between flow rate and mechanical strength depending on the device integrating the nanoporous membrane (pressure driven or free diffusion). Some applications integrating devices in harsh environment would consider critical the mechanical, chemical and thermal stability [10,11] while others would give priority to the surface chemistry. Typically, biomedical applications consider critical the biocompatibility of membranes as well as minimum fouling [4]. Specific molecular characteristics in drug delivery, protein separation and purification, can lead to high selectivity of the nanoporous materials [12–14]. Indeed, biomolecules can interact in diverse ways depending on the type of nanofilter used, leading to unique molecular separation and filtration methods [15].

The flexible and careful design of such sieving systems can lead to novel membrane functions. In order to transfer a synthetic nanoporous membrane technology to industrial fabrication, precise control over device performance and scalability for economical production are required.

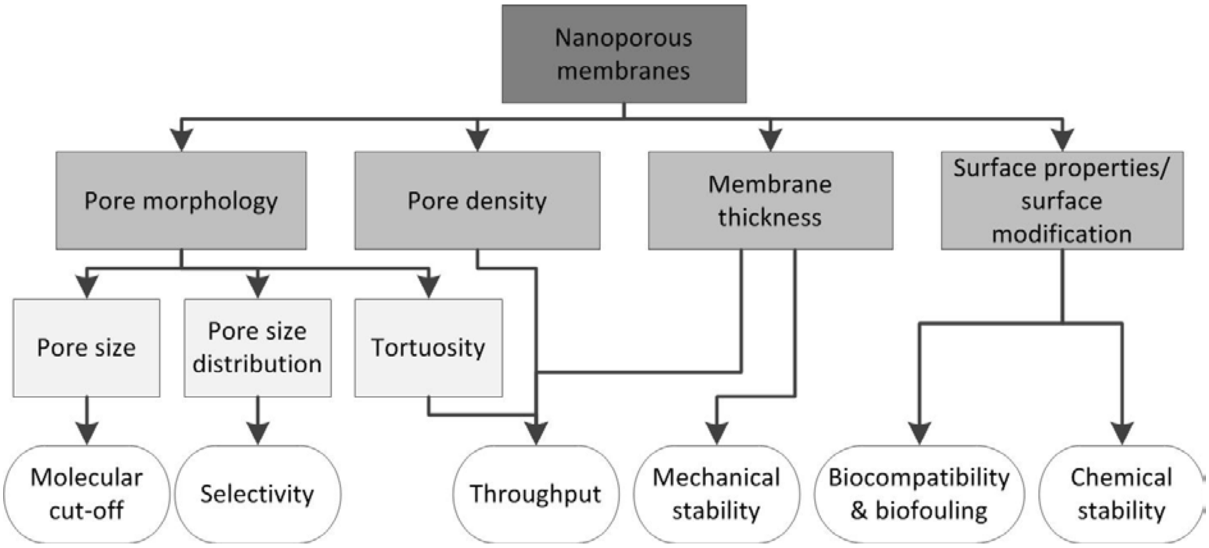

Figure 1.1 Diagram of key membrane characteristics that affect performance. (Adapted from [4])

Nanoporous membranes can be classified into three main categories, organic polymeric membranes, Anodic Aluminum Oxide (AAO) membranes, and silicon-based membranes. Polymeric nanoporous membranes and AAO membranes are two types of nanoporous membranes commercially available and widely used in laboratory experiments. A brief state of the art regarding these three main types of nanoporous membranes will be discussed in the next sections with a focus on the fabrication methods, the type of pores (order, shape and size) and their chemical and mechanical stability.

1.1.1 Organic polymeric membranes

Polymeric track etch membranes

Nanoporous polymeric materials have extensively been used in gas separation, reverse osmosis, ultrafiltration catalysis and lab-on-chip technologies [1]. The ion track etching (ITE) technique is by far the most employed technique to create nanopores in polymeric films such as polyethylene terephthalate (PET), polycarbonate (PC) and polyimide (PI) [16–19]. Most of the commercially available polymeric nanoporous membranes are fabricated using the ITE method. The ion track etching technique has been reported in the early 1960's by Fleischer et al. [20], this technique consists in irradiating the polymeric sheets with heavy ions or alpha particles in order to damage the material and create "latent-tracks". The polymeric sheets are submitted to a subsequent appropriate chemical etching depending on the material. Pore formation occurs along the damaged areas, with a pore geometry that can be conical or cylindrical depending on the ratio of the etching rates of the bulk over the tracks [21]. The track core diameter defines the future diameter of the pore during etching and can be controlled with the etching time [22]. Nanopore diameters ranging from 10 nm to 10 µm can be obtained with a pore density in the order of 10^8 pores/cm^2 and a film thickness ranging from 3 to 11 µm [3,16,21]. Nanoporous track-etched membranes exhibit in general a fair chemical and mechanical stability, whereas they present a good biocompatibility; the manufacturing is highly upscalable allowing low-cost production.

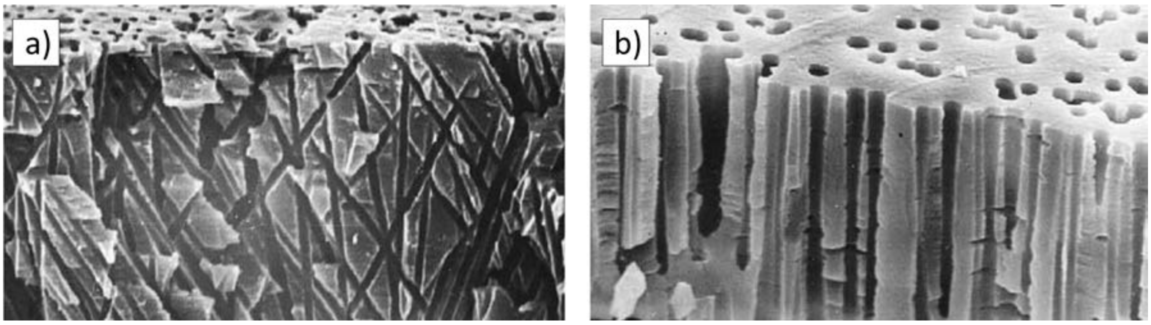

Figure 1.2 Examples of porous structures obtained with the ion track etching techniques. SEM cross section of **a)** PCTE membrane with cylindrical non parallel pore channels, **b)** PCTE membrane with slightly conical (tapered towards the center) parallel pores. (Adapted from [22])

Block copolymer self-assembled membranes

In the last few years, efforts have been made to develop a new class of organic polymeric membranes the so-called "self-assembled" nanoporous membranes. Improved knowledge about the self-assembly of *block*-copolymer allowed demonstrating their ability to phase separate on the nanoscale into various types of architectures (spheres, cylinders, gyroid, lamellae) depending on the relative length of the blocks, each having different intrinsic properties (e.g. polarity) [23]. Peinemann et al. reported the fabrication of 90 μm thick nanoporous membrane with the phase-inversion of amphiphilic poly(styrene-block-4-vinylpyridine) (PS-*b*-P4VP). The resulting non-ordered porous structure typical of the phase-inversion was covered by a 200 nm thick layer exhibiting well-ordered cylindrical pores perpendicular to the film surface with a mean diameter of 40 nm (Figure 1.3). This asymmetric morphology is a direct consequence of the combination of non-solvent-induce phase separation and the self-assembly of block copolymers [24]. Yin et al. produced 600 nm thick PS-*b*-P2VP films presenting cylindrical nanopores with mean pore diameter of 40 nm by annealing in a neutral solvent and subsequent immersion of the films in a selective solvent [25]. Dorin et al. reported the fabrication of 30-60 μm thick nanoporous membranes with a mean pore diameter of 7 nm and pore density as high as 10^{15} pores/cm^2. This type of membrane were fabricated using the self-assembly and non-solvent induced phase separation technique with triblock terpolymers [26].

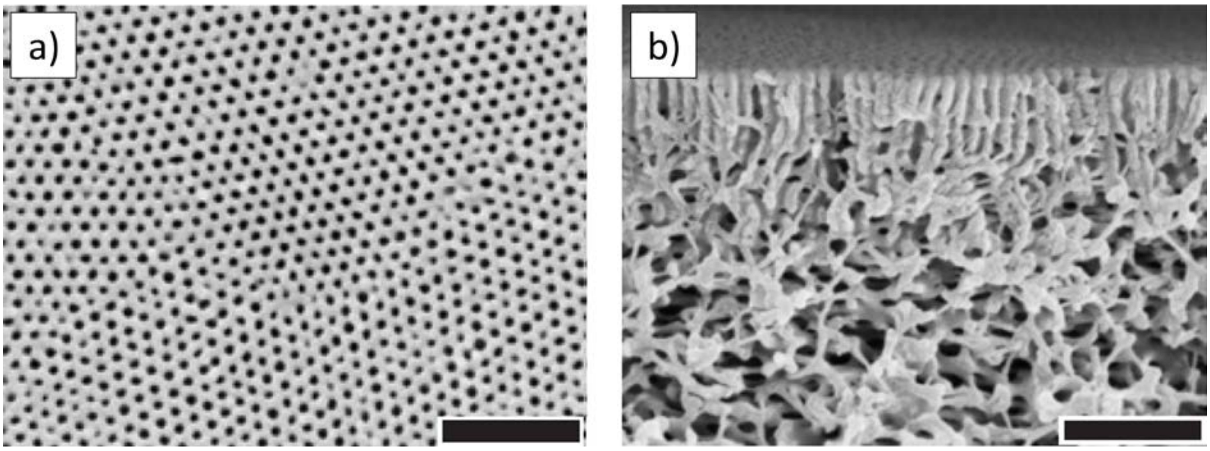

Figure 1.3 SEM images of **a)** the surface of an asymmetric PS-*b*-P4VP diblock copolymer film and **b)** its cross-sectional morphology. The scale bars correspond to 500 nm. (Adapted from [24])

Although self-assembled membrane systems present low-cost preparations, structural self-regulation and tunable properties, ultra-thin membranes with uniform pore in the size range of few nanometers is still difficult to achieve, and both the chemical and mechanical stability of these membranes remain fair. The upscalability of this fabrication method still remains a challenge.

1.1.2 Anodic Aluminum Oxide (AAO) membranes

Anodic Aluminium Oxide (AAO) nanoporous membranes have been fabricated, commercialized and widely used in various domains such as the selective transport of small molecules, energy charge transport, gas adsorption or ion exchange [3,4,14]. The fabrication of AAO is based on the electrochemical anodization with the self-ordering process of nanopores, producing densely packed hexagonal array and size controlled nanopores. The anodization process is performed by applying an electric potential on an aluminium substrate in a sulphuric, phosphoric, chromic or oxalic solution [27–29].

In AAO membranes, several parameters can be precisely tuned such as the pore diameter in the range of 10-400 nm which highly depends on the type of electrolyte and the anode voltage used [30], the interpore distance from 50 to 600 nm, the pore aspect ratio from 10 to 5000, the thickness of the porous layer can vary from 10 nm up to 150 µm, the pore density from 10^9 to 10^{11} pores/cm^2 and the porosity from 5 to 50 % [31–33]. It has been demonstrated that several parameters can affect the anodization conditions such as the applied potential [34,35], the current [36,37], the pH and electrolyte type [38,39], the temperature [40] and the pre-patterning of the surface [41,42]. All these parameters can be modified in order to improve the control over the self-ordering mechanism and obtain ordered AAO pore structure with tunable parameters such as the pore diameter and the interpore spacing.

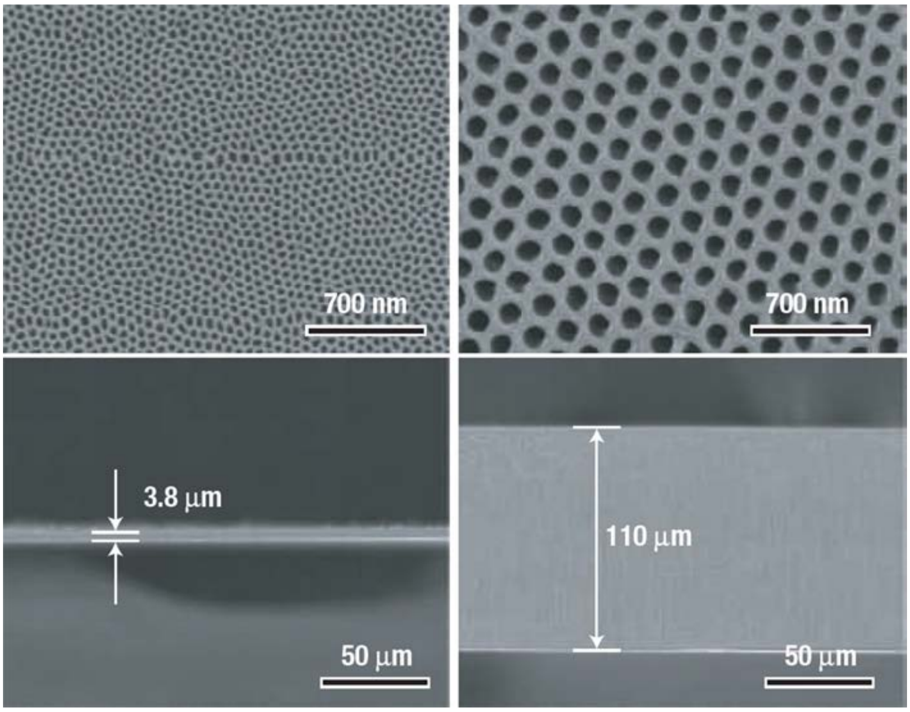

Figure 1.4 SEM micrographs of different AAO nanoprous structures. The arrangements of pores are shown in the upper SEM micrographs and the corresponding cross-sectional view below. (Adapted from [43])

A critical step in the fabrication of AAO suspended nanoporous membranes is the release of the porous layer in order to obtain a free standing structure. Several techniques have been developed to release the structures such as the chemical dissolution. This latter consists in partial anodization of the aluminium layer and subsequent chemical etching of the residual Al substrate [44,45]. AAO nanoporous films have also been processed onto silicon chips and the full release of the structure obtained via KOH etching through backside apertures defined by photolithography. In some cases sacrificial and supporting layers can be used to protect the structure to be released. Wu et al. used silicon nitride as a supporting layer to protect a nanoporous hetero structure made of AAO/a-Si during the KOH release, the supporting layer is then removed by selective etching [46].

The major disadvantage of AAO free standing nanoporous membranes is that alumina is a brittle material, and when attempting to increase the throughput of the membrane by decreasing its thickness the mechanical stability of these structures is highly impaired. On the other hand, manufacturing AAO nanoporous membranes remains low cost, they can present a wide variety of pore structures (size, interpore distance, thickness) and a good chemical stability and biocompatibility.

1.1.3 Silicon-based membranes

With the emergence of new micro and nanofabrication manufacturing technologies (especially for the microelectronic industry), producing nanoporous membranes in MEMS compatible substrates (silicon, silicon dioxide, silicon nitride) has attracted the interest of many research groups not only because these techniques allow the fabrication of ordered cylindrical nanopores, but also because these materials present an excellent mechanical stability, allowing the fabrication of ultrathin nanoporous membrane (below 100 nm) for high throughput systems. Additionally, the nature of the material make this type of membrane an excellent candidate for easy surface functionalization, or direct integration into MEMS and lab-on-chip devices aiming at molecule separation and sensing applications.

The flexibility in the porous structure design (ordering of the nanopores and nanopore density) achievable with the MEMS manufacturing technologies make silicon-based nanoporous membranes more attractive than polymeric-based membranes. In addition, the excellent mechanical strength of silicon-based nanoporous materials offer a good alternative to the brittle nanoporous alumina described earlier if integration in pressure driven devices is envisaged.

However the fabrication of silicon-based nanoporous membrane is in general expensive. Efforts are going towards increasing the fabrication yield and developing inexpensive large-scale patterning techniques of an intermediate material (typically photoresist or metallic hard mask) used as a photolithographic mask for subsequent dry etching in the underlying silicon-based material to create the nanopores. Membranes openings for the full release of the nanoporous structure are generally obtained by patterning the silicon support (typically 4, 6 or 8 inches wafer) with standard photolithography and subsequent wet or dry etch through the whole wafer. In some cases an etch stop and a protective layers are necessary in order not to damage the active nanoporous areas during the release process.

Direct writing with Electron Beam Lithography (EBL) and Focused Ion Beam (FIB)

For the fabrication of silicon-based nanoporous membranes, some techniques allow the "direct writing" of nanopores into the substrate. For instance, the fabrication of nanopores with a diameter of 25 nm in a 10 nm thick silicon nitride layer using Focus Ion Beam (FIB) has been reported [47]. Electron Beam Lithography (EBL) has also been used to create nanopores down to 2 nm in diameter in 40 nm thick silicon oxide layer [48,49]. However these two direct writing techniques are expensive, time consuming and large-scale manufacturing cannot be considered even if good uniformity, reproducibility and small pore dimensions can be achieved. Another technique that can be considered as almost direct is the ion track etching (ITE) technique. Indeed this technique described earlier can also be applied to silicon-based materials. Vlassiouk et al. reported the fabrication of ITE Si_3N_4 nanoporous membranes by irradiating Si_3N_4 with heavy ions and subsequent wet etching in H_3PO_4 to create nanopores along the damaged tracks [50]. 200 nm thick suspended silicon nitride membranes with conical or double conical nanopores with a maximum inlet and outlet diameters of 60 nm and 10 nm, respectively, were fabricated. The nanopore mean diameter can be controlled with the duration of the wet etching process. The main disadvantage of this technique is that there is no ordering of the nanopores due to the randomness of the impact position of the heavy ions onto the surface that can sometimes lead to the fusion of several nanopores creating larger undesired apertures. In addition, the nanopore density achievable with this fabrication technique remains low (~10^8 nanopores / cm^2).

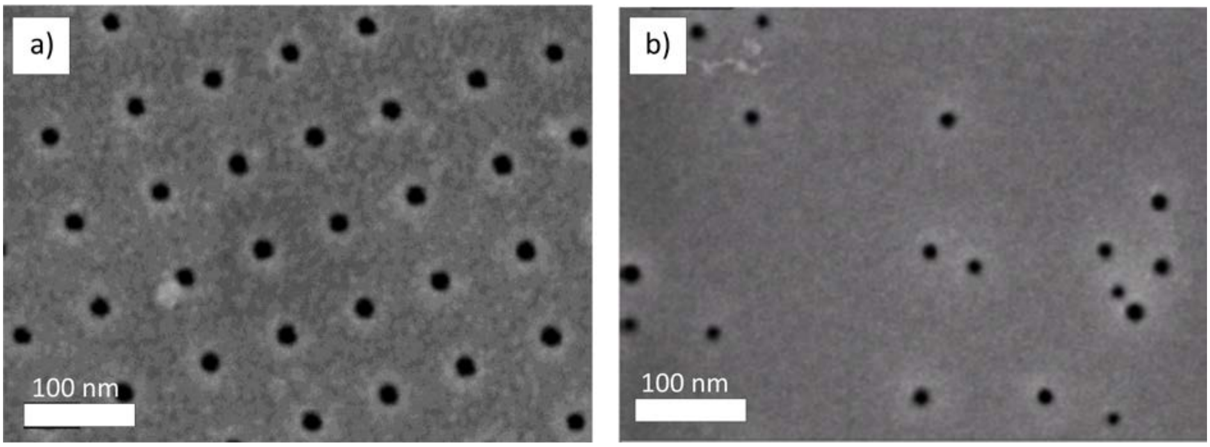

Figure 1.5 Top view SEM micrographs of nanopores in silicon nitride obtained by **a)** FIB and **b)** ITE. (Adapted from [47,50])

Thermal annealing of amorphous silicon

Striemer et al. reported the fabrication of nanoporous membranes resulting from a thermal annealing on a thin layer (15 nm) of amorphous silicon [51]. The pore diameter can be adjusted between 9 and 35 nm depending on the thermal annealing temperature (Figure 1.6). However, this method does not allow a control over the number of pores and the size distribution. These membranes are commercialized by SIMPore for Electron Microscopy, separation and purification, cell culture, lab-on-a-chip applications. The demonstrated mechanical strength of these ultrathin membranes should allow the construction of large-scale dialysis systems, and facilitate their use in pressurized filtration devices at the macro and microscale.

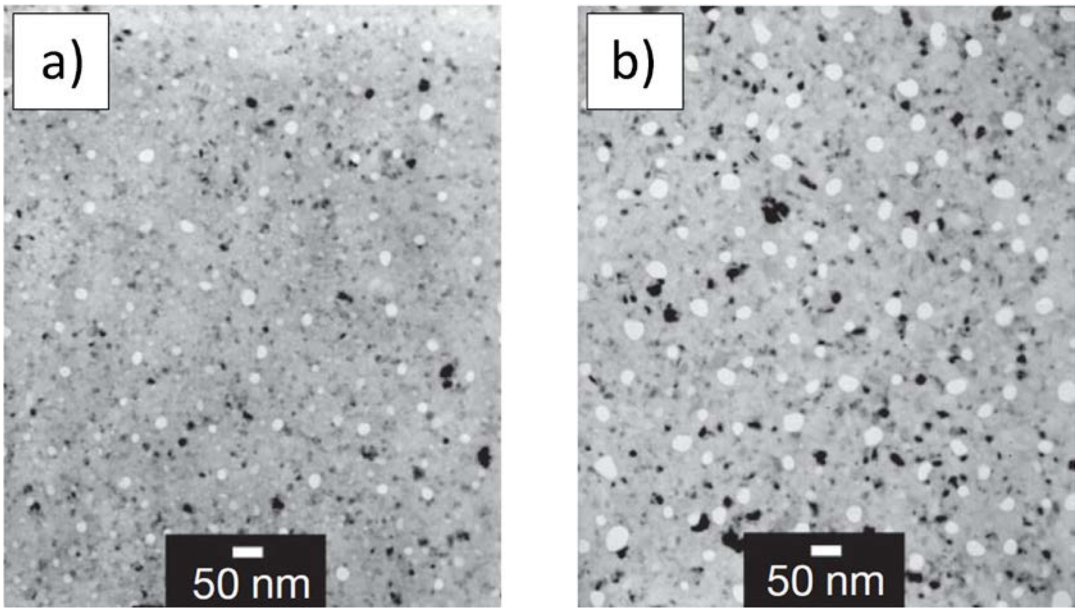

Figure 1.6 TEM images of a 15 nm thick pnc-Si nanoporous membrane obtained after thermal annealing at **a)** 729°C and **b)** 753°C. In these bright field pictures nanopores appear as bright spots. (Adapted from [51])

Laser Interference Lithography (LIL)

During the past decade, Laser Interference Lithography (LIL) has been widely used to produce highly uniform micron as well as sub-micron features over large areas and this in an inexpensive way. This process is based on interference of two or more laser beams on a surface generally composed of an anti-reflection coating and photoresist. The periodic pattern generated into the photoresist is as small as half the wavelength of the laser. The patterned photoresist is then used as template to create a nanolithographic mask by deposition of a “hard” material and lift-off of the patterned photoresist (Figure 1.7). This hard mask is then used for subsequent pattern transfer into the underlying silicon-based layer by dry etching. This technique is suitable for the fabrication of nanoporous membranes with perfect order and size distribution [52–54]. Recently, Ileri et al. have reported the fabrication of 340 nm thick suspended silicon nitride layer with nanopores ranging from 50 to 400 nm in diameter depending on the laser exposure conditions [55]. LIL has the potential to produce nanoporous membranes with high precision and at large scale; however some efforts should be made regarding the complexity of the process to align/re-align the lasers for successive exposure and the price of the instruments in order to adapt this technique for industrial production of nanoporous membranes.

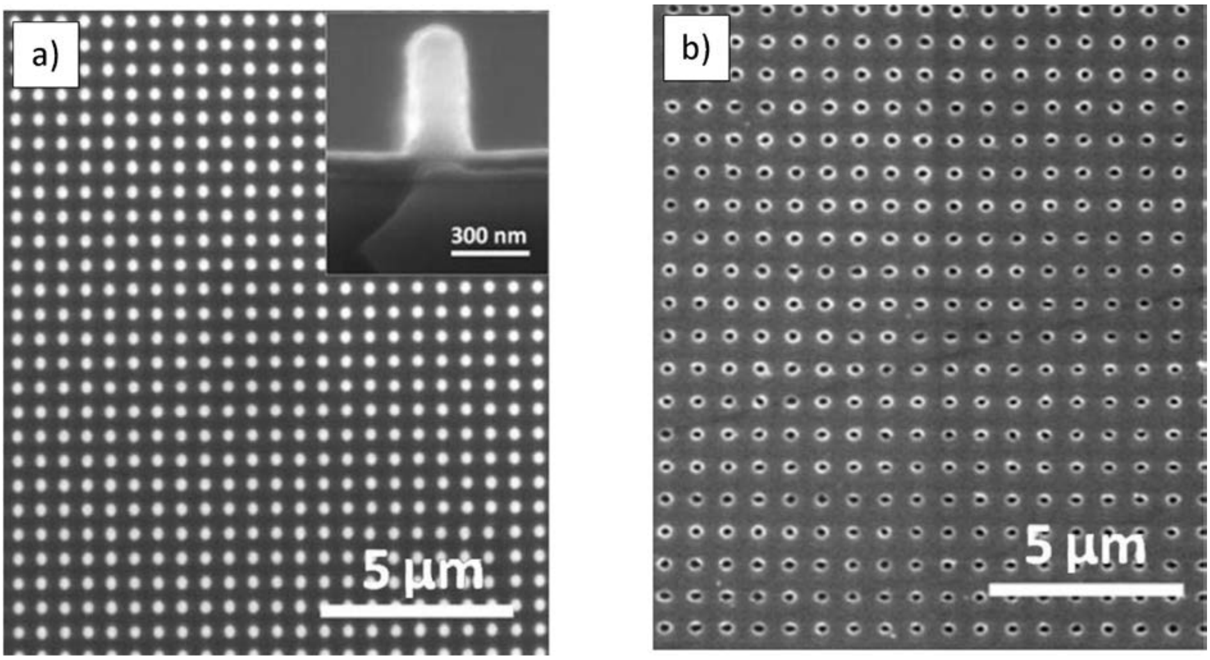

Figure 1.7 Top view SEM micrographs of **a)** initial pattern created in photoresist after lasers alignment and exposure, **b)** intermediate nanoporous chromium mask created by deposition of 75 nm of Cr and lift off of the patterned photoresist. (Adapted from [55])

Anodic Aluminum Oxide Lithography (AAOL)

As for laser interference lithography, other techniques use an intermediate nanoporous hard mask to transfer the nanopattern in the silicon-based material via dry etching. AAO nanoporous layer used as nanolithographic mask for subsequent etching into silicon has been reported in the early 2000’s [56]. Wolfrum et al. reported the fabrication of 130 nm thick suspended nanoporous silicon nitride layer with different pore size and pore density using a AAO nanoporous template [8]. The final nanoporous structure was obtained by depositing directly 500 nm of aluminum onto the silicon nitride and processing it to the anodization step. The different pore sizes and densities obtained reside in one critical step which is the thinning of the AAO template to enhance the effectiveness of the subsequent pattern transfer in silicon nitride using dry etching. Indeed, depending on the etching time of the thinning step, the AAO nanoporous pattern can either be completely or partially transferred (Figure 1.8). Porosities ranging from 0.2% up to 44% were thus achieved. However, the etching selectivity of alumina over silicon nitride is not high enough because both are usually used as “hard” etching mask. On the other hand, the selectivity of alumina over silicon has been demonstrated to be remarkably high in cryogenic conditions (1:70000) [57]. Wu et al. have used a thin AAO nanoporous template for pattern transfer by RIE into amorphous silicon for the fabrication of hetero-structured Al_2O_3/SiO_2 membranes used as nanofluidic diodes [46].

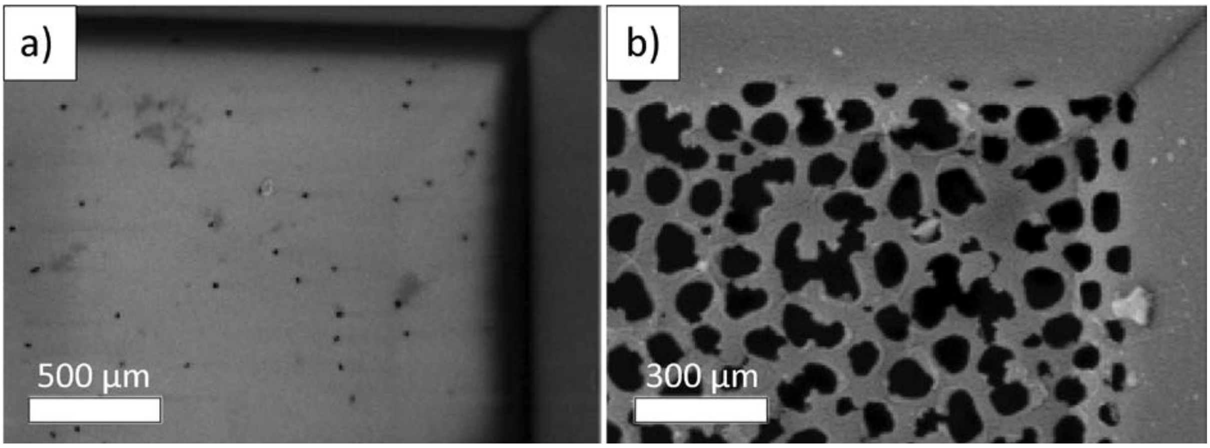

Figure 1.8 SEM micrographs of suspended silicon nitride nanoporous membranes with **a)** low porosity (~0.2%) and **b)** high porosity (~44%) obtained by changing the thinning conditions of the starting nanoporous AAO template before pattern transfer by RIE. (Adapted from [8])

NanoImprint Lithography (NIL)

Recently, Nano-Imprint Lithography (NIL) has been demonstrated to be a large scale, low-cost and high throughput technique to produce namometer scale apertures in an intermediate layer (typically resist) using a previously nanopatterned mold. The patterned resist is then used as a nanolithographic mask for subsequent RIE in silicon-based substrates for the fabrication of nanoporous layers and suspended membranes [58,59]. In some cases, the imprinted resist layer is not suitable for pattern transfer by RIE because it is not enough mechanically robust to endure the harsh etching environment, and therefore could create distortion when transferring the original pattern in the underlying layer. To overcome this issue, thin nanoporous metallic hard mask can be produced via a two steps lift-off process using the nano-imprinted resist layer as starting template [60,61]. However, this latter is adding extra fabrication steps increasing the overall complexity of the process flow for the fabrication of nanoporous membranes. Recently, Nabar et al. reported the fabrication of 1 μm silicon nitride nanoporous layer with a mean pore diameter of 385 nm using NIL (Figure 1.9) [61]. These nanoporous membranes were meant to be used as gas exchange interfaces in blood oxygenation systems. Smaller feature size (100 nm) can be achieved using silicon NIL stamps (mold) as demonstrated recently by Villanueva et al. [62]. Fabricating durable NIL molds using high resolution lithography techniques is of particular concern to apply NIL for the low-cost production of suspended nanoporous membranes in silicon-based materials. Nano-Stencil Lithography (nSL) has been demonstrated to be a very promising technique for direct nanopatterning of surfaces, and especially the low-cost fabrication of NIL molds [62,63]. nSL is generally based on the use of a previously nano-patterned thin nanoporous membrane as a nanolithographic mask (stencil) for metal deposition or direct dry etching of the underlying substrate through the defined apertures of the stencil. However, EBL is used for the fabrication of the stencil, which remains a time consuming and expensive technique.

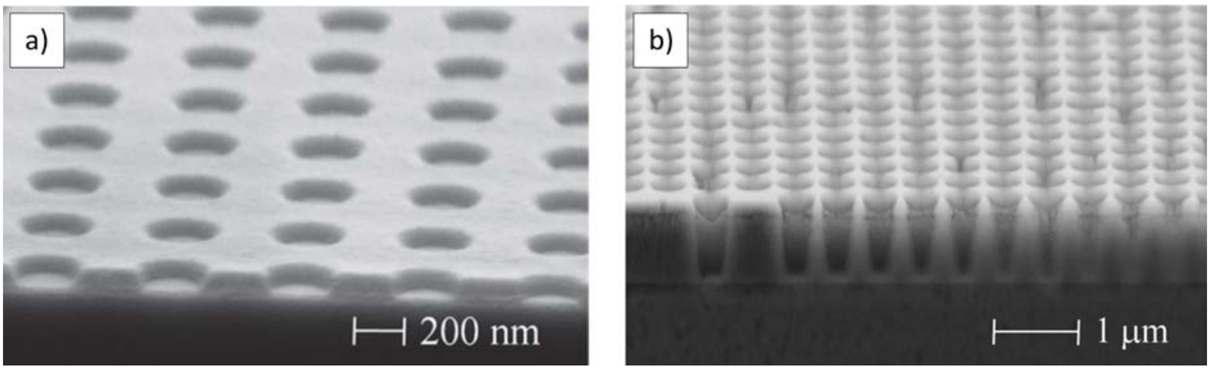

Figure 1.9 SEM micrographs of **a)** the nano-imprinted resist and **b)** the final silicon nitride nanoporous layer obtained by RIE through a Al_2O_3 nanoporous mask (obtained with a two-steps lift-off from the patterned resist). (Adapted from [61])

Block CoPolymer Lithography (BCPL)

Silicon-based nanoporous membranes have also been fabricated using an intermediate nanolithographic mask produced from the self-assembly of diblock copolymers, this technique is called Block Copolymer Lithography (BCPL). Indeed, as already mentioned previously, diblock copolymer may self-assemble into various architectures (spheres, cylinders, gyroid, lamellae) depending on the relative length of the blocks when dissolved in a good solvent for one of the two blocks [64]. Black et al. reported the fabrication of a 100 nm thick nanoporous silicon membrane with a mean pore diameter of 20 nm and a pore density as high as 10^{11} pores/cm^2 (Figure 1.10) by combining the self-assembly of polystyrene-*b*-polymethylmethacrylate (PS-*b*-PMMA) copolymer and standard microfabrication techniques [65]. The PS-*b*-PMMA thin film deposited onto silicon phase separate into closed pack cylindrical PMMA domains embedded in a PS matrix when annealed at high temperature. In this case a pre-treatment of the surface is necessary in order to promote the vertical orientation of the cylindrical PMMA domains. The PMMA is then removed by UV curing and dissolution into acetic acid. The nanoporous PS template is then transferred into the underlying silicon substrate. The mean pore size can be tailored by adjusting the polymer molecular weight adding flexibility to the design of the porous structure for the fabrication of membranes.

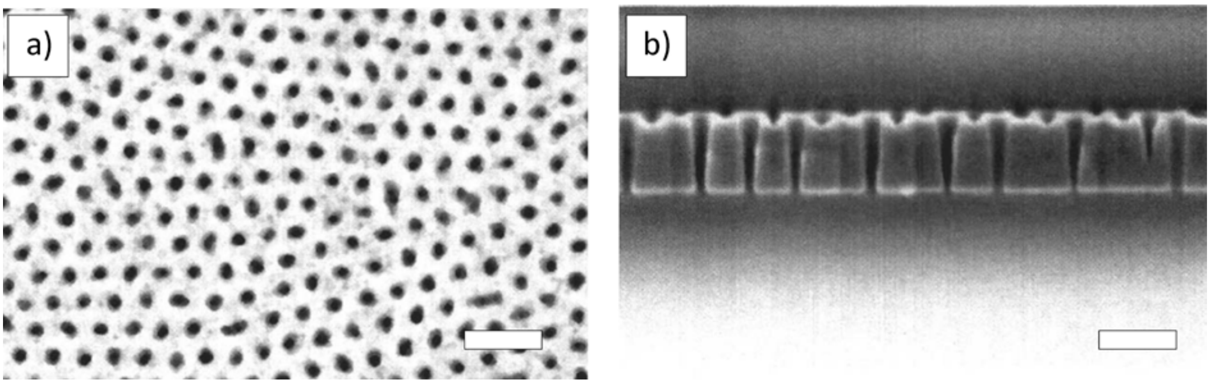

Figure 1.10 SEM micrographs of **a)** the nanoporous PS thin film (top view) and **b)** the 100 nm thick suspended nanoporous silicon membrane (cross sectional view), the scale bar is 100 nm. (Adapted from [66])

Krishnamoorthy et al. used polystyrene-*b*-poly(2-vinylpyridine) copolymer (PS-*b*-P2VP) reverse micelles as a starting nanoporous template for the fabrication of silicon nanoporous layers. A 2D monolayer of PS-*b*-P2VP reverse micelles is spin coated onto a silicon substrate, the micelles array can be inverted from nanobumps to nanoholes by liquid phase exposure to methanol [67,68] leaving a nanoporous polymeric layer that can be used for pattern transfer into the underlying silicon substrate. Popa et al. demonstrated the fabrication of 100 nm thick nanoporous silicon nitride membranes with a mean pore diameter of 85 nm and a pore density of 3x10^9 pores/cm^2 (30 pores/µm^2) using a monolayer of reverse PS-*b*-P2VP micelles as starting template [69,70] (Figure 1.11). A thin chromium layer evaporated onto the micelles followed by a lift-off step of the micelles allowed creating a metallic nanoporous hard mask. The nanoporous Cr layer was then used to create nanopores in silicon nitride using RIE. The mean nanopore diameter is defined by the mean diameter of the deposited micelles. This fabrication process has been demonstrated to be compatible for the nanopatterning of 4 inches wafer. However, several issues were encountered by Popa et al. and some efforts can still be made regarding the homogeneous deposition of micelles at wafer scale, the lift-off procedure, the dry etching of the nanopores and the release of the final structure. Depending on the molecular weight of the blocks, the diameter of diblock copolymer micelles can range from 10 nm up to 200 nm. This latter is adding flexibility to the design of the porous structure. In addition, it has been demonstrated that the pore density can be adjusted with the micellar solution concentration and the inter-micelle distance with the spin-coating speed [67]. The ability to generate a tunable nanopattern at large scale in a fast and low-cost way make BCPL a very promising technique for the fabrication of nanoporous membranes. However the size distribution and pore ordering of the features produced with BCPL cannot be compared to the high precision of EBL, FIB, LIL or NIL.

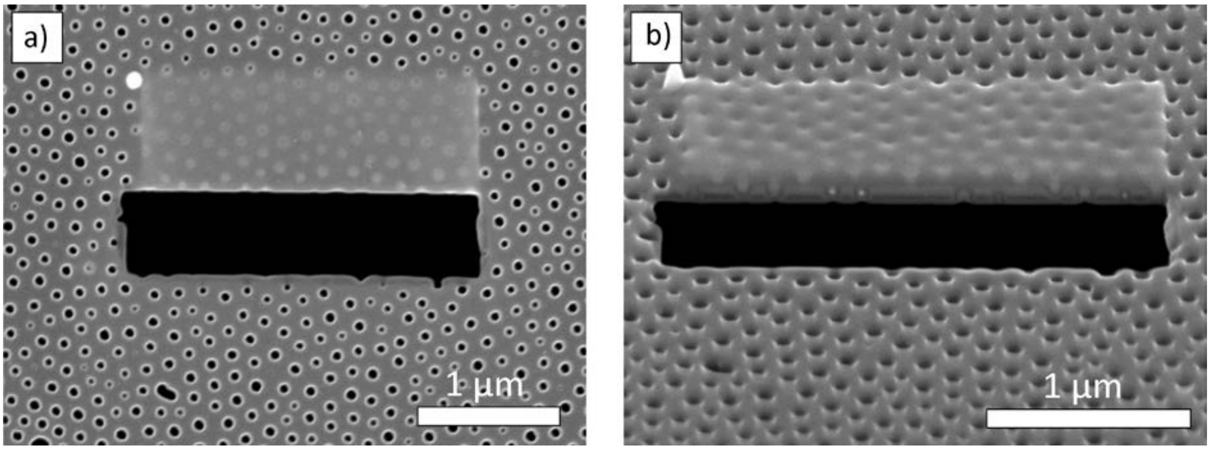

Figure 1.11 SEM micrographs **a)** top view and **b)** tilted view of the 100 nm suspended nanoporous silicon nitride membrane with a cross-section made by FIB. (Adapted from [70])

Nanosphere lithography has also been used to fabricate silicon-based nanoporous surfaces or membranes [71–73]. This approach is similar to the one employing block copolymer micelles. The surface is first patterned by the deposition of nanospheres, followed by the evaporation of a metallic layer and a subsequent lift-off of the nanospheres. The remaining nanoporous metallic hard mask is subsequently used to transfer the pattern by RIE in the underlying silicon-based layer. However, the diameter of the nanospheres (polystyrene) described in the work are too large (250 nm) to consider the fabrication of membranes with pores sizes down to 10-100 nm. Brieger et al. also described a similar process using the self-organization of $HAuCl_4$ loaded inverse micelles formed by PS-*b*-P2VP in toluene. The Au nanoparticles are then used as starting template for the fabrication of nanoporous silicon surfaces [74].

1.2. Aim of the thesis

The aim of this thesis work is the fabrication of responsive nanoporous membranes that can be used as “smart” nano-vales for the size-based separation and controlled transport of molecules.

Literature shows that several fabrication techniques are now available to produce nanoporous membranes made of different materials. However, some of the methods described earlier generally offer a limited control over the pore size, size distribution, throughput, mechanical stability, chemical stability, upscalability and cost. There is a need in finding the best compromise between the key membrane characteristics in order to identify a suitable nanoporous membrane fabrication technology able to fulfill all the requirements of the targeted applications.

In this work, the targeted applications are the size-based separation and controlled transport of biomolecules. These applications can both be achieved with the double specificity of responsive nanoporous membranes. The responsive behavior for the controlled transport of molecules can be achieved by grafting polymer chains able to operate a morphological change in order to physically close or open the nanopores. The nanoporous membranes must provide solutions to several challenges in order to be used effectively for the mentioned applications. The mean pore size should be sub-100 nm. The nanoporous membranes would need to be ultrathin and highly porous in order to achieve high throughput (high flux). The mechanical strength of the suspended nanoporous structure should be high enough to raise the possibility of integration into pressure-driven microfluidic devices. The material of the nanoporous membrane needs to be a good base chemistry for easy functionalization with a wide variety of reactive groups (grafting of “smart” polymers). The fabrication of nanoporous membranes has to be up-scalable in order to reduce the cost per membrane. The design of the membrane itself and the supporting structure should be suitable for integration into microfluidic devices for evaluation of their molecular transport properties.

In order to provide answers to the challenges mentioned above, the material and fabrication method used to produce nanoporous membranes will be chosen in consequence. This latter will be discussed in the following sections.

1.3. Choice of material and fabrication method

Choice of material

The material characteristics of particular concern for the fabrication of nanoporous membranes in biotechnology (e.g. molecular transport, biomolecule separation, sample preparation) are reported in Table 1.1.

Table 1.1 Summary of material characteristics for the fabrication of nanoporous membranes.

Material	Chemical stability	Mechanical stability	Biocompatibility	Cost
Polymer (PC, PP, PI, PE, PS)	Fair	Poor/Fair	Fair/Good	Low
Alumina	Good	Fair/Good	Good	Medium
Silicon based (Si, SiN, SiO_2)	Good	Good/Very good	Good	Medium/High

As mentioned earlier, a porous membrane system in biotechnology generally requires high throughput, especially in the case of molecular transport. In order to increase the throughput the membrane thickness has to be reduced to the lowest possible while keeping a good mechanical strength for easy manipulation or integration into pressure-driven microfluidic devices. Silicon nitride appears to be the ideal material because of its excellent mechanical strength compared to the other materials used and described in literature for the fabrication of ultrathin suspended nanoporous membrane. Silicon nitride also presents an excellent chemical stability. A wide variety of solvent can be used during the fabrication process without damaging the layer. In addition silicon nitride is a material compatible with the microelectronic manufacturing equipment, allowing processing this material in clean room environment. Fabricating nanoporous membranes in a dust free environment is extremely important because dust particles can be 10 to 100 times larger than the mean pore size targeted. Finally, silicon nitride is an interesting base chemistry for easy surface functionalization with a wide variety of reactive groups.

Choice of fabrication method

Earlier, several methods used to process silicon-based material combining a nanopatterning technique and conventional microfabrication processes for the fabrication of nanoporous membrane were reviewed. A summary of the advantages and disadvantages of each nanopatterning method is presented in Table 1.2.

Table 1.2 Summary of advantages and disadvantages of the nanopatterning techniques reviewed for the fabrication of silicon-based nanoporous membranes.

	Direct writing EBL/FIB	**LIL**	**AAOL**	**NIL**	**BCPL**
Process setup and complexity	+ + +	-	+ +	+	+ +
Process cost (materials, equipment)	- - -	-	+	+	+ + +
Process time	- - -	- -	+ +	+	+ + +
Large scale processing	+	+ + +	+ + +	+ + +	+ + +
Pore ordering	+ + +	+ + +	+ + +	+ + +	+
sub-100 nm	+ + +	-	+ + +	+ +	+ +
Tunability of porous structure (size, interpore)	+ + +	+	+ + +	+ + +	+ +
Pore size distribution	+ + +	+ + +	+ +	+ + +	-

Block copolymer lithography has been chosen as nanopatterning technique and combined to conventional microfabrication processes (e.g. RIE, KOH release) for the fabrication of nanoporous silicon nitride membranes. Indeed, this technique fulfills the requirements regarding the targeted dimensions for the mean nanopore size (sub-100 nm) and the tunability of the original nanopattern (density, feature size and interspace). In addition it is a very low cost technique in terms of materials and equipment required, and it can generate a nanopattern at large scale (4 inches wafer) in a very short time (~

1 min). The detailed process flow and the different fabrication steps will be described and discussed in the next chapter.

1.4. Structure of the thesis

This thesis work is composed of 6 chapters.

In the previous sections of this chapter was presented a short review of the different types of nanoporous membranes used in biotechnology for applications such as biomolecule separation, sensing or sample preparation. The fabrication techniques used and the membranes specifications were described and discussed. The material and the nanopatterning technique used in this thesis work were chosen by comparing the advantages and disadvantages of each technique described and reported in the literature.

Chapter 2 will describe the full fabrication process of silicon nitride nanoporous (NSiMs) membranes by combining block copolymer lithography and conventional microfabrication techniques. The tunability of the starting micellar template (feature size, density) will be demonstrated, and a standard micellar system will be chosen to pursue the fabrication. The membrane design (size of the active areas, arrays of membrane) will also be discussed and presented.

Chapter 3 will mostly deal with the characterization of the fabricated NSiMs. Indeed, the final control of full pore opening is the main criteria of validation of the membranes before using them for the targeted application. Several characterization techniques will be presented and compared. Then, the mechanical strength of the suspended nanoporous membranes will be characterized by processing the membranes to the bulge test. This test allows determining the maximum pressure one membrane can withstand, and therefore evaluate the possibility of integration into pressure driven microfluidic devices. Finally, the undesired effect of buckling of suspended thin films will be discussed.

In chapter 4 will be discussed the functionalization of NSiMs. First the possibility to tune the mean pore size after fabrication using Atomic Layer Deposition will be presented. Second, a thermo responsive polymer brush will be covalently grafted onto the NSiMs using the grafting to in melt technique which allows the easy and dense grafting of polymer brushes onto a functional surface. Finally, the thermo responsiveness of the polymer brush layer will be characterized and demonstrated using several techniques such as nanoindentation and atomic force microscopy in liquid environment.

In chapter 5, non-functionalized and functionalized NSiMs will be integrated into specifically designed microfluidic cell in order to evaluate the molecular transport properties of each type of membrane. NSiMs with different mean pore size will be used in diffusion experiments to demonstrate their ability to be used in size-based separation experiments. Finally, the functionalized membranes with thermo-responsive polymer brushes will be used in diffusion experiments with molecules of various sizes. The ability of these NSiMs to be used as nano-valves for the control diffusion of molecules of a certain size will be demonstrated.

The conclusion chapter will summarize the main achievements of this exploratory thesis work. Directions regarding future work or possible device optimization will also be discussed.

References

[1] M. Ulbricht, Advanced functional polymer membranes, Polymer (Guildf). 47 (2006) 2217–2262.

[2] G.Q. Lu, X.S. Zhao, Nanoporous Materials: Science and Engineering, Imperial College Press, London, 2003.

[3] P. Stroeve, N. Ileri, Biotechnical and other applications of nanoporous membranes, Trends Biotechnol. 29 (2011) 259–66.

[4] S.P. Adiga, C. Jin, L.A. Curtiss, N.A. Monteiro-riviere, R.J. Narayan, Nanoporous membranes for medical and biological applications, Wiley Interdiscip. Rev. Nanobiotechnology. 1 (2009) 568–581.

[5] S.P. Adiga, L.A. Curtiss, J.W. Elam, M.J. Pellin, C. Shih, C. Shih, et al., Nanoporous Materials for Biomedical Devices, J. Miner. (2008) 26–32.

[6] S.Y. Yang, J. Park, J. Yoon, M. Ree, S.K. Jang, J.K. Kim, Virus Filtration Membranes Prepared from Nanoporous Block Copolymers with Good Dimensional Stability under High Pressures and Excellent Solvent Resistance, Adv. Funct. Mater. 18 (2008) 1371–1377.

[7] P.-S. Cheow, E.Z.C. Ting, M.Q. Tan, C.-S. Toh, Transport and separation of proteins across platinum-coated nanoporous alumina membranes, Electrochim. Acta. 53 (2008) 4669–4673.

[8] B. Wolfrum, Y. Mourzina, F. Sommerhage, A. Offenhäusser, Suspended nanoporous membranes as interfaces for neuronal biohybrid systems, Nano Lett. 6 (2006) 453–457.

[9] Z. Long, D. Liu, N. Ye, J. Qin, B. Lin, Integration of nanoporous membranes for sample filtration/preconcentration in microchip electrophoresis, Electrophoresis. 27 (2006) 4927–4934.

[10] O.K. Varghese, C. a. Grimes, Metal Oxide Nanoarchitectures for Environmental Sensing, J. Nanosci. Nanotechnol. 3 (2003) 277–293.

[11] A. Imbault, Y. Wang, P. Kruse, E. Strelcov, E. Comini, G. Sberveglieri, et al., Ta2O5 nanoporous membrane for chemical sensing in harsh environment, in: 14th Int. Meet. Chem. Sensors, 2012: pp. 1316–1318.

[12] C.R. Martin, P. Kohli, The emerging field of nanotube biotechnology, Nat. Rev. Drug Discov. 2 (2003) 29–37.

[13] C. Dekker, Solid-state nanopores, Nat. Nanotechnol. 2 (2007) 209–215.

[14] S. Majd, E.C. Yusko, Y.N. Billeh, M.X. Macrae, J. Yang, M. Mayer, Applications of biological pores in nanomedicine, sensing, and nanoelectronics, Curr. Opin. Biotechnol. 21 (2010) 439–476.

[15] J. Han, J. Fu, R.B. Schoch, Molecular sieving using nanofilters: past, present and future., Lab Chip. 8 (2008) 23–33.

[16] C. Trautmann, W. Briichle, R. Spohr, J. Vetter, N. Angert, Pore geometry of etched ion tracks in polyimide, Nucl. Instruments Methods Phys. Res. B. 111 (1996) 70–74.

[17] S. Metz, C. Trautmann, a Bertsch, P. Renaud, Polyimide microfluidic devices with integrated nanoporous filtration areas manufactured by micromachining and ion track technology, J. Micromechanics Microengineering. 14 (2004) 324–331.

[18] L.T. Sexton, L.P. Horne, C.R. Martin, Developing synthetic conical nanopores for biosensing applications, Mol. Biosyst. 3 (2007) 667–685.

[19] V. V. Volkov, B. V. Mchedlishvili, V.I. Roldugin, S.S. Ivanchev, a. B. Yaroslavtsev, Membranes and nanotechnologies, Nanotechnologies Russ. 3 (2008) 656–687.

[20] R.L. Fleischer, P.B. Price, E.M. Symes, Novel Filter for Biological Materials, Science (80-.). 143 (1964) 249–250.

[21] S. Karim, W. Ensinger, S. a. Mujahid, K. Maaz, E.U. Khan, Effect of etching conditions on pore shape in etched ion-track polycarbonate membranes, Radiat. Meas. 44 (2009) 779–782.

[22] P. Apel, Swift ion effects in polymers: industrial applications, Nucl. Instruments Methods Phys. Res. Sect. B Beam Interact. with Mater. Atoms. 208 (2003) 11–20.

[23] P. van Rijn, M. Tutus, C. Kathrein, L. Zhu, M. Wessling, U. Schwaneberg, et al., Challenges and advances in the field of self-assembled membranes, Chem. Soc. Rev. 42 (2013) 6578–6592.

[24] K.-V. Peinemann, V. Abetz, P.F.W. Simon, Asymmetric superstructure formed in a block copolymer via phase separation, Nat. Mater. 6 (2007) 992–996.

[25] J. Yin, X. Yao, J.-Y. Liou, W. Sun, Y.-S. Sun, Y. Wang, Membranes with Highly Ordered Straight Nanopores by Selective Swelling of Fast Perpendicularly Aligned Block Copolymers, ACS Nano. (2013) 9961–9974.

[26] R.M. Dorin, W. a. Phillip, H. Sai, J. Werner, M. Elimelech, U. Wiesner, Designing block copolymer architectures for targeted membrane performance, Polymer (Guildf). 55 (2014) 347–353.

[27] H. Masuda, K. Fukuda, Ordered metal nanohole arrays made by a two-step replication of honeycomb structures of anodic alumina, Science. 268 (1995) 1466–1468.

[28] N. Itoh, K. Kato, T. Tsuji, M. Hongo, Preparation of a tubular anodic aluminum oxide membrane, J. Memb. Sci. 117 (1996) 189–196.

[29] a. P. Li, F. Müller, A. Birner, K. Nielsch, U. Gösele, Hexagonal pore arrays with a 50–420 nm interpore distance formed by self-organization in anodic alumina, J. Appl. Phys. 84 (1998) 6023–6026.

[30] J.W. Diggle, T.C. Downie, C.W. Goulding, ANODIC OXIDE FILMS ON ALUMINUM, Chem. Rev. 69 (1968) 365–405.

[31] R.C. Furneaux, W.R. Rigby, A.P. Davidson, The formation of controlled-porosity membranes from anodically oxidized aluminum, Nature. 337 (1989) 147–149.

[32] K. Nielsch, J. Choi, K. Schwirn, R.B. Wehrspohn, U. Gösele, Self-ordering Regimes of Porous Alumina: The 10 Porosity Rule, Nano Lett. 2 (2002) 677–680.

[33] A.M. Md Jani, D. Losic, N.H. Voelcker, Nanoporous anodic aluminium oxide: Advances in surface engineering and emerging applications, Prog. Mater. Sci. 58 (2013) 636–704.

[34] W. Lee, J.-C. Kim, Highly ordered porous alumina with tailor-made pore structures fabricated by pulse anodization, Nanotechnology. 21 (2010) 485304 (8pp).

[35] F. Zhang, X. Liu, C. Pan, J. Zhu, Nano-porous anodic aluminium oxide membranes with 6–19 nm pore diameters formed by a low-potential anodizing process, Nanotechnology. 18 (2007) 345302 (4pp).

[36] K. Lee, Y. Tang, M. Ouyang, Self-ordered, controlled structure nanoporous membranes using constant current anodization, Nano Lett. 8 (2008) 4624–4629.

[37] W. Lee, J.-C. Kim, U. Gösele, Spontaneous Current Oscillations during Hard Anodization of Aluminum under Potentiostatic Conditions, Adv. Funct. Mater. 20 (2010) 21–27.

[38] S. Ono, M. Saito, H. Asoh, Self-ordering of anodic porous alumina formed in organic acid electrolytes, Electrochim. Acta. 51 (2005) 827–833.

[39] S.Z. Chu, K. Wada, S. Inoue, M. Isogai, Y. Katsuta, A. Yasumori, Large-Scale Fabrication of Ordered Nanoporous Alumina Films with Arbitrary Pore Intervals by Critical-Potential Anodization, J. Electrochem. Soc. 153 (2006) B384–B391.

[40] G.D. Sulka, W.J. Stępniowski, Structural features of self-organized nanopore arrays formed by anodization of aluminum in oxalic acid at relatively high temperatures, Electrochim. Acta. 54 (2009) 3683–3691.

[41] A.P. Li, F. Müller, U. Gösele, Polycrystalline and Monocrystalline Pore Arrays with Large Interpore Distance in Anodic Alumina, Electrochem. Solid-State Lett. 3 (2000) 131–134.

[42] H. Masuda, H. Asoh, M. Watanabe, K. Nishio, M. Nakao, T. Tamamura, Square and Triangular Nanohole Array Architectures in Anodic Alumina, Adv. Mater. 13 (2001) 189–192.

[43] W. Lee, R. Ji, U. Gösele, K. Nielsch, Fast fabrication of long-range ordered porous alumina membranes by hard anodization., Nat. Mater. 5 (2006) 741–7.

[44] T.T. Xu, R.D. Piner, R.S. Ruoff, An Improved Method To Strip Aluminum from Porous Anodic Alumina Films, Langmuir. 80 (2003) 1443–1445.

[45] M. Tian, S. Xu, J. Wang, N. Kumar, E. Wertz, Q. Li, et al., Penetrating the oxide barrier in situ and separating freestanding porous anodic alumina films in one step., Nano Lett. 5 (2005) 697–703.

[46] S. Wu, F. Wildhaber, O. Vazquez-Mena, A. Bertsch, J. Brugger, P. Renaud, Facile fabrication of nanofluidic diode membranes using anodic aluminium oxide., Nanoscale. 4 (2012) 5718–23.

[47] H.D. Tong, H. V. Jansen, V.J. Gadgil, C.G. Bostan, E. Berenschot, C.J.M. van Rijn, et al., Silicon Nitride Nanosieve Membrane, Nano Lett. 4 (2004) 283–287.

[48] a J. Storm, J.H. Chen, X.S. Ling, H.W. Zandbergen, C. Dekker, Fabrication of solid-state nanopores with single-nanometre precision, Nat. Mater. 2 (2003) 537–540.

[49] a. J. Storm, J.H. Chen, X.S. Ling, H.W. Zandbergen, C. Dekker, Electron-beam-induced deformations of SiO[sub 2] nanostructures, J. Appl. Phys. 98 (2005) 014307.

[50] I. Vlassiouk, P.Y. Apel, S.N. Dmitriev, K. Healy, Z.S. Siwy, Versatile ultrathin nanoporous silicon nitride membranes, Proc. Natl. Acad. Sci. U. S. A. 106 (2009) 21039–21044.

[51] C.C. Striemer, T.R. Gaborski, J.L. McGrath, P.M. Fauchet, Charge- and size-based separation of macromolecules using ultrathin silicon membranes, Nature. 445 (2007) 749–753.

[52] C.J.M. Van van Rijn, G.J. Veldhuis, S. Kuiper, Nanosieves with microsystem technology for microfiltration applications, Nanotechnology. 9 (1998) 343–345.

[53] S. Kuiper, H. Van Wolferen, C. Van Rijn, W. Nijdam, G. Krijnen, M. Elwenspoek, Fabrication of microsieves with sub-micron pore size by laser interference lithography, J. Micromechanics Microengineering. 11 (2001) 33–37.

[54] J.M. Park, T.G. Kim, K. Constant, K.M. Ho, Fabrication of submicron metallic grids with interference and phase-mask holography, J. Micro/Nanolithography, MEMS, MOEMS. 10 (2011) 013011.

[55] N. Ileri, Fabrication of functional silicon-based nanoporous membranes, J. Micro/Nanolithography, MEMS, MOEMS. 11 (2012) 013012 (7pp).

[56] D. Crouse, Y.-H. Lo, a. E. Miller, M. Crouse, Self-ordered pore structure of anodized aluminum on silicon and pattern transfer, Appl. Phys. Lett. 76 (2000) 49–51.

[57] K. Grigoras, L. Sainiemi, J. Tiilikainen, a Säynätjoki, V.-M. Airaksinen, S. Franssila, Application of ultra-thin aluminum oxide etch mask made by atomic layer deposition technique, J. Phys. Conf. Ser. 61 (2007) 369–373.

[58] S.Y. Chou, P.R. Krauss, P.J. Renstrom, Nanoimprint lithography, J. Vac. Sci. Technol. B Microelectron. Nanom. Struct. 14 (1996) 4129–4133.

[59] L.J. Guo, Nanoimprint Lithography: Methods and Material Requirements, Adv. Mater. 19 (2007) 495–513.

[60] S.-S. Song, E.-U. Kim, H.-S. Jung, K.-S. Kim, G.-Y. Jung, Reverse pattern duplication utilizing a two-step metal lift-off process via nanoimprint lithography, J. Micromechanics Microengineering. 19 (2009) 105022 (5pp).

[61] B.P. Nabar, Z. Çelik-Butler, B.H. Dennis, R.E. Billo, A nanoporous silicon nitride membrane using a two-step lift-off pattern transfer with thermal nanoimprint lithography, J. Micromechanics Microengineering. 22 (2012) 045012.

[62] L. Villanueva, O. Vazquez-Mena, C. Martin-Olmos, V. Savu, K. Sidler, J. Brugger, Resistless Fabrication of Nanoimprint Lithography (NIL) Stamps Using Nano-Stencil Lithography, Micromachines. 4 (2013) 370–377.

[63] G. Villanueva, O. Vazquez-Mena, M. a. F. van den Boogaart, K. Sidler, K. Pataky, V. Savu, et al., Etching of sub-micrometer structures through Stencil, Microelectron. Eng. 85 (2008) 1010–1014.

[64] M. Luo, T.H. Epps, Directed Block Copolymer Thin Film Self-Assembly: Emerging Trends in Nanopattern Fabrication, Macromolecules. 46 (2013) 7567–7579.

[65] C.T. Black, K.W. Guarini, G. Breyta, M.C. Colburn, R. Ruiz, R.L. Sandstrom, et al., Highly porous silicon membrane fabrication using polymer self-assembly, J. Vac. Sci. Technol. B Microelectron. Nanom. Struct. 24 (2006) 3188–3191.

[66] C.T. Black, K.W. Guarini, G. Breyta, M.C. Colburn, R. Ruiz, R.L. Sandstrom, et al., Highly porous silicon membrane fabrication using polymer self-assembly, J. Vac. Sci. Technol. B Microelectron. Nanom. Struct. 24 (2006) 3188–3191.

[67] S. Krishnamoorthy, Self-assembly of tunable, responsive polymer nanostructures: tools for nanofabrication of functional interfaces, Ecole Polytechnique Fédérale de Lausanne, 2006.

[68] S. Krishnamoorthy, Y. Gerbig, C. Hibert, R. Pugin, C. Hinderling, J. Brugger, et al., Tunable, high aspect ratio pillars on diverse substrates using copolymer micelle lithography: an interesting platform for applications, Nanotechnology. 19 (2008) 285301 (6pp).

[69] A.-M. Popa, P. Niedermann, H. Heinzelmann, J. a Hubbell, R. Pugin, Fabrication of nanopore arrays and ultrathin silicon nitride membranes by block-copolymer-assisted lithography., Nanotechnology. 20 (2009) 485303 (11pp).

[70] A.M. Popa, Stimuli-responsive nanostructured surfaces, Ecole Polytechnique Fédérale de Lausanne, 2009.

[71] U.C. Fischer, H.P. Zingsheim, Submicroscopic pattern replication with visible light, J. Vac. Sci. Technol. 19 (1981) 881–885.

[72] M.J.K. Klein, Wafer-scale fabrication of thin SiN membranes and Au films and membranes with arrays of sub-µm holes using nanosphere lithography, Ecole Polytechnique Fédérale de Lausanne, 2010.

[73] M.J.K. Klein, F. Montagne, N. Blondiaux, O. Vasquez-Mena, H. Heinzelmann, R. Pugin, et al., SiN membranes with submicrometer hole arrays patterned by wafer-scale nanosphere lithography, J. Vac. Sci. Technol. B. 29 (2011) 0210121–0210125.

[74] S. Brieger, O. Dubbers, S. Fricker, A. Manzke, C. Pfahler, A. Plettl, et al., An approach for the fabrication of hexagonally ordered arrays of cylindrical nanoholes in crystalline and amorphous silicon based on the self-organization of polymer micelles, Nanotechnology. 17 (2006) 4991–4994.

Chapter 2

Fabrication of Ultrathin Nanoporous Silicon Nitride Membranes (NSiMs) by Block-Copolymer Lithography

Abstract

This chapter will describe the fabrication of nanoporous silicon nitride membranes combining block copolymer lithography and standard microfabrication techniques.

First, the generation of a homogeneous nanopattern of PS-P2VP block copolymer micelles at wafer scale that will be used as starting template for the batch fabrication of NSiMs will be shown. The possibility of tuning independently the mean micelle height, diameter and density will be demonstrated. A specific micellar nanopattern will be chosen to start a 8 wafers batch fabrication of NSiMs.

Second, standard microfabrication techniques, such as pattern transfer by RIE, lift-off for pattern inversion, photolithography and wet etching will be used to fabricate 160 Si chips containing a single NSiM or an array of NSiMs of sizes ranging from 0.5 x 0.5 mm^2 up to 2.5 x 2.5 mm^2 on 4 inches wafer substrate. The 200 nm thick suspended NSiMs present a nanopore density of 2.8x10^9 nanopores/cm^2 and mean nanopore diameter of 85 ± 15 nm.

2.1. Process outline

The nanoporous silicon nitride membranes (NSiMs) have been fabricated by combining block copolymer lithography (BCPL) and standard microfabrication techniques. As seen in figure 2.1. The starting substrates on which the block copolymer micelle nanopattern is generated are 4 inches <100> silicon wafer (390 ± 10 µm thick) coated on both sides with a 200 nm thick low stress silicon nitride (LS-SiN) layer deposited by LPCVD. An additional 150 nm thick amorphous silicon (a-Si) layer is sputtered on the front side (FS) (A1-A3). A 2D monolayer of polystyrene-block-poly(2-vinylpyridine) (PS-b-P2VP) micelles with respective blocks molecular weights of 74 and 199 kg.mol^{-1} were obtained by spin coating a $C = 0.3\ \%\ w/v$ solution of the BCP in m-xylene at 2000 rpm (A4). The residual PS layer in between neighboring micelles is removed with a short anisotropic O_2 plasma etching step (A5). Then proceeding to a dry etching step of the underlying amorphous silicon layer, each micelle acts as a single polymeric mask producing a nanopillar array at wafer scale (A6). A 20 nm thick layer of chromium is then evaporated onto the surface (A7). By executing a lift-off step using KOH wet etching to remove the amorphous silicon nanopillars, a nanoporous chromium mask is created on top of the low stress silicon nitride layer (A8). A standard UV photolithography step is then necessary to define the active areas of the final nanoporous silicon nitride membranes (A9-A11). The nanopores in the LS-SiN layer are formed using specific dry etching recipe (A12). The remaining photoresist and the chromium layer are then removed, and the nanoporous front side of the wafer is protected by sputtering a SiO_2 layer (A13-A15). A second photolithograpy step is also performed on the backside of the wafer to define the apertures in the Si wafer to proceed to the full release of the NSiMs in order to make them free standing (A16-A18). The back side release is performed by successive RIE of the LS-SiN, deep reactive ion etching (DRIE) of the first 360 µm of Si and KOH wet etching of the remaining 30 µm (A19-A22). The protective layer is finally removed by dipping the full wafer quickly in a buffered HF solution (A23). The final wafer carries approximately 160 chips of 6 x 6 mm^2 with single NSiMs or an array of NSiMs of different sizes.

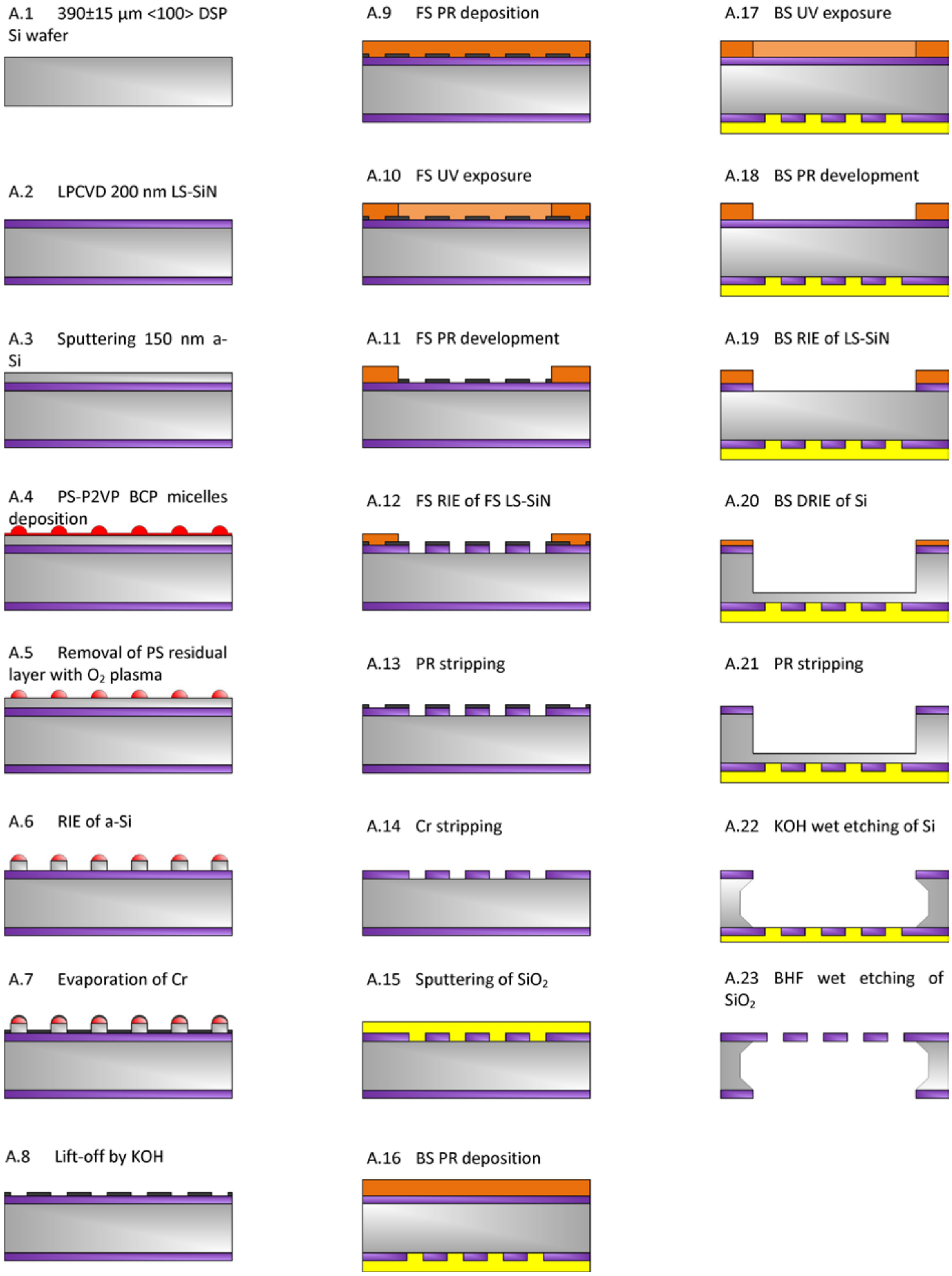

Figure 2.1 Schematic process flow for the batch fabrication of NSiMs at wafer scale.

2.2. Fabrication of the nano-patterned BCP micelle mask

2.2.1 Experimental

Materials

Block Copolymer

The block copolymer used for the formation of micelles in solution is a poly(styrene)-*block*-poly(2-vinylpyridine) (PS-*b*-P2VP) with a molecular weight of the two blocks of 74 and 199 kg.mol^{-1}, respectively. This specific BCP was synthesized by living anionic polymerization and exhibits a low polydispersity index $PI = 1.1$. A total of 4 g of this BCP was kindly provided by Prof. Stephan Förster from Hamburg University.

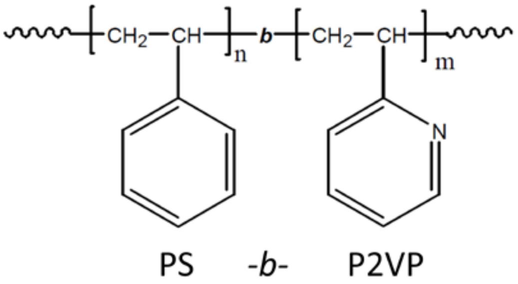

Figure 2.2 Poly(styrene)-*block*-poly(2-vinylpyridine)

Solvents

Solvent m-xylene ($C_6H_4(CH_3)_2$) anhydrous, ≥99% was purchased from Sigma Aldrich (Switzerland). m-xylene is used for the dissolution of the BCP.

2-propanol ($(CH_3)_2CHOH$) is used to clean the consumables (e.g. laboratory glass bottles magnetic stirrers, pipette tips) used in the chemistry laboratory for the preparation of the BCP micellar solution in order to remove possible contaminants and dust. The standard cleaning procedure of materials with 2-propanol is achieved by immersion of the material in the solvent and ultrasonication for 5 minutes. The procedure is performed twice and the solvent is renewed each time. Consumables cleaned are dried with nitrogen gun and stored in clean environment (plastic bags or under laminar flow) if not used immediately.

Substrates

The starting substrate for the fabrication of NSiMs is a <100> silicon wafer with a thickness of 390 µm ± 10 µm. 200 nm of LS-SiN is deposited on both sides of the wafer by LPCVD in a horizontal vacuum furnace at 820°C. The resulting LS-SiN film is a homogeneous SiN_x film exhibiting a tensile film stress between 100 MPa and 250 MPa (approximate value given by the provider). The LS-SiN coated wafers are purchased from SiMat (Germany). 150 nm of amorphous silicon is then deposited on the front side by sputtering with a *Pfeiffer SPIDER 600* sputtering machine (Pfeiffer Vacuum, Germany) depositing a-Si at a rate of 105 nm/min, using Ar (29 sccm), DC source and a power of 800W. Deposition of a-Si is performed in the clean room facilities of the Center for Micronanotechnology (CMi) in Lausanne (Switzerland).

The substrates used for the experiments concerning the tuning of the morphology of the micelles (diameter, height) and density are 10 x 10 mm^2 Si chips diced from a 390 µm ± 10 µm <100> Si wafer with a *Disco DAD321* automatic dicing saw (DISCO, Japan).

Procedure

Preparation of BCP micellar solution

In a standard procedure, PS-*b*-P2VP block copolymer is dissolved in m-xylene at a concentration $C = 0.3\ \%\ w/v$. m-xylene being a selective solvent for PS block, reverse spherical micelles made of PS corona and P2VP core are formed. The micellar solution is stirred overnight in a 50 mL laboratory glass bottle. The micellar solution is then purified by centrifugation. The purified micellar solution is again stirred for an additional 30 minutes and is now ready for deposition on Si-based substrates.

In earlier works, purified micellar solutions have been intensively characterized by Dynamic Light Scattering (DLS). This technique allows to determine precisely the hydrodynamic radius r_h, the aggregation number N, and the ratio ρ (ratio of the gyration radius over the hydrodynamic radius indicating the micelle morpholgy). Information obtained by DLS is not representative of the mean micelle size and morphology after deposition on Si-based substrate and in the dried state (collapse of the macromolecular chains upon solvent evaporation). In this work, AFM analysis has been therefore preferred and systematically used to characterize the mean micelle size (diameter/height) and density of the obtained micelle monolayer after deposition.

Substrate cleaning and activation

Prior deposition, the substrates are activated with a short O_2 plasma. The hydroxyl groups created by the O_2 plasma onto the substrate will increase the surface wettability avoiding a dewetting effect of the spin coated micellar solution. The oxygen plasma is performed with a *Oxford Plasmalab 80+* equipment (Oxford Instruments, UK). The parameters of the activation recipes are the following, O_2 mass flow of 50 sccm, chamber pressure 200mTorr (= 26 mbar) and forward power of 100 W (the process is done at room temperature). The micellar solution is now ready to be spin coated onto the substrate.

Deposition of BCP micellar solution

The deposition of the BCP micellar solution is performed by spin-coating using a *DELTA6 RC BM* spin-coater (SÜSS MicroTec, Germany) mounted under a *Kojair* laminar flow (SKAN, Switzerland) to keep a dust-free spin-coating environment. The relative humidity in the spin-coating chamber is controlled with a *Humidifier P-10* humidification unit (Cellkraft, Sweden) and monitored with a temperature/humidity probe *Probe-3087* (Elpro, Switzerland). The generation of the micellar nanopattern used for the fabrication of NSiMs is obtained with the developed and optimized “standard” spin-coating parameters described in table 2.1.

Table 2.1 Spin-coating parameters for generation of the micellar nanopattern used in the fabrication of NSiMs.

Rotational speed	Acceleration ramp	Temperature	Relative air humidity	Volume of solution	Spin time
2000 rpm	0	23 ± 2°C	65 ± 2%	1.5 mL (4” wafer) 70 µL (10 x 10 mm^2 sample)	1 minute

Micelles morphological properties (diameter/height) and density after deposition on the 4” substrates (or 10 x 10 mm^2 Si chips) are characterized by standard AFM analysis.

These properties can be tuned by changing independently several parameters such as the spin-coating rotational speed, the relative humidity in the spin-coating chamber during deposition, or the temperature of BCP dissolution prior deposition. The tunable properties of the micelles will be discussed further in this chapter.

Applying a thermal treatment to the micellar solution

Once the solution of PS-b-P2VP (74–199 kg.mol^{-1}) in m-xylene ($C = 0.3\,\%\,w/v$) is prepared, a thermal treatment can be applied to the solution to modify the micelle morphology and density per surface area as discussed further in the results section. To do so, 2 mL of micellar solution is placed in a previously cleaned 4 mL container, and placed under stirring in a temperature controlled (20-80°C) water bath for one hour. New micellar solutions prepared need to be cooled down at room temperature before deposition with standard spin-coating conditions on 10 x 10 mm^2 Si chips.

Etching of PS residual layer

The deposition of the BCP micellar solution results in a 2D monolayer of reverse spherical PS-b-P2VP micelles. During the film formation, the micelles partly collapse on the surface forming a continuous residual PS layer in between neighboring micelles. In a previous work, the thickness of the PS residual layer has been characterized to be 8-12 nm thick by scratching manually the surface with a needle and AFM analysis. In order to obtain a micellar nanopattern on a 4 inches Si substrate with each micelle acting as a single polymeric mask for further pattern transfer in the underlying a-Si layer, the PS residual layer needs to be removed. The removal of the residual layer is performed with an *RIE Oxford Plasmalab 80+* equipment (Oxford Instruments, UK) using an optimized anisotropic O_2 plasma etching with an etch rate of polymeric materials of 12 nm/min (O_2 mass flow: 20 sccm, chamber pressure: 20 mTorr, forward power: 25W and process time: 45 seconds). This etching step also modifies the mean micelle diameter and height. Full removal of the PS residual layer and new morphological properties of micelles (diameter and height) are characterized by standard AFM analysis.

AFM analysis

In this work, all the AFM characterizations were performed using a *Dimension 3100* Atomic Force Microscope (Veeco Digital Instruments, USA). All the data were acquired in tapping mode using Tap 150-G AFM Si probes (Budget Sensors, Bulgaria). The specifications of the AFM probe are detailed in table 2.2.

Table 2.2 Specifications of Tap-150G AFM probe

	Resonant frequency	**Force constant**	**Length**	**Mean width**	**Thickness**	**Tip height**	**Tip Set back**	**Tip radius**	**Reflex coating**
Value	150 kHz	5 N/m	125 µm	25 µm	2.1 µm	17 µm	15 µm	<10nm	none
Range	± 75 kHz	1.5 to 15N/m	±10µm	±5µm	±1 µm	±2µm	±5µm		

Darkfield wafer inspection

Darkfield wafer inspection is a well-suited technique to observe micron and sub-micron particles present on the wafer surface. This technique is extensively used by semiconductor manufacturers to increase and maintain a good fabrication yield. In dark field microscopy, the light reaches the sample with an angle with the help of an opaque disk, the observed background appears dark and particles present at the surface will scatter light producing bright dots on the dark background. The size and shape of these particles cannot be determined, only the amount of particles can be calculated by processing the captured pictures with an image analysis software (*image J*). The optical microscope used for dark field inspection is a *Nikon Optiphot* (Nikon, Japan).

2.2.2 Results and Discussion

Tuning of the mean micelle height

Varying the relative humidity in the spin-coating chamber

Regarding the steps of the process flow, the micelles deposited onto the surface will act as single polymeric masks for further transfer into the underlying a-Si layer. For this transfer step, one critical parameter is the height of the micelles. Using an etching recipe with an etching selectivity of silicon over polymer of about 7:1, the maximum micelle height will define the maximum thickness of a-Si that can be etched. While keeping the spin-coating parameters and conditions of the micellar solution standard for the fabrication of NSiMs, the mean micelle height can be tuned independently by varying only the relative humidity in the spin-coating chamber during deposition. As it can be seen in figure 2.3, a variation of 20 nm in height was found while varying the relative humidity from $R_H = 20\%$ to $R_H = 70\%$ with a maximum in height around $R_H = 65\%$ which will be the standard relative humidity used in the spin-coating process for the generation of the nanopattern for the fabrication of NSiMs.

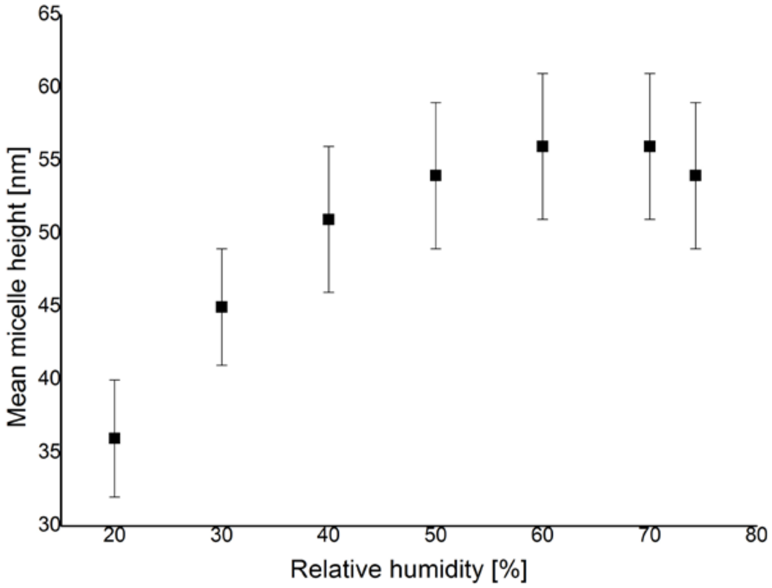

Figure 2.3 Plot shows the variation in the mean micelle height as a function of the relative humidity in the spin-coating chamber during deposition of a $C = 0.3\ \%w/v$ PS-b-P2VP in m-xylene solution with standard spin-coating parameters on 10 x 10 mm^2 Si chips.

No variation of the micelle density per surface area (within error bars) was noticed when varying the relative humidity (table 2.3), indicating that the humidity influences the mean height parameter at a late stage of the film formation process when the position of the micelles onto the substrate has already been fixed. It can be explained by the fact that the temperature of the surface decreases during the spin-coating process due to the evaporation of the solvent favoring condensation of moisture at the surface. The moisture preferably gets distributed within the hydrophilic P2VP cores swelling it [1] and changing the interfacial surface tension between PS and P2VP. The influence of the interfacial surface tension on the aspect ratio of micelles deposited on a surface is a phenomenon mentioned in the literature [2,3]. Krishnamoorthy et al. demonstrated that the increase in micelle height induces a proportional decrease of the PS residual film in between neighboring micelles [4].

Table 2.3 Data extracted from AFM analysis of the micelle morphology (height and diameter) and density depending on the relative humidity in the spin-coating chamber during deposition of the micellar solution on 10 x 10 mm^2 Si chips.

Relative Humidity *%*	**Diameter** *nm*	**Height** *nm*	**Density** *micelles/µm^2*
20	91 ± 9	36 ± 4	51 ± 2
30	94 ± 8	45 ± 4	45 ± 2
40	93 ± 8	51 ± 5	51 ± 2
50	91 ± 9	54 ± 5	51 ± 2
60	94 ± 8	56 ± 5	47 ± 2
70	94 ± 8	56 ± 5	45 ± 2
74.3 (maximum)	92 ± 9	54 ± 5	46 ± 2

Tuning of the micelle density

Varying the initial BCP concentration in solution

Solutions of PS-b-P2VP micelles were prepared at different concentrations and deposited onto 10 x 10 mm^2 Si samples with the standard spin coating parameters mentioned in the experimental section. The influence of the concentration of BCP in solution onto the final micelle size and surface density was characterized by standard AFM analysis. As it can be expected the concentration of BCP in solution influences the surface density of micelles [5]. While the deposition of low concentrated ($C = 0.1\ \%w/v$) block-copolymer leads to medium micelle surface density (28 ± 2 micelles/µm^2), the deposition of higher concentrated solution ($C = 0.3\ \%w/v$) allows us to increase micelle surface density up to 46 ± 2 micelles/µm^2 (see Table 2.4). In contrast the mean micelle height and diameter does not change with the increase in concentration.

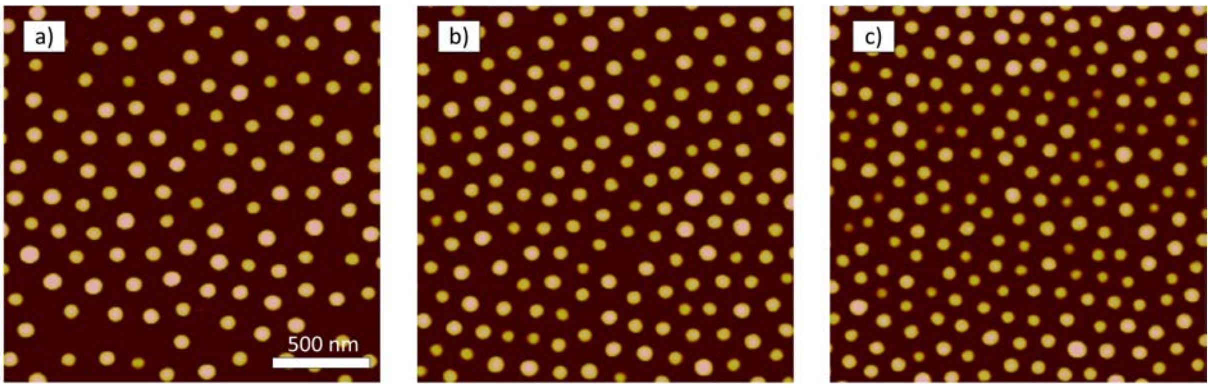

Figure 2.4 AFM micrographs of PS-b-P2VP reverse micelles deposited with standard spin coating conditions with initial solution concentration in BCP of **a)** $C = 0.1\ \%w/v$, **b)** $C = 0.2\ \%w/v$, **c)** $C = 0.3\ \%w/v$. (max Z scale of the micrographs is 50 nm).

Table 2.4 Data extracted from AFM analysis of the micelle morphology (height and diameter) and density depending on the concentration in BCP of the initial solution before deposition on 10 x 10 mm^2 Si chips.

Concentration in BCP *% w/v*	**Diameter** *nm*	**Height** *nm*	**Density** *micelles/µm^2*
0.1	95 ± 8	57 ± 5	28 ± 2
0.2	93 ± 7	58 ± 5	37 ± 2
0.3	90 ± 9	55 ± 6	46 ± 2

Varying the spin coating speed

The density of micelle per surface area can also be tuned by varying the rotational speed of the spin-coating process and keeping the initial BCP solution concentration constant ($C = 0.3\ \%\ w/v$). With increased spin-coating speeds, the volume of BCP solution spread across the sample per unit area decreases and the evaporation rate of the solvent increases [6,7], reducing the number of micelles to be frozen onto the surface. The inter-micelle distance increases with the spin-coating speed and no major difference in the morphology of the micelles (mean height and diameter) was observed with standard AFM characterization.

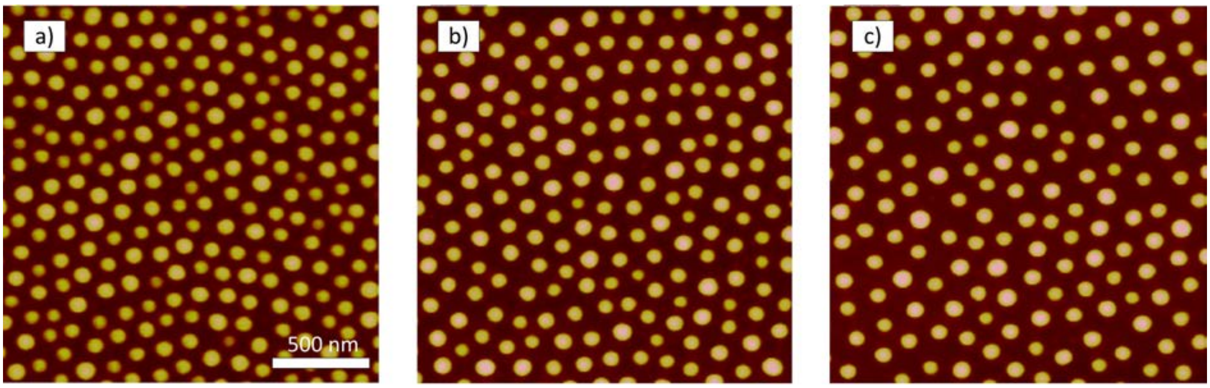

Figure 2.5 AFM micrographs of PS-b-P2VP reverse micelles deposited in standard conditions with spin-coating rotational speeds of **a)** 1000 rpm, **b)** 3000 rpm and **c)** 5000 rpm. (max Z scale of the micrographs is 50 nm).

Table 2.4 Data extracted from AFM analysis of the micelle morphology (height and diameter) and density depending on the spin-coating rotational speed of the micellar solution on 10 x 10 mm^2 Si chips.

Spin coating speed *rpm*	**Diameter** *nm*	**Height** *nm*	**Density** *micelles/µm²*
1000	89 ± 9	50 ± 5	52 ± 2
2000	89 ± 9	55 ± 5	46 ± 2
3000	92 ± 9	57 ± 5	43 ± 2
4000	96 ± 9	57 ± 5	39 ± 2
5000	93 ± 9	58 ± 5	36 ± 2

Tuning of both the micelle mean size and density

Influence of the blocks molecular weight

Using diblock copolymers with smaller blocks molecular weights will produce smaller micelle in solution as it can be expected from the scaling theories [8,9]. With same standard spin coating conditions, a decrease in the mean micelle diameter induces an increase in the density of micelles. Starting with PS-*b*-P2VP with blocks molecular weights of 74 and 199 kg.mol^{-1}, respectively, and PS-*b*-P2VP with blocks molecular weights of 55 and 50 kg.mol^{-1}, respectively, micellar solutions were prepared in m-xylene at a concentration of $C = 0.3\,\%\,w/v$ and deposited with standard spin conditions on 10 x 10 mm^2 Si chips. The AFM micrographs in figure 2.6 and the data in table 2.5 show the large difference in micelle morphology and density. Substituting the initial BCP 74–199 kg.mol^{-}1 by its analog BCP 55–50 kg.mol^{-1}, the mean diameter of the deposited micelles was decreased by a factor 2 and the mean height by a factor of 2 to 3. In contrast the micelle surface density was increased by a factor of 5.

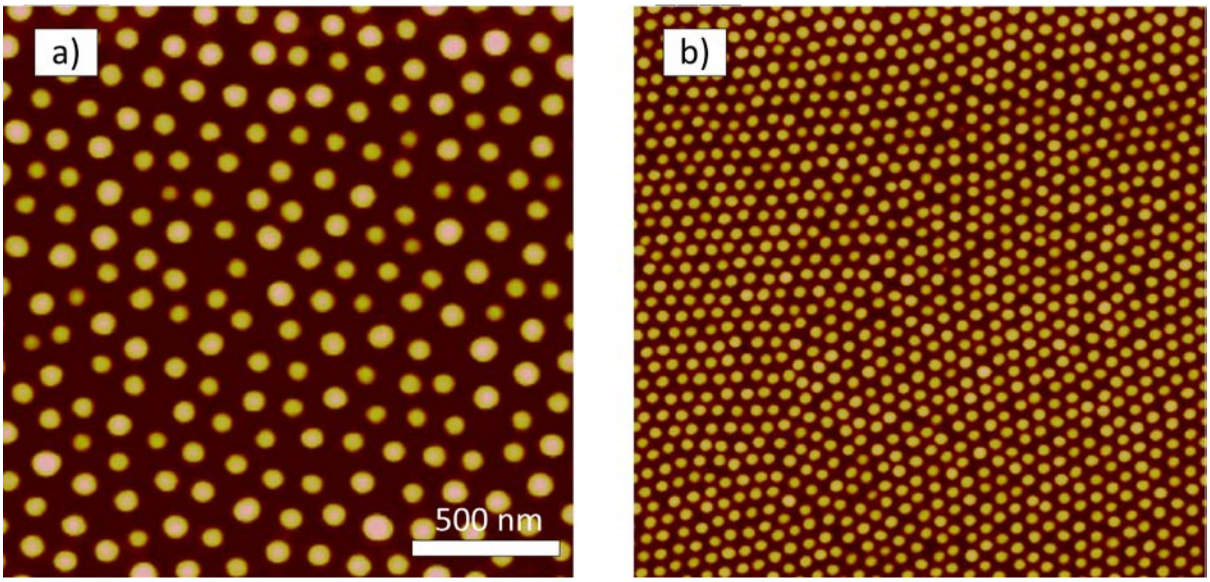

Figure 2.6 AFM micrographs of **a)** PS-b-P2VP 74-199 kg.mol^{-}1 and **b)** PS-b-P2VP 55-50 kg.mol^{-1} reverse micelles prepared in m-xylene at $C = 0.3\ wt\%$ and deposited with standard spin coating conditions on 10 x 10 mm^2 Si chips.

Table 2.5 Data extracted from AFM analysis of the micelle morphology (height and diameter) and density depending on the blocks molecular weights of the PS-b-P2VP copolymer prepared and deposited in the same standard conditions on 10 x 10 mm^2 Si chips.

PS-b-P2VP blocks Mw	**Diameter**	**Height**	**Density**
kg.mol^{-1}	***nm***	***nm***	***micelles / µm^2***
74 - 199	89 ± 9	55 ± 6	46 ± 2
55 – 50	46 ± 3	21 ± 1.5	252 ± 10

Applying a thermal treatment to the BCP micellar solution

The micelle morphology and density per surface area can also be tuned prior deposition by applying a thermal treatment to the micellar solution. Micelles are not fixed entities, increasing the temperature of the solvent decreases its selectivity and therefore a decrease in the aggregation number and the dimensions of the core of the micelles can be observed [10,11]. This phenomenon was observed by changing the temperature of the dissolution of PS-*b*-P2VP (74–199 kg.mol^{-1}) in m-xylene from 20 to 80°C. The AFM micrographs in figure 2.7 show the micelle morphology and density after deposition in standard conditions.

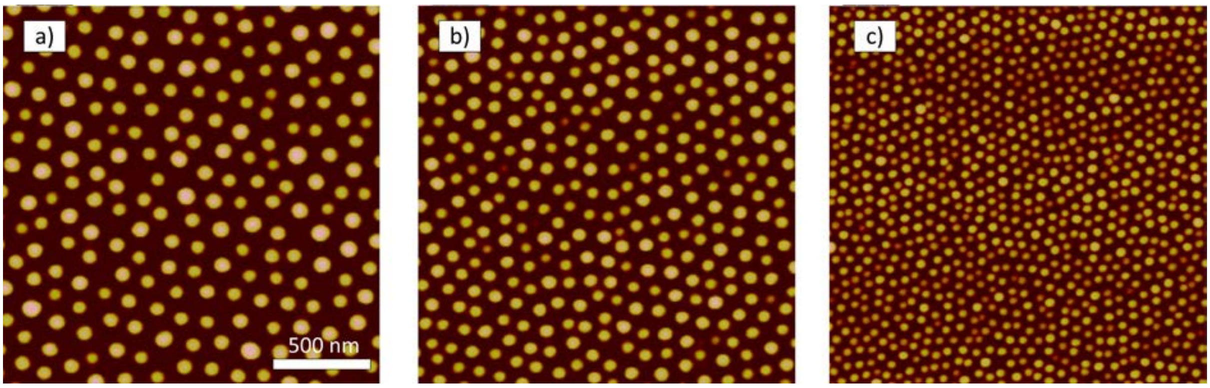

Figure 2.7 AFM micrographs of PS-b-P2VP reverse micelles prepared in m-xylene at **a)** 20°C (max Z scale is 50 nm), **b)** 60°C (max Z scale is 40 nm) **c)** 80°C (max Z scale is 30 nm) and deposited with standard spin-coating conditions on 10 x 10 mm^2 Si chips.

Figure 2.8 shows the evolution of the mean micelle diameter, height and density depending on the temperature of the thermal treatment applied to the micellar solution prior deposition. Applying a thermal treatment from 20°C to 80°C to the BCP micellar solution, the mean micelle density is increased approximately by a factor 4 and the mean diameter is being reduced by a factor 2. The small micelles (48 ± 3 nm) produced with a thermal treatment of the solution prior deposition at 80°C exhibit a mean height of 25 ± 4 nm, which is too low to be considered as an etch mask for the pattern transfer by RIE in the underlying 150 nm a-Si layer, therefore this micellar system cannot be used for the fabrication of NSiMs. Other micellar systems with PS-*b*-P2VP (74-199 kg.mol^{-1}) in m-xylene prepared at $C = 0.3\ \%\ w/v$ and with a thermal treatment of the solution prior deposition ranging from 20 to 70 °C appear to be good micellar systems for the fabrication of NSiMs with tunable pore size and pore density ranging from 95 ± 9 nm to 61 ± 5 nm and 48 ± 2 to 131 ± 5 micelles/µm^2, respectively.

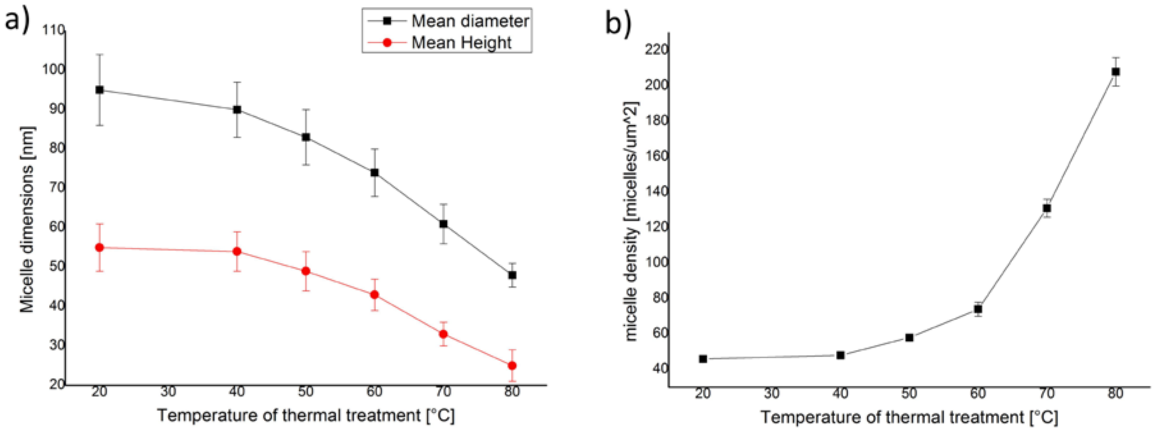

Figure 2.8 Plots of the mean micelle **a)** diameter, height and **b)** density after deposition of a $C = 0.3wt\%$ solution of PS-b-P2VP (74 – 199 kg.mol^{-1}) in m-xylene as a function of the thermal treatment applied to the micellar solution prior deposition.

Generation of a homogeneous micellar nanopattern at wafersacle

Influence of the volume of micellar solution dispensed onto the 4” substrate

Depositing the micellar solution from small samples (10 x 10 mm^2) to large scale samples (4 inches Si wafer) requires an optimization of the volume of solution dispensed onto the wafer. The linear speed of an object (solution of BCP) positioned on a disk in rotation is the product of the angular speed by its position on the rotating disk (distance from the center). In other terms, the volume of BCP solution spread across the sample per unit area decreases while moving away from the center of the wafer, and a gradient of micelle density can be expected from the center to the edge leading to the formation of non-homogeneous micellar films at large scale [7]. To overcome this issue, the volume of solution to be dispensed needs to be in excess as seen in figure 2.9 b) where a minimum volume of 1.5 mL of micellar solution is needed to obtain the same density of micelle per surface area everywhere on the wafer.

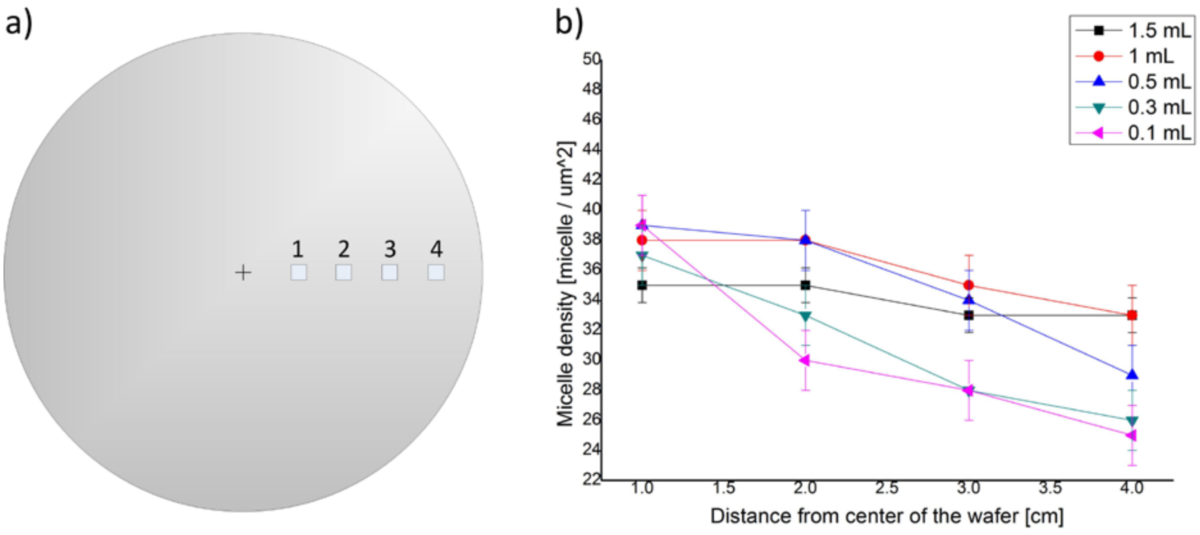

Figure 2.9 a) Schematic representation of a 4” silicon wafer with positions of the AFM measurements indicated and **b)** the analysis of the evolution of the micelle density along the wafer for different amount of micellar solution dispensed during the spin-coating process.

Purification of the micellar solution with centrifugation

Even if all the precautions were taken in terms of cleaning all the laboratory equipment and materials with 2-propanol, and also by setting the spin-coating machine and process in a dust free environment, an inspection of the wafer with an optical microscope in dark field showed that many large undesired particles were present onto the surface (figure 2.10 a)). Centrifugation is an easy step for purifying solution by sedimentation of large particles/aggregates [12–14]. The centrifugation step for solution purification was preferred to a standard filtration step with 0.2 or 0.45 μm because of the swollen micelle "trapping" effect into these large tortuous filters (PVDF or PTFE 10 μm thick filters), reducing considerably the final concentration at the output of the filters. 1.5 mL of micellar of non-purified and purified micellar solution was deposited onto 4" wafer substrates with standard spin-coating conditions and a dark filed inspection was performed (figure 2.10). The shape and size of the particles scattering the light observed in dark field mode cannot be defined, only the amount of particles. Processing the images to a particle analysis showed that the non-purified solution deposited presents an amount of particle of 129 particles/mm^2, while the purified solution, the amount of particle on the surface after deposition is only of 14 particles/mm^2.

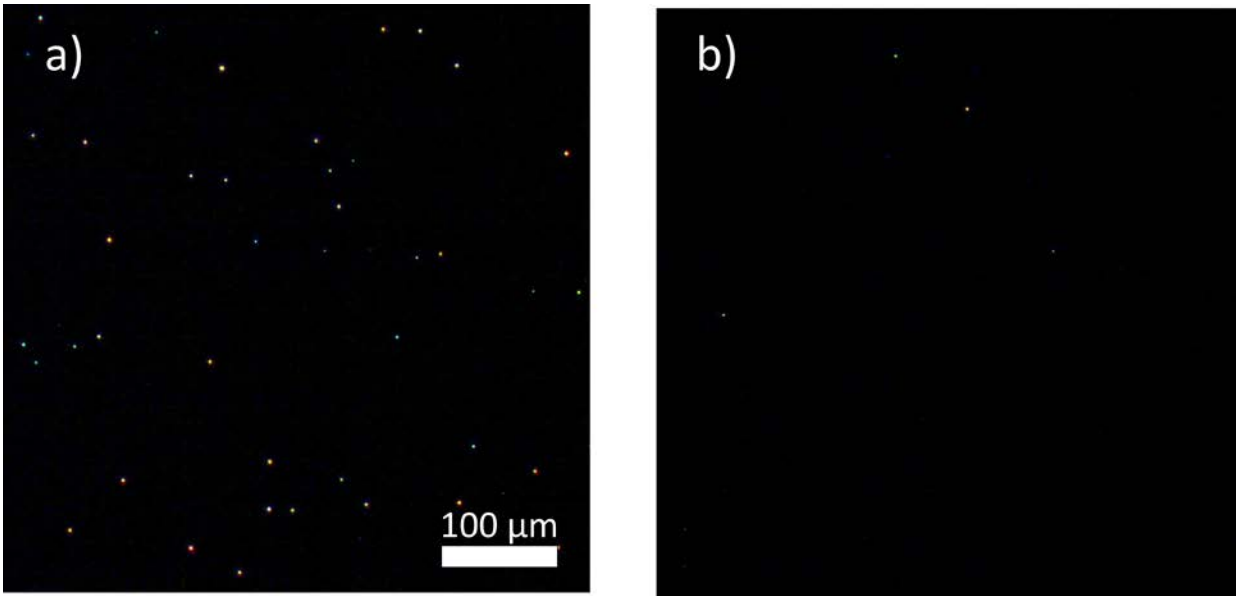

Figure 2.10 Wafer inspection with optical microscope in dark field mode of **a)** non-purified and **b)** purified micellar solution deposited on 4" wafer with standard spin coating conditions.

Purifying the solution with centrifugation and sampling the supernatant (typically 50% of the solution) slightly reduced the micelle density per surface area once deposited on a 4 inches substrate with standard spin-coating conditions (figure 2.11). This can be explained by a slight decrease of the micelle concentration due to the sedimentation of larger micelles during the centrifugation step [15]. The decrease of micelle surface density observed when using the purified micellar solution was quantified to be < 10% (within error bars). The decrease of micelle surface density is not relevant compared to the cleanliness of the substrate obtained with a purified micellar solution.

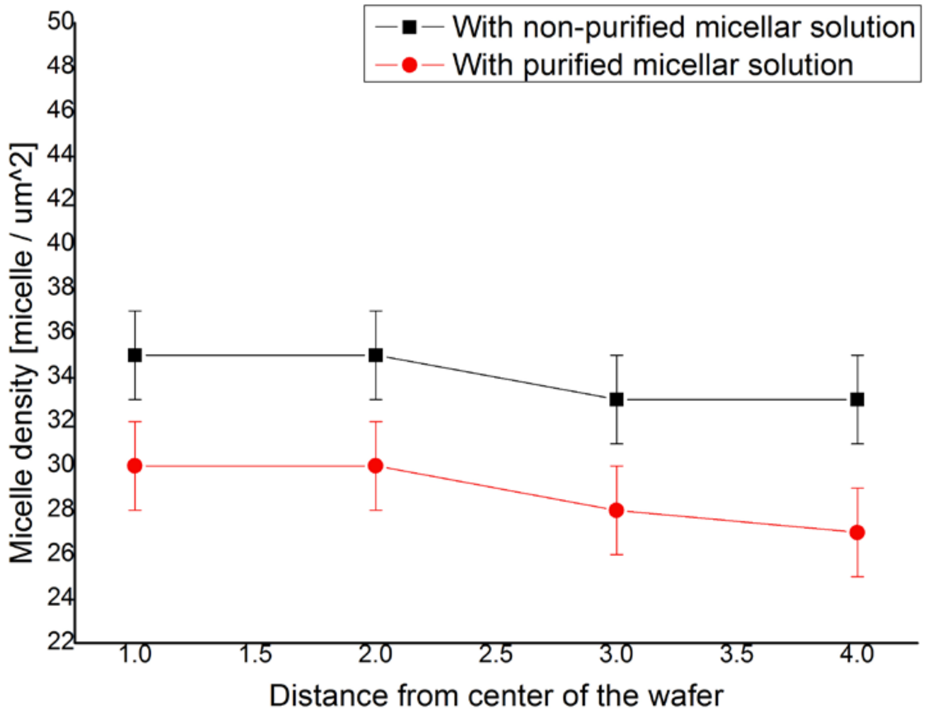

Figure 2.11 AFM analysis of the evolution of the micelle density along the wafer for a non-purified and purified micellar solution deposited with standard spin-coating conditions.

Etching of the PS residual layer

During the deposition of the micellar solution and formation of the film, the micelles partly collapse onto the surface forming a continuous residual layer of PS that has been characterized by scratching manually the surface and AFM analysis to be 8-12 nm thick. It is important to remove this residual layer in order to have each micelles acting as a single polymeric mask for the subsequent step consisting in transferring the micellar nanopattern in the underlying a-Si layer via DRIE. Figure 2.12 show the micelle morphology and size distribution before etching the residual layer.

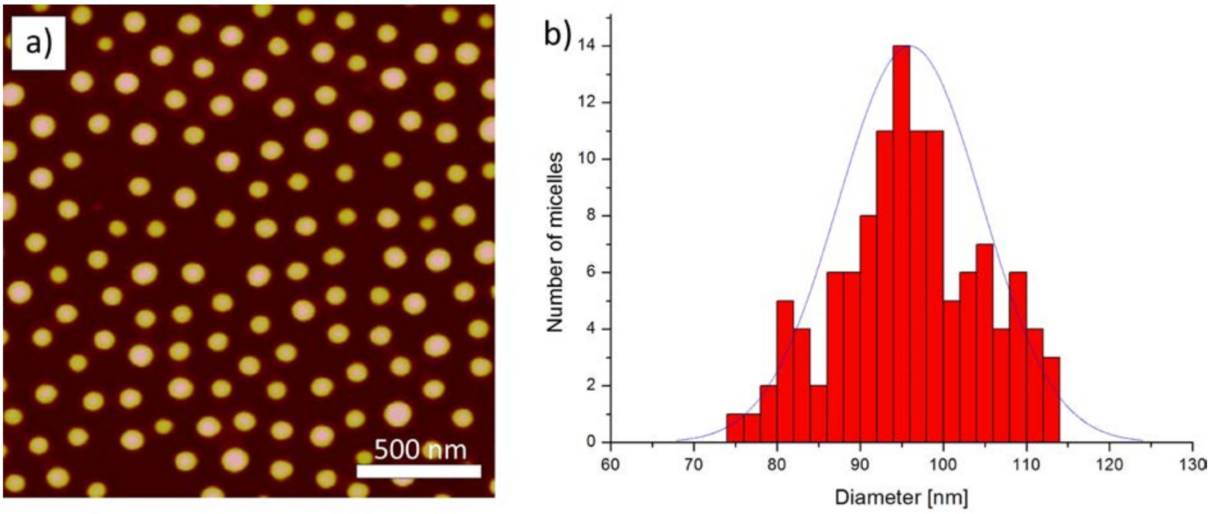

Figure 2.12 a) AFM micrograph of micellar film before etching the PS residual layer (max Z scale is 50 nm) and **b)** the corresponding graph showing the size distribution of the micelles.

Proceeding to the short optimized oxygen plasma to remove the PS residual layer, the final micellar nanopattern is obtained. The anisotropic etch of the residual layer also etches the micelles modifying the mean diameter and height. Figure 2.13 and table 2.6 show the micelle morphology (diameter and height), density and size distribution after etching the residual layer. The mean height and diameter obtained with the particle analysis tool of the AFM software are reduced by 11 ± 3 nm and 15 ± 3 nm, respectively.

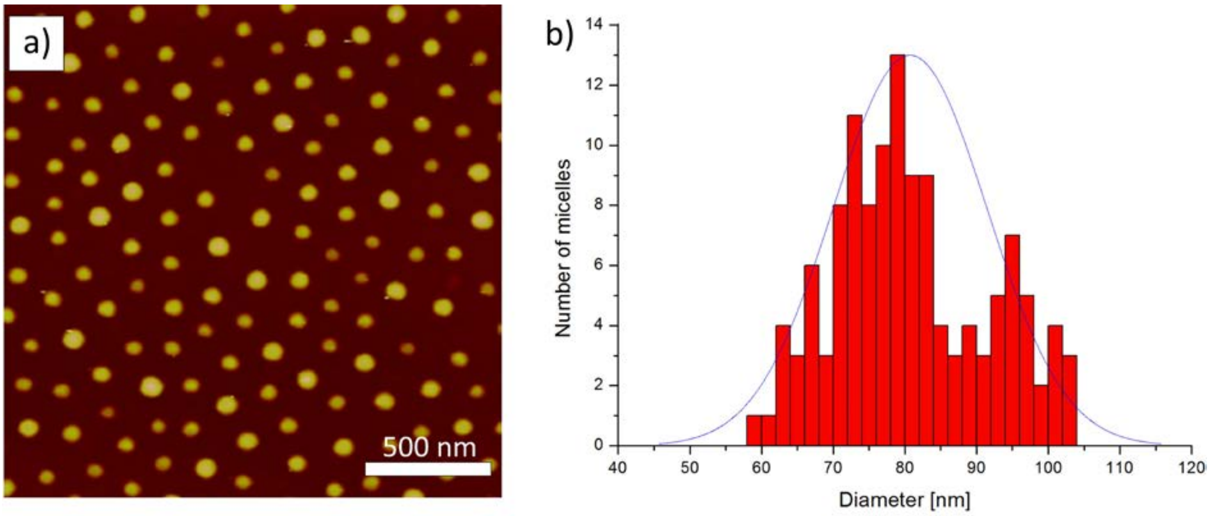

Figure 2.13 a) AFM micrograph of micellar film after etching the PS residual layer (max Z scale is 50 nm) and **b)** the corresponding graph showing the size distribution of the micelles.

Table 2.6 Data extracted from AFM analysis of the micelle height and density before and after the etching of the PS residual layer by oxygen plasma.

	Height ***nm***	**Density** ***micelles / µm^2***
Before etching residual layer	55 ± 6	30 ± 2
After etching residual layer	44 ± 6	31 ± 2

For the next transferring step into a-Si by RIE, one critical parameter is the remaining height of the deposited micelles after etching the residual layer. For the etching of a 150 nm thick a-Si layer using an etching recipe with a selectivity of Si over polymer of about 7:1, the deposited micelles should be at least 20-25 nm in height. From the mean height values indicated in table 2.6, the remaining height of the micelles was measured by AFM to be around 44 nm, which is enough to play the role of an efficient etch mask.

2.2.3 Preliminary conclusions

The possibility of tuning the micelle diameter, height and density was demonstrated. The dimensions of the BCP micelles after etching of the PS residual layer reflect the final dimensions of the nanopores in the process flow for the fabrication of NSiMs. Attention should be given to the fact that a large surface coverage of the self-assembled monolayer of the PS-*b*-P2VP (74-199 kg.mol^{-1}) micelles will lead to highly porous surfaces, making the membrane mechanically fragile. Generating a micellar nanopattern on a 4 inches wafer using a $C = 0.3\ \%\ w/v$ solution of PS-*b*-P2VP (74-199 kg.mol^{-1}) in m-xylene (without thermal treatment of the solution) leads to a 15-20% surface coverage and therefore future porosity, being an acceptable value to pursue the fabrication process and superior to the porosity of PCTE membrane (≈5%) [16,17] or silicon based membranes fabricated via interference lithography (≈4%) [17,18], and in the range of what can be achieved with AAO membranes (10-35%) [17,19,20] for sub-100 nm pore diameter. This micellar system exhibits a mean micelle diameter of 85 ± 10 nm and a density of 28 ± 2 micelles / µm^2. A batch fabrication of 8 wafers using this starting template was processed to produce NSiMs with detailed critical steps explained in the following section.

2.3. Microfabrication of NSiMs using BCP lithography

2.3.1 Experimental

Materials

Substrate

The substrates used at this stage of the fabrication of NSiMs are 4 inches <100> silicon wafers (390 µm ± 10 µm thick) with 200 nm of LS-SiN deposited on both sides of the wafer by LPCVD and 150 nm of sputtered a-Si on the front side. As seen previously, a 2D PS-*b*-P2VP (74–199 kg.mol^{-1}) reverse micelle monolayer is generated on the front side with a mean micelle diameter of 85 ± 10 nm and a density of 28 ± 2 micelles / µm^2.

Wet etchants

All the wet etchants used in the fabrication of NSiMs are listed in table 2.7 below.

Table 2.7 Wet etchants used for the fabrication of NSiMs.

Wet etchant	Material etched	Composition	Temperature of use	Etch rate
KOH	Silicon	KOH 40%	60°C	≅ 20 µm/h
SVC-14	Photoresist	60 % DMSO / 40% cyclic ester-	70°C	*
CR1	Chromium	$(NH_4)_2Ce(NO_3)_6$ + $HClO_4$	20°C	65 nm/min
BHF	SiO_2	Buffered HF 7:1	20°C	72 nm/min

**The etch rate of photoresist in SVC-14 can vary if it has been exposed to gases in dry etching processes*

Procedure

Etching of the a-Si nanopillars

The formation of the nanopillars is obtained using a “pseudo” Bosch dry etch process with an ICP plasma etcher *Alcatel AMS 200* (Alcatel Micro Machining Systems, France). The process is continuous and combines two gases, SF_6 as the etching gas and C_4F_8 as a passivation gas allowing an anisotropic etch of the silicon leaving nanopillars with smooth sidewalls. The ratio in between the mass flow of gases introduced into the chamber defines the taper angle of the nanopillars, the ideal ratio producing a-Si nanopillars with vertical sidewalls was found to be 25 sccm/55 sccm. The etching process is performed at low temperature (0°C) and with a chuck power reduced to 15W in order to decrease the etch rate of a-Si. The ICP source power is set to 1500W. The etch rate of this recipe was measured to be 100 nm/min with a selectivity over polymer close to 7:1.

Evaporation of chromium

The evaporation of chromium is performed with a *Leybold-Optics LAB 600H* evaporator machine (Leybold optics, Germany). The deposition rate of chromium is 0.4 nm/s and a 20 nm thick layer will be deposited onto the 4 inches substrates with the nanopillar array. The thickness of Cr deposited is measured with the deviation in frequency of a quartz oscillator. In the evaporation machine the distance source–substrate is of 1010 mm, minimizing the angle between the normal to the substrate at the edge of the wafers and the incident flux down to 6°. This angle is called the maximum lift-off angle.

Chemical lift-off

The nanopattern is inverted from nanopillars to nanoholes into the Cr layer by proceeding to a chemical lift-off using a 40% potassium hydroxide (KOH) solution prepared at 60°C. KOH is a strong base mostly used in microfabrication for the wet etching of silicon. It has to be used carefully due to its corrosive nature when concentrations are higher than 2%. The structured wafers are dipped for 10 minutes for the etching of nanopillars with mean height of 150 nm and mean diameter of 85 nm. Wafers are rinsed in 3 successive ultrapure water baths for 10 minutes each. Possible Cr residues are removed by dipping the wafers in an ultrasonic cleaning water bath for 10 minutes. The wafers are then dried with a homemade dry spinning device.

Front side (FS) photolithography

Just before the deposition of the photoresist wafers are prepared with a dehydration step by placing the wafers in an oven at 130°C for one hour to enhance the adhesion of the resist on the chromium layer. It allows removing the water present onto the substrate (chromium) to get a homogeneous coating along the wafer. Vapor HMDS is useless onto chromium surface to enhance photoresist adhesion (HMDS is usually used to improve the adhesion of photoresist onto silicon substrates), and oxygen plasma should be avoided in order not to create chromium oxide that will be hard to remove afterwards with wet chemical etchant. It is strongly recommended to proceed to the photoresist deposition right after the dehydration step. 2.0 µm of photoresist AZ1512HS (AZ Electronic Materials, France) is spin coated at 2300 rpm for 30 seconds on the front side of the wafer (nanoporous chromium) followed by a soft bake step at 112°C which removes the excess of solvent contained in the photoresist (generally 20-40%) to make the photoresist film more stable at room temperature afterwards. Right after the soft bake step, the wafer is placed on a cool plate in order to stop the baking process. The whole process is automatically performed with an automatic coater *Cluster EVG 150* (EVGroup, Austria). The photoresist film has to observe a certain rehydration time because during the softbake the water concentration of the film drops. A certain water content in the resist during exposure is required to allow a reasonable high development rate and a high contrast. The missing water has to diffuse from the air into the resist film before exposure. For thin photoresist films in the order of few µm, a few seconds are generally needed for full rehydration. The photolithography mask was designed with CleWin software and the layout was sent for the fabrication to the company Photronix (UK), the specific design will be discussed later. The photoresist is then exposed to UV light through the photolithographic mask with an exposure tool *SÜSS MicroTec MA6&BA6* (SÜSS MicroTec, Germany). The photoresist exposed to UV light will observe a change in its solubility making the exposed areas very soluble in a basic developer. In order to avoid any spatial variation in solubility of the resist in developer, the correct exposure dosis should be provided to the exposed areas, this can be found in the datasheet depending on the type of photoresist, its thickness and the nature of the substrate. The light intensity in the machine is of 10 mW/cm^2 and a suitable exposure dosis was found to be of 32 mJ/cm^2, meaning an exposure time of 3.2 seconds. Once exposed, the photoresist should be developed right after. The machine processing the development of the exposed photoresist (*Cluster EVG 150*) is combining the “spray” and “puddle” technique. With the spray technique, developer is sprayed through a nozzle on the wafer producing a fine mist of developer over the wafer, giving more uniform developer coverage and reducing the amount of developer used. The “puddle” development technique uses the developer sprayed on the surface, and the solution stays onto the stationary wafer for the duration of the development time. The wafer is then spin rinsed thoroughly with water and dried. A post-bake step at 112°C after development is performed to harden the final resist, making it more thermally stable, so that it can be able to withstand harsh environment such as dry etching conditions. Optical control with microscope (*Nikkon Optiphot 200*, Nikkon, Japan) should be performed to characterize the development of the photoresist in the defined apertures, making sure that the underlying layer has been reached, and that no photoresist residues are present. If so, the residues can be removed with a short descum with an oxygen plasma (*TEPLA Gigabatch plasma stripper*, PVA Tepla, Germany; O_2 mass flow: 200 sccm, power: 200 W, process time: 10 sec), or by proceeding again to the development procedure.

Deep Reactive Ion Etching (DRIE) of LS-SiN

The creation of the nanopores is achieved by Reactive Ion Etching with an ICP plasma etcher *Alcatel AMS 200*. For the etching of the nanopores in LS-SiN through the nanoporous Cr mask, two different etching processes will be used. The first one will be referred to as *Etch_SiN* in this work, and uses the following gases and parameters, C_4F_8 / CH_4 and He, source power of 1500 W and chuck power of 180 W. *Etch_SiN* exhibits an etch rate of stoichiometric Si_3N_4 of 200 nm/min. The second recipe will be referred to as *Etch_LS-SiN* and uses the following gases and parameters, C_4F_8, source power of 1500 W and chuck power of 100 W. *Etch_LS-SiN* exhibits an etch rate of LS-SiN of 250 nm/min. The etching time and the selectivity over Cr of both these recipes will be discussed further.

Stripping of photoresist and Chromium

After creating the nanopores into the LS-SiN layer in the areas defined, the remaining photoresist needs to be removed from the surface. A well-known quick way to strip photoresist is to proceed to a barrel oxygen plasma, in which photoresist of several micrometers can be stripped in a few minutes. Regarding the process used for the fabrication of NSiMs, if oxygen plasma is used, it will oxidize the underlying chromium, and chromium oxide will be removed with difficulty using wet etchant. Therefore the photoresist is stripped by dipping the wafers into a remover bath for 2 hours. The remover used is a SVC-14, it has to be used carefully, because of its corrosive properties and breathing the vapors should be avoided. The residual fluorocarbon compounds present at the surface of the wafer due to the dry etching step with C_4F_8 might slow the stripping process, dipping time should be extended if necessary after optical control (the etch rate was not communicated by the provider). After stripping, the wafers are rinsed successively in a quick dump rinse (QDR) water bath and an ultra-clean (UC) water bath. Finally the wafers are dried by spinning under nitrogen flow.

The etching of chromium is performed by dipping the wafers in a solution of *CR1* which is a mixture of $(NH_4)_2Ce(NO_3)_6$ + $HClO_4$. CR1 is a strong acid and should be handled with care. The etch rate of chromium in CR1 is 65 nm/min. The etching time necessary might be a little longer because of the presence of a native chromium oxide layer. The etching time is set to 5 minutes in order to be sure of removing all the chromium. CR1 is not etching the underlying LS-SiN layer. After soaking in CR1, the wafers are rinsed 3 times in a QDR water bath, and dried with a spin drier.

Energy Dispersive X-ray (EDX) analysis

The wafers are analyzed by Energy Dispersive X-ray (EDX) to detect the possible presence of Cr residues after Cr wet etching in CR1 that might not be visible with optical microscope inspection. The analysis is performed at different positions on each wafer of the fabrication batch. EDX is a technique used for elemental analysis of a sample. This analysis is performed in a SEM microscope *Philips XL30 ESEM* (Philips) with an electron beam and an energy dispersive spectrometer. The incident electron beam hits the sample surface creating secondary electrons and leaving holes in the electron shells of the sample atoms. When these holes are in an inner shell, electrons from an outer shell are dropping into an inner shell to stabilize the state of the atom. By dropping from a shell to another, the atom loses some energy in the form of X-rays emissions. These X-ray emissions have a characteristic energy and wavelength depending on the element atom and the shells concerned. Each element has a characteristic X-ray line (or lines depending on the number of shells) which allows the user to identify the elemental composition of the sample. This method is non-destructive.

Front side protection coating

Before processing the back side of the wafer to create the apertures, the front side is protected by sputtering a layer of SiO_2 in order not to damage the future active areas. The sputtering process is performed with a *Pfeiffer SPIDER600* sputtering machine (Pfeiffer Vacuum, Germany). This protection coating will protect the front side from mechanical shocks while manipulating the wafer with the subsequent operations (contact with chucks from spin coater or in ICP plasma etcher), and it will also prevent the NSiMs from breaking during the KOH wet etch by making the suspended areas more mechanically stable.

Back side (BS) photolithography

The procedure for the patterning of the apertures into the photoresist coating on the backside of the wafer is slightly different from the one for the front side since the thickness to be deposited is 4 times larger (8 µm). The substrate on the backside of the wafer is a thin polished 200 nm thick LS-SiN. To enhance the adhesion of photoresist onto LS-SiN, a strong oxygen plasma is performed (typically O_2 mass flow: 400sccm, power: 600 W, process time: 10 minutes with a *TEPLA Gigabatch plasma stripper*). A photoresist AZ9260 (AZ Electronic Materials, France) is spin coated at 2800 rpm for 1 minute and 40 seconds onto the backside of the wafer, followed by a soft bake at 112°C. The substrates are then put on a cool plate for 15 seconds. The rehydration time needed for such resist and this thickness is about 20 minutes with air humidity at 45% (controlled humidity in the clean room facilities). But a variation of few % in the air humidity influences strongly the rehydration time of thick resist. The wafers coated with photoresist were therefore left for rehydration for a couple of hours. A photomask designed in house and fabricated by Photronix (UK) was made to expose the photoresist on the back side of the wafer with the right pattern. The global pattern on the backside of the wafer is the mirror of the pattern of the front side photomask. Specificities in the design of the photomask will be discussed further. The necessary exposure dosis for 8 µm thick AZ9260 photoresist on LS-SiN is 260 mJ/cm^2. With the exposure tool *SÜSS MicroTec MA6&BA6* with a light intensity of 10 mW/cm^2, an exposure time of 26 seconds is needed. The exposure tool allows a back side alignment of the wafer with cameras placed on both sides of the wafers to visualize and align the corresponding alignment marks. The development of the exposed photoresist should be operated right after exposure. The development is based on the "spray" technique using the *Cluster EVG 150* automatic coater. Optical control of the apertures in the photoresist is necessary after development to identify any photoresist residues not well developed and increase the development time if necessary.

Back side DRIE of 200 nm of LS-SiN and 360 µm of Si

After creating the apertures in the 8 µm thick photoresist on the backside, a first dry etching step using *Etch_LS-SiN* (parameters of etching recipe discussed previously) needs to be performed to remove the 200 nm LS-SiN layer. The etching selectivity of LS-SiN over photoresist was calculated to be of 2.4:1. There is still approximately 7.9 µm of photoresist to etch through 360 µm of silicon. The process used is a standard Bosch process allowing deep anisotropic etching in silicon with vertical sidewalls without loss of lateral dimensions. The etching parameters are the following, SF_6 mass flow of 300 sccm and cycle time of 7 seconds, CH_4 mass flow of 150 sccm and cycle time of 2 seconds. The Source power is set to 1800 W and the chuck power is set to 45 W during the SF_6 cycles. The average calculated etch rate is of 6 µm/min and the selectivity over photoresist is greater than 75 : 1, meaning that with 7.9 µm of photoresist left, over 592 µm of Si can be etched. The depth in apertures of different lateral dimension is controlled using *Bruker Dektak XT* surface profiler (Bruker, Germany).

KOH we etching of the remaining 30 µm of Si

Before KOH wet etching, the remaining photoresist is stripped by O_2 plasma ashing with a *TEPLA Gigabatch plasma stripper*. Parameters of the etching step are the following, O_2 mass flow of 400 sccm, power of 600 W and process time of 10 minutes is used for full stripping of the remaining resist. The etch rate of positive resist with this recipe can vary from 250 nm/min to 1.2 µm/min depending on the process time and the number of wafer to be processed in the batch. Therefore the end point detector system of the machine is really useful. It helps visualizing the plasma intensity that becomes constant once all the organic compounds present in the chamber have been burnt out. This O_2 plasma step also enhances the wettability inside small backside apertures of the wafer just before KOH wet etching.

The etching of the remaining 30 µm of Si inside the backside aperture is performed in a 40% KOH solution at 60°C during two hours. The LS-SiN layer with apertures on the backside acts as an etch mask with high etching selectivity in KOH over silicon (>1:2000). After etching, optical control is necessary to visualize eventual silicon left at the bottom of the apertures and increase the KOH etching time. After KOH wet etching, the wafers are rinsed by simple dipping in Ultra Clean water bath three times 3 minutes with the water renewed each time. Wafers carrying the membranes are then transferred into a 2-propanol bath for 3 minutes, and pulled out to dry in air. Drying in air with isopropyl-alcohol is a commonly used technique in clean room facilities for fragile suspended structures because of the elevated surface tension of water (0.0729 N/m at 20°C) compared to the one of 2-propanol (0.022 N/m) that can generate a movement of the structure and affect the performance.

Removal of SiO_2 protection coating

The final release of the membrane is performed by stripping the SiO_2 protective layer on the front side. Stripping is performed in a buffered HF (7:1) bath at room temperature. The rinsing and drying procedure of the wafers are the same as the ones after KOH wet etching.

2.3.2 Results and discussion

Etching of a-Si nanopillars via BCP lithography

In a previous work done in our group, Klein et al. demonstrated the possibility of tuning the sidewall taper angle of silicon nanopillars by changing the ratio between SF_6 and C_4F_8 gases used in the continuous "pseudo Bosch" etching process specially developed for this purpose [21]. Using PS nanospheres as starting template, Si nanopillar arrays from negative to positive sidewall taper angle were achieved (figure 2.14).

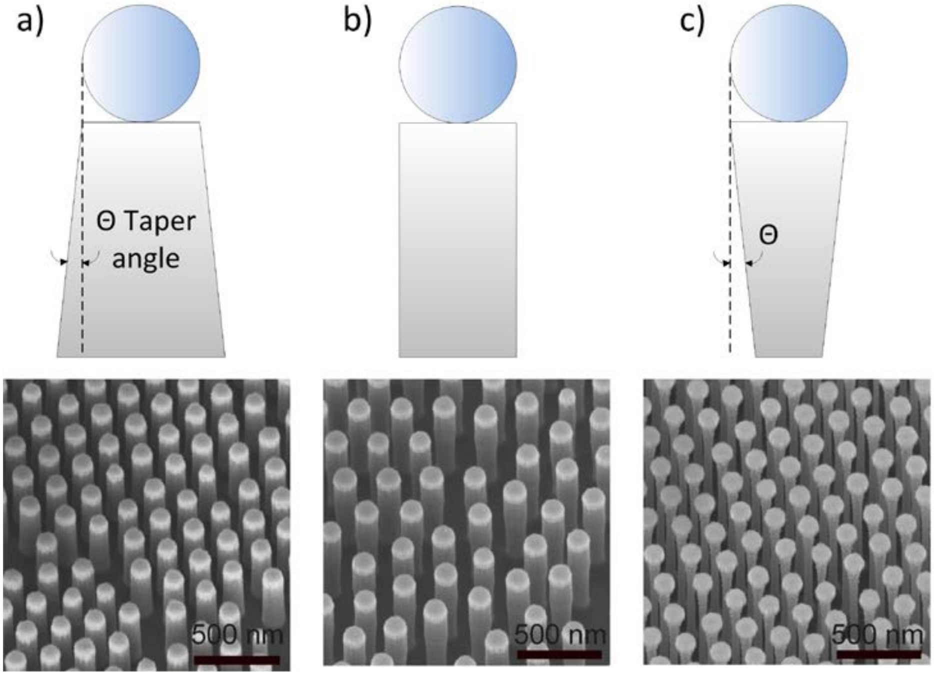

Figure 2.14 Schematic representations and associated SEM pictures of nanopillars with **a)** positive sidewall taper angle, **b)** perfectly vertical and **c)** negative sidewall taper angle obtained by increasing the SF_6 / C_4F_8 gas ratio from **a)** to **c)** of the pseudo "Bosch" dry etching process. (Adapted from [21]).

For the fabrication of NSiMs, regarding the next steps of the fabrication process being the evaporation of chromium and subsequent lift-off of the nanopillars, no Cr should be evaporated onto the sidewalls of the nanopillars (figure 2.15). It is therefore important to obtain perfectly vertical sidewalls of the nanopillars, or even a slight negative sidewall taper angle.

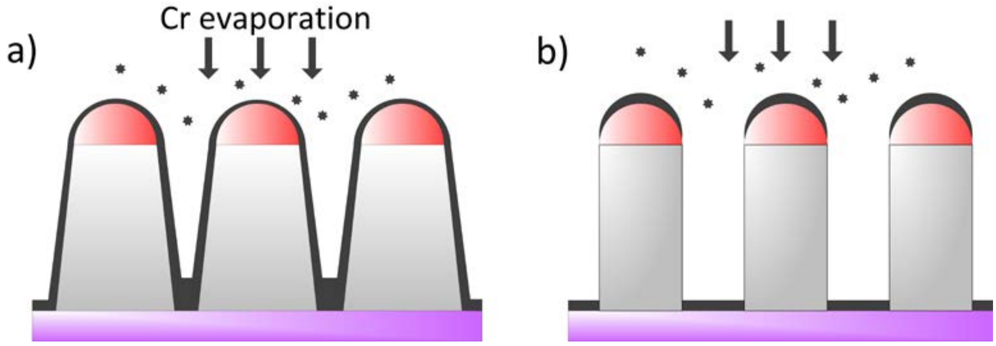

Figure 2.15 Cr evaporation onto nanopillars with **a)** positive sidewall taper angle and **b)** vertical sidewalls.

The maximum lift-off angle being really small (6°) during the evaporation process (evaporation process almost vertical), the parameter to be played on to avoid deposition of Cr onto the sidewalls is the taper angle of the nanopillars. Producing high aspect ratio nanopillars by adjusting the etching recipe has been studied using different starting templates [22–27]. Using BCP micelles with a mean diameter of 85 ± 15 nm as starting template, 150 nm high a-Si nanopillars with vertical sidewalls were obtained by using gases mass flow of 25 sccm of SF_6 and 55 sccm of C_4F_8 in the continuous “pseudo Bosch” dry etching process. In addition the overetch of the a-Si pillars should be absolutely avoided in order not to damage the underlying LS-SiN layer that will be the final free standing nanoporous structure after release of the NSiMs. Therefore it is crucial to perfectly control the etch rate of a-Si and reduce it as much as possible by lowering both the chuck power and the chamber temperature. The machine is equipped with and End Point Detection (EPD) system allowing the user to visualize when the next layer is reached in the etching process by monitoring the intensity change of a laser spot reflected onto the surface of the wafer. Figure 2.16 shows a SEM cross section picture of the a-Si nanopillar array obtained and the associated AFM image with section analysis to measure precisely the mean height of the nanopillar array. The height measured is about 170 nm, including the height of the nanopillars (150 nm) and the remaining micelle on top used as an etching mask (15-25 nm).

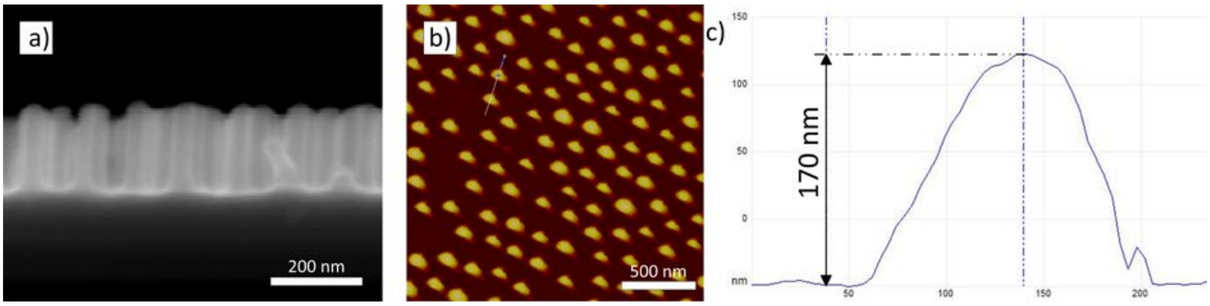

Figure 2. 16 a) cross section SEM picture, **b)** AFM micrograph (max Z scale is 150 nm) of the final nanopillar array and **c)** AFM section profile of a nanopillar determining the precise pillar height. **b)** and **c)** do not give information on the sidewall profile of the pillars due to the tip convolution artefact.

Control of full lift-off

The etch rate of a-Si in KOH is way slower than crystalline silicon because a-Si deposited by sputtering is boron doped, reducing the etch rate in alkaline solutions [28–30]. Therefore the wet etching time to complete the lift-off was increased and stopped after the reaction was finished. After performing the full lift-off procedure detailed earlier, the wafers are analyzed individually by SEM at different places to control the cleanliness and identify any Cr residues. The Cr residues present at the surface come from the Cr caps on top of the micelles or probable Cr particles on the sidewalls of the nanopillars. If residues are observed, the wafers are submitted to an ultrasonic cleaning step in ultrapure deionized water which is a well-known technique to remove sub-micron particles adhering to the surface [31–33]. Figure 2.17 shows the schematic representation and associated SEM pictures of the lift-off process with Cr particles detected onto the surface.

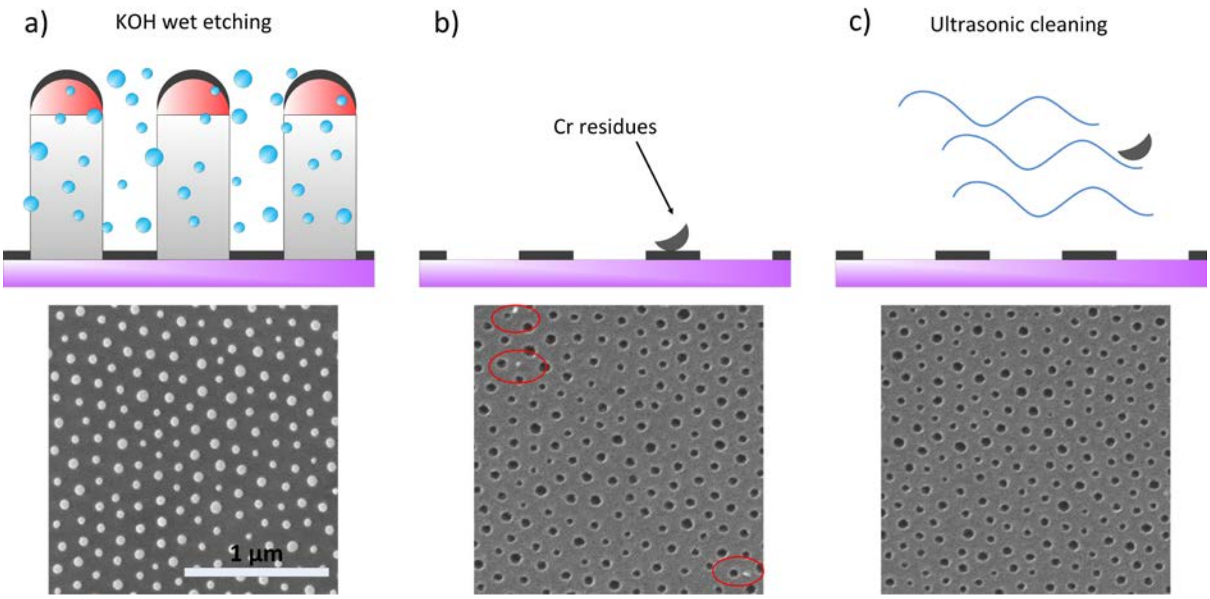

Figure 2.17 Schematic representation and associated SEM top view pictures of **a)** the nanopillars coated with Cr before KOH lift-off, **b)** The nanoporous Cr layer with Cr residues directly after KOH lift-off, **c)** the nanoporous Cr layer after KOH lift-off and ultrasonic cleaning in water to remove Cr residues.

Figure 2.18 shows the size distribution of the mean diameter of the nanopillars coated with Cr before lift-off and the size distribution of the mean diameter of the nanopores in the Cr layer after lift-off. Results obtained are in good agreement with the original mean diameter of the BCP micelles used as starting template, thus demonstrating reliable pattern transfer into a-Si and pattern inversion into Cr after lift-off. From a mean diameter of 85 ± 15 nm of the deposited micelle, 20 nm thick porous Cr mask with mean nanopore diameter of 85 ± 15 nm could be fabricated at wafer scale.

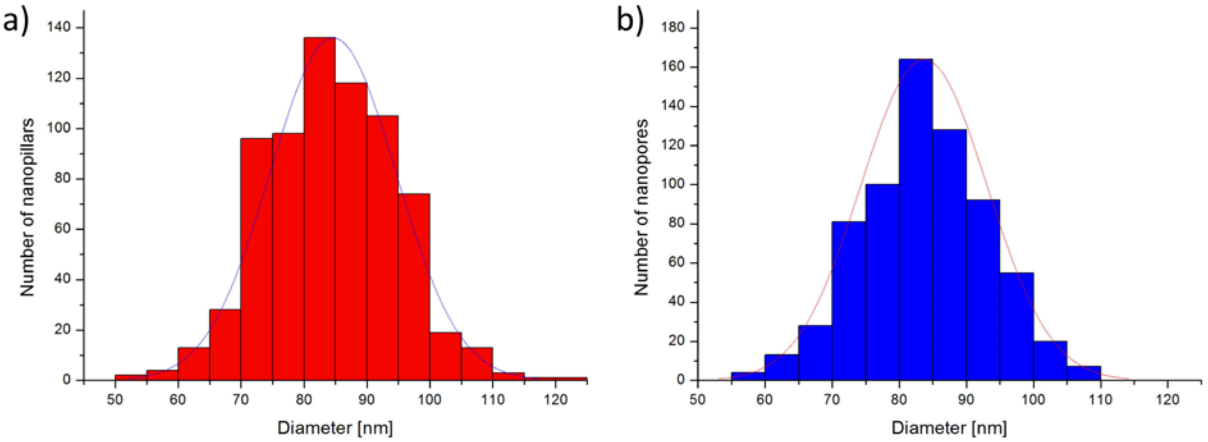

Figure 2.18 Size distribution of the mean diameter of **a)** a-Si nanopillars coated with Cr before lift-off and **b)** nanopores in the Cr layer after lift-off. (Size distribution was calculated from 4 x 4 µm^2 top view SEM pictures).

Design of front side photomask

The front side photolithography step defines the active areas of the final NSiMs. Square openings of different size (from 800 x 800 µm^2 up to 2.5 x 2.5 mm^2) have been patterned into the photoresist layer using the front side photomask designed for this purpose. Figure 2.19 shows half of the design desired on the 4 inches wafer, the active areas are defined onto 6 x 6 mm^2 chips labelled with the membrane size and separated with dicing marks. Alignment marks are also displayed on the wafer extremities in order to perform a backside alignment during the backside photolithography. This step is crucial to make the backside apertures coinciding with the front side active areas. A combination of several sizes of active areas is proposed in the design in order to characterize the mechanical properties of the suspended nanoporous structure that are dependent on the lateral dimensions of the membrane. The study of the mechanical properties will be discussed in the next chapter. Also, to increase the active area per chip, several small membranes (more mechanically stable) of the same lateral dimension have been integrated onto the same chip for the production of membrane arrays.

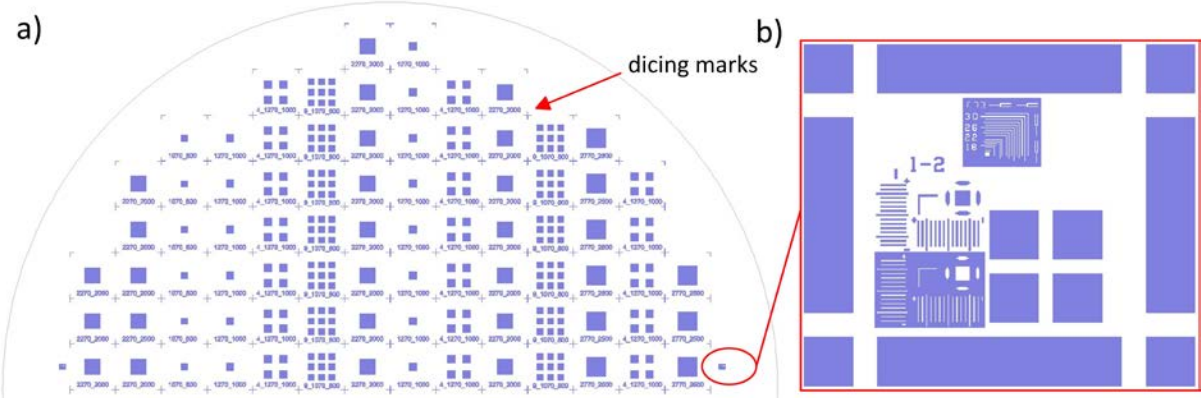

Figure 2.19 Image of **a)** the design of the front side photolithographic mask with apertures of different size and organisation to determine the active areas of the future NSiMs and **b)** the alignment marks used in the design.

Etching of the nanopores in the LS-SiN layer

For the etching of the nanopores in LS-SiN through the nanoporous Cr mask, several important parameters have to be taken into account, the sidewall angle of the nanopores, the etching rate of LS-SiN and the selectivity LS-SiN:Cr. *Etch_SiN* (described in the procedure earlier) is a well-defined etching recipe generally used to etch stoichiometric silicon nitride producing smooth vertical sidewalls with an etch rate of 200 nm/min. In this recipe He gas is used to dilute the fluorocarboned chemistry in order to reach low gas residence time which is a key parameter to obtain a control over the profile angle of the structures [34]. EPD system allowed the visualization of the consumption of the nanoporous Cr mask. After 1'30" of etching, the 20 nm of Cr were entirely consumed and the wafer was sacrificed to control the shape and depth of the nanopores with a cross section SEM analysis. Figure 2.20 a) shows the average depth of the nanopores measured to be of 115 nm while it was expected to be around 200 nm into the LS-SiN layer. Therefore the nanopores will not go through the entire 200 nm thick LS-SiN layer and the fabrication of NSiMs could not be processed any further. The decrease in etch rate using fluorocarbon plasma has already been described in previous works [34,35]. It is explained by polymer deposition on both the sidewalls and the bottom of the nanopores during the etching because addition of H and C atoms increases the C/F ratio which is known to increase polymer deposition in etching processes. As a consequence the etch rate of LS-SiN and the selectivity over Cr are decreased. The vertical etching of nanopores was stopped.

The solution proposed to overcome the previously described extra-polymerization was to use the etching recipe *Etch_LS-SiN* involving only C_4F_8. By suppressing the CH_4 gas, less polymer was expected to be formed and therefore deeper etching in the LS-SiN layer could be achieved. Since the ICP source and the RF chuck power control the ion flux and the ion energy, respectively, the chuck power was lowered from 180W to 100W in order to decrease the physical etch of the nanoporous Cr mask. Using this optimized recipe, 1 minute and 15 seconds of etching was sufficient to etch completely through the 200 nm of LS-SiN (figure 2.20 b)); the etch rate of LS-SiN has been found to be of 250 nm/min. The nanoporous Cr mask was fully consumed after 2 minutes of etching; therefore the selectivity Cr:LS-SiN was found to be of 1:25 approximately.

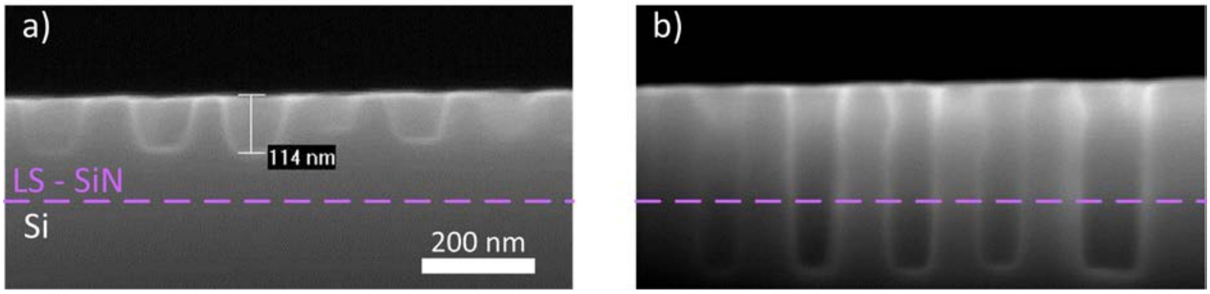

Figure 2.20 Cross sectional SEM pictures of nanopores dry etched with **a)** *Etch_SiN* for 1’30” and with **b)** *Etch_LS-SiN* for 1’15”.

Stripping of photoresist and Cr

After completing the stripping procedure of photoresist and chromium, the wafers have been analyzed with EDX to detect if Cr was still present on the surface. Indeed fluorocarbon chemistry used in the dry etching process might have created a protection coating onto the Cr layer making its removal more difficult. Figure 2.21 a) shows an example of EDX analysis detecting Cr residues after the Cr etch step. A second Cr etch was performed and final EDX analysis showed that all the Cr was finally removed (figure 2.21 b)). The presence of aluminium detected by EDX is explained by the nature of the substrate holder made of this material. The traces of Fluor detected are coming from the fluorocarbon chemistry used during the dry etching process causing polymerization into the nanopores.

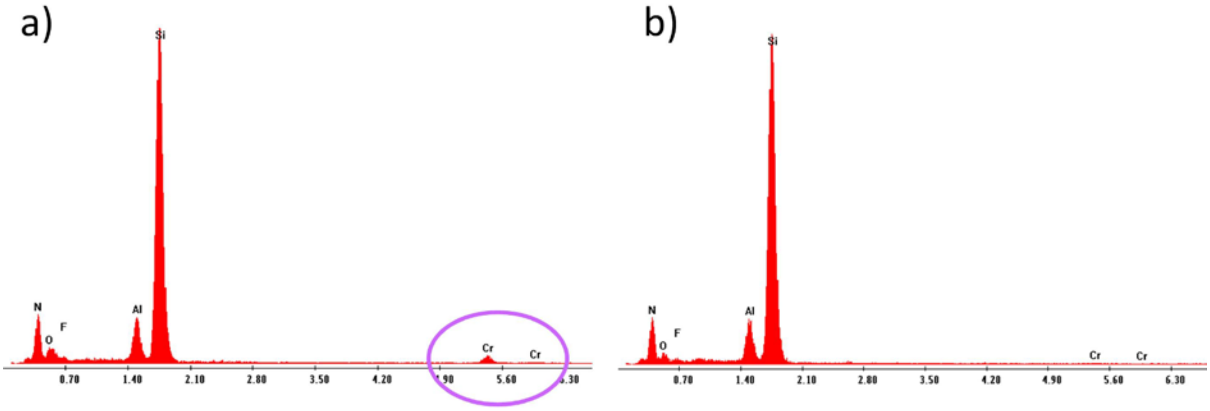

Figure 2.21 EDX analysis of Cr residues after **a)** first Cr etch step and **b)** second iterative Cr etch to remove all the residues.

Design of back side photomask

The global pattern of the back side photomask is the mirror of the pattern of the front side photomask. All the apertures in the BS photomask were made larger than the coinciding ones on the FS photomask because the final square suspended nanoporous areas should be framed by a non-porous suspended area in order to improve the mechanical stability and resistance of the final NSiMs [36–38]. The size of the apertures in the design of the photomask has to take into account that a non-porous suspended frame in the range order of 100 ± 15 μm wide is desired after proceeding to DRIE through the silicon for 360 μm and final release with KOH for the remaining 30 μm. The etching of <100> oriented silicon using aqueous KOH creates V-shaped grooves with (111) planes at an angle of 54.74° from the (100) surface. The slow etch rate of silicon in the <111> direction is a consequence of the diamond lattice structure because the (111) plane is a double layer bound together with more atomic bonds than the other planes [39]. A schematic representation of the final desired structure is represented in figure 2.22.

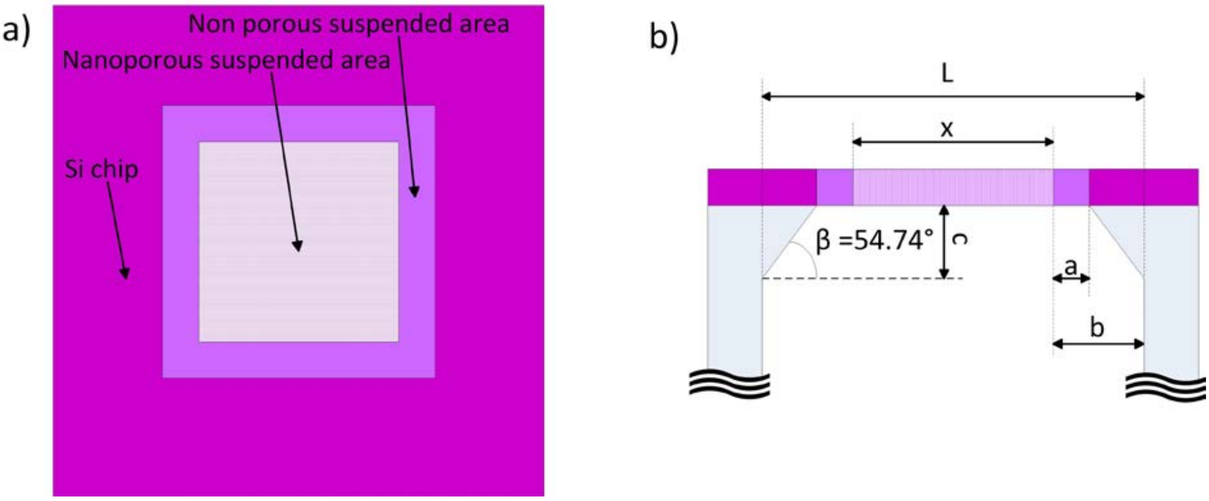

Figure 2.22 Schematic representations of **a)** top view and **b)** cross sectional side view of the final structure of the NSiM after DRIE through 360 μm of Si and final KOH release for the remaining 30 μm. *L: Lateral dimension of the square apertures in the BS photomask; x: Lateral dimension of the square aperture in the FS photomask; a: width of the non-porous suspended frame; β: angle between (111) and (100) Si planes due to KOH etching; c: remaining Si depth to be etched with KOH.*

A simple trigonometric calculus gives all the information on the lateral size of the apertures to be designed in the BS photomask. With L the lateral dimension of the square apertures in the BS photomask, x the lateral dimension of the corresponding square aperture in the FS photomask, a the distance between the border of the porous and non-porous suspended areas, c the remaining thickness of Si to be etched with KOH and β the angle of 54.74° between the (111) plane of Si and the (100) surface due to KOH etching.

$$L = x + 2a + \frac{2c}{\tan \beta} \qquad (2.1)$$

With a non-porous frame of $a = 115$ µm wide, and with $c = 30$ µm of remaining Si to be etched with KOH, the lateral dimensions L of the apertures in the BS photomask were calculated to be designed 270 µm wider than the corresponding front side apertures with lateral dimension x ($L - x = 270$ µm). Figure 2.23 a) shows the design of the BS photomask with the overlaid layer of the FS photomask. Before exposure to UV light of the BS photoresist through the BS photomask, the wafer needs to be properly aligned by overlaying the FS and BS alignment marks (Figure 2.23 b)). A slight misalignment during exposure will make the non-porous suspended frame not properly centered respectively to the nanoporous area. A frame not centered can lead to mechanical instability issues, such as less mechanical resistant suspended structures or buckling. 10 µm wide trenches were also added to the BS photomask's design to mark the 6 x 6 mm^2 chips borders for manual cleavage.

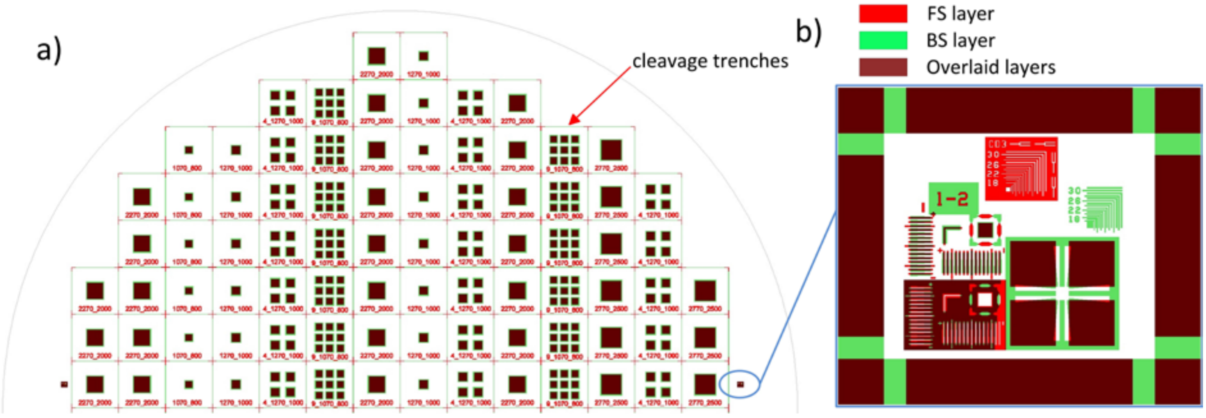

Figure 2.23 Image of **a)** the overlaid designs of the BS and FS photolithographic mask and **b)** the overlaid FS and BS alignment marks.

Membrane release combining DRIE and KOH wet etching

Combining DRIE and KOH for the release of micro structures has been used in the past to obtain vertical surfaces or to cancel the scalloping effect obtained using a Bosch process with DRIE [40–42]. In the case of the release of NSiMs there are two major advantages of combining DRIE and KOH wet etching. First, the limitation for the aperture size on the backside is considerably decreased compared to only KOH release through 390 µm of silicon where the resulting pyramidal shape due to the etching has to be anticipated. By combining DRIE and KOH wet etching, the lateral dimension of the backside apertures has to be increased by only 270 µm. In contrast the release only with KOH wet etching would require an increase of the lateral dimension of the back side apertures of 780 µm.

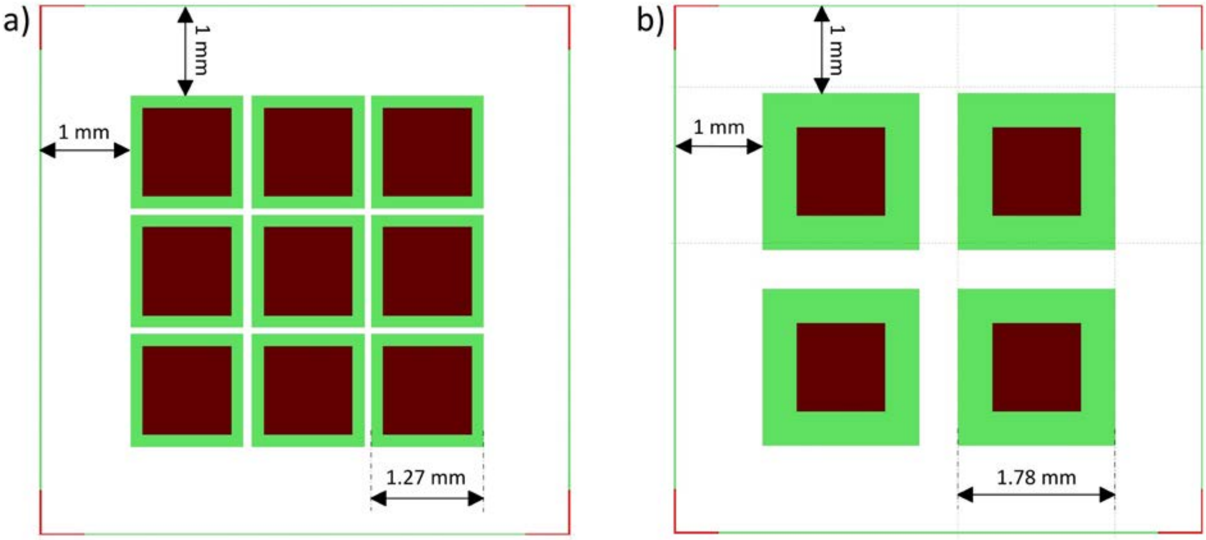

Figure 2.24 Example of designs of FS and BS layers of the photomasks for the fabrication of Si chip containing a maximum array of **a)** 3 x 3 NSiMs for a total active area of 9 mm^2 using DRIE and KOH release and **b)** 2 x 2 NSiMs for a total active area of 4 mm^2 using only KOH release

As it can be seen in figure 2.24, combining DRIE and KOH wet etching allows defining larger active nanoporous area per Si chip. When considering a 6 x 6 mm^2 Si chip on which 4 x 4 mm^2 can be patterned (1 mm has to be left free between the border of the Si chip and the first aperture for handling reasons), an array of 3x3 NSiMs with total active area of 9 mm^2 can be patterned when combining DRIE and KOH; an array of only 2x2 NSiMs with total active area of 4 mm^2 can be patterned when using only KOH wet etching. Table 2.8 shows theoretical values of the influence of the release technique used (only KOH wet etching and DRIE combined to KOH wet etching) on the maximum

NSiMs array and corresponding active area that can be patterned per Si chip depending on the lateral dimension of the active area of one NSiM of the array.

Table 2.8 Theoretical calculation of the maximum active area that can be defined on a 4 x 4 mm^2 surface depending on the release technique; only KOH wet etching and combining DRIE and KOH wet etching.

Active area on front side ***μm²***	**Side length of backside aperture** ***μm***		**Larger array possible**		**Total active area** ***mm²***	
	Release KOH	Release KOH+DRIE	Release KOH	Release KOH+DRIE	Release KOH	Release KOH+DRIE
10 x 10	790	280	5 x 5	13 x 13	0.0025	0.0169
100 x 100	880	370	4 x 4	10 x 10	0.16	1
1000 x 1000	1780	1270	2 x 2	3 x 3	4	9

The second major advantage of combining DRIE and KOH wet etching compared to using only KOH wet etching for the full release of the suspended membranes is the decrease of the operational time. Combining DRIE and KOH wet etching 2 hours and 45 minutes were needed for the complete release of NSiMs (1 hour for DRIE, 1 hour and 45 minutes for 40% KOH at 60°C, figure 2.25 shows the KOH wet etching rate of <100> silicon at different temperatures [29]). In contrast a complete release through 390 μm of <100> silicon wafer using only KOH wet etching would take 19 hours and 30 minutes. On the batch fabrication of 8 wafers carried out in this work, combining DRIE and KOH for the release of the nanoporous suspended structure allowed the reduction of operational time by almost 10 hours compared to a release procedure employing only KOH wet etching.

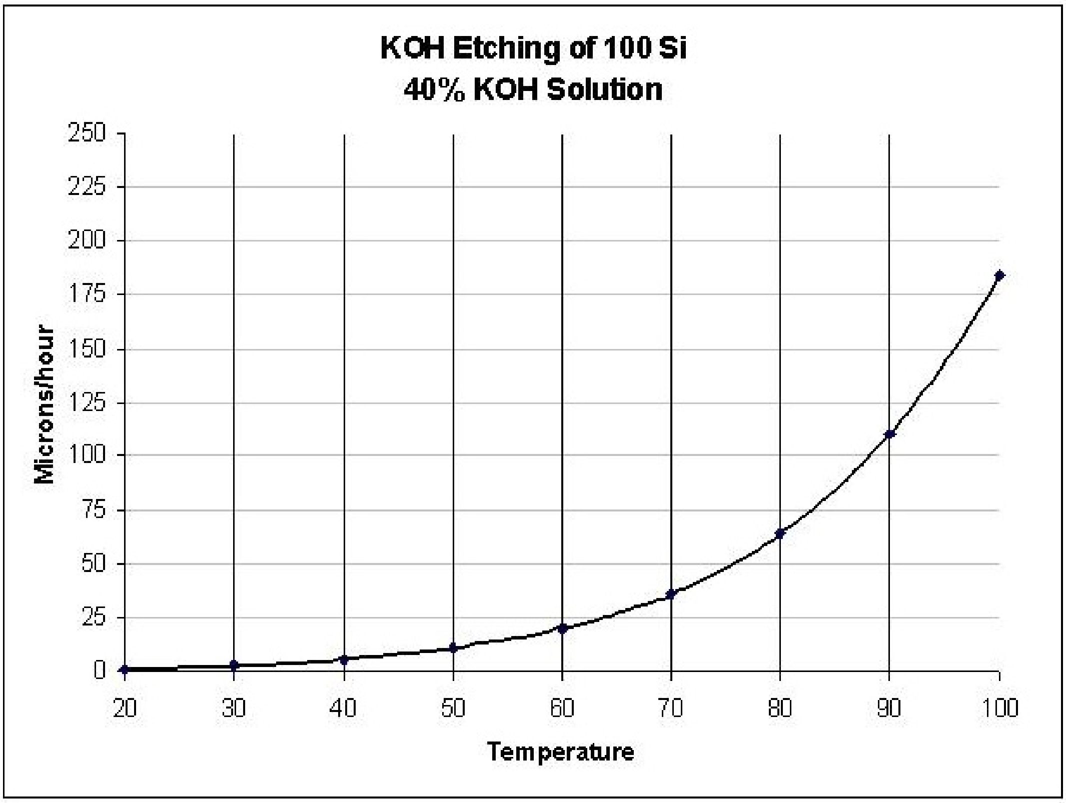

Figure 2.25 Etch rate of <100> silicon in a 40% KOH solution depending on the temperature of the solution. (Adapted from [29]).

The final release of the membrane is achieved through the wet etching of the front side SiO_2 protective layer. In previous work done in our group, the front side was only protected before the KOH wet etch for the final release with ProTEK (Brewer Science, USA) which is a temporary protective coating which is resistant to KOH [21]. Issues were observed using the ProTEK layer, such as the delamination of the layer during KOH wet etching or final removal. Therefore SiO_2 appeared to be a good protective layer and has been widely used in previous works because of its ease of deposition, removal and its low etch rate into KOH [43–45].

Quality control

The fabrication yield of NSiMs at wafer scale should be evaluated by performing a standard SEM analysis on each membrane of the wafer to detect major defaults and count the number of good and operational NSiMs. But non automated characterization in electron microscopy analysis remains time consuming and expensive. Therefore the fabrication yield of NSiMs at waferscale was estimated by only counting the number of broken membranes during the fabrication process. NSiMs used for diffusion and filtration experiments will be submitted to strong defect analysis with SEM before integration into microfluidic devices. An overall fabrication yield of 91.6% was achieved. Table 2.9 shows the detailed fabrication yield depending on the membrane size. Large NSiMs with active areas of 2.5 x 2.5 mm^2 exhibit a poor fabrication yield of 43.75% due to the low mechanical strength of such large suspended structure.

Table 2.9 Fabrication yields of NSiMs of different lateral size displayed in various arrays on the Si chips.

Lateral dimension of NSiM *µm*	**Array**	**Total active area per chip** *mm²*	**Fabrication yield** *%*
800	1 x 1	0.64	100
800	3 x 3	5.76	96
1000	1 x 1	1	100
1000	2 x 2	4	96.58
2000	1 x 1	4	94.67
2500	1 x 1	6.25	43.75

Filter makers widely use the bubble point testing technique to characterize the pore size rating of membranes [46,47]. This test method consists in wetting the membrane and filling the pores with a solvent, the membrane is then pressurized gradually with an inert gas until the solvent is pushed out. The gas pressure level at which the solvent from the largest pore is completely pushed out is called the bubble point, determining the maximum pore size. Since the bubble point is directly proportional to the solvent surface tension and inversely proportional to the membrane pore size, the bubble point technique allows detecting large defects into the nanoporous suspended layer but again this technique is time consuming if not optimized to be performed at the wafer level. Such equipment was not available to be tested onto NSiMs.

2.3.3 Preliminary conclusions

Using the previously described optimized fabrication process, wafers carrying 160 Si chips with arrays of NSiMs of different sizes were successfully fabricated processing batch fabrication of 8 wafers. Several major issues encountered during the fabrication process such as the vertical etch stop of nanopores in LS-SiN due to high polymerization during the etching process or the removal of Cr residues have been discussed, understood and overcome. Figure 2.26 shows pictures of a wafer carrying 160 chips and cleaved Si chips carrying arrays of NSiMs of different lateral dimensions.

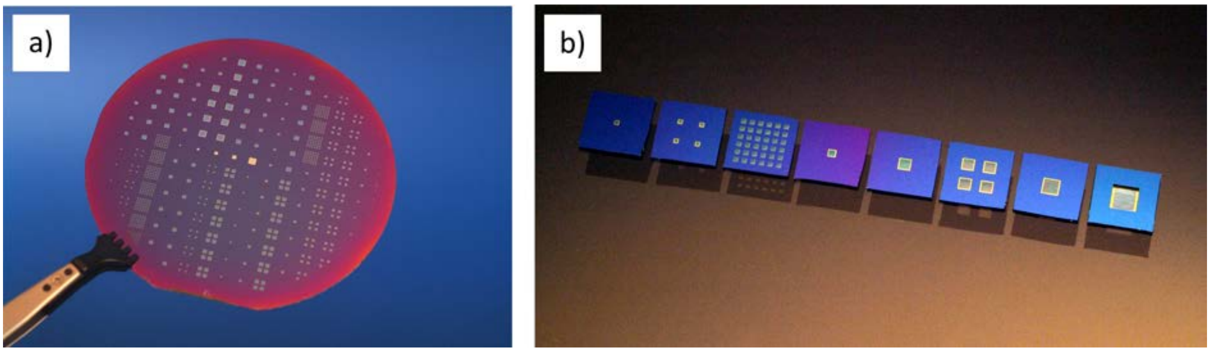

Figure 2.26 Pictures of **a)** 4” wafer carrying 160 chips integrating NSiMs and **b)** Si chips carrying various arrays of NSiMs of different lateral dimensions.

2.4. Conclusions

In this work we focused on optimizing procedures to develop a reliable and robust process combining block copolymer lithography and standard microfabrication techniques for the wafer scale batch production of nanoporous silicon nitride membranes. The mean diameter of the block copolymer micelles used as templating structure reflects the mean diameter of the nanopores in the suspended low stress silicon nitride layer. The nanopores in the final 200 nm thick suspended structure exhibit a diameter size distribution of 85 ± 15 nm, final characterization of the final NSiMs produced will be discussed in the next chapter.

Using block copolymer lithography for the fabrication of NSiMs adds flexibility to the process since the starting micellar template has been demonstrated to be tunable in diameter and in density of micelles per surface area. The major critical parameter we identified for the fabrication of NSiMs using block copolymer micelles is the mean micelle height of 25-30 nm necessary to propose a resistant etch mask for the subsequent pattern transfer into amorphous silicon using DRIE. Obviously the monodispersity of the micelles as well as the homogeneity of the nanopattern obtained over 4 inches wafer after micelle deposition are also important issues to be considered.

The standard UV photolithography allowed to pattern single nanoporous membranes as large as 2 x 2 mm^2 with an overall batch fabrication yield above 90%.

References

[1] M. Sprenger, S. Walheim, A. Budkowski, U. Steiner, Hierarchic Structure Formation in Binary and Ternary Polymer Blends, Interface Science. 11 (2003) 225–235.

[2] E.Y. Kramarenko, I.I. Potemkin, A.R. Khokhlov, R.G. Winkler, P. Reineker, Surface Micellar Nanopattern Formation of Adsorbed Diblock Copolymer Systems, Macromolecules. 32 (1999) 3495–3501.

[3] I.I. Potemkin, E.Y. Kramarenko, A.R. Khokhlov, R.G. Winkler, P. Reineker, P. Eibeck, et al., Nanopattern of Diblock Copolymers Selectively Adsorbed on a Plane Surface., Langmuir. 15 (1999) 7290–7298.

[4] S. Krishnamoorthy, Self-assembly of tunable, responsive polymer nanostructures: tools for nanofabrication of functional interfaces, Ecole Polytechnique Fédérale de Lausanne, 2006.

[5] J. Liou, Y. Sun, Monolayers of Diblock Copolymer Micelles by Spin-Coating from o-Xylene on SiO, Macromolecules. 45 (2012) 1963–1971.

[6] W. Huang, C. Luo, J. Zhang, Y. Han, Formation of ordered microphase-separated pattern during spin coating of ABC triblock copolymer., The Journal of Chemical Physics. 126 (2007) 104901 (9pp).

[7] O. Mellbring, Spin Coating and Characterization of Thin High-Density Polyethylene Films, Macromolecules. 34 (2001) 7496–7503.

[8] T.M. Birshtein, E.B. Zhulina, Scaling theory of supermolecular structures in block copolymer-solvent systems: 1. Model of micellar structures, Polymer. 30 (1989) 170–177.

[9] E.B. Zhulina, O. V Borisov, Theory of Block Polymer Micelles : Recent Advances and Current Challenges, Macromolecules. 45 (2012) 4429–4440.

[10] J. Bang, K. Viswanathan, T.P. Lodge, M.J. Park, K. Char, Temperature-dependent micellar structures in poly(styrene-b-isoprene) diblock copolymer solutions near the critical micelle temperature., The Journal of Chemical Physics. 121 (2004) 11489–11500.

[11] V. Castelletto, I.W. Hamley, J.S. Pedersen, A small-angle neutron scattering investigation of the structure of highly swollen block copolymer micelles, The Journal of Chemical Physics. 117 (2002) 8124–8129.

[12] K.V. Agrawal, B. Topuz, Z. Jiang, K. Nguenkam, B. Elyassi, L.F. Francis, et al., Solution-Processable Exfoliated Zeolite Nanosheets Purified by Density Gradient Centrifugation, AIChE Journal. 59 (2013) 3458–3467.

[13] A. V. Heydenreich, R. Westmeier, N. Pedersen, H.S. Poulsen, H.G. Kristensen, Preparation and purification of cationic solid lipid nanospheres—effects on particle size, physical stability and cell toxicity, International Journal of Pharmaceutics. 254 (2003) 83–87.

[14] J. a Jamison, K.M. Krueger, C.T. Yavuz, J.T. Mayo, D. LeCrone, J.J. Redden, et al., Size-dependent sedimentation properties of nanocrystals., ACS Nano. 2 (2008) 311–319.

[15] G. Dalwadi, H. a. E. Benson, Y. Chen, Comparison of Diafiltration and Tangential Flow Filtration for Purification of Nanoparticle Suspensions, Pharmaceutical Research. 22 (2005) 2152–2162.

[16] D.A. Bernards, T.A. Desai, Nanoscale porosity in polymer films : fabrication and therapeutic applications, Soft Matter. 6 (2010) 1621–1631.

[17] P. Stroeve, N. Ileri, Biotechnical and other applications of nanoporous membranes, Trends in Biotechnology. 29 (2011) 259–66.

[18] N. Ileri, S.E. Létant, J. Britten, H. Nguyen, C. Larson, S. Zaidi, et al., Efficient Nanoporous Silicon Membranes for Integrated Microfluidic Separation and Sensing Systems, MRS Proceedings. 1191 (2011) 1191–OO09–02.

[19] N. Itoh, K. Kato, T. Tsuji, M. Hongo, Preparation of a tubular anodic aluminum oxide membrane, Journal of Membrane Science. 117 (1996) 189–196.

[20] W. Lee, R. Ji, U. Gösele, K. Nielsch, Fast fabrication of long-range ordered porous alumina membranes by hard anodization., Nature Materials. 5 (2006) 741–7.

[21] M.J.K. Klein, Wafer-scale fabrication of thin SiN membranes and Au films and membranes with arrays of sub-µm holes using nanosphere lithography, Ecole Polytechnique Fédérale de Lausanne, 2010.

[22] V. Gowrishankar, N. Miller, M.D. McGehee, M.J. Misner, D.Y. Ryu, T.P. Russell, et al., Fabrication of densely packed, well-ordered, high-aspect-ratio silicon nanopillars over large areas using block copolymer lithography, Thin Solid Films. 513 (2006) 289–294.

[23] K.J. Morton, G. Nieberg, S. Bai, S.Y. Chou, Wafer-scale patterning of sub-40 nm diameter and high aspect ratio (>50:1) silicon pillar arrays by nanoimprint and etching, Nanotechnology. 19 (2008) 345301 (6pp).

[24] Ü. Sökmen, A. Stranz, S. Fündling, H.-H. Wehmann, V. Bandalo, A. Bora, et al., Capabilities of ICP-RIE cryogenic dry etching of silicon: review of exemplary microstructures, Journal of Micromechanics and Microengineering. 19 (2009) 105005 (8pp).

[25] M.D. Henry, ICP ETCHING OF SILICON FOR MICRO AND NANOSCALE DEVICES, California Institute of Technology, 2010.

[26] Y.-J. Hung, S.-L. Lee, B.J. Thibeault, L. a. Coldren, Realization of silicon nanopillar arrays with controllable sidewall profiles by holography lithography and a novel single-step deep reactive ion etching, MRS Proceedings. 1258 (2011) 1258–Q14–02.

[27] Ü. Sökmen, a. Stranz, S. Fündling, S. Merzsch, R. Neumann, H.-H. Wehmann, et al., Shallow and deep dry etching of silicon using ICP cryogenic reactive ion etching process, Microsystem Technologies. 16 (2010) 863–870.

[28] I. Haller, Y.H. Lee, J.J. Nocera, M.A. Jaso, Selective Wet and Dry Etching of Hydrogenated Amorphous Silicon and Related Materials, Journal of The Electrochemical Society. 135 (1988) 2042–2045.

[29] H. Seidel, L. Csepregi, A. Heuberger, H. Baumgärtel, Anisotropic etching of crystalline silicon in alkaline solutions, Journal of The Electrochemical Society. 137 (1990) 3612–3632.

[30] K. Yokota, T. Kitagawa, D. Yamamoto, K. Nakamura, F. Miyashita, Luminescence from hydrogenated amorphous silicon treated in microwave hydrogen plasma , KOH solution , and oxygen atmosphere, Thin Solid Films. 343-344 (1999) 191–194.

[31] T. Kani, T. Suzuki, M. Tsukada, H. Kamiya, Influence of surface-adhered nanoparticles and nanoporous structure on bulk flowability of silica, Powder Technology. 176 (2007) 108–113.

[32] A. Busnaina, I. Kashkoush, The effect of time, temperature and particle size on submicron particle removal using ultrasonic cleaning, Chemical Engineering Communications. 125 (1993) 47–61.

[33] I. Kashkoush, A. Busnaina, Submicron particle removal using ultrasonic cleaning, Particulate Science and Technology: An International Journal. 11 (1993) 11–24.

[34] M. Pavius, C. Hibert, P. Flückiger, P. Renaud, L. Rolland, M. Puech, Profile angle control in SiO2 deep anisotropic dry etching for MEMS fabrication, in: IEEE MICRO ELECTRO MECHANICAL SYSTEMS WORKSHOP, 2004: pp. 669–672.

[35] P. Verdonck, Plasma Etching, UNICAMP São Paulo. (n.d.) http://www.ccs.unicamp.br/novosite/ie521/files/201.

[36] Á. Kovács, a. Kovács, U. Mescheder, Estimation of elasticity modulus and fracture strength of thin perforated SiN membranes with finite element simulations, Computational Materials Science. 43 (2008) 59–64.

[37] TED-PELLA, PELCO, PELCO Holey Silicon Nitride Support Film for TEM, (n.d.) http://www.tedpella.com/grids_html/silicon–nitride.

[38] a Kovacs, M. Pogany, U. Mescheder, Mechanical investigation of perforated and porous membranes for micro- and nanofilter applications, Sensors and Actuators B: Chemical. 127 (2007) 120–125.

[39] K.E. Bean, W.R. Runyan, Semiconductor integrated circuit processing technology, 1990th ed., Addison-Wesley, 1990.

[40] D. Nilsson, S. Jensen, A. Menon, Fabrication of silicon molds for polymer optics, Journal of Micromechanics and Microengineering. 13 (2003) 57–61.

[41] S.-S. Yun, S.-K. You, J.-H. Lee, Fabrication of vertical optical plane using DRIE and KOH crystalline etching of (110) silicon wafer, Sensors and Actuators A: Physical. 128 (2006) 387–394.

[42] D. Lee, Kyoungsik Yu, U. Krishnamoorthy, O. Solgaard, Vertical Mirror Fabrication Combining KOH Etch and DRIE of (110) Silicon, Journal of Microelectromechanical Systems. 18 (2009) 217–227.

[43] J.T. Santini, M.J. Cima, R. Langer, Acontrolled-releasemicrochip, Nature. 397 (1999) 335–338.

[44] D.Z. Fang, C.C. Striemer, T.R. Gaborski, J.L. Mcgrath, P.M. Fauchet, Methods for controlling the pore properties of ultra-thin nanocrystalline, Journal of Physics Condensed Matter. 22 (2010) 1–8.

[45] V. Grigaliūnas, B. Abakevičienė, I. Grybas, R. Naujokaitis, S. Tamulevičius, Two-step Fabrication of Large Area SiO 2 / Si Membranes, Materials Science. 18 (2012) 325–329.

[46] A. Hernandez, J.I. Calvo, P. Pradanos, F. Tejerina, Pore size distributions in microporous membranes . A critical analysis of the bubble point extended method, Journal of Membrane Science. 112 (1996) 1–12.

[47] J. Yu, X. Hu, Y. Huang, A modification of the bubble-point method to determine the pore-mouth size distribution of porous materials, Separation and Purification Technology. 70 (2010) 314–319.

Chapter 3

Characterization of Nanoporous Silicon Nitride Membranes

Abstract

The characterization of the nanoporous silicon nitride membranes in terms of nanopore morphology, density and mechanical properties will be studied in this chapter.

First, several techniques such as AFM, SEM working in STEM mode and TEM will be proposed to characterize the full opening of the nanopores through the 200 nm thick suspended low stress silicon nitride layer. The important parameters to be characterized are the mean nanopore diameter, the profile of the nanopores (vertical sidewalls) and the density of nanopores per surface area.

Second, the produced membranes will be submitted to the bulge test in order to characterize the mechanical properties of the NSiMs depending on the lateral dimensions of the square active areas and the thickness. The bulge test is used to determine the maximum burst pressure of the membranes, the Young's modulus and residual stress of the suspended layer analyzed.

Finally, buckling problems that can appear during the fabrication process depending on the initial type of silicon nitride used will be discussed and a solution to overcome this issue will be proposed.

3.1. Characterization of nanoporous membrane morphological properties

While processing the 8 wafers batch fabrication of silicon nitride nanoporous membranes, the nanoporous layer was not characterized systematically for each wafer. Especially regarding the dry etching of the nanopores into the low stress silicon nitride layer, only one wafer was sacrificed to confirm that the etching has been performed through the entire 200 nm thick LS-SiN layer. Reproducibility of the etching process was therefore supposed, and final characterization of several membranes from each wafer confirmed it and allowed us determining the final characteristics of the NSiMs namely the mean pore diameter and the pore density.

3.1.1 Using Atomic Force Microscopy

Experimental

Front side AFM analysis

The AFM tool used is a *Dimension 3100* Atomic Force Microscope (Veeco Digital Instruments, USA) and the scanning parameters are identical as the one described in section 2.2.1. A single NSiM was placed on the AFM chuck previously cleaned with 2-propanol. All the data acquired was processed using the *Nanoscope Analysis* software (Bruker, Germany), *imageJ* (National Institute of Health, USA) and *Origin* (OriginLab, USA).

Back side AFM analysis

Since the AFM tip cannot access into the 390 μm deep backside aperture to scan the backside of the suspended nanoporous area, the NSiM was stuck from the front side onto a double sided carbon adhesive tab usually used in SEM analysis. The Si chip was then peeled off with tweezers, leaving the suspended nanoporous area stuck from the front side onto the adhesive tab. Figure 3.1 shows a schematic representation of the procedure. The adhesive tab with the suspended area stuck on it was then submitted to strong oxygen plasma (O_2 mass flow: 50 sccm; voltage bias: 260 V; forward power: 100 W; process time: 10 minutes) with a *Oxford Plasmalab 80+* machine in order to remove all the acrylic glue of the adhesive tab that could have penetrate into the nanopores and alter the AFM analysis of the surface. AFM tool used and parameters of the analysis were the same as described earlier.

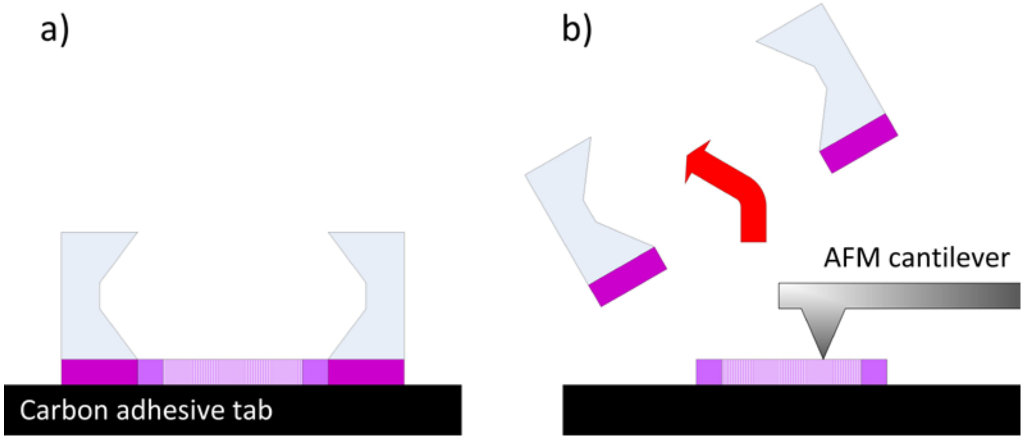

Figure 3.1 Schematic representations of **a)** the sticking and **b)** peeling procedures of the Si chip carrying a NSiM to allow the access of the AFM cantilever and tip to the backside of the nanoporous area.

Results and discussion

Using AFM for scanning a nanoporous surface generally gives precise information about the mean diameter of the nanopores since the tip convolution artefacts do not alter the measurement of a structured surface with a negative profile compared to a structured surface with a positive profile. The depth of the nanopores cannot be defined by scanning only the frontside of the NSiMs because the AFM tip is not shaped properly to enter small apertures in the sub-100 nm range. By applying the procedure described earlier, the AFM analysis of the frontside and the backside of the active area of the NSiM has been performed; resulting AFM micrographs are shown in figure 3.2. When analyzing the backside of the membrane, this latter stuck on the adhesive tab was not perfectly flat. Therefore the plane fit tool used in the image processing software could not be as effective as on flat surface and the overall quality of the image was slightly altered.

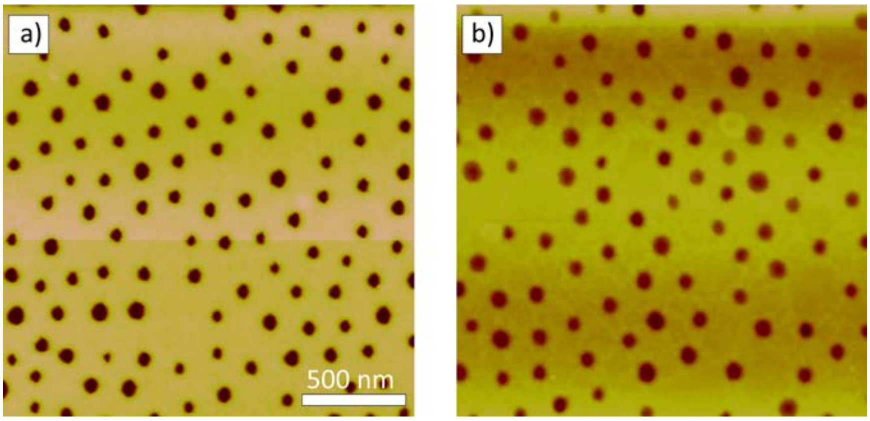

Figure 3.2 AFM micrographs of the **a)** frontside and **b)** backside of the suspended nanoporous area. (max Z scale is 20 nm).

Processing the data to obtain the mean density and size distribution of the diameter of the nanopores has demonstrated that the etching of the nanopores was performed through the entire 200 nm of low stress silicon nitride. The density of nanopores was calculated to be of 27 ±2 nanopores/μm^2 and of 24 ± 2 nanopores/μm^2 on the frontside and the backside, respectively. These values are in good agreement (within error bars) with the mean density of micelles used as starting template (28 ± 2 micelles / μm^2) and demonstrated the complete opening of the nanopores through the 200 nm thick suspended membrane. The mean diameter obtained from the size distribution analysis (figure 3.3) shows that the nanopores present vertical sidewalls since the mean diameter was calculated to be of 83 ± 15 nm and 85 ± 15 nm for the frontside and backside, respectively. These values are in good agreement with the mean diameter of 85 ± 15 nm of the micelles used as starting template.

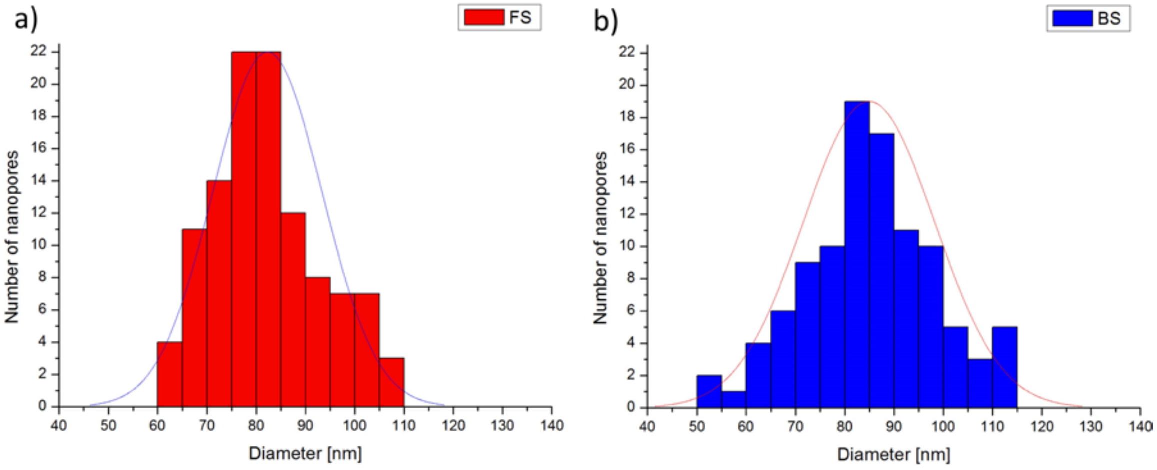

Figure 3.3 Size distribution of the mean diameter of the nanopores processed from **a)** 4 μm^2 frontside and **b)** 4 μm^2 backside AFM micrographs of the NSiM.

3.1.2 Using Scanning Transmission Electron Microscopy

Experimental

Procedure

The Si chip carrying a NSiM was placed onto a holey aluminium substrate holder. The substrate holder was then placed on top of the back scattered electron detector and introduced into the chamber of the *Philips XL30 ESEM* (Philips). The acceleration voltage was set to 10 kV. All the data acquired was processed using *imageJ* (National Institute of Health, USA) and *Origin* (OriginLab, USA).

Results and discussion

A standard SEM cross section analysis can be performed to obtain this information but this technique is destructive and it remains difficult to obtain a clear image of a 200 nm thick and non-conductive free standing film. This latter issue was encountered in a previous work performed by Popa et al. who imaged 100 nm thick free standing nanoporous silicon nitride membrane after performing a cross section by focused ion beam (FIB) [1]. A recent study has also demonstrated the characterization of nanoporous membranes using field emission scanning electron microscopy (FESEM) [2]. This method employs narrower probing beams resulting in both improved spatial resolution and minimized sample charging effect. Finally, the internal geometry of nanopores can also be identified with an optofluidic method [3] but this technique requires reference data to characterize a given sample.

The Scanning Transmission Electron Microscopy (STEM) mode works on the same principle as a standard Scanning Electron Microscope (SEM), where a focused beam of electrons is scanned over the sample to be analyzed while some signal is collected by a detector placed beneath the sample to form an image [4]. Transmission mode of imaging is possible because of the ultrathin specimen being scanned. Secondary or backscattered electrons can be used for imaging. In our case, a mobile back scattered electron detector is placed beneath the sample to collect transmitted electrons to control the full pore opening. Images obtained can be processed in a more reliable way to determine the mean diameter of the nanopores and if they are entirely opened.

Figure 3.4 shows the pictures taken in SEM mode detecting the secondary electrons and in STEM mode detecting the back scattered electrons with detector placed beneath the NSiM. Transmitted electrons showed the full opening of the nanopores and corroborated results previously obtained with AFM analysis. The information concerning the sidewall profile of the nanopores cannot be obtained with the STEM analysis.

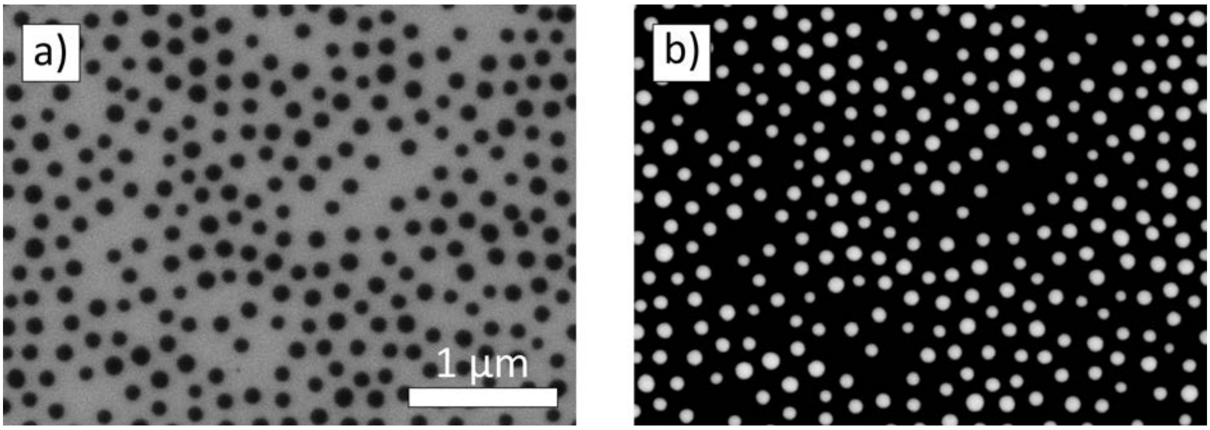

Figure 3.4 a) SEM and **b)** STEM pictures of the suspended nanoporous area.

The difference in resolution and image contrast between the SEM and STEM images acquired was observed while processing both images to a size distribution analysis in order to determine the mean diameter of the final NSiMs. Figure 3.5 shows that the mean diameter obtained from the SEM data analyzed is of 112 ± 15 nm while the mean diameter obtained from STEM data is of 93 ± 15 nm, a value closer from the one obtained with AFM analysis performed in section 3.1.1 and in good agreement with the mean micelle diameter (85 ± 15 nm) of the starting template (within error bars). The mean diameter calculated from the SEM picture (obtained with secondary electron) is larger compared to the mean diameter calculated from the STEM image (obtained with back scattered electrons) because of the global image contrast difference being lower, decreasing the precision of the image analysis. In addition, the mean nanopore density calculated from a 9 μm^2 STEM image was of 27 ± 2 nanopores/μm^2, which is in very good agreement with the mean micelle density (28 ± 2 micelles/μm^2) of the starting template.

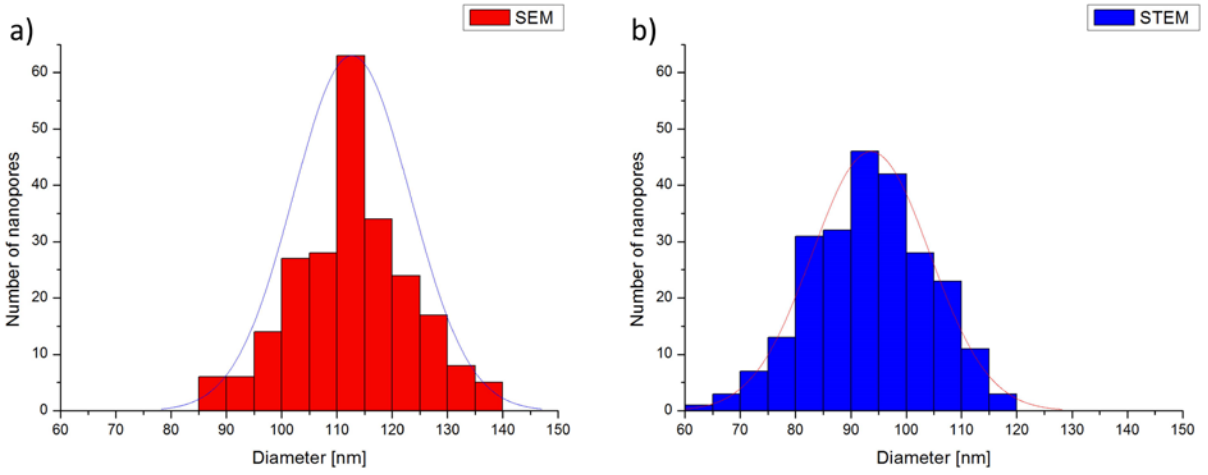

Figure 3.5 Size distribution of the mean diameter of the nanopores processed from **a)** 9 μm^2 SEM picture and **b)** 9 μm^2 STEM picture.

3.1.3 Using Transmission Electron Microscopy

Because Transmission Electron Microscopy (TEM) has a higher magnification power and greater resolution than Scanning Electron Microscopy (SEM), this technique will allow characterizing precisely both the mean pore diameter of the fabricated NSiMs but also the nanopores profile.

Experimental

The instrument used for this study is a *Philips CM200* (FEI Company, USA) with 200kV accelerating voltage, with a maximum achievable resolution of 0.14 nm with ultrathin samples. The images may be taken digitally using a Peltier-cooled Tietz (TVIPS) 2k x 2k CCD camera mounted below the viewing chamber, or on electron image film, using the built-in plate camera. The instrument has a Philips Compustage for precise control of specimen holder/specimen movement. Top view images of the nanoporous area were taken as well as images taken by tilting the sample 40° to the surface normal to obtain a transparent view of the nanopores. The sample preparation is quite delicate since the maximum size of the sample has to be a disk of 3 mm in diameter. The Si chip carrying a NSiM was cleaved manually to reach the adequate size to fit into the sample holder and precaution was taken for preventing any particles re-deposition during the cleavage operation. All the data acquired is processed using *imageJ* (National Institute of Health, USA) and *Origin* (OriginLab, USA).

Results and discussion

In a Transmission Electron Microscope (TEM), a highly focused electron beam is accelerated towards the specimen to be analyzed. The electrons transmitted through the ultra-thin specimen form an image due to their interaction with the material of the specimen. TEM is widely used in the industrial world to characterize commercially available nanoporous membranes [5]. The images obtained with the TEM analysis (figure 3.6 a)) confirmed the full opening of the nanopores through the entire 200 nm thick low stress silicon nitride layer. The high resolution of the TEM analysis allowed the visualization of the sharp edges of the nanopores. A mean nanopore density of 25 ± 2 nanopores/μm^2 was calculated from a large 9 μm^2 TEM picture, which is in good agreement within error bars with the mean micelle density of the starting template (28 ± 2 micelles/μm^2) and previously described STEM analysis (27 ± 2 micelles / μm^2). The images obtained while tilting the sample by an angle of 40° to the surface normal (figure 3.6 b)) demonstrated the vertical sidewall profile of the nanopores since the high energy electrons were transmitted through the ultrathin specimen allowing to visualize a transparent image of the nanoporous low stress silicon nitride layer. Figure 3.6 c) shows a typical example of TEM analysis performed on a NSiM containing nanopores that were not completely opened (non-optimized etching process). This image was taken voluntarily where a large opened defect could be observed to compare the difference in image contrast between opened and non-opened parts.

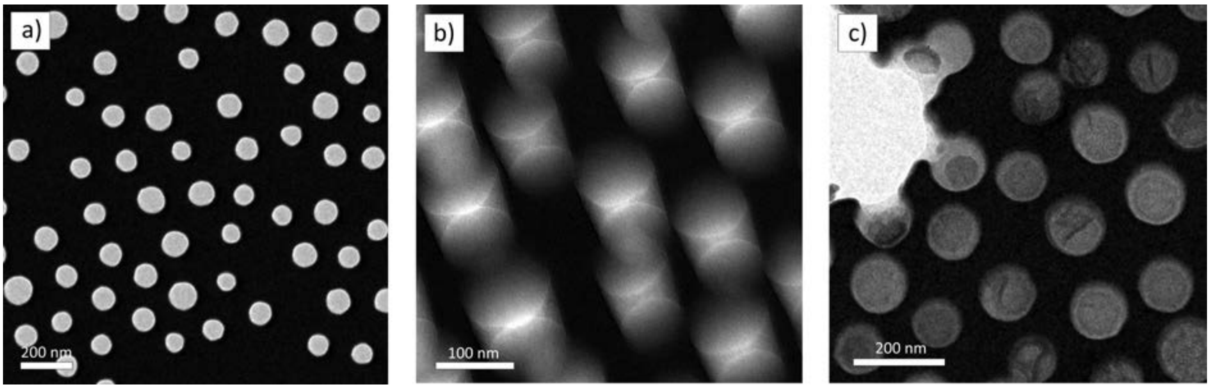

Figure 3.6 TEM **a)** top view and **b)** tilted view of the suspended nanoporous area demonstrating the vertical sidewall profile of the nanopores and **c)** example of TEM analysis performed on a NSiM with nanopores not completely opened.

The size distribution analysis of the mean diameter of the nanopores shown in figure 3.7 is probably the most precise analysis and the closest to the reality due to the high resolution and high contrast TEM images obtained facilitating the image processing. A mean diameter of the nanopores of 92 ± 15 nm was calculated from a 9 μm^2 TEM picture, in good agreement with the mean micelle diameter of the starting template (85 ± 15 nm).

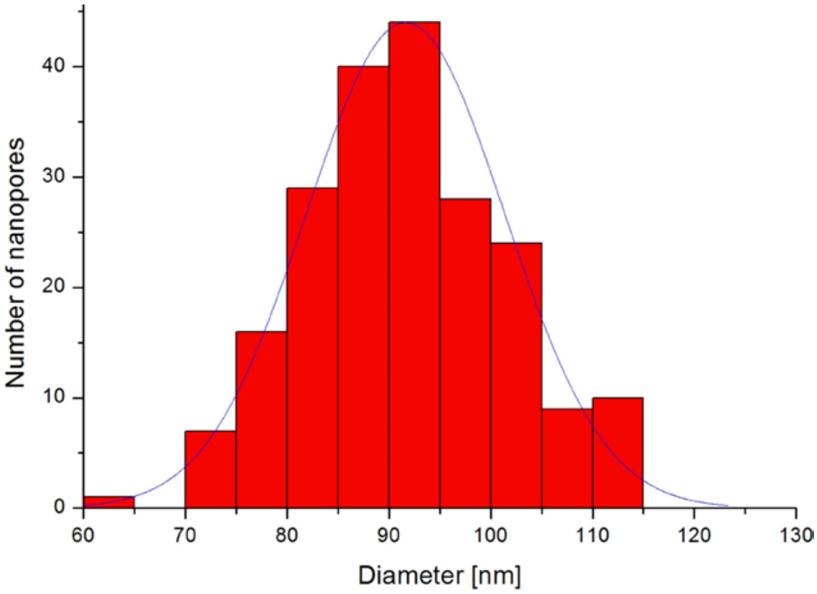

Figure 3.7 Size distribution of the mean diameter of the nanopores processed from 9 μm^2 TEM picture.

3.1.4 Preliminary conclusions

In section 3.1, three different techniques were used to characterize the final suspended nanoporous membrane, each having advantages and disadvantages summarized in table 3.1.

First AFM analysis has allowed us to evaluate in a systematic manner the density of nanopores on both the frontside and the backside of the membranes and demonstrated that those values are in very good agreement with the one found in chapter 2 regarding the starting block copolymer micelle template. By detecting the back scattered electrons in STEM analysis has showed the full opening of the nanopores through the entire 200 nm thick low stress silicon nitride layer and confirmed the pore diameter measured by AFM. Finally the vertical sidewall profile of the nanopores could be deduced from the AFM analysis and observed in detail with TEM.

Table 3.1 Summary of the strengths and weaknesses of each characterization used for the porosity control.

Porosity control technique	**Complexity of sample preparation**	**Destructive**	**Resolution**	**Information on sidewall profile**	**Time consuming**
AFM	+ + +	YES	+ +	YES	+ +
STEM	+	NO	+ +	NO	+
TEM	+ + +	YES	+ + +	YES	+ + +

+ : low   + + : medium   + + + : high

3.2. Characterization of mechanical properties with the bulge test method

The bulge technique has been widely used for the determination of in-plane mechanical properties such as the Young's modulus, the residual stress or the Poisson's ratio, of free standing membranes. The principle of the bulge test is to apply a variable uniform pressure on one side of the free standing film and measure the resulting deflection. This method was first introduced by Beams in 1959 [6], who tested thin films of gold and silver. This technique has been widely used for evaluating the mechanical properties of polymeric [7] and metallic [8] thin free standing films.

More recently, extensive investigations have been carried out on silicon nitride membranes to characterize how their mechanical properties were depending on the deposition technique and deposition parameters used [9–15]. Mechanical properties of composite membranes made of stacked layers of different materials have also been studied using the bulge technique [16,17]. The bulge technique usually allows the evaluation of the mechanical properties of free standing tensile stressed layers. However, using composite membranes made of both a tensile stressed dominant SiN layer and a compressive stressed layer, the bulge technique allows also the characterization of the mechanical properties of the compressive stressed layers [18–20]. The mechanical strength of suspended membranes has been demonstrated to be strongly dependent on the geometrical design such as the shape (round, square or rectangular) and the thickness [21–23]. Recently, efforts have been made to consolidate findings regarding the bulge test equations and propose rigorous experimental procedures to increase the reliability and accuracy of the bulge technique [24–27]. Orther et al. recently developed a high speed bulge test at waferscale [28] making this technique an interesting large scale characterization tool applicable to the industrial world.

Young's modulus and residual stress of thin films deposited on a bulk substrate can also be characterized respectively using the nano indentation and the substrate bending techniques, respectively. These techniques will be used in the following work to corroborate values found performing the bulge test on suspended membranes. The nano indentation tester uses an already established method where an indenter tip with a known geometry is driven into a specific site of the material to be tested, by applying an increasing normal load. When reaching a pre-set maximum value, the normal load is reduced until partial or complete relaxation occurs. This procedure is performed repetitively; at each stage of the experiment the position of the indenter relative to the sample surface is precisely monitored with a differential capacitive sensor. The substrate bending technique consists in measuring the curvature radius of a substrate pre- and post- deposition of the thin film to be characterized and hence extract the residual stress of the thin film. Other techniques can be used to measure the stress in thin films such as Raman spectroscopy [29], Fourier transform infrared spectroscopy [30] and X-rays [31] but these technique require simplified assumptions about the film (e.g. microstructure, defect density) and might require a long sampling time during the analysis.

3.2.1 Experimental

Materials

Nanoporous low stress silicon nitride membranes

NSiMs fabricated and characterized as mentioned in the earlier section have been used. Focus was made on NSiMs with a side length of the active area of 1mm and 2mm. The membranes were 200 nm thick but 100 nm thick NSiMs were also produced to evidence the impact of the membrane thickness on their resulting mechanical stability.

Non porous low stress and super low stress silicon nitride membranes

Non porous low stress silicon nitride membranes were fabricated following the fabrication process as described in chapter 2 without considering the nanostructuring steps performed on the front side of the membranes. Membranes with a side length of 1 mm and 2 mm with a thickness of 100 nm and 200 nm were fabricated to characterize the mechanical properties of the non-porous low stress thin film. Super low stress suspended silicon nitride membrane with the same geometrical values exhibiting buckling effect were produced and efforts were conducted to understand when the buckling phenomenon appears and how to avoid it.

Procedure

Bulge test

Using this method, pressure with N_2 gas is applied to a thin film that has been clamped over a circular or square opening. Stable and continuous pressure is applied into the opening via a *Alicat Scientific* pressure control system (Alicat, USA) and pressure is monitored via a pressure sensor. The bulged surfaced topography of the specimen is observed directly using a *Wyko Interferometer NT_1100* interference microscope (Veeco, USA). It is also useful to characterize the initial shape of the suspended membrane that should be perfectly flat before data acquisition. The pressure is generally increased step by step until bursting of the membrane, several load-unload pressure cycles can be performed to demonstrate the elastic deformation of the thin film being analyzed. The load-deflection behavior of the film allows the extraction of the biaxial modulus and in-plane residual stresses using bulge equations. A schematic representation of the set-up used is represented in figure 3.8.

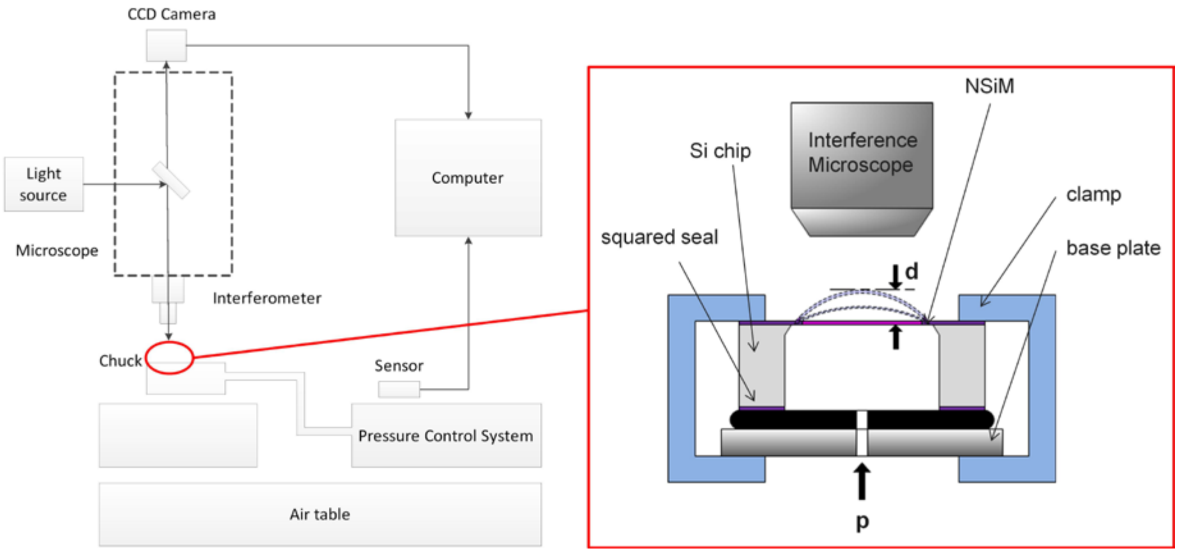

Figure 3.8 Schematic representation of the bulge test set up integrating a NSiM

Nano indentation

Several tests have been performed on the layers of interest deposited onto silicon wafer using the *CSM Ultra Nano Indentation Tester UNHT* (CSM instruments, Switzerland). Hardness and Young's modulus were determined using the Instrumented Indentation Technique (IIT). For each loading/unloading cycle, the applied load value is plotted with respect to the corresponding position of the indenter. The resulting load/displacement curves provide data specific to the mechanical nature of the material under examination. Established models are used to calculate Young's elastic modulus values. Specifications about the head used are summarized in Table 3.2.

Table 3.2. Specifications of the nano indentation head

Load application measurement: Piezo actuator / capacitive sensor	
Load range	0 – 50 mN (optional 100 mN) - fine range: 10 mN - standard range: 50 mN
Load resolution	1 nN, noise floor ≈ 0.1 µN
Minimum usable load	25 µN
Maximum load	50 mN (optional 100 mN)
Minimum contact force	0.1 µN (= noise floor)
Contact force hold time	unlimited
Displacement measurement: differential capacitive sensor	
Displacement resolution	0.0004 nm, noise floor ≈ 0.03 nm
Thermal drift	≈ 0.5 nm / min
Maximum indentation depth	- fine range: 10 µm - standard range: 100 µm
Maximum indenter travel range	100 µm
Typical measurement time	
Less than 5 minutes including first measurement on a new sample	
No thermal stabilization is required after loading of a new sample	
Indentation performances	
Loading rate	From 0 to 1000 mN / min
Usable load	From 0.025 to 100 mN

Measurement of residual stress from the substrate bending

The stress in the thin films deposited onto Si wafers is measured using a *FLX-2320S* (Toho Technology, Japan). The FLX-2320S determines stress by measuring the curvature change of pre- and post-deposition of the film. This difference in curvature is used to calculate stress by way of Stoney's equation (Eq 3.1) [32], which relates the biaxial modulus of the substrate $E_s/(1-\nu_s)$, thickness of the film t_f and substrate t_s, and the radius of curvatures of pre- and post-process, R_{pre} and R_{post}, respectively. Curvature is measured by directing a laser at a surface with a known spatial angle. The reflected beam strikes a position sensitive photodiode. The geometry of the film is recorded by scanning the surface. Figure 3.9 shows the schematic representation of the principle of curvature measurement.

$$\sigma_f = \frac{1}{6}\left(\frac{1}{R_{post}} - \frac{1}{R_{pre}}\right)\frac{E_s}{(1-\nu_s)}\frac{t_s^2}{t_f} \qquad (3.1)$$

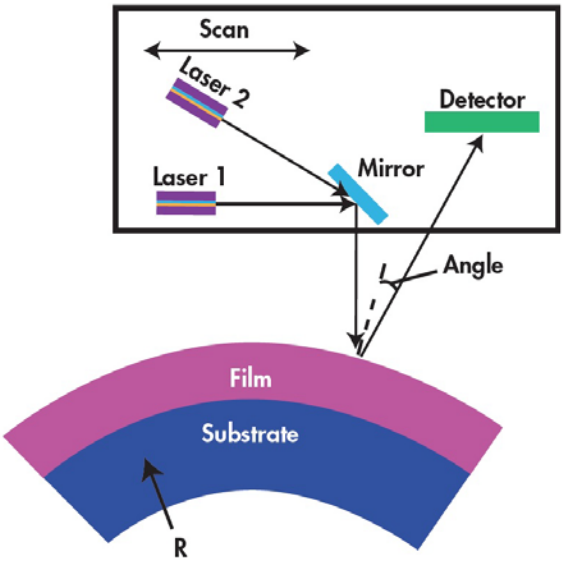

Figure 3.9 Schematic representation of the principle of curvature measurement.

3.2.2 Results and Discussion

Extracting the mechanical properties of non-porous and porous suspended thin film

The bulge test was first performed on non-porous low stress silicon nitride membranes with a side length of 1270 µm and fitted with Eq. 3.2 in order to determine the mechanical properties of the non-porous suspended film [6].

$$P = C_1 t \frac{h}{a^2} \sigma + C_2 t \frac{h^3}{a^4(1-\nu)} E \qquad (3.2)$$

P is the differential pressure applied during the bulge test, C_1 and C_2 are constants discussed in the literature with variable values for thin square films, here the constants values used are 3.04 and $1.473(1-0.272\nu)$, respectively [7], and the Poisson's ratio ν for a low stress silicon nitride suspended thin film was chosen to be of 0.23 [12]. t represents the thickness of the suspended thin film, a is half the side length of the square thin film and h is the deflection of the membrane at a given pressure. σ and E are the residual stress and the Young's modulus of the suspended square thin film, respectively, to be extracted when fitting the experimental data obtained with the bulge equation. Figure 3.10 shows the load-deflection curves until burst pressure obtained with the bulge test on 1270 x 1270 µm^2 non porous LS-SiN membranes exhibiting a burst pressure of 960 mbar ($= 9.6 \times 10^4$ Pa); and 1270 x 1270 µm^2 LS-SiN membranes with a porous area of 1000 x 1000 µm^2 (non-porous frame of 135 µm wide) exhibiting a burst pressure of 575 mbar ($= 5.75 \times 10^4$ Pa).

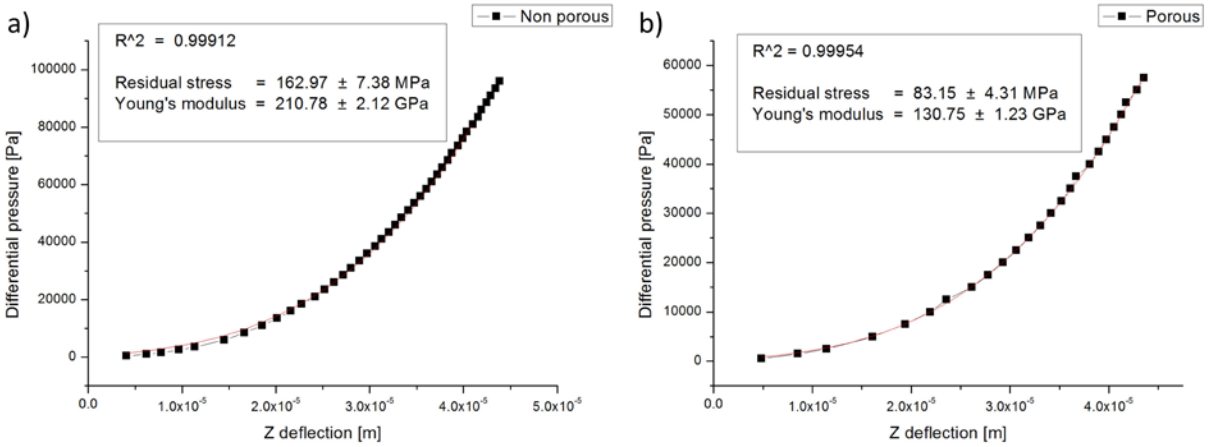

Figure 3.10 Load-deflection curves fitted with the bulge equation to determine the Young's modulus and residual stress of **a)** Non porous 1270 x 1270 μm^2 suspended LS-SiN layer and **b)** 1270 x 1270 μm^2 suspended LS-SiN layer with 1000 x 1000 μm^2 of porous area.

The values of the Young's modulus and the residual stress obtained from the fitting of the bulge data with the bulge equation (Eq. 3.2) for the non-porous suspended LS-SiN layer are in good agreement with the values found by performing the nano indentation and the substrate bending techniques (Stoney's equation) giving the values of the Young's modulus and residual stress, respectively. The nano indentation performed on the LS-SiN layer gave a Young's modulus of $E = 219 \pm 2.7$ GPa, while the value extracted from the bulge test was of $E = 210.78 \pm 2.2$ GPa. The pre- and post-deposition wafer bending analysis gave back a residual stress of $\sigma = 155.70$ MPa while the value extracted from the bulge test was of $\sigma = 162.97 \pm 7.38$ MPa. Therefore the bulge test itself and the bulge equation used for the characterization of the mechanical properties of non-porous suspended layer appeared to be enough accurate and can be trusted for extraction of the mechanical properties of other membranes (with different geometrical properties or made of a different material).

When applying the same bulge test characterization and data processing to 1 mm^2 suspended nanoporous membrane surrounded by a 135 μm wide non-porous suspended frame, values of the Young's modulus and the residual stress of the overall structure are 130.75 ± 1.23 GPa and 83.15 ± 4.31 MPa, respectively. These values are not representative of the mechanical properties of the porous area only and therefore could not be confirmed using nano indentation or substrate bending techniques. Indeed the particular design of our NSiMs is integrating both a suspended central porous area and a surrounding non-porous frame. In other groups studies have been made to evaluate the impact of the porosity on the mechanical properties of thin films using nano indentation [33–35] and substrate bending [36,37] techniques. First, Kovacs et al. studied the influence of a non-porous frame surrounding the porous area by FEM analysis and demonstrated that the larger is the frame, the higher is the mechanical stability of the membrane [38]. In a more quantitative study, Van Rijn et al. proposed a linear relationship to calculate the mechanical properties of porous suspended thin films using the mechanical properties of closed membranes and the perforation rate P of the porous thin film (the perforation rate being the ratio of the perforated area over the total area) [39]. This linear relationship is described as follows: $E_{eff} = E(1-P)$ and $\sigma_{eff} = \sigma(1-P)$ where E and σ refer to the Young's modulus and the residual stress of the non-perforated material, respectively. Unfortunately this model does not take into account the influence of a non-porous suspended frame surrounding the nanoporous area; therefore in our case the obtained values could not be properly fitted with this linear relationship depending only on the perforation rate. Because of the targeted application involving the integration of NSiMs into pressure driven filtration devices we decided from this point to consider the maximum burst pressure as the key parameter to be quantified precisely for each membrane design.

Influence of the side length and thickness of the NSiM on mechanical strength

Two controllable design parameters can improve the mechanical strength of the NSiMs. These two parameters are the membrane thickness and the side length. These parameters can be chosen prior the fabrication of the NSiMs. To demonstrate the improvement of the mechanical strength by increasing the thickness and reducing the membrane side length, NSiMs with a thickness of 100 nm and 200 nm and a square nanoporous area of 1 x 1 mm^2 and 2 x 2 mm^2 (with a 135 µm wide non porous frame) each have been fabricated and submitted to the bulge test. Figure 3.11 shows the load-deflection curve until burst pressure of NSiMs with different thicknesses and different side lengths. The bulge test was processed several times on identical NSiMs in order to obtain a standard deviation error due to experimental procedure. The burst pressure of 1 x 1 mm^2 and 100 nm thick NSiMs was found to be of 370 ± 90 mbar (= 3.7×10^4 Pa) while it was measured to be of 671 ± 125 mbar (= 6.71×10^4 Pa) for a 1 x 1 mm^2 and

200 nm thick NSiMs. The burst pressure of 2 x 2 mm^2 NSiMs with thicknesses of 100 nm and 200 nm was found to be of 225 ± 60 mbar ($= 2.25 \times 10^4$ Pa) and 350 ± 110 mbar ($= 3.5 \times 10^4$ Pa), respectively. Therefore, increasing the membrane thickness and reducing the side length of the square nanoporous suspended structure increases the mechanical strength of the NSiMs.

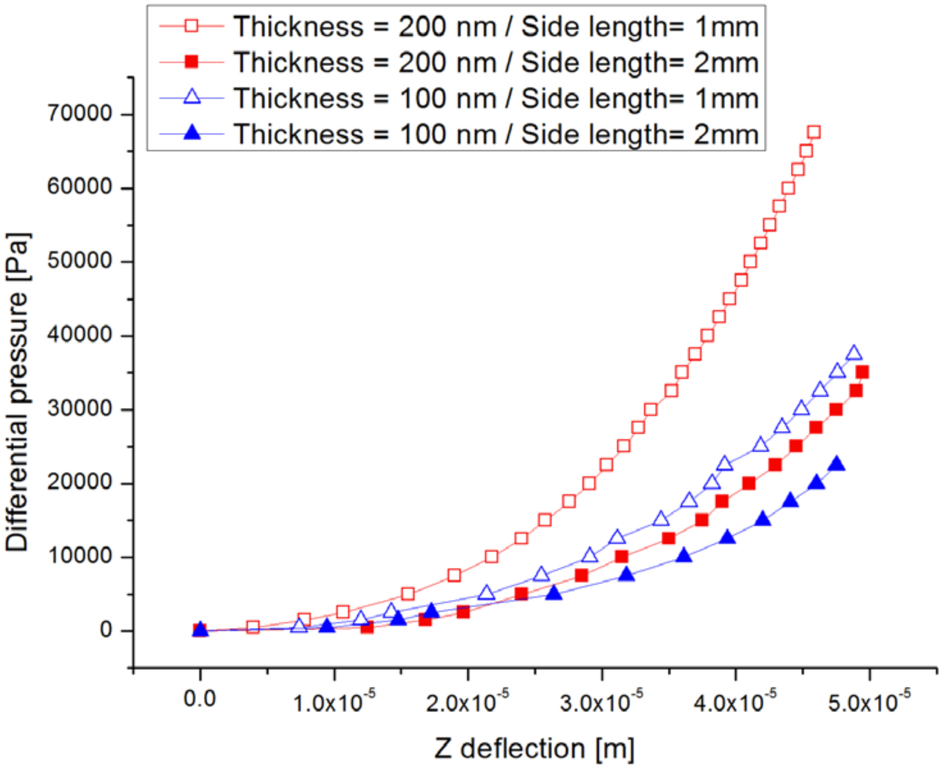

Figure 3.11 Load-deflection curves of NSiMs with different side lengths and thicknesses (all the NSiMs are surrounded with a 135 µm wide non porous frame).

3.3. Buckling in suspended membranes

Buckling issues generally arise in thin suspended structures from the residual stress of the thin film being compressive or not high enough when it is tensile. The buckling of suspended structures is mostly considered as a failure phenomenon in the fabrication process of membranes used in optics or filtration, but studies have also taken advantage of this phenomenon to voluntarily produce buckled membranes used as thermo-actuated microvalves, micropumps or switches [40–45]. Most of the time buckling is an undesired effect that can be avoided with a specific device design or fabrication process [46–48]. Few studies were made to understand and characterize the mechanical and thermal buckling configurations [49–51] and to evaluate directly the mechanical properties of buckled membranes [52,53]. The tensile stress in the suspended structure should be sufficient to prevent buckling [16]. Tensile-stressor overlayers can be considered in order to suppress the buckling of compressive stressed layers and evaluate the mechanical properties of the overall composite suspended structure with the bulge test [18–20].

In this work, buckling was mostly observed when fabricating 200 nm thick non-porous silicon nitride membranes using super low stress silicon nitride (SLS-SiN) with a value of the tensile stress $\sigma < 100$ MPa given by the provider (SiMat, Germany). Figure 3.12 shows images of the buckling observed with an interference microscope on non-porous SLS-SiN suspended membranes with a side length of 1270 µm. An unbuckling procedure using tensile stressor overlayers of Al_2O_3 deposited by atomic layer deposition has been developed and will be discussed further.

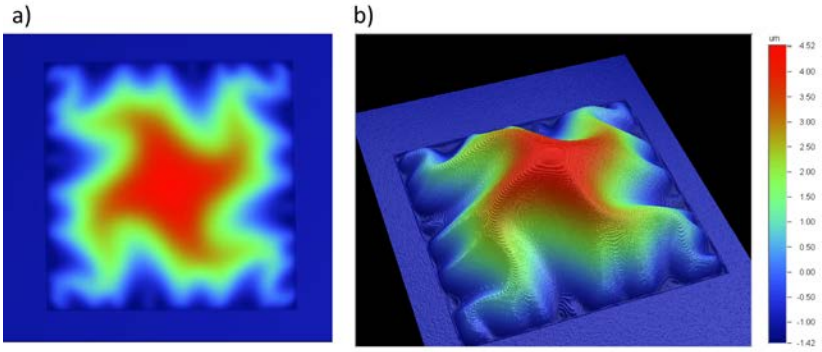

Figure 3.12 a) Top view and **b)** 3D reconstruction images taken with an interference microscope of the buckling observed on a 200 nm thick SLS-SiN non porous suspended membrane with a side length of 1270 µm.

3.3.1 Experimental

Atomic Layer Deposition (ALD) of Al_2O_3

Deposition of Al_2O_3 onto nanoporous and non-porous suspended membranes was performed with ALD tool *Beneq TFS 200* (Beneq, Finland). ALD allows deposition of highly conformal and ultrathin (< 1 nm up to few hundreds of nm) dielectric or metallic layers. The deposition is performed at 200°C and under vacuum (5 mbar). The deposition process layer by layer of Al_2O_3 is achieved by the successive introduction of two chemical precursors (H_2O and TMA) in the reactor. N_2 purge steps are performed after introduction of each precursor to remove the excess of chemical introduced and leave only a monolayer. A full cycle allowing the deposition of a single monolayer of Al_2O_3 ($\approx$ 1.1 Å) takes approximately 3 seconds and involves the following steps:

1 - TMA precursor is pulsed in the reactor chamber and reacts with surface by chemisorption with hydroxyl groups from the native oxide surface of the sample ($Al(CH_3)_3$ (g) + Si-O-H (s) -> Si-O-$Al(CH_3)_2$ (s) + CH_4). The product of the reaction is CH_4.

2 - Purge of the reactor chamber with N_2 for removal of the excess of TMA and methane reaction product.

3 - H_2O precursor is pulsed into the chamber and reacts with the surface (2 H_2O (g) + Si-O-$Al(CH_3)_2$ (s) -> Si-O-$Al(OH)_2$ (s) + 2 CH_4).

4 - Final purge of the reactor with N_2 for the removal of methane reaction product.

3.3.2 Results and Discussion

An unbuckling procedure has been developed by creating a non-porous composite suspended membrane made of 200 nm of SLS-SiN and 20 nm of Al_2O_3 deposited in a conformal way by Atomic Layer Deposition (ALD), making the final suspended structure 240 nm thick. Depositing Al_2O_3 on the membrane increases the overall tensile stress of the structure, making the membrane flat again as it can be seen in Figure 3.13.

The Young's modulus of the ALD Al_2O_3 layer was characterized by nano indentation and the residual stress by the substrate bending technique; those values were found to be of $E_{Al_2O_3} = 238.1 \pm 12.9$ GPa and $\sigma_{Al_2O_3} = 326.8$ MPa, respectively, in good agreement with the values that can be found in the literature [54–57].

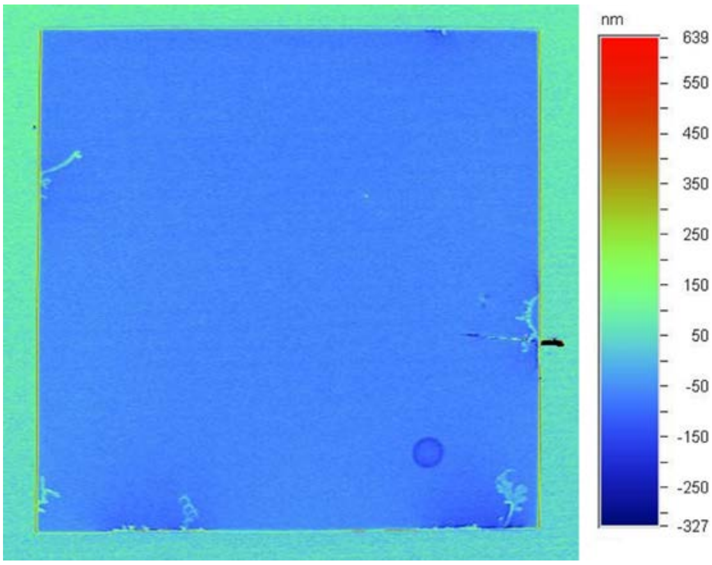

Figure 3.13 Image taken with an interference microscope of the composite membrane flattened after the conformal deposition of 20 nm of Al_2O_3 by ALD.

Eq 3.3 describes a simple rule of mixtures that can be used to calculate the mechanical properties of the composite structure in which M_i is either the residual stress or the Young's modulus of the composite, and t_i/t_{total} the volume fraction of the component i.

$$M_{composite} = \frac{t_{SLS-SiN}}{t_{total}} M_{SLS-SiN} + \frac{t_{Al_2O_3}}{t_{total}} M_{Al_2O_3} \qquad (3.3)$$

Since the bulge test has been demonstrated previously to be a reliable technique to determine the mechanical properties of non-porous suspended thin films, the flat composite non-porous membrane with a side length of 1270 μm made of 200 nm of SLS-SiN and 40 nm of Al_2O_3 was submitted to the bulge test and a value of $\sigma = 121.39 \pm 2.39$ MPa was found for the residual stress of the composite suspended structure. In addition, the elastic behaviour of the suspended structure was confirmed by performing a load-unload cycle on the same sample. The membrane returned to its initial state without residual deformation after a load-unload cycle. Figure 3.14 shows the results of the bulge test performed on the composite membrane with a first load until a differential pressure of 525 mbar ($= 5.25 \times 10^4$ Pa), and a second load cycle until burst pressure at 925 mbar ($= 9.25 \times 10^4$ Pa). The curves superpose without hysteresis demonstrating the elastic deformation of the suspended membrane.

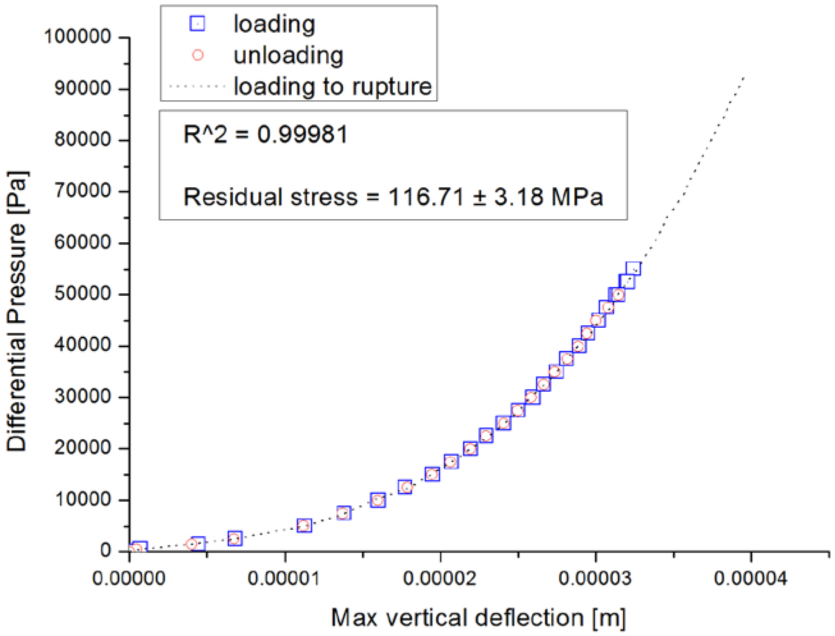

Figure 3.14 Load-deflection curve until bursting of the 1.27 x 1.27 mm^2 composite membrane made of 200 nm of SLS-SiN and 40 nm of Al_2O_3 with a first load cycle until 525 mbar ($= 5.25 \times 10^4$ Pa).

Knowing the residual stress of both the Al_2O_3 and global composite layers, the rule of mixtures (Eq. 3.3) can be applied to calculate the residual stress of the SLS-SiN layer and was found to be of $\sigma_{SLS-SiN} = 74.69$ MPa (which is in good agreement with the approximate value given by the provider). From this starting value, the critical residual stress σ_{cr} necessary to unbuckle and keep flat the 200 nm thick SLS-SiN suspended membrane can be found by depositing an Al_2O_3 layer nanometer by nanometer, measuring the vertical deflection of the unpressurized structure with an interference microscope and applying the mixtures rule until complete flatness is reached. Figure 3.15 shows the vertical deflection of the composite membrane measured with an interference microscope depending on the thickness of Al_2O_3 deposited in a conformal way by ALD on the starting buckled non porous 200 nm thick SLS-SiN suspended membrane with a side length of 1270 µm.

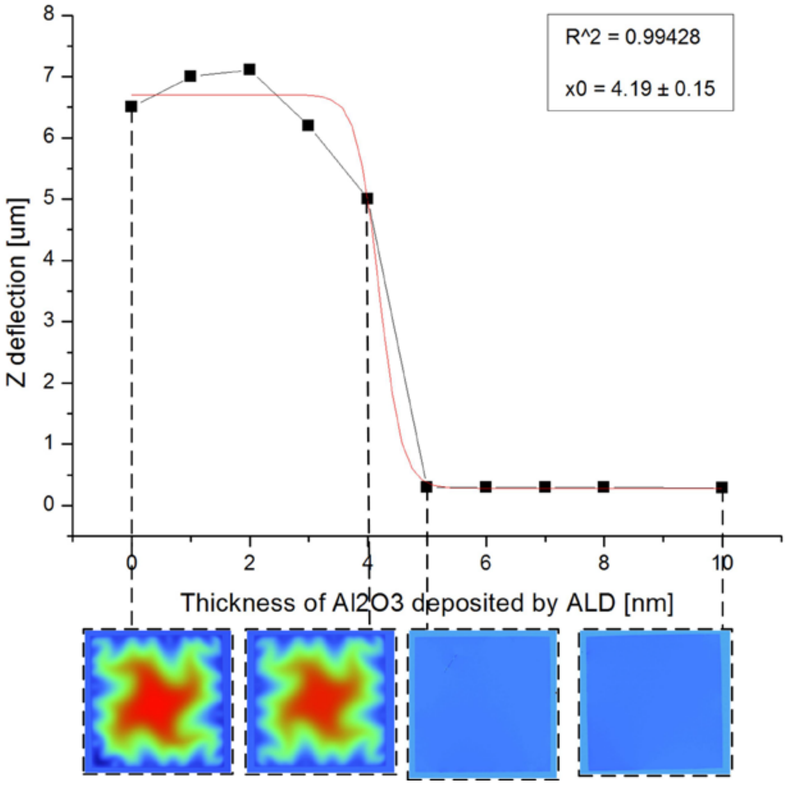

Figure 3.15 Plot of the max deflection of the unpressurized composite SLS-SiN / Al_2O_3 membrane depending on the thickness of Al_2O_3 deposited by ALD in a conformal way on the starting buckled 200 nm thick SLS-SiN suspended membrane with a side length of 1270 µm. (Plot fitted with a sigmoidal Boltzmann model)

The full unbuckling of the membrane was achieved when depositing 5 nm of Al_2O_3 on both sides of the membrane. Using the mixture rule, the minimum critical tensile residual stress needed in a 200 nm thick and 1.27 x 1.27 mm^2 non porous membrane was calculated to be of $\sigma_{cr} = 86.69$ MPa. Increasing the tensile stress of the initial buckled 200 nm thick SLS-SiN non porous suspended membrane by 12 MPa was enough to reach complete flatness.

The unbuckling procedure by deposition of Al_2O_3 could then be successfully applied to buckled NSiMs (porous) fabricated with SLS-SiN. Figure 3.16 shows the vertical deflection of the composite membrane measured with an interference microscope depending on the thickness of Al_2O_3 deposited in a conformal way by ALD on the starting buckled 200 nm thick SLS-SiN suspended membrane with a 1 mm^2 porous area surrounded by a 135 µm wide non porous suspended frame. In that case, full unbuckling of the nanoporous membrane was achieved when depositing 6 nm of Al_2O_3 on both sides of the membrane. The critical stress necessary to flatten the membrane could not be calculated since the rule of mixture cannot be applied to our system made of a suspended porous layer surrounded by a non-porous frame. Simultaneously, this unbuckling procedure will induce a pore size reduction and a change in the material chemistry. This part will be discussed in the next chapter concerning the membrane functionalization.

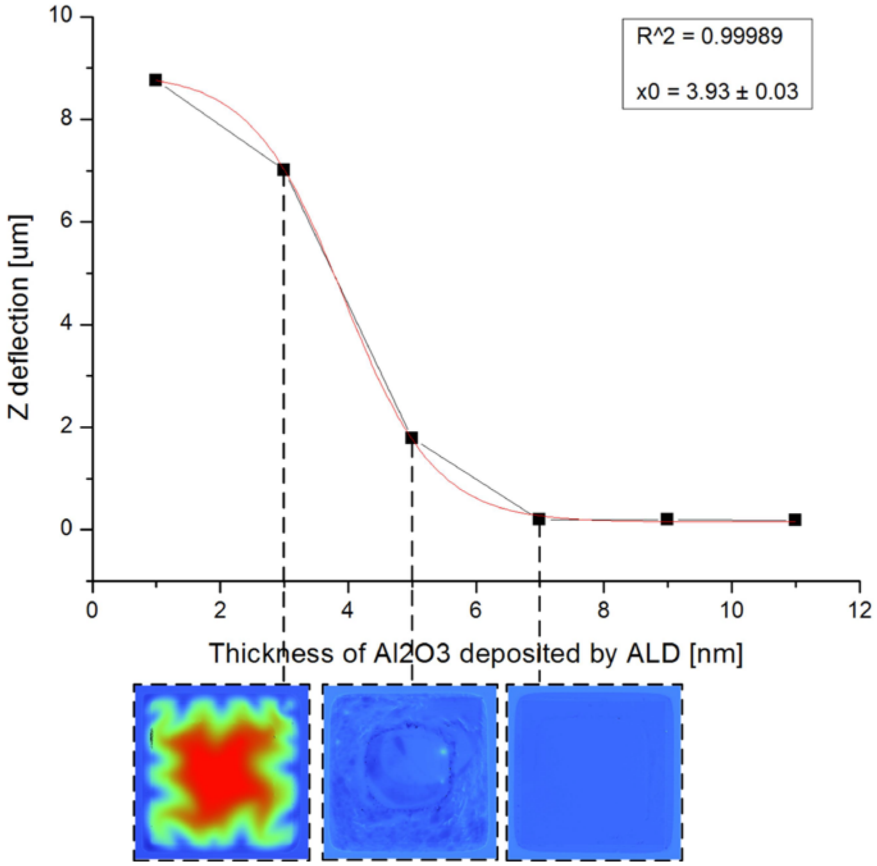

Figure 3.16 Plot of the max deflection of the unpressurized composite SLS-SiN / Al_2O_3 nanoporous membrane depending on the thickness of Al_2O_3 deposited by ALD in a conformal way on the starting buckled 200 nm thick SLS-SiN suspended membrane with a 1 mm^2 porous area surrounded by a 135 µm wide non porous suspended frame. (Plot fitted with a sigmoidal Boltzmann model)

3.4. Conclusions

In this chapter was discussed the full characterization of previously fabricated 200 nm thick NSiMs in terms of pore opening, pore morphology and mechanical properties.

AFM, STEM and TEM analysis were conducted onto NSiMs to successfully characterize the morphology and complete opening of the nanopores. Performing an AFM analysis on the front side and the back side of the suspended nanoporous layer allowed determining the mean pore diameter, the pore density and the complete opening of the nanopores by correlating the measures performed on both sides of the membranes. The STEM analysis has allowed us to confirm the full opening of the nanopores but no information could be obtained on the nanopore morphology. The TEM analysis performed allowed determining both the full opening of the nanopores and the nanopore profile with a higher resolution compared to AFM and STEM analysis. In summary our NSiMs present a mean nanopore density per surface area of 25 ± 2 nanopores/μm^2 and a mean nanopore diameter of 92 ± 15 nm. These values are in good agreement with the ones of the original micellar nanopattern exhibiting a mean micelle density per surface area and mean nanopore diameter of 28 ± 2 nanopores/μm^2 and 85 ± 15 nm, respectively. The reliability and reproducibility of the fabrication process was thus confirmed and final specifications of the NSiMs were determined.

The mechanical properties of porous and non-porous suspended membranes such as the Young's modulus and the residual stress were obtained using the bulge technique. For non-porous suspended membranes, values obtained were confirmed by nano-indentation and substrate bending technique, demonstrating the accuracy and reliability of the bulge test. The maximum pressure the membranes can withstand was also measured, and the increase of the mechanical strength of the suspended nanoporous layer has been demonstrated by reducing the square membrane side length and increasing the membrane thickness. Typically for a 200 nm thick non-porous square membrane with a side length of 1270 µm and the corresponding 1 mm^2 porous membrane surrounded by a 135 µm wide non-porous suspended frame, maximum burst pressures of 960 mbar ($= 9.6 \times 10^4$ Pa) and 671 ± 125 mbar ($= 6.71 \times 10^4$ Pa) were found, respectively.

Buckling of ultrathin suspended square membrane has been observed when fabricating nanoporous and non-porous super low stress silicon nitride membrane. Flattening of both membranes types was achieved by depositing by ALD a tensile-stressor overlayer of Al_2O_3 to reach an overall tensile stress of the composite structure superior to the minimum critical tensile stress necessary to avoid buckling in the suspended structure. For both 200 nm thick non-porous super low stress silicon nitride membranes with a side length of 1270 µm and the corresponding 1 mm^2 porous membrane surrounded by a 135 µm wide non-porous suspended frame, complete flatness was reached after depositing 5 nm and 6 nm of Al_2O_3, respectively.

References

[1] A.M. Popa, Stimuli-responsive nanostructured surfaces, Ecole Polytechnique Fédérale de Lausanne, 2009.

[2] C. a. León-Patiño, E. a. Aguilar-Reyes, C. Ruiz-Aguilar, Fabrication and Characterization of Highly Ordered Porous Alumina Templates by a Two-Step Anodization Process, Materials Science Forum. 755 (2013) 75–81.

[3] R. Urteaga, L.N. Acquaroli, R.R. Koropecki, A. Santos, M. Alba, J. Pallarès, et al., Optofluidic characterization of nanoporous membranes, Langmuir : the ACS Journal of Surfaces and Colloids. 29 (2013) 2784–9.

[4] O.T. Guenat, S. Generelli, M. Dadras, L. Berdondini, N.F. De Rooij, M. Koudelka-Hep, Generic technological platform for microfabricating silicon nitride micro- and nanopipette arrays, Journal of Micromechanics and Microengineering. 15 (2005) 2372–2378.

[5] J.L. Snyder, a Clark, D.Z. Fang, T.R. Gaborski, C.C. Striemer, P.M. Fauchet, et al., An experimental and theoretical analysis of molecular separations by diffusion through ultrathin nanoporous membranes., Journal of Membrane Science. 369 (2011) 119–129.

[6] J.W. Beams, Mechanical properties of thin films of gold and silver, in: International Conference on Structure and Properties of Polymer Films, Bolton Landing, NY, 1959: pp. 183–192.

[7] M.G. Allen, M. Mehregany, R.T. Howe, S.D. Senturia, Microfabricated structures for the in situ measurement of residual stress, Young's modulus, and ultimate strain of thin films, Applied Physics Letters. 51 (1987) 241–243.

[8] B.B. Jung, S.H. Ko, H.K. Lee, H.C. Park, Measurement of Young's Modulus and Poisson's Ratio of Thin Film by Combination of Bulge Test and Nano-Indentation, Advanced Materials Research. 33-37 (2008) 969–974.

[9] E.I. Bromley, J.N. Randall, D.C. Flanders, R.W. Mountain, A technique for the determination of stress in thin films, Journal of Vacuum Science & Technology B: Microelectronics and Nanometer Structures. 1 (1983) 1364–1366.

[10] G.F. Cardinale, R.W. Tustison, Fracture strength and biaxial modulus measurement of plasma silicon nitride films, Thin Solid Films. 207 (1992) 126–130.

[11] J.G.E. Gardeniers, H.A.C. Tilmans, C.C.G. Visser, LPCVD silicon-rich silicon nitride films for applications in micromechanics , studied with statistical experimental design, Journal of Vacuum Science & Technology A. 14 (1996) 2879–2892.

[12] B.A. Walmsley, Y. Liu, X.Z. Hu, M.B. Bush, J.M. Dell, L. Faraone, et al., Poisson ' s Ratio of Low-Temperature PECVD Silicon Nitride Thin Films, Journal of Microelectromechanical Systems. 16 (2007) 622–627.

[13] W. Zhou, J. Yang, Y. Li, A. Ji, F. Yang, Y. Yu, Bulge testing and fracture properties of plasma-enhanced chemical vapor deposited silicon nitride thin films, Thin Solid Films. 517 (2009) 1989–1994.

[14] C.-H. Hsueh, M.K. Ferber, Apparent coefficient of thermal expansion and residual stresses in multilayer capacitors, Composites Part A: Applied Science and Manufacturing. 33 (2002) 1115–1121.

[15] Y. Hwangbo, J.-M. Park, W.L. Brown, J.-H. Goo, H.-J. Lee, S. Hyun, Effect of deposition conditions on thermo-mechanical properties of free standing silicon-rich silicon nitride thin film, Microelectronic Engineering. 95 (2012) 34–41.

[16] M.K. Small, J.J. Vlassak, S.F. Powell, B.J. Daniels, W.D. Nix, Accuracy and Reliability of Bulge Test Experiments, Material Research Society Symposium Proceedings. 308 (1993) 159–164.

[17] A. Karimi, O.. Shojaei, T. Kruml, J.. Martin, Characterisation of TiN thin films using the bulge test and the nanoindentation technique, Thin Solid Films. 308-309 (1997) 334–339.

[18] O. Tabata, K. Kawahata, S. Sugiyama, I. Igarashi, Mechanical Property Measurements of Thin Films Using Load-Deflection of Composite Rectangular Membrane, Micro Electro Mechanical Systems, 1989, Proceedings, An Investigation of Micro Structures, Sensors, Actuators, Machines and Robots. IEEE. (1989) 152–156.

[19] X.Y. Ye, J.H. Zhang, Z.Y. Zhou, Y. Yang, Measurement of Young's Modulus and Residual Stress of Micromembranes, Micro Machine and Human Science, 1996., Proceedings of the Seventh International Symposium. (1996) 125–129.

[20] S. Maruthoor, A. Ajayakumar, T. Fuchs, O. Jakovlev, H. Reinecke, J. Wilde, Mechanical Characterization of Polycrystalline and Amorphous Silicon Carbide Thin Films Using Bulge Test, Journal of Microelectromechanical Systems. 22 (2013) 140–146.

[21] J.J. Vlassak, W.D. Nix, A new bulge test technique for the determination of Young's modulus and Poisson's ratio of thin films, Journal of Material Research. 7 (1992) 3242–3249.

[22] H.K. Lee, S.H. Ko, J.S. Han, H. Park, Mechanical properties measurement of silicon nitride thin films using the bulge test, Proceedings of SPIE. 6798 (2007) 1–8.

[23] T. Lu, C. Chen, K. Zhao, W. Zhang, T.J. Wang, Bulge test at nano-scale: The surface effects, Applied Physics Letters. 103 (2013) 1–4.

[24] D. Maier-schneider, J. Maibach, E. Obermeier, A New Analytical Solution for the Load-Deflection of Square Membranes, Journal of Microelectromechanical Systems. 4 (1995) 238–241.

[25] J.S. Mitchell, C.A. Zorman, T. Kicher, S. Roy, M. Mehregany, Examination of Bulge Test for Determining Residual Stress, Young's Modulus , and Poisson's Ratio of 3C-SiC Thin Films, Journal of Aerospace Engineering. 16 (2003) 46–54.

[26] Y. Xiang, X. Chen, J.J. Vlassak, Plane-strain bulge test for thin films, Journal of Material Research. 20 (2005) 2360–2370.

[27] H. Youssef, a. Ferrand, P. Calmon, P. Pons, R. Plana, Methods to improve reliability of bulge test technique to extract mechanical properties of thin films, Microelectronics Reliability. 50 (2010) 1888–1893.

[28] M.P. Orthner, L.W. Rieth, F. Solzbacher, High speed wafer scale bulge testing for the determination of thin film mechanical properties., The Review of Scientific Instruments. 81 (2010) 1–7.

[29] M.S. Benrakkad, M.A. Benitez, J.M. Lopez-Villegas, J. Samitier, J.R. Morante, Stress measurement by microRaman spectroscopy of polycrystalline silicon structures, Journal of Micromechanics and Microengineering. 5 (1995) 132–135.

[30] J. Samitier, S. Marco, O. Ruiz, J.R. Morante, J. Esteve-Tinto, J. Bausells, Analysis by FT-IR spectroscopy of SiO2-polycrystalline structures used in micromechanics : stress measurements, Sensors and Actuators A: Physical. 32 (1992) 347–353.

[31] K. Kusaka, T. Hanabusa, M. Nishida, F. Inoko, Residual stress and in-situ thermal stress measurement of aluminum film deposited on silicon wafer, Thin Solid Films. 290-291 (1996) 248–253.

[32] G.G. Stoney, The Tension of Metallic lFilnms depostted by Electrolysis, Proceedings of the Royal Society of London. Series A, Containing Papers of a Mathematical and Physical Character. 82 (1909) 172–175.

[33] X. Chen, Novel technique for measuring the mechanical properties of porous materials by nanoindentation, Journal of Material Research. 21 (2006) 715–724.

[34] Y. Xiang, X. Chen, Mechanical properties of porous and fully dense low- k dielectric thin films measured by means of nanoindentation and the plane-strain bulge test technique, Journal of Material Research. 21 (2006) 386–395.

[35] Z. Chen, X. Wang, V. Bhakhri, F. Giuliani, A. Atkinson, Nanoindentation of porous bulk and thin films of La0.6Sr0.4Co0.2Fe0.8O3−δ, Acta Materialia. 61 (2013) 5720–5734.

[36] Y. Xu, Y. Tsai, D.W. Zheng, K.N. Tu, C. Wo Ong, C.L. Choy, et al., Measurement of mechanical properties for dense and porous polymer films having a low dielectric constant, Journal of Applied Physics. 88 (2000) 5744–5750.

[37] Y.X. Di, X.H. Ji, M. Hu, Y.W. Qin, J.L. Chen, Residual Stress Measurement of Porous Silicon Thin Film by Substrate Curvature Method, Key Engineering Materials. 326-328 (2006) 223–226.

[38] a Kovacs, M. Pogany, U. Mescheder, Mechanical investigation of perforated and porous membranes for micro- and nanofilter applications, Sensors and Actuators B: Chemical. 127 (2007) 120–125.

[39] C.J.M. van Rijn, Nano and microengineered membrane technlology, Elsevier, 2004.

[40] R. Arya, M.M. Rashid, D. Howard, S.D. Collins, R.L. Smith, Thermally actuated, bi-stable, snapping silicon membranes, TRANSDUCERS ’03. 12th International Conference on Solid-State Sensors, Actuators and Microsystems. 2 (2003) 1411–1414.

[41] R. Arya, M.M. Rashid, D. Howard, S.D. Collins, R.L. Smith, Thermally actuated, bistable, oxide/silicon/metal membranes, Journal of Micromechanics and Microengineering. 16 (2006) 40–47.

[42] E. Epp, N. Ponnampalam, J.N. McMullin, R.G. Decorby, Thermal tuning of hollow waveguides fabricated by controlled thin-film buckling., Optics Express. 17 (2009) 17369–17375.

[43] V. Mulloni, F. Solazzi, F. Ficorella, A. Collini, B. Margesin, Influence of temperature on the actuation voltage of RF-MEMS switches, Microelectronics Reliability. (2013).

[44] D.S. Popescu, D.C. Dascalu, M. Elwenspoek, T. Lammerink, Silicon Active Microvalves Using Buckled Membranes For Actuation, Proceedings of the International Solid-State Sensors and Actuators Conference - TRANSDUCERS ’95. (1995) 305–308.

[45] G.-E. Song, K.-H. Kim, Y.-P. Lee, Simulation and experiments for a phase-change actuator with bistable membrane, Sensors and Actuators A: Physical. 136 (2007) 665–672.

[46] N. Yamamoto, D.J. Quinn, N. Wicks, J.L. Hertz, J. Cui, H.L. Tuller, et al., Nonlinear thermomechanical design of microfabricated thin plate devices in the post-buckling regime, Journal of Micromechanics and Microengineering. 20 (2010) 1–9.

[47] E. Iwase, P.-C. Hui, D. Woolf, A.W. Rodriguez, S.G. Johnson, F. Capasso, et al., Control of buckling in large micromembranes using engineered support structures, Journal of Micromechanics and Microengineering. 22 (2012) 1–7.

[48] G. Gopalakrishnan, D. a. Czaplewski, K.M. McElhinny, M. V. Holt, J.C. Silva-Martínez, P.G. Evans, Edge-induced flattening in the fabrication of ultrathin freestanding crystalline silicon sheets, Applied Physics Letters. 102 (2013).

[49] V. Pradeep, N. Ganesan, Thermal buckling and vibration behavior of multi-layer rectangular viscoelastic sandwich plates, Journal of Sound and Vibration. 310 (2008) 169–183.

[50] Z.-H. Jin, Buckling Of Thin Film Thermoelectrics, International Journal of Fracture. 180 (2013) 129–136.

[51] K. Kerman, T. Tallinen, S. Ramanathan, L. Mahadevan, Elastic configurations of self-supported oxide membranes for fuel cells, Journal of Power Sources. 222 (2013) 359–366.

[52] V. Ziebart, O. Paul, H. Baltes, Strongly buckled square micromachined membranes, Journal of Microelectromechanical Systems. 8 (1999) 423–432.

[53] M. Józwik, C. Gorecki, A. Sabac, P. Delobelle, M. Kujawińska, Evaluation of micromechanical properties of buckled SiOxNy-loaded membranes by combining the Twyman–Green interferometry with nanoindentation and point-wise deflection technique, Optics and Lasers in Engineering. 41 (2004) 703–716.

[54] M.K. Tripp, C. Stampfer, D.C. Miller, T. Helbling, C.F. Herrmann, C. Hierold, et al., The mechanical properties of atomic layer deposited alumina for use in micro- and nano-electromechanical systems, Sensors and Actuators A: Physical. 130-131 (2006) 419–429.

[55] C.F. Herrmann, F.W. DelRio, D.C. Miller, S.M. George, V.M. Bright, J.L. Ebel, et al., Alternative dielectric films for rf MEMS capacitive switches deposited using atomic layer deposited Al2O3/ZnO alloys, Sensors and Actuators A: Physical. 135 (2007) 262–272.

[56] R.L. Puurunen, J. Saarilahti, H. Kattelus, Implementing ALD Layers in MEMS Processing, ECS Transactions. 11 (2007) 3–14.

[57] K. Tapily, J.E. Jakes, D.S. Stone, P. Shrestha, D. Gu, H. Baumgart, et al., Nanoindentation Investigation of HfO2 and Al2O3 Films Grown by Atomic Layer Deposition, Journal of The Electrochemical Society. 155 (2008) H545–H551.

Chapter 4

Functionalization of Nanoporous Silicon Nitride Membranes

Abstract

In this chapter will be discussed the surface modification of nanoporous silicon nitride membranes in terms of material deposition for pore size reduction and surface modification via silanization and the grafting of responsive polymer chains.

First, Atomic Layer Deposition will be used to deposit in a conformal way Al_2O_3 onto the NSiMs to reduce the pore size of the nanoporous membrane. The mean nanopore diameter will be systematically characterized after the different pore size reductions to confirm the homogeneity and conformity of the deposition technique employed. In addition, the pore size reduction with Al_2O_3 induces a change of the surface chemistry that will be characterized by XPS.

Second, a successful method for the grafting-to in melt of thermo-responsive PNIPAM chains onto NSiMs will be reported. The successful grafting of PNIPAM brush layer will be characterized by XPS analysis, the characteristics of the grafted PNIPAM layer (surface coverage, grafting density, and distance between grafting sites) will be calculated from the ellipsometric measurements of the dry PNIPAM film.

Finally the thermo-responsive behaviour of the grafted PNIPAM brush layer will be demonstrated using in situ nano indentation technique and in situ AFM analysis. Cell adhesion/detachment experiments using PNIPAM functionalized NSiMs will be conducted to demonstrate the ability of these smart nanosurfaces to be used for cell culture applications.

4.1. Pore size reduction (PSR) with Atomic Layer Deposition of Al2O3 and modification of surface chemistry

The deposition of material to achieve the pore size reduction of membranes has been reported using techniques such as Chemical Vapor Deposition based techniques, allowing a non-conformal pore size reduction with material mostly deposited both at the inlet and outlet of the pores but not along the sidewalls [1].

Atomic Layer Depostion (ALD) allows the deposition of a wide class of materials in an extremely conformal way on plane or nanostructured surfaces [2–5]. This technique consists in depositing one single atomic layer at a time based on the principle of dissociative chemisorption of a precursor molecule onto the surface or structure. ALD is a self-limiting technique in the sense that the amount of a material deposited after each reaction cycle is constant. Tailoring porous membrane features such as the mean pore size and density has attracted interest over the past two decades especially in the field of molecular separation. The ability to tune the nanopore size post- membrane fabrication allows producing size selective sieving membranes depending on the specific needs without modifying the membrane fabrication processes. Because of the accurate film thickness control, excellent conformity and uniformity, ALD is an interesting technique to modify the morphology of nanoporous materials. ALD has been widely used for the pore size reduction of mesoporous silica membranes by deposition of SiO_2, TiO_2, Al_2O_3, demonstrating the tuning of the mean nanopore size and the selective reduction of defective pores [6–8]. The pore size reduction technique using ALD has also been extensively used and demonstrated onto commercially available nanoporous alumina membranes [9–15], nanoporous silicon surfaces fabricated by E-beam [1] and nanoporous polymeric membranes [16]. Several techniques derived from ALD have also been developed, such as Catalyzed Atomic layer Deposition (C-ALD) and vacuum-assisted vapour deposition (VVD). C-ALD is a technique derived from standard ALD using the appropriate catalyst to promote the surface reaction and reduce the reaction temperature, it has also been used to reduce the mean pore size of mesoporous silica membranes [17,18]. Recently, Jambhrunkar et al. proposed a facile VVD technique to reduce the pore size of mesoporous silica at the angstrom precision [19]. The pore size reduction of membranes by grafting different kinds of polymers has also been reported using the plasma polymerization [20], Reversible Addition-Fragmentation chain Transfer (RAFT) polymerization [21] and Atom Transfer Radical Polymerization (ATRP) [22].

Depositing a material by ALD onto a nanoporous substrate of a different nature can change the surface properties and influence the molecular transport through the membrane due to different surface charges [12], chemical selectivity [11] or improved hydrophobicity [16]. The characterization of the pore size reduction performed by ALD onto a nanoporous membrane is generally done using AFM [20,23], SEM [15,20], TEM [15,16], gas permeance measurements [7,17], or with more complicated set up systems such as in situ FTIR [9] or in situ ellipsometric porosimetry measurements [8] for real time monitoring of the thickness deposited.

In the following section will be described the procedure to reduce the pore size of NSiMs by ALD of Al_2O_3 with control over the precision of the thickness deposited at the nanometer level. Characterization of the openings of the nanopores and the thickness of Al_2O_3 deposited will be performed using TEM. The chemical composition of the layer deposited will be characterized by XPS to confirm the stoichiometry of the Al_2O_3 coating by looking at the respective atomic concentrations.

Experimental

Atomic Layer Deposition (ALD) of Al_2O_3

Deposition of Al_2O_3 onto nanoporous suspended membranes was performed with ALD instrument *Beneq TFS 200* (Beneq, Finland). The deposition is performed at 200°C and under vaccum (5 mbar). The deposition process layer by layer of Al_2O_3 is achieved by the successive introduction of two chemical precursors (H_2O and TMA) in the reactor. N_2 purge steps are performed after introduction of each precursor to remove the excess of chemical introduced and promote the formation of Al_2O_3 monolayer. A full cycle allowing the deposition of a single monolayer of Al_2O_3 ($\approx$ 1.1 Å) takes approximately 3 seconds.

Transmission Electron Microscopy (TEM) analysis

The instrument used and the parameters of analysis are the same as described in chapter 3 section 3.1.2.

X-ray Photoelectron Spectroscopy (XPS) of the Al_2O_3 coating

The XPS instrument used for the surface analysis and the detection of amide groups composing the backbone of the PNIPAM is a XPS/ESCA KRATOS AXIS ULTRA equipped with a concentric hemispherical analyser. The spectra were acquired using a monochromatic Al Kα X-ray radiation source operating at 15kV and 150W in ultra-high vacuum (base pressure of 10^{-9} mbar) with the electrons emitted at 60° to the surface normal. The acquired data were processed using the CasaXPS software. A 10 x 10 mm Si chip coated with 200 nm of low stress SiN and 20 nm of Al_2O_3 deposited by ALD will serve as reference sample on which the XPS measurements will be performed.

Results and Discussion

Pore Size Reduction (PSR) of NSiMs by Atomic Layer Deposition (ALD) of Al_2O_3

The accuracy of the thickness deposited by ALD has been confirmed by calibrating the equipment prior deposition onto NSiMs. The calibration has been performed by depositing 100 nm of Al_2O_3 on a 4 inches silicon wafer; the thickness of the deposited film was measured by ellipsometric measurement at different positions onto the wafer and has been demonstrated to be conformal with an error estimated to be of ± 2%. Reducing the pore size of the NSiMs is expected to modify the device's properties regarding the cut-off of the membranes when used in size-selective molecular separation experiments. The PSR of NSiMs has been performed by ALD of different thicknesses typically 20 nm, 30 nm and 40 nm of Al_2O_3 requiring 182, 273 and 364 ALD deposition cycles, respectively.

Figure 4.1 shows the TEM pictures of the NSiMs after PSR, the conformal deposition of Al_2O_3 can be observed. Size distributions graphs could not be computed from these images because of the contrast difference between the initial porous layer, the inner structure of the pore where only Al_2O_3 has been deposited and the opened part. Therefore areas with large defects were observed when possible in order to visualize and measure directly from the top view TEM pictures the thickness of Al_2O_3 deposited on the sidewalls. The nanopores were still characterized to be opened after the deposition of 20 and 30 nm of Al_2O_3 (Figure 4.1 b) and c)), meaning a pore size reduction of the initial 85 ± 15 nm nanopore diameter by 40 and 60 nm, respectively. However, after deposition of 40 nm of Al_2O_3 (figure 4.1 d)), most of the nanopores are closed. In addition, the TEM analysis of the NSiMs after the PSR revealed an irregular inner structure. (figure 4.1 b)). This latter is due to the initial irregular round shape of the nanopores being increased when reducing its size. Reducing the pore size also reduces the overall porosity of the NSiMs, affecting the molecular transport properties. This part will be discussed in the next chapter.

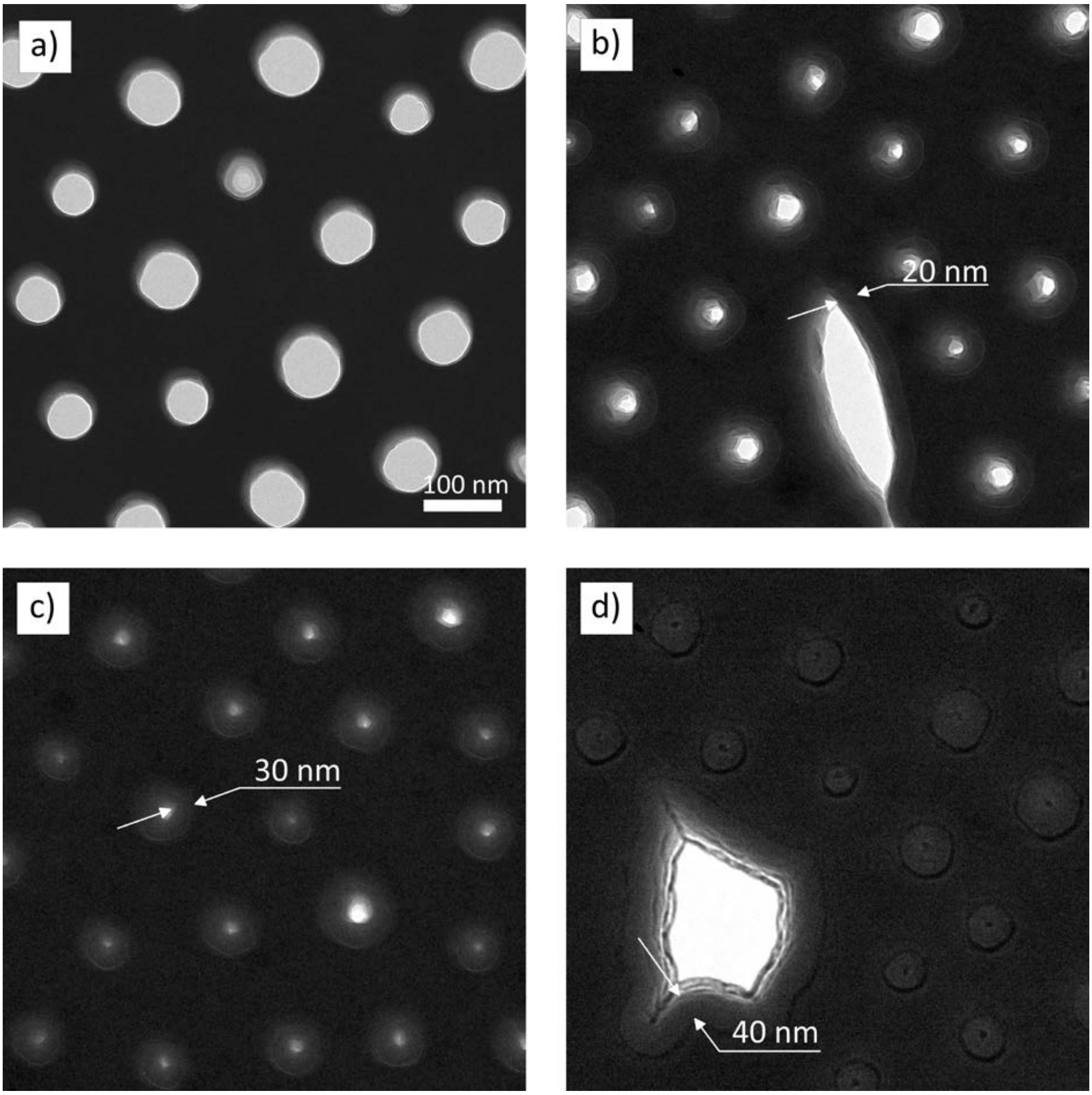

Figure 4.1 TEM pictures of NSiMs **a)** before the PSR, with PSR with ALD of **b)** 20 nm **c)** 30 nm **d)** 40 nm of Al_2O_3.

The XPS analysis of the 20 nm thick Al_2O_3 film deposited by ALD shown in figure 4.2 revealed only oxidized Al 2p peak and O 1s peak typical of metal oxide. The XPS spectra of the Al 2p and O 1s core-level reveals peaks at the binding energies of 74.8 eV and 531.4 eV, respectively, being the characteristic values of the Al-O bonds. The atomic concentrations calculated from the XPS measurements (using the area under the curves of corresponding peaks) reveal a concentration in Al and O of 39.74% and 60.26%, respectively. Therefore, stoichiometric Al_2O_3 film growth by ALD has been confirmed. Al_2O_3 is a hydrophilic material while SiN is hydrophobic, the modification of the surface chemistry can be considered to enhance the diffusional properties of NSiMs.

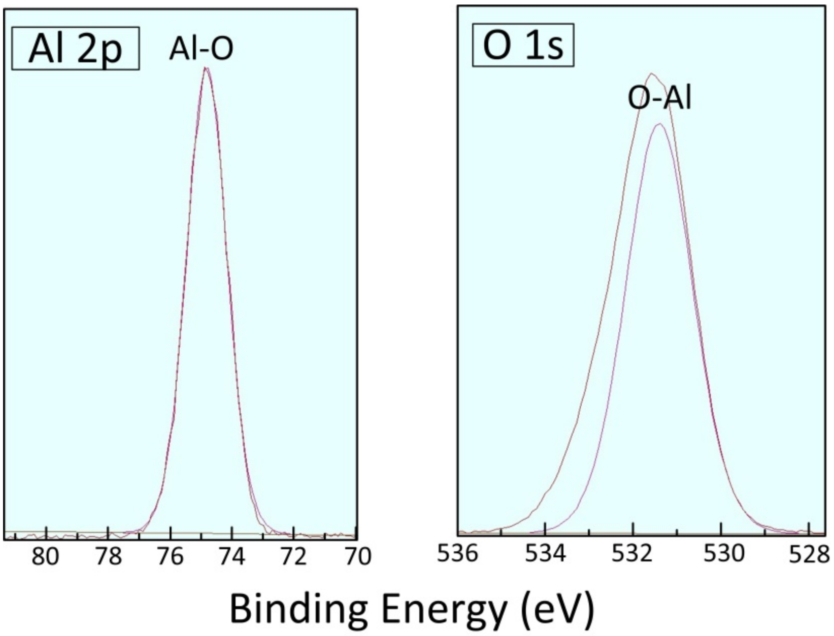

Figure 4.2 Al 2p and O 1s core-level XPS spectra recorded for a 20 nm thick Al_2O_3 layer grown by ALD. (arbitrary units are used for y axis)

4.2. Grafting of poly(N-isopropylacrylamide) onto nanoporous silicon nitride membranes

Over the past two decades, stimuli-responsive polymers, or so called « intelligent » or « smart » polymers have attracted the interest of many research groups because of their amazing properties allowing these materials to observe a conformational morphological change in the polymer grafted layer upon variation of an external parameter in their environment [24–27]. The external stimulus can be a variation in the temperature [28,29], pH [30], electric potential [31], or light [32]. Poly(N-isopropylacrylamide) (PNIPAM), a thermo-responsive polymer, is of particular interest because it has been well demonstrated that this polymer observe a reversible morphological change upon temperature variation. A sharp lower critical solution temperature (LCST) of 32°C in pure water has been evidenced by Heskins and Guillet [33] which is close to the physiological conditions temperature, making this polymer very interesting for biomedical applications. The thermo-responsive behaviour of the PNIPAM chains has been extensively studied and is now well understood, it is now admitted that below the LCST the PNIPAM chains form an expanded swollen structure because the PNIPAM chains are hydrated by the surrounding water molecules, this state is known as the "expanded coil" shape of the PNIPAM chains. Above the LCST, the PNIPAM chains collapse to a so called "globule" shape because the hydrogen bonds between the amide groups composing the backbone of the PNIPAM and the surrounding water molecules are suppressed (formation of H-bonds with adjacent side groups).

PNIPAM functionalized surfaces, micro/nanostructured substrates, or particles find many applications in cell culture [34–36], sensing [37–39], or controlled drug delivery [40,41]. This work will mostly focus on PNIPAM grafted onto micro/nanoporous membranes [22,41–58] to obtain a control over the permeability of the membranes for the diffusion and filtration of (bio)molecules. PNIPAM has been grafted onto various porous membranes made of different materials such as polyethylene terephthalate [22,43,54,57] (PET), polytetrafluoroethylene [44] (PTFE), polycarbonate track etch [49] (PCTE), polyethylene [45,56] (PE), anodic aluminium oxide [46] (AAO), Nylon-6 [42,47], copper mesh film [53], silicon [52], polypropylene [48] (PP). PNIPAM grafted films can be prepared according to different methods, a commonly used and well-described technique is the plasma polymerization technique [42,45,48,56,59,60] in which a precursor gas is broken into ions, free electrons, radicals and neutral fragments that are all involved in the recombination of these fragments into plasma polymers on the surface of the substrate [61]. Another well-known and described technique in the literature allowing the PNIPAM polymer chains to grow directly from the substrate is the atom transfer radical polymerization (ATRP). ATRP has been successfully used to grow PNIPAM chains on different types of substrate with a precise control over molecular weight with narrow molecular weight distribution and grafting density [22,49,62–67]. An alternative method consisting in grafting covalently end-functionalized polymers in the molten state (above the glass transition temperature of the polymer) to a suitable functional surface has been demonstrated by Luzinov et al. in order to obtain a high grafting density [68]. This method is called “grafting to” in melt technique unlike ATRP which is a “grafting from” technique. This grafting under melt process allows a better access of the polymer chains to the functional surface for covalent binding. Densely packed PNIPAM brush layers were successfully grafted on functional surfaces [52,69] and their thermo-responsive behavior has been demonstrated. The coil to globule morphological change of the PNIPAM brushes upon temperature variation depends strongly on the molecular weight of the chains and the grafting density [65,70,71]; the immobilized chains might not exhibit any morphological change if these two parameters are not suitable. In order to monitor the change in morphology of the PNIPAM brush layer from a swollen to a collapsed state, different methods have been used such as quartz crystal microbalance [72], surface plasmon resonance [73], neutron reflectivity [74], sum-frequency generation spectroscopy [75], atomic force microscopy [52,69,76–78] and attenuated total reflection Fourier transform infrared spectroscopy (ATR-FTIR) [52,79].

In this section we report a successful and easy method for grafting-to in melt PNIPAM chains onto nanoporous silicon nitride membranes (NSiMs). First, the successful grafting of PNIPAM brush layer was characterized by XPS analysis. Second, the characteristics of the grafted PNIPAM layer (surface coverage, grafting density and distance between grafting sites) were calculated from the ellipsometric measurements of the dry PNIPAM film. In addition, the thermo-responsive behaviour was demonstrated using in situ nano indentation technique and in situ AFM analysis in liquid environment. Finally, we also demonstrated the possible use of our grafted PNIPAM layers for cell adhesion/detachment experiments.

Experimental

Materials

Two different end-functionalized PNIPAM will be used in this study to be grafted onto NSiMs, carboxy-terminated (COOH) and amino-terminated (NH_2). The anchoring layer allowing the grafting of the carboxy-terminated PNIPAM on the NSiMs is a self-assembled monolayer (SAM) of glycidylpropyloxytrimethoxysilane (GPS, Sigma-Aldrich, Switzerland). The carboxy-terminated PNIPAM used has a molecular weight of M_w = 66 400 g/mol (referred as PNIPAM-COOH 66k in this work), a polydispersity index PI = 1.35 and was purchased from Polymer source (Canada). For the amino-terminated PNIPAM, the anchoring layer is obtained by silanizing the surface with isocyanatopropyltriethoxysilane (ICPES, Sigma-Aldrich, Switzerland) SAM. The amino-terminated PNIPAMs used for the grafting (Polymer Source, Canada) have molecular weights of M_w = 66 000 g/mol and M_w = 50 500 g/mol referred to as PNIPAM-NH_2 66k and PNIPAM-NH_2 50k and PIs of 2.6 and 1.53, respectively. The solvents used for the grafting process, namely tetrahydrofuran (THF) and toluene were purchased from Sigma-Aldrich (Switzerland) and used as received.

Substrate cleaning and activation

The NSiMs used for grafting were cleaned in a piranha solution at 110°C (H_2SO_4/H_2O_2 4:1) for 10 minutes and then rinsed in five consecutive bath of ultrapure deionized water (Milli-Q purification system from Millipore) and then dried with a nitrogen gun. (***Caution:*** *Piranha solution is strongly acidic and oxidizing, it should not be in contact with organic solvents because it can react in a violent way and explode, and therefore piranha solution must be handled with care*). The piranha solution will eliminate the possible organic matter present on the surface of the NSiMs, it will also hydroxylate the native SiO_2 layer on top of the low stress silicon nitride layer. Once the samples are cleaned and activated, if they are not used immediately for silanization, a short O_2 plasma (100W, bias voltage 260V) for 10 minutes can be done to re-hydroxylate the surface just before silanization.

NSiMs silanization with ICPES and GPS (anchoring layer)

The 6 mm x 6 mm silicon chips with the 1 mm x 1mm free standing nanoporous silicon nitride membrane at the center were immersed overnight (approx. 14 hours) in a 2 vol% solution of ICPES in toluene or in a 1 vol% solution of GPS in toluene to create an anchoring layer for subsequent covalent grafting of PNIPAM-NH_2 or PNIPAM-COOH, respectively. By proceeding to this liquid phase reaction, we obtain a self-assembled monolayer of the silane molecules. The NSiMs are then rinsed 4 times in a beaker with toluene (toluene changed every 4 hours) by stirring and finally dried with a nitrogen gun.

Grafting-to by melt technique of PNIPAM onto NSiMs

Solutions of PNIPAM-NH_2 66k and PNIPAM-NH_2 50k were prepared in ethanol with a concentration of 10 mg/mL each. Solutions of PNIPAM-COOH 66k were prepared in THF with a concentration of 10 mg/mL. The solutions are then filtered with a PVDF 0.45 µm syringe filter. Then 60 µL of solution is spin coated per NSiM at 2000 rpm for 25 seconds with a SUSS MicroTec DELTA 6 RC BM spin coater, and the samples are held with an appropriate vacuum chuck designed especially for this purpose. The samples are then placed in an oven at 160°C for 12 hours. This temperature has been chosen higher than the glass transition temperature of the PNIPAM (133°C) but lower than the thermal degradation temperature of this polymer (350°C) [80]. The NSiMs are then thoroughly rinsed 2 times first in a THF bath for 1 hour in order to remove the non-covalently grafted polymeric chains, then in Milli-Q water for 4 hours (water changed every hour), and finally dried with a nitrogen gun.

Ellipsometric measurements

The thickness of the dry PNIPAM films (PNIPAM-COOH 66k, PNIPAM-NH_2 66k and PNIPAM-NH_2 50k) was controlled with ellipsometric measurements on reference samples. The reference samples were typically 10 x 10 mm^2 silicon chips coated with a 200 nm thick low stress silicon nitride deposited by LPCVD, on which the same grafting protocol as the one performed on the NSiMs was carried out. The ellipsometric measurements have been performed using a spectroscopic ellipsometer (Jobin Yvon – Horiba HR460) in a range of wavelength from 270 nm to 1 700 nm at an angle of incidence of 70°. The refractive index of the low stress SiN was obtained by linear regression and set to n_{SiN} = 2.255, the one of the silanes GPS and ICPES was set to n_{silane} = 1.44, the one of the PNIPAMs to n_{PNIPAM} = 1.501 [81]. The refractive index of the native silicon dioxide layer is n_{SiO2} = 1.447 and was set according to the literature mentioning the refractive index of ultrathin silicon dioxide layers deposited by atomic layer deposition (ALD) [82]. To proceed to measurements of this multistack layer, a multilayer model was used and is composed as followed, silicon nitride, silane (actually composed of the self-assembled monolayer of silane and the native oxide layer), and PNIPAM layer.

X-ray Photoelectron Spectroscopy

The XPS instrument used for the surface analysis and the detection of amide groups composing the backbone of the PNIPAM is a XPS/ESCA KRATOS AXIS ULTRA equipped with a concentric hemispherical analyser. The spectra were acquired using a monochromatic Al Kα X-ray radiation source operating at 15kV and 150W in ultra-high vacuum (base pressure of 10^{-9} mbar) with the electrons emitted at 60° to the surface normal. The acquired data were processed using the CasaXPS software.

Nano-indentation of PNIPAM brush layers in liquid environment

A Nanowizard II AFM (JPK Instruments, Germany) mounted on an Axiovert 200 inverted optical microscope (Carl Zeiss, Germany) has been used. A Petri dish heater (JPK Instruments, Germany) allowed performing the nanoindentation in liquid environment by controlling the temperature with a precision of ± 0.1°C. 500 µm long silicon tipless cantilevers (Arrow TL1, Nanoworld, Switzerland) with a nominal spring constant of 0.03 N/m were used for all indentation measurements. Arrow TL1 tipless cantilevers were modified (Novascan, IA) by gluing glass spheres (radius = 5 µm, Novascan, USA) to the end of each cantilever to give well-defined indenters. Force-distance curves were acquired with an approaching and retracting speed of 2.0 µm/s until a maximum force of 15 nN was reached. Data analysis was carried out using Image Processing software (JPK Data Processing, JPK Instruments, Germany) to determine the contact point and evaluate the indentation depth.

Contact mode AFM in liquid environment

The same AFM instrument and temperature controller were used as for the nano-indentation. The AFM probe used is a CSC37 silicon cantilever (lever B) without any aluminium coating (Mikromasch, Estonia). The tip curvature radius is less than 10 nm, the stiffness is k = 0.3 N/m. A force of 10 nN applied by the tip on the surface was determined to be ideal for imaging the three kinds of grafted PNIPAM onto the NSiMs (PNIPAM-COOH 66k, PNIPAM-NH_2 66k and PNIPAM-NH_2 50k). The line scan rate was of 1 Hz. All the experiments were carried out in standard deionized water. The acquired data were processed using the software *JPK data processing.*

Attachment and detachment of cells on PNIPAM functionalized NSiMs

The human osteosarcoma cell line, Saos-2, was obtained from American Type Culture Collection (VA, USA) and was maintained in continuous culture in McCoy's 5A medium (Sigma, MO, USA) supplemented with 10% heat-inactivated standardized fetal bovine serum (Biochrom AG, Germany), 50 units/ml of penicillin (Sigma, MO, USA), 50 μg/ml of streptomycin (Sigma, MO, USA) and 1.5 mM of L-glutamine (Sigma, MO, USA) at 37°C in a humidified 5% CO2 atmosphere. Cells were detached from their culture dishes by incubating with a solution of 2.5 g/l trypsin and 0.38 g/l of ethylenediaminetetraacetic acid (EDTA) for 5 min. The dissociated cells were seeded on a bare NSiM and functionalized NSiMs and incubated for 24 h to allow the cells to spread and their adhesion proteins to be renewed. Cell detachment experiments were conducted at both 37°C (above the LCST) and 23°C (below the LCST).

Results and Discussion

Fabrication of PNIPAM-grafted NSiMs

The grafting of three different PNIPAM was conducted under melt onto previously coated functional Self Assembled Monolayers (SAMs). In contrast to standard grafting techniques often conducted in solution and involving the covalent binding of polymer chains to surface functional groups, the under melt approach allows the preparation of thin polymer films with higher grafting densities and brush-like structures that represent the 2 main conditions to preserve the responsive properties of the grafted polymer chains. The grafting to under melt technique has been extensively used to graft different polymers onto silicon based substrates [68,83,84]. By heating the coated films above the polymer glass transition temperature the under melt grafting process enables PNIPAM end groups to easily access and react with the reactive SAMs. However the process should be conducted below the polymer thermal degradation temperature [80].

In previous papers we reported simple under melt grafting protocols for the tethering of carboxy- and amine-terminated PNIPAM brushes onto both silicon based substrates and gold thin film. It resulted in the formation of uniform, dense and responsive PNIPAM films which the temperature-induced chain conformational changes could be demonstrated by Atomic Force Microscopy investigations in liquid environment and Fourier transform infrared spectroscopy (FT-IR) enhanced by Single-Beam Sample Reference attenuated total reflection method (SBSR-ATR) [52,69].

In this work similar under melt grafting processes have been used and adapted to the freestanding structure of our ultrathin nanoporous membrane. First carboxy-terminated PNIPAM-COOH 66k has been covalently grafted onto glycidylpropyloxytrimethoxysilane (GPS) functionalized membranes. After an annealing step at 170°C of the spin coated polymer on the GPS-coated NSiMs the functionalized membrane has been thoroughly rinsed with water/THF and DMF in order to remove the nonconvalently grafted polymeric chains.

In parallel the grafting of amino-terminated PNIPAM-NH_2 (50k and 66k) was carried out by spin coating PNIPAM-NH_2 solutions onto isocyanatopropyltriethoxysilane (ICPES) functionalized membranes. Here also the coated membranes were then annealed at 160°C and thoroughly rinsed with THF and Milli-Q water. A schematic representation of the chemical reactions involved during this grafting procedure is shown in Figure 4.3.

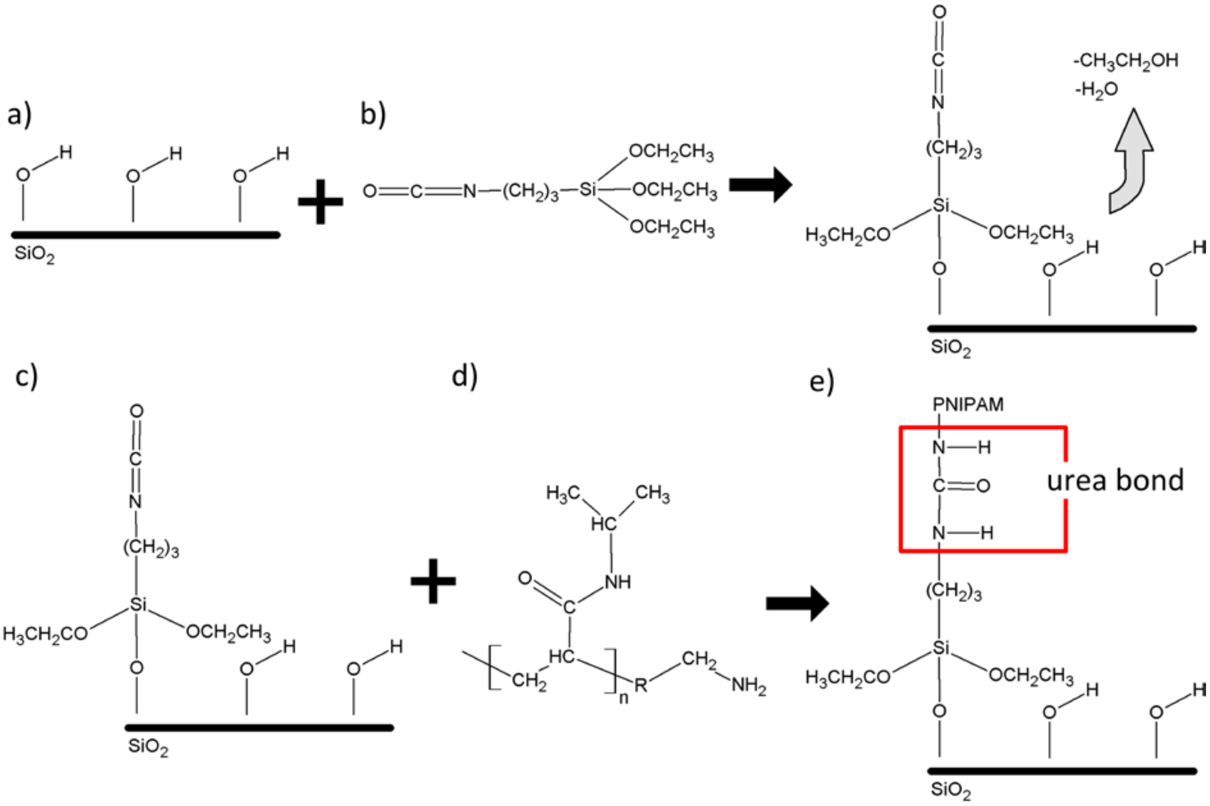

Figure 4.3 Schematic representation of the chemical reaction between **a)** the surface with native oxide and hydroxyl groups and **b)** ICPES silane, and the reaction between **c)** the silanized surface and **d)** the amino-terminated PNIPAM.

The characterization of the successful grafting of PNIPAM onto NSiMs has been performed using X-Ray Photoelectron Spectroscopy (XPS) to analyze the chemical composition of grafted surfaces. The XPS spectra of PNIPAM-NH_2 functionalized reference SiN samples following the same grafting procedure as on NSiMs are shown in Figure 4.4. For the C 1S core-level, the typical fingerprint of the amide groups composing the backbone of the PNIPAM were recorded at 286.12 eV (C-N) and 287.92 eV (C=O). For the O 1S core-level, two main peaks are recorded at 532.94 eV (O-Si) and 531.3 eV (C=O) and for the N 1S core-level peaks at 398.5 eV (Si-N) and 399.75 eV (C-N) are recorded. From the above data, it has been confirmed that PNIPAM has been successfully grafted onto the SiN reference surface.

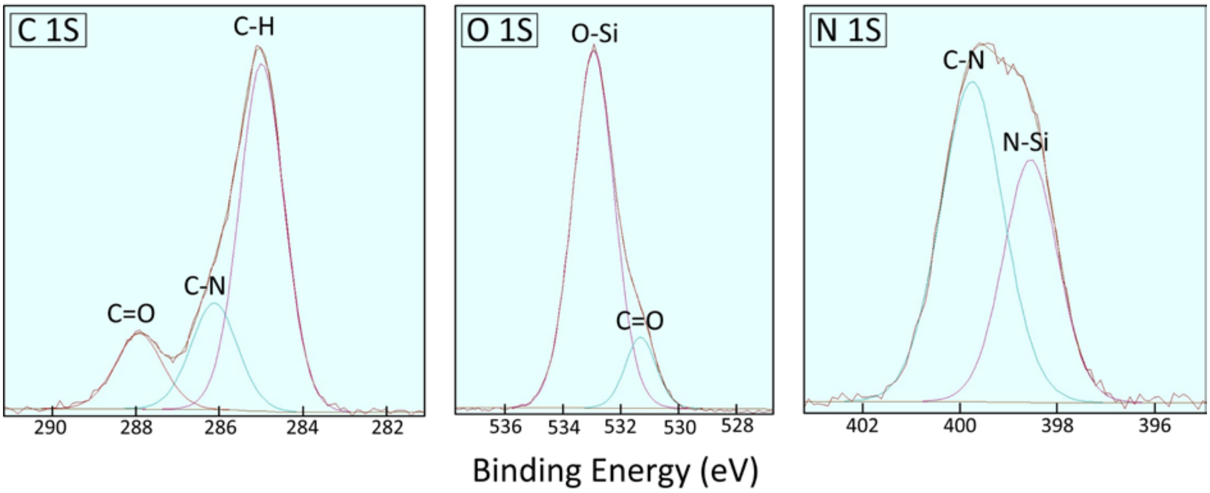

Figure 4.4. C 1S, O 1S and N 1S core-level XPS spectra recorded for PNIPAM $-NH_2$ 50k functionalized reference SiN samples. (arbitrary units are used for y axis)

To monitor the surface functionalization with silane SAMs as well as the subsequent grafting of carboxy or amine terminated PNIPAM, ellipsometry measurements have been performed in ambient condition on 1 cm^2 Si chips coated with 200 nm of LS-SiN deposited by LPCVD reference substrates that have been processed to the grafting procedure under similar conditions as for NSiMs. The ellipsometric thicknesses of the functional SAMs are reported in Table 4.1 (column A). The stack composed of the GPS layer and the native oxide layer thickness was thus found to be 2.5 nm. The stack composed of the ICPES layer and native oxide layer thickness was measured to be 3.8 nm. The native oxide layer is well known to be approximately 1 nm thick [85], therefore the thickness of the GPS layer and the ICPES layer were calculated to be of 1.5 nm and 2.8 nm, respectively. The thicknesses of the functional SAMs are greater than the ideal supposed thicknesses of one single monolayer for each silane. This might be explained explained by the formation of several monolayers due to the silane deposition without strict humidity control [86].

The ellipsometric thicknesses of the different dry PNIPAM brush layers are also reported in Table 4.1 (column B). The thickness of the dry PNIPAM-NH_2 66k brush layer is lower than the one of the PNIPAM-NH_2 50k indicating already a low grafting density for the first one mentioned, probably due to its high polydispersity index [87,88]. Grafted chains in close proximity to each other forces the chains to stretch away from the surface, therefore the grafting density is directly linked to the dry brush layer thickness.

Table 4.1 Ellipsometric measurements of dry PNIPAM on silanized SiN reference surfaces.[a]

PNIPAM type	Ellipsometric thickness (nm)	
	A *(silane and native oxide)*	**B** *(PNIPAM layer)*
COOH 66k	2.5	15.7
NH_2 66k	3.8	6.8
NH_2 50k	3.8	7.5

[a] *(A)Thickness of the corresponding silane (GPS for PNIPAM-COOH and ICPES for PNIPAM-NH_2) and native oxide layer; (B) thickness of the grafted PNIPAM layer on reference samples.*

In order to evaluate the conformation of the PNIPAM grafted layers on NSiMs, several grafting parameters including surface coverage S (g/m^2), the grafting density σ (polymer chains/nm^2) and the average distance between grafting sites D (nm) have been calculated using Eqs. 4.1 - 4.3 [68] With h the previously measured PNIMAM film thickness, ρ the density of the dry PNIPAM film considered to be 1.27 g/cm^3 [89], N_A the Avogadro's number and M_n the number-average molecular weight of PNIPAM chains.

$$S = \rho h \qquad (4.1)$$

$$\sigma = \frac{SN_A \times 10^{-21}}{M_n} \qquad (4.2)$$

$$D = \left(\frac{4}{\pi\sigma}\right)^{1/2} \qquad (4.3)$$

The PNIPAM chain conformation in the grafted layer in a good solvent (water in this case) can be deduced by evaluating the ratio between the distance separating two adjacent grafting sites (D) to the Flory radius (R_f) of the unperturbed chains. If the degree of stretching $D/2R_f$ is >1, then the PNIPAM layer can be considered loosely grafted, whereas when $D/2R_f$ is <<1, it is characteristic of strongly stretched chains that form polymer brushes [88]. The Flory radius can be calculated from Eq. 4.4, with b the length of the statistical segment, which was assumed to be 0.3 nm for flexible polymers [88] and N is the number average degree of polymerization. It is also interesting to have a look at the calculation of the theoretical length of the swollen PNIPAM chains L (nm) using Eq. 4.5 proposed by Alexander and De Gennes [90,91] which is valid for tethered polymer chains in a good solvent with M and M_0 the average polymer and monomer molecular weight, respectively. The calculated values of R_f and L do not take into account the polydispersity index of the polymers, which can be pretty high in some of the cases studied here (e.g. PI of PNIPAM-NH_2 66k is 2.6).

$$R_F = bN^{\frac{3}{5}} \qquad (4.4)$$

$$L = \frac{M}{M_0} b \left(\frac{b}{D} \right)^{\frac{2}{3}} \qquad (4.5)$$

Table 4.2 Grafting parameters calculated for the tethered PNIPAM brush layer.[b]

PNIPAM type	*h*	*S*	*σ*	*D*	R_f	$D/2R_f$	*L*
	(nm)	*(g/m²)*	*(chains/nm²)*	*(nm)*	*(nm)*		*(nm)*
COOH 66k	15.7	0.0168	0.152	2.89	13.76	0.105	38.93
NH_2 66k	6.8	0.00728	0.0664	4.38	13.71	0.16	29.34
NH_2 50k	7.5	0.00803	0.0957	3.65	11.67	0.156	25.36

[b] *h is the dry PNIPAM film thickness measured by ellipsometry, S the surface coverage calculated from (1), σ is the grafting density calculated from (2), D is the average distance between two grafting sites calculated from (3), R_f is the Flory radius deduced from (4), $D/2R_f$ is the degree of stretching of the PNIPAM chains, and L is theoretical length of the swollen PNIPAM chains extracted from the Alexander – De Gennes model.*

From those data we can confirm that all the different PNIPAM studied are in the brush layer conformation since $D/2R_f$ is <<1, and exhibit grafting densities comparable to what can be find in the literature [22,52,71].

The successful grafting of the different PNIPAM layers was thus evidenced by characterizing the chemical composition of the surface by XPS analysis and the characteristics of the PNIPAM layers have been calculated from the ellipsometric measurements of the dry PNIPAM films on flat reference samples. In the next section experiments will be conducted to observe the thermo responsive behaviour of the grafted PNIPAM brush layers

Observation of the thermo-responsive morphological change of the grafted PNIPAM brush layer

Nano-indentation is usually performed to determine the elastic modulus of “hard surfaces” or “soft” polymeric materials [92] based on a load-penetration data analysis. In this precise case, the nano-indentation of ultrathin PNIPAM brush layer was used to visualize the difference in penetration depth between the swollen and collapsed state of the PNIPAM brush layer depending on the temperature of the liquid medium (Figure 4.5).

The load-penetration curve of a non-functionalized surface showed in Figure 4.5 a) served as a reference to identify the nano-indentation of “hard” surfaces. The nano-identation performed at 38°C on each type of PNIPAM grafted layer confirmed the collapsed state conformation of the brush layer with a very small penetration depth measured after the contact point with the surface. Indeed, these load-penetration curves obtained are similar to the reference load-penetration curve of “hard” surfaces.

The morphological change was evidenced for each type of PNIPAM (COOH 66k, NH_2 66k, NH_2 50k) by acquiring the load-penetration curves at 23°C when the PNIPAM brush layers are swollen. Unfortunately, the difference in penetration depth measured between the collapsed and swollen state could not be correlated with the theoretical values of the chain length calculated with Eq. 4.5. The values obtained for the thickness of the swollen PNIPAM COOH 66k brush layer (Figure 4.5 b)) were up to 3-4 fold larger than the theoretical values. Several studies attributed this phenomenon to both the steric repulsion of the PNIPAM brush layer when approaching the AFM probe and repulsive contributions due to Van der Walls interactions [76,89]. Popa et al. attributed the increase of the repulsive thickness to the interaction between the AFM tip and the unreacted epoxy groups of the silane generating carboxylic groups [93]. In our case, the high repulsive thickness measured for the PNIPAM COOH 66k compared to the PNIPAM NH_2 66k (Figure 4.5 c)) and the PNIPAM NH_2 50k (Figure 4.5 d)) brush layer is explained by a higher grafting density and a better monodispersity of chain length.

Therefore the combined steric and electrostatic repulsive interactions are increased for this specific PNIPAM brush layer. Data obtained can only be interpreted qualitatively as the elastic properties modification of the PNIPAM brush layers upon temperature variation, indicating the thermo-responsive collapse of the grafted PNIPAM brush layers.

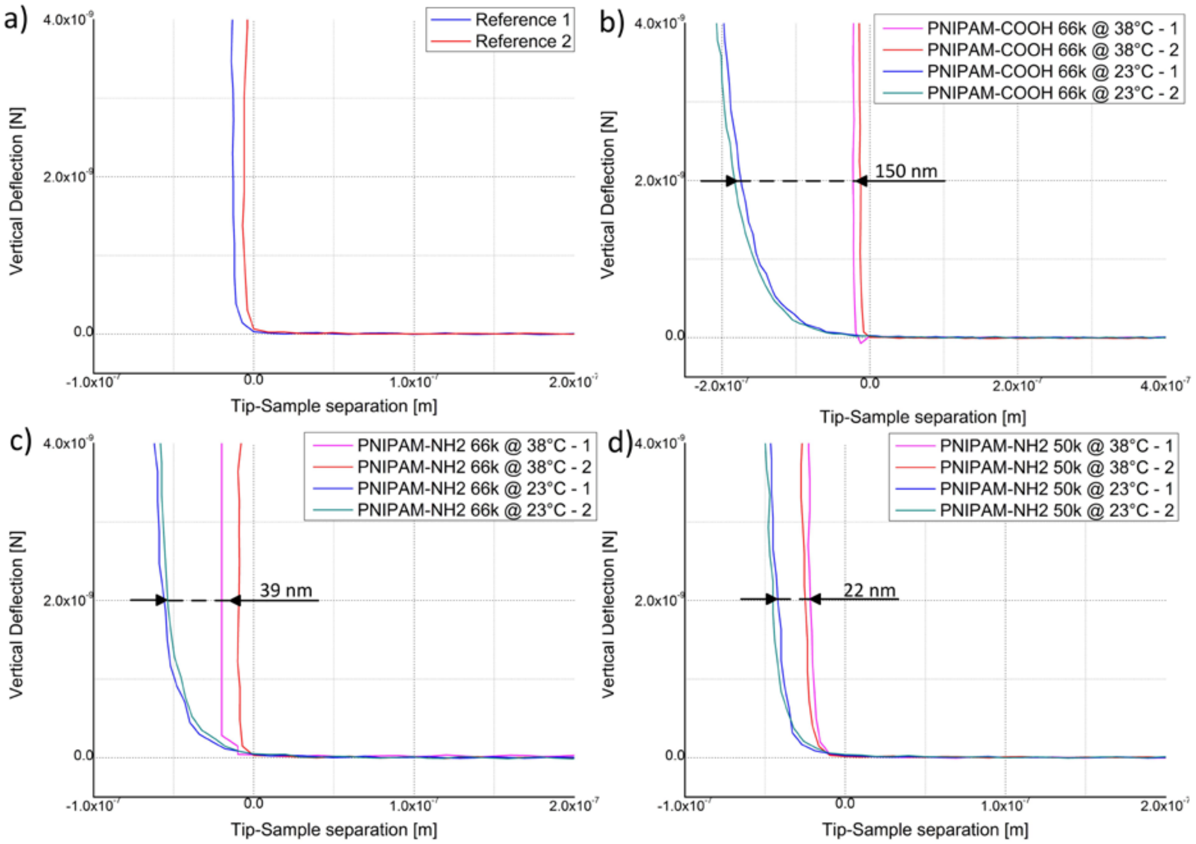

Figure 4.5 Load-penetration curves at room temperature and 38°C of **a)** a bare reference NSiM, NSiMs grafted with **b)** PNIPAM COOH 66k, **c)** PNIPAM NH_2 66k and **d)** PNIPAM NH_2 50k.

In addition, the morphological change from a hydrated state (below LCST of 32°C) to a dehydrated state (above LCST) of the PNIPAM chains grafted onto the NSiMs has also been observed with an atomic force microscope in liquid environment by monitoring the variation of the pore morphology. Figure 4.6 shows the AFM micrographs of the nanoporous surface grafted with different PNIPAM below and above the LCST. Figure 4.6 a) and b) show a difference in topography of the PNIPAM COOH 66k brush layer upon temperature variation. This phenomenon is attributed to the collapse of the chains above the LCST forming compact globules increasing the surface roughness making the imaging of the nanopores more difficult. The same phenomenon has been observed in previous studies [89,93]. No drastic difference in topography below and above the LCST has been observed for both the PNIPAM NH_2 66k (Figure 4.6 c) and d)) and 50 k (Figure 4.6 e) and f)) functionalized NSiMs. This latter was explained by the fact that these brush layers are composed with shorter chain lengths and lower grafting densities. Therefore these characteristics induce a less compact globular shape above the LCST and less dense brush layer below the LCST allowing an easier access of the AFM tip between the chains. It has been demonstrated that in case of low grafting density and short chain length, the morphological transition might not occur [65,71]. The qualitative results obtained can be correlated with the previous ones obtained by the nano-indentation of the PNIPAM brush layers grafted onto the NSiMs, with an evident thermo-responsive collapse of the PNIPAM COOH 66k brush layer.

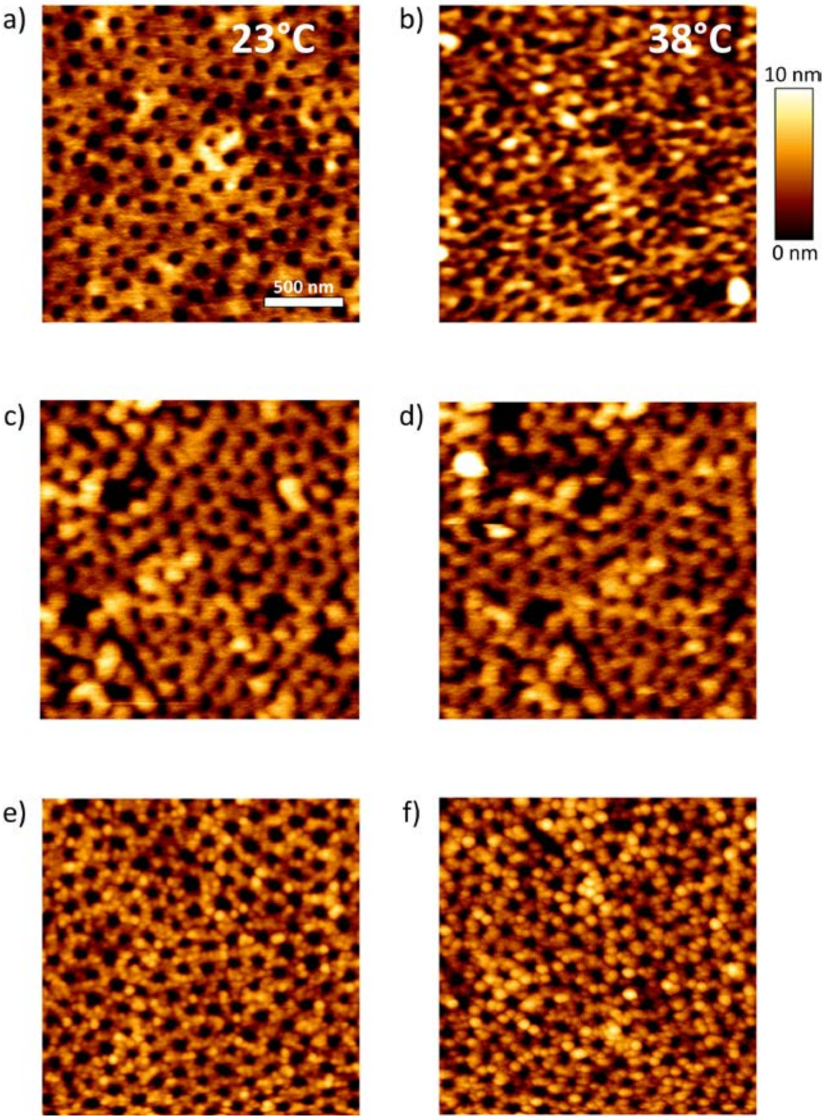

Figure 4.6 2µm x 2µm AFM scans of NSiMs immersed in water and grafted with PNIPAM-COOH 66.4k at **a)** 23°C and **b)** 38°C, PNIPAM-NH2 66k at **c)** 23°C and **d)** 38°C, PNIPAM-NH2 at **e)** 23°C and **f)** 38°C.

Detachment of cells from PNIPAM functionalized NSiMs

PNIPAM based smart surfaces have been used for cell sheet tissue engineering for the treatment of damaged or diseased organs [34–36]. NSiMs grafted with different PNIPAM layers (COOH 66k, NH_2 66k and NH_2 50k) were used in a cell adhesion/detachment experiment to demonstrate the ability of these smart surfaces to be used for cell culture. Functionalized NSiMs were placed in a culture medium during one day in an incubator at 37°C, allowing cells to adhere onto the surface. When the samples in the culture medium were taken out of the incubator, the attachment of the cells onto the surface has been controlled with an optical microscope. Then, after 20 minutes of cooling down to room temperature (23°C), the functionalized NSiMs are again observed at the same place and the cell density compared to the one observed at 37°C. Figure 4.7 a) and b) show the attachment of cells onto a non-functionalized NSiM at 37°C and 23°C, respectively. No major difference is observed in cell density demonstrating that there is no effect of the temperature onto the adhesion of cells onto bare NSiMs. PNIPAM COOH 66k (Figure 4.7 c) and d)) and PNIPAM NH_2 66k (Figure 4.7 e) and f)) demonstrated a good ability to detach the cells from the membrane when lowering the temperature down to 23°C below the LCST of the PNIPAM. The cell density is considerably lowered when the PNIPAM brush layer is in the swollen state allowing the cells to be pulled off the surface. Therefore the responsiveness of these two grafted layers has been demonstrated due to a good compromise between the grafting density and chain length. Whereas the PNIPAM NH_2 50k brush layer (Figure 4.7 g) and h)) could not detach the cells upon temperature variation, with a cell density almost equal at 37°C and 23°C. No responsive behaviour of this polymer could be demonstrated with this experiment due to short chain length. The results obtained with the cell adhesion experiments upon temperature variation correlate the previous results obtained by nano-indentation and AFM analysis in liquid environment demonstrating a good thermo-responsive behaviour of PNIPAM COOH 66k and NH_2 66k brush layers.

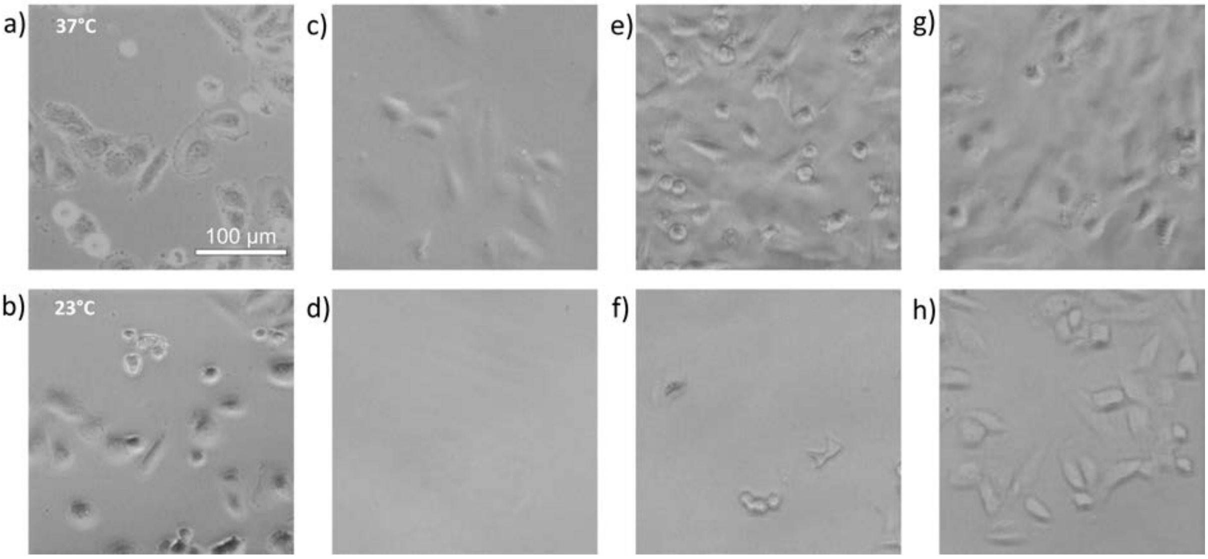

Figure 4.7 Optical microscope images of cells on NSiMs at 37°C and 23°C for **a) b)** bare NSiM, NSiM grafted with **c) d)** PNIPAM-COOH 66k, **e) f)** PNIPAM-NH_2 66k and **g) h)**PNIPAM-NH_2 50k.

4.3. Conclusions

In this chapter was presented the membrane surface modification in terms of pore size reduction using Atomic Layer Deposition (ALD) and by grafting thermo-responsive polymer poly(N-isopropylacrylamide) chains (PNIPAM).

Pore size reduction and induced modification of the surface chemistry of the NSiMs was achieved by depositing in a conformal way Al_2O_3 by Atomic Layer Deposition. The pore size reduction was characterized by Transmission Electron Microscopy (TEM) and the resulting surface chemical composition by X-ray Photoelectron Spectroscopy (XPS). The ability to tune the pore size will allow tuning the cut-off of the NSiMs for size selective molecular separation experiments. This latter will be demonstrated in the next chapter by characterizing the diffusional properties of NSiMs with different mean nanopore size.

The grafting of thermo-responsive PNIPAM brush layers has been achieved by the grafting to in melt technique of different end functionalized PNIPAM (COOH and NH_2). The successful grafting has been confirmed by proceeding to XPS measurements to detect the typical fingerprint of amide groups composing the backbone of the PNIPAM chains. The characteristics of the grafted PNIPAM brush layer (e.g. grafting density, distance between grafting sites, theoretical chain length) were calculated from the ellipsometric measurements of the dry PNIPAM film.

The thermo responsive behavior of the grafted PNIPAM brush layers has been demonstrated by proceeding to in situ nano indentation and AFM imaging in liquid environment. These qualitative experiments allowed visualizing a difference in the nano indentation depth and a change in surface topography upon temperature variation. PNIPAM COOH 66k brush layer demonstrated the best ability to switch from swollen to collapsed state. All the PNIPAM grafted NSiMs (COOH 66k, NH_2 66k and NH_2 50k) were used in cell detachment experiments where only NSiMs functionalized with long chains (COOH 66k and NH_2 66k) were able to detach the cells from the surface when lowering the temperature below the LCST. From these experiments, the stronger conformal morphological change of the brush layer from swollen to collapsed state was observed for PNIPAM COOH 66k and NH_2 66k functionalized NSiMs. Based on these results, only NSiMs functionalized PNIPAM COOH 66k and NH_2 66k will be integrated into a diffusion cell to demonstrate the controlled diffusion of molecules upon temperature variation.

References

[1] B.R. Srijanto, S.T. Retterer, J.D. Fowlkes, M.J. Doktycz, Nanostructured silicon membranes for control of molecular transport, Journal of Vacuum Science & Technology B: Microelectronics and Nanometer Structures. 28 (2010) 48–52.

[2] S.M. George, A.W. Ott, J.W. Klaus, Surface Chemistry for Atomic Layer Growth, The Journal of Physical Chemistry. 100 (1996) 13121–13131.

[3] M. Ritala, M. Leskelä, Atomic layer epitaxy — a valuable tool for nanotechnology ?, Nanotechnology. 10 (1999) 19–24.

[4] M. Leskelä, M. Ritala, Atomic layer deposition (ALD): from precursors to thin film structures, Thin Solid Films. 409 (2002) 138–146.

[5] M. Leskelä, M. Ritala, Atomic layer deposition chemistry: recent developments and future challenges., Angewandte Chemie (International Ed. in English). 42 (2003) 5548–5554.

[6] D. Cassidy, S. Higgins, B.A. McCool, W.J. DeSisto, Atomic Layer Deposition as a Tool to Modify Mesoporous Silica Membranes, ECS Transactions. 16 (2008) 151–157.

[7] D.E. Cassidy, W.J. DeSisto, Atomic Layer Deposition-Modified Ordered Mesoporous Silica Membranes, Chemical Vapor Deposition. 18 (2012) 22–26.

[8] J. Dendooven, K. Devloo-Casier, E. Levrau, R. Van Hove, S.P. Sree, M.R. Baklanov, et al., In situ monitoring of atomic layer deposition in nanoporous thin films using ellipsometric porosimetry., Langmuir : the ACS Journal of Surfaces and Colloids. 28 (2012) 3852–3859.

[9] A.W. Ott, J.W. Klaus, J.M. Johnson, S.M. George, K.C. Mccarley, J.D. Way, Modification of Porous Alumina Membranes Using Al2O3 Atomic Layer Controlled Deposition, Chemistry of Materials. 9 (1997) 707–714.

[10] M. Daub, M. Knez, U. Goesele, K. Nielsch, Ferromagnetic nanotubes by atomic layer deposition in anodic alumina membranes, Journal of Applied Physics. 101 (2007) 09J111.

[11] L. Velleman, G. Triani, P.J. Evans, J.G. Shapter, D. Losic, Structural and chemical modification of porous alumina membranes, Microporous and Mesoporous Materials. 126 (2009) 87–94.

[12] V. Romero, V. Vega, J. García, R. Zierold, K. Nielsch, V.M. Prida, et al., Changes in morphology and ionic transport induced by ALD SiO_2 coating of nanoporous alumina membranes, ACS Applied Materials & Interfaces. 5 (2013) 3556–3564.

[13] R.J. Narayan, S.P. Adiga, M.J. Pellin, L. a Curtiss, A.J. Hryn, S. Stafslien, et al., Atomic layer deposition-based functionalization of materials for medical and environmental health applications., Philosophical Transactions. Series A, Mathematical, Physical, and Engineering Sciences. 368 (2010) 2033–2064.

[14] R.J. Narayan, S.P. Adiga, M.J. Pellin, L. a Curtiss, S. Stafslien, B. Chisholm, et al., Atomic layer deposition of nanoporous biomaterials, Materials Today. 13 (2010) 60–64.

[15] G. Pardon, H.K. Gatty, G. Stemme, W. van der Wijngaart, N. Roxhed, Pt-Al2O3 dual layer atomic layer deposition coating in high aspect ratio nanopores, Nanotechnology. 24 (2013) 015602 (11pp).

[16] F. Li, L. Li, X. Liao, Y. Wang, Precise pore size tuning and surface modifications of polymeric membranes using the atomic layer deposition technique, Journal of Membrane Science. 385-386 (2011) 1–9.

[17] B. a. McCool, W.J. DeSisto, Self-Limited Pore Size Reduction of Mesoporous Silica Membranes via Pyridine-Catalyzed Silicon Dioxide ALD, Chemical Vapor Deposition. 10 (2004) 190–194.

[18] D.E. Koutsonikolas, S.P. Kaldis, G.P. Sakellaropoulos, Pore Size Reduction and Performance Upgrade of Silica Membranes with an Ambient Temperature C-ALD Post-Treatment Method, Separation Science and Technology. 46 (2011) 1414–1418.

[19] S. Jambhrunkar, M. Yu, J. Yang, J. Zhang, A. Shrotri, L. Endo-Munoz, et al., Stepwise pore size reduction of ordered nanoporous silica materials at angstrom precision, Journal of the American Chemical Society. 135 (2013) 8444–8447.

[20] D. Losic, M. a Cole, B. Dollmann, K. Vasilev, H.J. Griesser, Surface modification of nanoporous alumina membranes by plasma polymerization, Nanotechnology. 19 (2008) 245704 (7pp).

[21] M. Barsbay, O. Güven, H. Bessbousse, T.L. Wade, F. Beuneu, M.-C. Clochard, Nanopore size tuning of polymeric membranes using the RAFT-mediated radical polymerization, Journal of Membrane Science. 445 (2013) 135–145.

[22] H. Alem, A.-S. Duwez, P. Lussis, P. Lipnik, A.M. Jonas, S. Demoustier-Champagne, Microstructure and thermo-responsive behavior of poly(N-isopropylacrylamide) brushes grafted in nanopores of track-etched membranes, Journal of Membrane Science. 308 (2008) 75–86.

[23] D. Losic, G. Triani, P.J. Evans, A. Atanacio, J.G. Mitchell, N.H. Voelcker, Controlled pore structure modification of diatoms by atomic layer deposition of TiO2, Journal of Materials Chemistry. 16 (2006) 4029–4034.

[24] B. Jeong, A. Gutowska, Lessons from nature: stimuli-responsive polymers and their biomedical applications., Trends in Biotechnology. 20 (2002) 305–311.

[25] I.Y. Galaev, B. Mattiasson, "Smart" polymers and what they could do in biotechnology and medicine., Trends in Biotechnology. 17 (1999) 335–340.

[26] P. Bawa, V. Pillay, Y.E. Choonara, L.C. du Toit, Stimuli-responsive polymers and their applications in drug delivery., Biomedical Materials. 4 (2009) 022001 (15pp).

[27] A. Kumar, A. Srivastava, I.Y. Galaev, B. Mattiasson, Smart polymers: Physical forms and bioengineering applications, Progress in Polymer Science. 32 (2007) 1205–1237.

[28] C. Wang, R.J. Stewart, J. Kopecek, Hybrid hydrogels assembled from synthetic polymers and coiled-coil protein domains., Nature. 397 (1999) 417–20.

[29] Y. Qiu, K. Park, Environment-sensitive hydrogels for drug delivery., Advanced Drug Delivery Reviews. 53 (2001) 321–39.

[30] D. Schmaljohann, Thermo- and pH-responsive polymers in drug delivery., Advanced Drug Delivery Reviews. 58 (2006) 1655–1670.

[31] T. Shiga, Deformation and Viscoelastic Behavior of Polymer Gels in Electric Fields, Advances in Polymer Science. 134 (1997) 131–163.

[32] A. Mamada, T. Tanaka, D. Kungwatchakun, M. Irief, Photoinduced Phase Transition of Gels, Macromolecules. 23 (1990) 1517–1519.

[33] M. Heskins, J.E. Guillet, Solution Properties of Poly(N-isopropylacrylamide), Journal of Macromolecular Science: Part A - Chemistry. 2 (1968) 1441–1455.

[34] Y. Akiyama, A. Kikuchi, M. Yamato, T. Okano, Ultrathin poly(N-isopropylacrylamide) grafted layer on polystyrene surfaces for cell adhesion/detachment control., Langmuir. 20 (2004) 5506–5511.

[35] H. Takahashi, N. Matsuzaka, M. Nakayama, A. Kikuchi, M. Yamato, T. Okano, Terminally functionalized thermoresponsive polymer brushes for simultaneously promoting cell adhesion and cell sheet harvest, Biomacromolecules. 13 (2012) 253–260.

[36] B. Voit, D. Schmaljohann, S. Gramm, M. Nitschke, C. Werner, Stimuli-responsive polymer layers for advanced cell culture technologies, International Journal of Materials Research. 98 (2007) 646–650.

[37] M. Mueller, M. Tebbe, D. V Andreeva, M. Karg, R.A.A. Puebla, N.P. Perez, et al., Large-Area Organization of pNIPAM-Coated Nanostars as SERS Platforms for Polycyclic Aromatic Hydrocarbons Sensing in Gas Phase, Langmuir. 28 (2012) 9168–9173.

[38] H. Morohashi, T. Nakanoya, H. Iwata, T. Yamauchi, N. Tsubokawa, Novel Contamination and Gas Sensor Materials from Amphiphilic Polymer-Grafted Carbon Black, Polymer Journal. 38 (2006) 548–553.

[39] N.I. Abu-Lail, M. Kaholek, B. LaMattina, R.L. Clark, S. Zauscher, Micro-cantilevers with end-grafted stimulus-responsive polymer brushes for actuation and sensing, Sensors and Actuators B: Chemical. 114 (2006) 371–378.

[40] W. Minghong, B. Bao, J. Chen, Y. Xu, S. Zhou, Z.-T. Ma, Preparation of thermosensitive hydrogel (PP-g-NIPAAm) with one–off switching for controlled release of drugs, Radiation Physics and Chemistry. 56 (1999) 341–346.

[41] G. Jeon, S.Y. Yang, J.K. Kim, Functional nanoporous membranes for drug delivery, Journal of Materials Chemistry. 22 (2012) 14814–14834.

[42] Y.-C. Chen, R. Xie, M. Yang, P.-F. Li, X.-L. Zhu, L.-Y. Chu, Gating Characteristics of Thermo-Responsive Membranes with Grafted Linear and Crosslinked Poly(N-isopropylacrylamide) Gates, Chemical Engineering & Technology. 32 (2009) 622–631.

[43] C. Geismann, F. Tomicki, Separation Science and Technology Block Copolymer Photo-Grafted Poly (Ethylene Terephthalate) Capillary Pore Membranes Distinctly Switchable by Two Different Stimuli, Separation Science and Technology. 44 (2009) 3312–3329.

[44] C.-C. Han, T.-C. Wei, C.-S. Wu, Y.-L. Liu, Temperature-responsive poly(tetrafluoroethylene) membranes grafted with branched poly(N-isopropylacrylamide) chains, Journal of Membrane Science. 358 (2010) 60–66.

[45] J. Huang, X. Wangb, W. Qi, X. Yu, Temperature sensitivity and electrokinetic behavior of a NGsopropylacrylamide grafted microporous polyethylene membrane, Desalination. 146 (2002) 345–351.

[46] J.S. Kim, T.G. Kim, W.H. Kong, T.G. Park, Y.S. Nam, Thermally controlled wettability of a nanoporous membrane grafted with catechol-tethered poly(N-isopropylacrylamide)., Chemical Communications. 48 (2012) 9197–9320.

[47] P.-F. Li, X.-J. Ju, L.-Y. Chu, R. Xie, Thermo-Responsive Membranes with Cross-linked Poly(N-Isopropyl-acrylamide) Hydrogels inside Porous Substrates, Chemical Engineering & Technology. 29 (2006) 1333–1339.

[48] L. Liang, M. Shi, V. V Viswanathan, L.M. Peurrung, J.S. Young, Temperature-sensitive polypropylene membranes prepared by plasma polymerization, Journal of Membrane Science. 177 (2000) 97–108.

[49] I. Lokuge, X. Wang, P.W. Bohn, Temperature-controlled flow switching in nanocapillary array membranes mediated by poly(N-isopropylacrylamide) polymer brushes grafted by atom transfer radical polymerization, Langmuir. 23 (2007) 305–311.

[50] S.J. Lue, J.-J. Hsu, C.-H. Chen, B.-C. Chen, Thermally on–off switching membranes of poly(N-isopropylacrylamide) immobilized in track-etched polycarbonate films, Journal of Membrane Science. 301 (2007) 142–150.

[51] Y.S. Park, Y. Ito, Y. Imanishi, Permeation Control through Porous Membranes Immobilized with Thermosensitive Polymer, Langmuir. 14 (1998) 910–914.

[52] A.M. Popa, S. Angeloni, T. Bürgi, J. a Hubbell, H. Heinzelmann, R. Pugin, Dynamic perspective on the function of thermoresponsive nanopores from in situ AFM and ATR-IR investigations., Langmuir. 26 (2010) 15356–15365.

[53] W. Song, F. Xia, Y. Bai, F. Liu, T. Sun, L. Jiang, Controllable water permeation on a poly(N-isopropylacrylamide)-modified nanostructured copper mesh film., Langmuir. 23 (2007) 327–331.

[54] R. Spohr, N. Reber, A. Wolf, G.M. Alder, V. Ang, C.L. Bashford, et al., Thermal control of drug release by a responsive ion track membrane observed by radio tracer flow dialysis., Journal of Controlled Release. 50 (1998) 1–11.

[55] W.C. Wang, G.T. Ong, S.L. Lim, R.H. Vora, E.T. Kang, K.G. Neoh, Synthesis and Characterization of Fluorinated Polyimide with Grafted Poly(N -isopropylacrylamide) Side Chains and the Temperature-Sensitive Microfiltration Membranes, Industrial & Engineering Chemistry Research. 42 (2003) 3740–3749.

[56] X. Wang, J. Huang, X. Chen, X. Yu, Graft polymerization of N-isopropylacrylamide into a microporous polyethylene membrane by the plasma method : technique and morphology, Desalination. 146 (2002) 337–343.

[57] B. Yang, W. Yang, Thermo-sensitive switching membranes regulated by pore-covering polymer brushes, Journal of Membrane Science. 218 (2003) 247–255.

[58] L. Ying, E.T. Kang, K.G. Neoh, K. Kato, H. Iwata, Drug permeation through temperature-sensitive membranes prepared from poly(vinylidene fluoride) with grafted poly(N-isopropylacrylamide) chains, Journal of Membrane Science. 243 (2004) 253–262.

[59] X. Cheng, H.E. Canavan, M.J. Stein, J.R. Hull, S.J. Kweskin, M.S. Wagner, et al., Surface chemical and mechanical properties of plasma-polymerized N-isopropylacrylamide., Langmuir : the ACS Journal of Surfaces and Colloids. 21 (2005) 7833–41.

[60] D. Schmaljohann, D. Beyerlein, M. Nitschke, C. Werner, Thermo-reversible swelling of thin hydrogel films immobilized by low-pressure plasma., Langmuir : the ACS Journal of Surfaces and Colloids. 20 (2004) 10107–14.

[61] A. Brooks, S. Woollard, G. Hennighan, T. von Werne, PLASMA POLYMERIZATION : A VERSATILE AND ATTRACTIVE PROCESS FOR CONFORMAL COATING, in: SMTA International Conference Proceedings, 2012: pp. 1–6.

[62] B.D.M. Jones, J.R. Smith, W.T.S. Huck, C. Alexander, Variable Adhesion of Micropatterned Thermoresponsive Polymer Brushes: AFM Investigations of Poly(N-isopropylacrylamide) Brushes Prepared by Surface-Initiated Polymerizations, Advanced Materials. 14 (2002) 1130–1134.

[63] M. Kaholek, W. Lee, S. Ahn, H. Ma, K.C. Caster, B. Lamattina, et al., Brushes and Nanopatterns Prepared by Surface-Initiated Polymerization, Chemistry of Materials. 16 (2004) 3688–3696.

[64] M. Mitsuishi, Y. Koishikawa, H. Tanaka, E. Sato, T. Mikayama, J. Matsui, et al., Nanoscale actuation of thermoreversible polymer brushes coupled with localized surface plasmon resonance of gold nanoparticles., Langmuir. 23 (2007) 7472–7474.

[65] K.N. Plunkett, X. Zhu, J.S. Moore, D.E. Leckband, PNIPAM chain collapse depends on the molecular weight and grafting density., Langmuir. 22 (2006) 4259–4266.

[66] T. Sun, W. Song, L. Jiang, Control over the responsive wettability of poly(N-isopropylacrylamide) film in a large extent by introducing an irresponsive molecule., Chemical Communications. (2005) 1723–1725.

[67] F.J. Xu, S.P. Zhong, L.Y.L. Yung, E.T. Kang, K.G. Neoh, Hybrids from Surface-Initiated Atom Transfer Radical Polymerization for Control of Cell Adhesion, Biomacromolecules. 5 (2004) 2392–2403.

[68] I. Luzinov, D. Julthongpiput, H. Malz, J. Pionteck, V. V. Tsukruk, Polystyrene Layers Grafted to Epoxy-Modified Silicon Surfaces, Macromolecules. 33 (2000) 1043–1048.

[69] F. Montagne, J. Polesel-Maris, R. Pugin, H. Heinzelmann, Poly(N-isopropylacrylamide) thin films densely grafted onto gold surface: preparation, characterization, and dynamic AFM study of temperature-induced chain conformational changes., Langmuir. 25 (2009) 983–991.

[70] E. Bittrich, S. Burkert, M. Müller, K.-J. Eichhorn, M. Stamm, P. Uhlmann, Temperature-sensitive swelling of poly(N-isopropylacrylamide) brushes with low molecular weight and grafting density, Langmuir. 28 (2012) 3439–3448.

[71] H. Yim, M.S. Kent, S. Mendez, G.P. Lopez, S. Satija, Y. Seo, Effects of Grafting Density and Molecular Weight on the Temperature-Dependent Conformational Change of Poly(N -isopropylacrylamide) Grafted Chains in Water, Macromolecules. 39 (2006) 3420–3426.

[72] H. Ma, L. Fu, W. Li, Y. Zhang, M. Li, Real-time measurement of the mass of water expelled by poly(N-isopropylacrylamide) brushes upon thermo-induced collapse., Chemical Communications. (2009) 3428–3430.

[73] S. Balamurugan, S. Mendez, S.S. Balamurugan, M.J. O'Brien II, G.P. Lopez, Thermal Response of Poly (N-isopropylacrylamide) Brushes Probed by Surface Plasmon Resonance., Langmuir. 19 (2003) 2545–2549.

[74] H. Yim, M.S. Kent, D.L. Huber, S. Satija, J. Majewski, G.S. Smith, Conformation of End-Tethered PNIPAM Chains in Water and in Acetone by Neutron Reflectivity, Macromolecules. 36 (2003) 5244–5251.

[75] V. Kurz, M. Grunze, P. Koelsch, In situ characterization of thermo-responsive poly(N-isopropylacrylamide) films with sum-frequency generation spectroscopy., Chemphyschem : a European Journal of Chemical Physics and Physical Chemistry. 11 (2010) 1425–1429.

[76] S. Kidoaki, S. Ohya, Y. Nakayama, T. Matsuda, Thermoresponsive Structural Change of a Poly (N-isopropylacrylamide) Graft Layer Measured with an Atomic Force Microscope, Langmuir. 17 (2001) 2402–2407.

[77] M. Callewaert, C. Grandfils, L. Boulangé-Petermann, P.G. Rouxhet, Adsorption of poly(N-isopropylacrylamide) on glass substrata., Journal of Colloid and Interface Science. 276 (2004) 299–305.

[78] N. Ishida, M. Kobayashi, Interaction forces measured between poly(N-isopropylacrylamide) grafted surface and hydrophobic particle., Journal of Colloid and Interface Science. 297 (2006) 513–519.

[79] Y. Katsumoto, T. Tanaka, H. Sato, Y. Ozaki, Conformational Change of Poly(N -isopropylacrylamide) during the Coil−Globule Transition Investigated by Attenuated Total Reflection/Infrared Spectroscopy and Density Functional Theory Calculation., The Journal of Physical Chemistry A. 106 (2002) 3429–3435.

[80] V.S. Shinde, M.R. Girme, V.U. Pawar, Thermoresponsive polystyrene-b-poly (N-isopropylacrylamide) copolymers by atom transfer radical polymerization, Indian Journal of Chemistry. 50A (2011) 781–787.

[81] H. Tu, C.E. Heitzman, P. V Braun, Patterned poly(N-isopropylacrylamide) brushes on silica surfaces by microcontact printing followed by surface-initiated polymerization., Langmuir. 20 (2004) 8313–8320.

[82] W. Lee, M. Chun, K. Cheong, K. Park, C.O. Park, G. Cao, et al., Characteristics of SiO 2 Film Grown by Atomic Layer Deposition as the Gate Insulator of Low-Temperature Polysilicon Thin-Film Transistors, Solide State Phenomena. 124-126 (2007) 247–250.

[83] S. Minko, S. Patil, V. Datsyuk, F. Simon, K. Eichhorn, M. Motornov, et al., Synthesis of Adaptive Polymer Brushes via " Grafting To " Approach from Melt, Langmuir. 18 (2005) 289–296.

[84] B. Zdyrko, V. Klep, I. Luzinov, Synthesis and Surface Morphology of High-Density Poly (ethylene glycol) Grafted Layers, Langmuir. 19 (2003) 10179–10187.

[85] A. Ourmazd, D.W. Taylor, J. Bevk, B.A. Davidson, L.C. Feldman, J.P. Mannaerts, Observation of (5x5) Surface Reconstruction on Pure Silicon and its Stability Against Native-Oxide Formation, Physical Review Letters. 57 (1986) 1332–1335.

[86] M.W. Daniels, J. Sefcik, L.F. Francis, A. V. McCormick, Reactions of a Trifunctional Silane Coupling Agent in the Presence of Colloidal Silica Sols in Polar Media., Journal of Colloid and Interface Science. 219 (1999) 351–356.

[87] H. Yim, M.S. Kent, S. Mendez, S.S. Balamurugan, S. Balamurugan, G.P. Lopez, et al., Temperature-Dependent Conformational Change of PNIPAM Grafted Chains at High Surface Density in Water, Macromolecules. 37 (2004) 1994–1997.

[88] X. Zhu, C. Yan, F.M. Winnik, D. Leckband, End-grafted low-molecular-weight PNIPAM does not collapse above the LCST., Langmuir. 23 (2007) 162–169.

[89] N. Ishida, S. Biggs, Direct observation of the phase transition for a poly(N-isopropylacryamide) layer grafted onto a solid surface by AFM and QCM-D., Langmuir. 23 (2007) 11083–11088.

[90] S. Alexander, Adorption of chain molecules with a polar head a scaling description, Journal De Physique. 38 (1977) 983–987.

[91] P.G. de Gennes, Polymers at an interface; a simplified view., Advances in Colloid and Interface Science. 27 (1987) 189–209.

[92] B.J. Briscoe, L. Fiori, E. Pelillo, Nano-indentation of polymeric surfaces, Journal of Physics D: Applied Physics. 31 (1998) 2395–2405.

[93] A.M. Popa, Stimuli-responsive nanostructured surfaces, Ecole Polytechnique Fédérale de Lausanne, 2009.

Chapter 5

Evaluation of Molecular Transport Properties of NSiMs

Abstract

In this chapter the NSiMs will be integrated into a specifically designed diffusion device and the molecular transport properties of modified NSiMs will be studied.

First, the ability to tune the molecular transport properties of NSiMs with the pore size reduction technique described earlier will be demonstrated. The diffusion coefficient of fluoerescein molecules across NSiMs with different mean pore size will be measured and the results discussed. Size-based separation experiments using fluorescein-isothiocyanate-dextrans (FITC-dextrans) of different molecular weights will be conducted to demonstrate the ability to perform precise size-based filtration experiments with NSiMs.

Second, PNIPAM COOH 66k and PNIPAM NH_2 *66k NSiMs modified with the grafting protocol described in the previous chapter will be used in molecular transport experiments. The reversibility and reproducibility of the thermo-responsive behaviour of the PNIPAM modified NSiMs for the controlled diffusion of vitamin B12 molecules will be demonstrated.*

Finally, diffusion experiments with FITC-dextrans of different molecular weights across PNIPAM-COOH 66k modified NSiM will be conducted. These experiments will allow determining the cut-off value of the membranes below the lower critical solution temperature when the nanopores are supposedly closed. The temperature-controlled nanovalve behaviour (ON-OFF) will be demonstrated for molecules with a hydrodynamic radius superior to 3 nm.

5.1. Molecular transport through NSiMs with different pore size

The main goal of these experiments was to show the ability to tune the molecular transport properties of NSiMs using the pore size reduction (PSR) technique. This latter has been demonstrated by measuring the variation in the diffusion coefficient of fluorescein molecules across NSiMs with different mean pore size. Diffusion experiments were carried out using a specifically designed polycarbonate fluidic cell composed of a donor (D) and an acceptor (A) chamber (Figure 5.1). After proceeding to the PSR and characterization using Transmission Electron Microscopy (TEM) analysis, the NSiMs with different mean pore size are sealed in between the two chambers. In all the diffusion experiments, only the steric hindrance (contribution of the pore geometry and the size of the molecules) of both the non-functionalized and functionalized nanopores will be discussed. All the electrostatic interactions due to both the surface and molecule charges will not be considered.

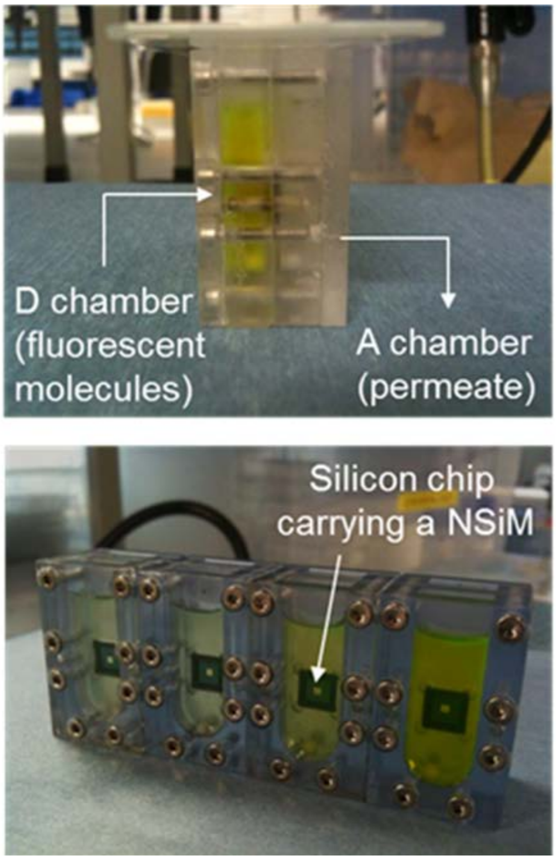

Figure 5.1 Specifically designed polycarbonate fluidic cell for diffusion experiments.

The diffusion coefficient of a solute across a flat membrane can be calculated using an equation derived from Fick's first law of diffusion. Fick's first law of diffusion described in Eq. 5.1 states that the diffusion rate of substance dm/dt in moles per unit of time, is proportional to the surface area of diffusion A in m^2, the diffusion coefficient D in m^2/s and the concentration gradient which is the rate of change in the concentration c with distance x in an isotropic medium [1].

$$\frac{dm}{dt} = -DA\frac{dc}{dx} \qquad (5.1)$$

Applying this law to our system for the transport of molecules from the donor to the acceptor chamber through the NSiM we can write Eq. 5.2 where V_a and C_a are the volume and the concentration in the acceptor chamber, respectively; X is the membrane thickness, A the nanoporous area, D the apparent diffusion coefficient and ΔC the difference between C_a and C_d being the concentration between the acceptor and donor chamber, respectively (Eq. 5.3).

$$V_a\frac{dC_a}{dt} = -DA\frac{\Delta C}{X} \qquad (5.2)$$

$$\Delta C = C_a - C_d \qquad (5.3)$$

Since only the intermediary concentration in the acceptor chamber C_a is monitored, it is necessary to express the gradient of concentration ΔC as a function of C_a and C_i (being the concentration in the acceptor chamber and the initial concentration in the donor chamber, respectively), V_a and V_d (being the volume in the acceptor and donor chambers, respectively) only. To do so we can write Eq. 5.4 and use it with Eq. 5.3 to obtain Eq. 5.5.

$$C_iV_d = C_dV_d + C_aV_a \qquad (5.4)$$

$$\Delta C = C_a\left(1+\frac{V_a}{V_d}\right) - C_i \qquad (5.5)$$

ΔC in Eq. 5.2 can now be replaced with Eq. 5.5 to obtain the following expression (Eq .5.6):

$$dt = -\frac{X}{DA} Va \frac{1}{C_a\left(1+\frac{V_a}{V_d}\right)-C_i} dCa \qquad (5.6)$$

This resulting expression can now be integrated (Eq. 5.7) and the diffusion coefficient can now be extracted and expressed as written in Eq. 5.8, with C_{ta} the intermediary concentration at time t in the acceptor chamber. A similar equation has been used in previous diffusion and permeation experiments to calculate the diffusion coefficient [2–6].

$$\int_0^t dt = -\frac{X}{DA} V_a \int_0^{C_{ta}} \frac{1}{C_a\left(1+\frac{V_a}{V_d}\right)-C_i} dC_a \qquad (5.7)$$

$$D = -XV_d \frac{1}{A}\frac{1}{t}\frac{1}{1+\frac{V_d}{V_a}} \ln\left[1-\frac{C_{ta}}{C_i}\left(1+\frac{V_a}{V_d}\right)\right] \qquad (5.8)$$

In all the diffusion experiments, plots of $-1/(1+V_d/V_a)\ln[1-(C_{ta}/C_i)(1+V_a/V_d)]$ versus t (from Eq. 5.8) show a straight line. The slopes K of these plots are used to calculate the diffusion coefficient using Eq. 5.9.

$$D = K\frac{XV_d}{A} \qquad (5.9)$$

5.1.1 Experimental

Materials

NSiMs with different mean pore diameter achieved with the pore size reduction technique will be used for diffusion experiments. Fluorescein sodium molecules were purchased from Sigma-Aldrich (Switzerland). Fluorescein-isothiocyanate coupled to dextran polymers of various molecular weights (4’000, 10’000, 20’000 and 40’000 g/mol referred as FITC-dextran 4k, 10k, 20k and 40k respectively) were purchased from TdB Consultancy (Sweden). Deionized water (18.2 MΩ, Milli-Q, Millipore) was used throughout the experiments.

Molecular transport across NSiMs

Diffusion experiments were carried out using a polycarbonate fluidic cell composed of a donor (D) and an acceptor (A) chambers. In brief, the NSiM is sealed between the two chambers. The chamber D is filled with 1mL of a concentrated solution of the chosen-analyte in water and A is filled with 1mL water and both chambers are stirred continuously. The initial concentrations were set at 0.5 mmol/L for fluorescein sodium, FITC-dextran 4k, 10k, 20k and 40k. The effective area of diffusion is 1 mm^2. The transport rate and the diffusion coefficient of fluorescein and FITC-dextrans molecules across the modified NSiMs are obtained by monitoring the increase of the fluorescent signal *versus* time in the acceptor chamber with a monochromator spectrophotometer (TECAN Infinite M200, Switzerland) with the excitation wavelength set at 480 and 493 nm for fluorescein molecules and FITC-dextrans, respectively. Calibration curves were constructed for each molecule using a series of standard solutions with different known concentrations in order to obtain a correlation between the normalized fluorescent signal and the concentration. The emission wavelength is set at 520 nm for all molecules. The diffusion coefficient is deduced from these measurements using an equation derived from Fick’s first law of diffusion (Eq. 5.8).

5.1.2 Results and Discussion

Variation of the diffusion coefficient as a function of the mean pore size

The concentration gradient in these experiments is the driving parameter creating a flux of water molecules down the gradient. The magnitude of this flux depends both on the magnitude of the concentration gradient and the diffusive properties of the NSiMs represented by the diffusion coefficient *D*. The NSiMs were submitted to the pore size reduction technique (described in the previous chapter), with a conformal deposition of material at the nanometer scale. NSiMs with different mean pore size were used in diffusion experiments described in the experimental section. Figure 5.2 shows the measured diffusion coefficient of fluorescein sodium molecules (hydrodynamic radius of 0.5 nm) across the different NSiMs. The diffusion coefficient evolves linearly with the mean pore size, from D=2.63.10^{-13} to 1.52.10^{-12} m^2/s in average for a mean pore size of 10 nm and 90 nm, respectively. The values obtained for the diffusion coefficient are comparable to what can be found in the literature for commercially available nanoporous silicon membranes with mean pore sizes equivalent to the ones of our NSiMs [7].

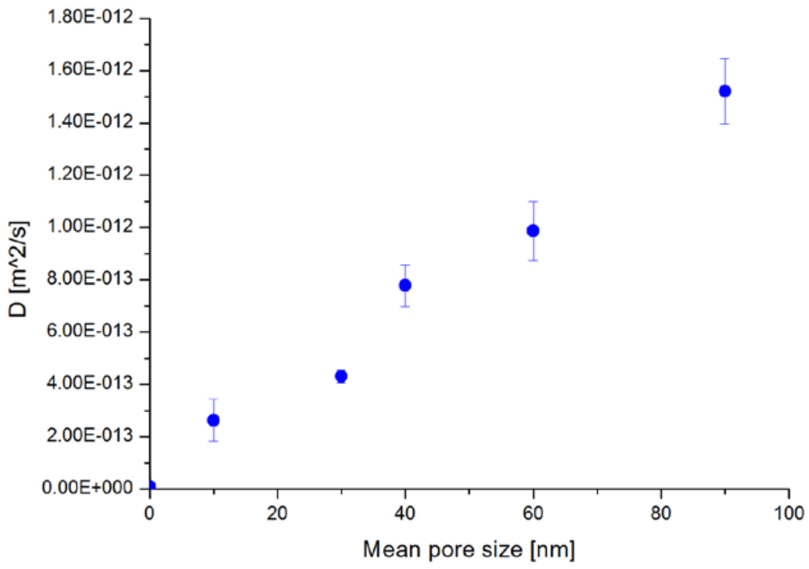

Figure 5.2 Diffusion coefficients of fluorescein sodium molecules across NSiMs with different mean pore size and thickness obtained with the pore size reduction technique.

The decrease in the diffusion coefficient of fluorescein sodium molecules across NSiMs with the decrease of the mean pore size can be explained by the effect of solute size on the rate of penetration through pores expressed by the well-known Renkin Equation (Eq. 5.10). In the Renkin equation the first term represents the exclusion of solute from the pores of the membrane based on geometrical considerations; the second term represents the additional hydrodynamic drag of the solute molecules due to the proximity of the pore walls [8–11]. The Renkin equation is representative of steric interactions only between the molecules and the nanopores. R_s/R_p is the ratio of the solute hydrodynamic radius to nanopore radius, D_m/D_0 is the ratio of the diffusion coefficient inside the porous channel and the free diffusion coefficient of the same solute calculated with the Stoke-Einstein equation (Eq. 5 .11) function of k_B the Boltzmann's constant, T the absolute temperature, μ_{H2O} the viscosity of water and r_s the Stokes-Einstein radius of the molecule [3,12,13].

$$\frac{D_m}{D_0} = \left(1 - \frac{R_s}{R_p}\right)^2 \left[1 - 2.10\left(\frac{R_s}{R_p}\right) + 2.09\left(\frac{R_s}{R_p}\right)^3 - 0.95\left(\frac{R_s}{R_p}\right)^5\right] \qquad (5.10)$$

$$D_0 = \frac{k_B T}{6\pi\mu_{H_20} r_s} \qquad (5.11)$$

In our case, the values obtained could not be properly fitted with the Renkin equation because the value obtained for the diffusion coefficient are considerably small due to both the steric hindrance of the pores and the electrostatic hindrance due to the charges involved between the molecules transported and the pore walls [14]. A common technique used to screen the long range electrostatic interactions is to conduct the diffusion experiments in a solution of high ionic strength (e.g. 0.1 M NaCl) [15]. In this thesis the influence of the electrostatic interactions between the molecules and the pore walls were not considered but can be the main topic of further investigations regarding the surface functionalization chemistry that can influence positively or negatively the diffusion of molecules regarding the length of the electric double layer [16].

Size-based filtration with NSiMs with a mean pore diameter of 10 nm

NSiMs with a minimum mean pore size of 10 nm in diameter achieved by PSR were used in diffusion experiments in order to demonstrate the ability of these NSiMs to be used in size-based filtration experiments. This mean pore size was the minimum achievable before the clogging of most of the nanopores due to their wide size distribution before pore size reduction. Dextran molecules are forming globular shape structures when dissolved in water with a hydrodynamic radius depending on the molecular weight. Fluorescein sodium, FITC-dextrans 4k, 10k, 20k, 40k with hydrodynamic radii (r_h) of 0.5 nm, 1.4 nm, 2.4 nm, 3.3 nm and 4.5 nm, respectively (values given by the provider), are used in size-based filtration experiments. As expected, results shown in Figure 5.3 reveal that the molecular transport across nanoporous membrane is highly dependent on the size of the analyte. Fluorescein sodium molecules (r_s = 0.5nm) are diffusing rapidly across the NSiMs with a mean pore diameter of 10 nm, whereas the diffusion of FITC-dextrans 4k, 10k and 20k (r_s = 1.4 nm, 2.4 nm and 3.3 nm) is much slower and almost completely hindered for FITC-dextrans 40k (r_s = 4.5nm). The slopes of these curves give an indication on the transport rate of each molecule across the modified NSiM. Selectivities of ~ 3 and ~ 17 have been calculated between the diffusion rate of FITC-dextran 10k/fluorescein sodium molecules and FITC-dectran 40k/fluorescein sodium molecules.

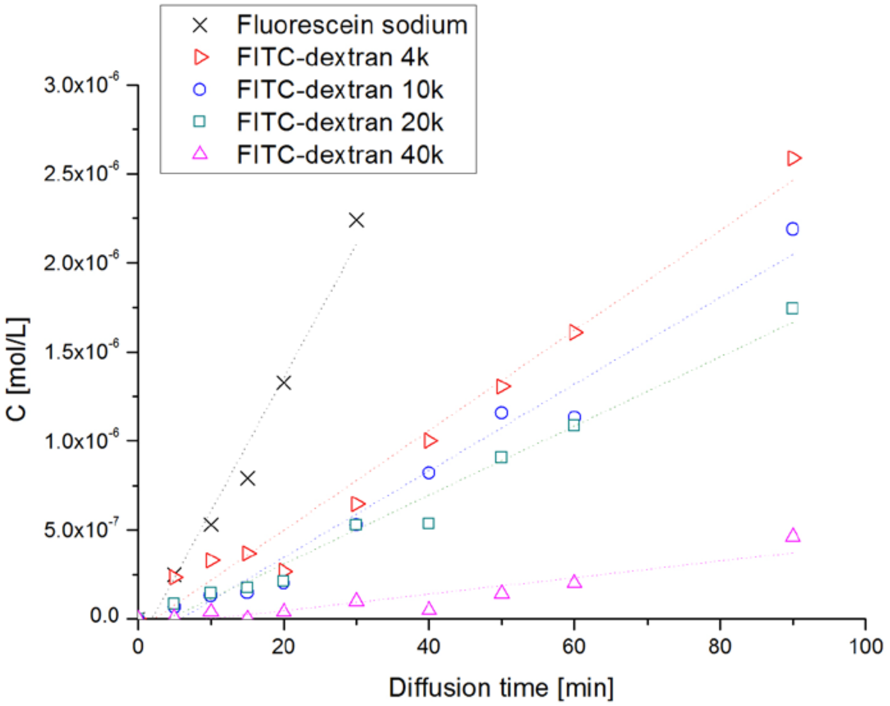

Figure 5.3 Size-based separation of fluorescein sodium, FITC-dextrans using NSiMs with a mean pore size of 10 nm in diameter. Plots show the evolution of the concentration in the acceptor chamber *versus* time for fluorescein sodium, FITC-dextrans 4k, 10k, 20k and 40k (hydrodynamic radii of 0.5nm, 1.4 nm, 2.4 nm, 3.3 nm, 4.5 nm, respectively).

The hindered diffusion of FITC-dextran 40k, with a hydrodynamic radius close to the mean pore radius of the NSiM, becomes more obvious when the diffusion coefficient is measured. Table 5.1 shows a summary of the values of the self-diffusion coefficient D_0 of each molecule calculated with the Stoke-Einstein equation (Eq. 5.11) and the measured diffusion coefficient D of each molecule across the modified NSiM. The ratios $S_{0,molecule}$ of the self-diffusion coefficient of the smallest molecule used (fluorescein) over the self-diffusion coefficents of FITC-dextrans 4k, 10k, 20k and 40k were calculated (Eq. 5.12); and the ratios $S_{molecule}$ of the measured diffusion coefficient of the smallest molecule over the measured diffusion coefficient of FITC-dextrans 4k, 10k, 20k and 40k across NSiMs are also shown (Eq. 5.13).

$$S_{0,molecule} = \frac{D_{0,fluorescein}}{D_{0,molecule}} \qquad (5.12)$$

$$S_{molecule} = \frac{D_{fluorescein}}{D_{molecule}} \qquad (5.13)$$

Table 5.1 Summary of the self-diffusion coefficient and measured diffusion coefficient of fluorescein sodium, FITC-dextrans 4k, 10k, 20k, 40k molecules.

Molecule	r_h *nm*	D_0 *(x10^{-10}) m^2/s*	$S_{0,molecule}$	***D*** *(x10^{-13}) m^2/s*	$S_{molecule}$
Fluorescein	0.5	4.05	1	2.50	1
FITC-dextran 4k	1.4	1.45	2.80	0.96	2.62
FITC-dextran 10k	2.4	1.07	3.80	0.80	3.14
FITC-dextran 20k	3.3	0.81	5	0.61	4.12
FITC-dextran 40k	4.5	0.45	8.99	0.09	27.78

The ratios $S_{molecule}$ are sensibly equal to the ratios $S_{0,molecule}$ for FITC-dextrans 4k, 10k and 20k showing no particular hindered diffusion of these molecules across the membrane. Whereas for FITC-dextran 40k, $S_{FITC\text{-}dextran\ 40k}$ is 3 fold larger than $S_{0,\ FITC\text{-}dextran\ 40k}$ demonstrating an effective blocking of analytes with a hydrodynamic radius close to the mean pore radius (5 nm).

5.2. Molecular transport across PNIPAM functionalized NSiMs

The reversibility and reproducibility of the thermo-responsive behavior of the PNIPAM modified NSiMs for the controlled diffusion of vitamin B12 molecules will be demonstrated integrating PNIPAM COOH 66k and PNIPAM NH_2 66k grafted NSiMs into the specifically designed diffusion cell and performing the experiments in temperature-controlled water bath. The "nano-valve" behaviour for the controlled diffusion of molecules using PNIPAM COOH 66k grafted NSiMs will also be demonstrated using FITC-dextrans of various molecular weights.

5.2.1 Experimental

Materials

PNIPAM COOH 66k and PNIPAM NH_2 66k grafted NSiMs according to the grafting protocol described in the previous chapter will be used. Vitamin B12 molecules (α-(5,6-Dimethylbenzimidazolyl)cyanocobamide with a molecular weight of 1355 g/mol) were purchased from Sigma-Aldrich (Switzerland). Vitamin B12 was selected for diffusion experiments because of the small molecule size (hydrodynamic radius r_h = 0.85 nm) and because it has been demonstrated that these molecules do not affect the responsiveness of PNIPAM brush layers [5,17] Fluorescein-isothiocyanate coupled to dextran polymers of various molecular weights (10'000, 20'000, 40'000 and 70'000 g/mol referred as FITC-dextran 10k, 20k, 40k and 70k, respectively) were purchased from TdB Consultancy (Sweden). Deionized water (18.2 MΩ, Milli-Q, Millipore) was used throughout the experiments.

Molecular transport across PNIPAM functionalized NSiMs

Diffusion experiments were carried out using the diffusion cell described earlier. The whole system integrating PNIPAM grated NSiMs is placed in a temperature-controlled water bath and both chambers are stirred continuously, a temperature probe is placed in the donor chamber to control and regulate the temperature. The initial concentrations were set at 5g/L (3.7 mmol/L) for vitamin B12, 16.7 g/L (1.67 mmol/L) for FITC-dextran 10k, 4g/L (0.1 mmol/L) for FITC-dextran 20k and 5g/L (0.07 mmol/L) for FITC-dextran 40k. The effective area of diffusion is 1 mm^2. The transport rate and the diffusion coefficient of vitamin B12 across the functionalized NSiM is obtained by monitoring the increase of the absorbance signal *versus* time in the acceptor chamber with a monochromator spectrophotometer (TECAN Infinite M200, Switzerland) at λ = 362 nm. For the fluorescent molecules FITC-dextran, the fluorescent signal *versus* time in the acceptor chamber is measured with the same spectrophotometer TECAN Infinite M200 in fluorescence mode with the excitation wavelength set at 493 nm and the emission wavelength set at 520 nm. Calibration curves were constructed for each molecule using a series of standard solutions with different known concentrations in order to obtain a correlation between the normalized fluorescent signal and the concentration. The diffusion coefficient is deduced from these measurements using Fick's first law of diffusion.

5.2.2 Results and discussion

To quantitatively characterize the thermo-responsive permeability of the membranes, Li et al. described the thermo-response factor (Eq. 5.14) of a membrane as the ratio of the diffusion coefficient of a molecule across the membrane at a high temperature to the diffusion coefficient of the same molecule at a low temperature [2] (in the case of this study 50°C and 18°C, respectively).

$$R = \frac{D_{50}}{D_{18}} \qquad (5.14)$$

According to Chu et al. the obstruction constant ($k_{m,T}$) of a nanoporous membrane (Eq. 5.15) can be defined as the ratio of the diffusion coefficient of a molecule across the membrane at a given temperature (D_T) to the self-diffusion coefficient of the same molecule at the same temperature ($D_{0,T}$) [3]. Using this parameter allows for the comparison of the diffusional properties of NSiMs before and after grafting, while excluding the effect of the variations of the diffusion coefficient due to the temperature. In order to calculate the obstruction constant, the self-diffusion coefficient of a molecule depending on the temperature is calculated using the Stokes-Einstein equation and the viscosity of the medium at a given temperature. Eq. 5.16 describes the viscosity of the liquid medium (water) as a function of the temperature, having a direct influence on the self-diffusion coefficient of small molecules calculated with Eq. 5.11 [18,19]. Parameters A,B and C are constants found in the literature [20] with A=2.414x10^{-5} [Pa.s], B=247.8 [K] and C=140 [K].

$$k_{m,T} = \frac{D_T}{D_{0,T}} \qquad (5.15)$$

$$\mu_{H_2O} = A \times 10^{\frac{B}{T-C}} \qquad (5.16)$$

As mentioned earlier, in all the diffusion experiments, the slopes K of the plots of $-1/(1+V_d/V_a)\ln[1-(C_{ta}/C_i)(1+V_a/V_d)]$ versus t (from Eq. 5.8) for different temperatures were used to calculate the diffusion coefficient.

In Figure 5.4 plots of $-1/(1+V_d/V_a)\ln[1-(C_{ta}/C_i)(1+V_a/V_d)]$ versus time for the diffusion of vitamin B12 at different temperature across a non-functionalized NSiM are shown. The plots start at *t=300* seconds which corresponds to the time needed for the diffusion cell and the solute to reach stability. Figure 5.5 shows the average diffusion coefficient of vitamin B12 across a non-functionalized NSiM at different temperatures.

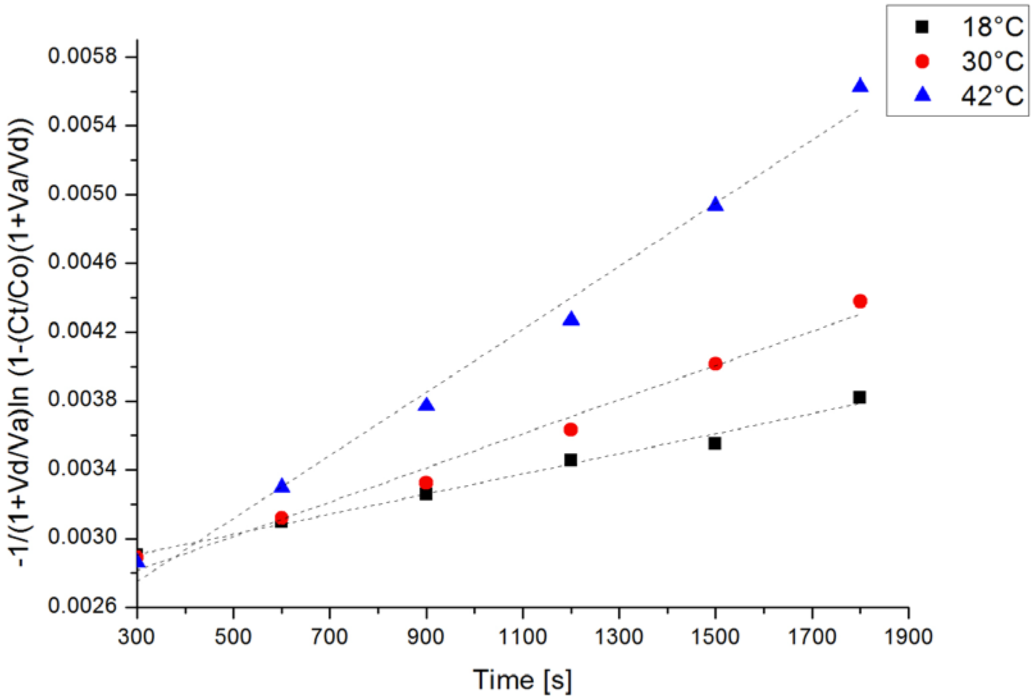

Figure 5.4 Vitamin B12 release plots of $-1/(1+V_d/V_a)\ln[1-(C_{ta}/C_i)(1+V_a/V_d)]$ versus time at different temperatures for a non-functionalized NSiM.

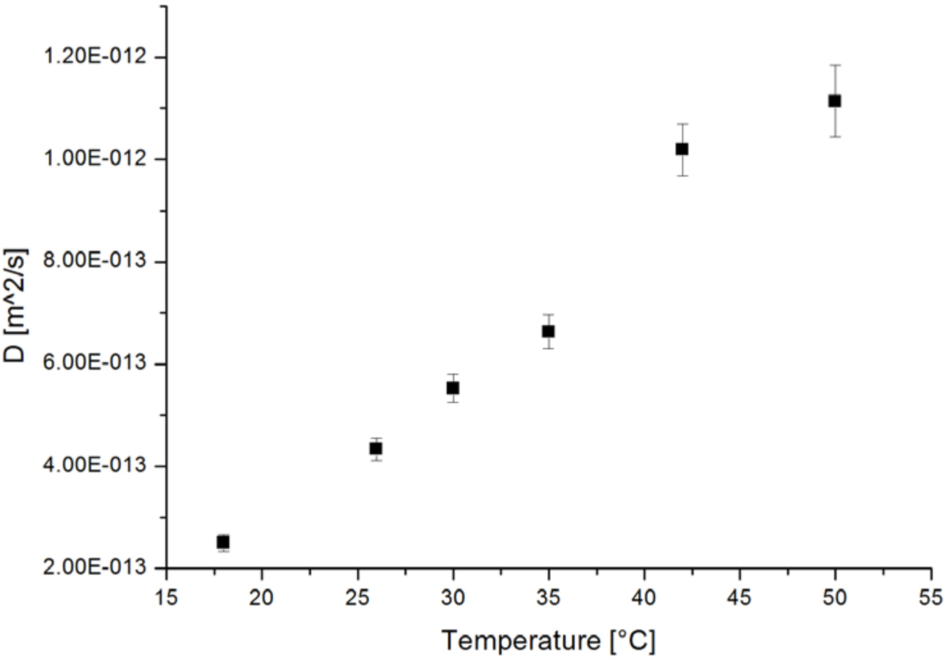

Figure 5.5 Thermo-responsive release of vitamin B12 for a non-functionalized NSiM with a mean pore size of 85 ± 15nm.

For the virgin NSiM (uncoated), a thermo-response factor of R_{virgin}=4.44 has been calculated. The obstruction constants of a non-coated NSiM at 18°C and 50°C were calculated to be of $k_{m,18}$=0.00105 and $k_{m,50}$=0.0022, respectively, demonstrating that the diffusion of molecules across bare NSiMs is less hindered at high temperatures because the self-diffusion coefficient of molecules inside the nanopores is increased. These values were used as reference to characterize the influence of the PNIPAM brush layers grafted onto the NSiMs during the diffusion of vitamin B12 molecules.

Figure 5.6 shows the thermo-responsive release of vitamin B12 across PNIPAM COOH 66k functionalized NSiM. The average thermo-response factor calculated from the four cold/hot cycles performed with the same membrane is R=8.46, significantly higher than the same factor for a virgin membrane. The average obstruction constants for the PNIPAM COOH 66k functionalized NSiM at 18 and 50°C are $k_{m,18}$=0.00063 and $k_{m,50}$=0.00223, respectively. The diffusion is slowed below the LCST, but not completely stopped. Indeed, the extended brushes of PNIPAM slow the diffusion of small molecules such as vitamin B12 but do not entirely stop it. Whereas above the LCST, the diffusion coefficient measured (at 50°C) is almost equal to the one of a non-functionalized NSiM, demonstrating that the collapsed PNIPAM brush layer occurs efficiently and do not slow the diffusion of molecules.

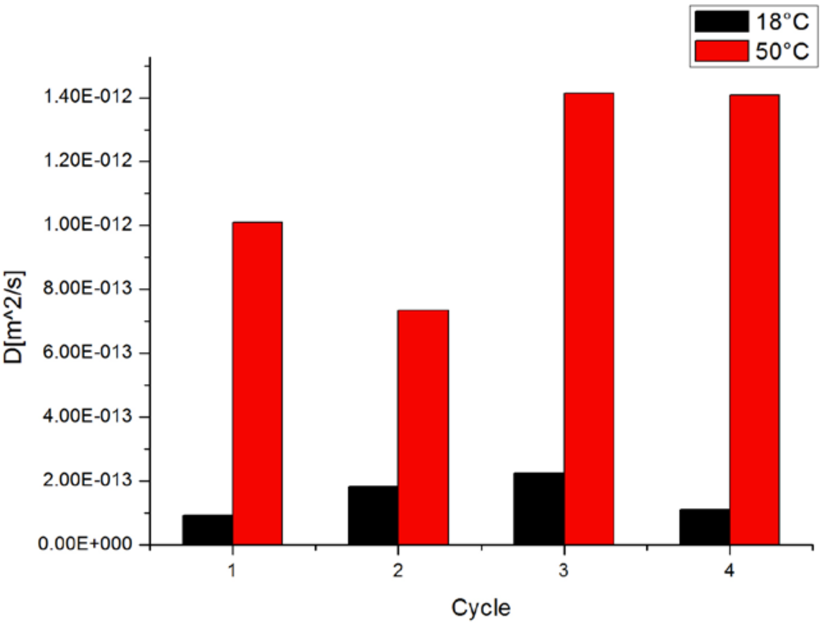

Figure 5.6 Reversible and reproducible thermo-responsive release characteristics of PNIPAM COOH 66k functionalized NSiM.

The same experiment and calculations were conducted with a PNIPAM NH_2 66k functionalized NSiM and results are shown in Figure 5.7. The average thermo-response factor calculated was found to be R=4.27. The average obstruction constant for the PNIPAM NH_2 66k functionalized NSiM at 18 and 50°C have been calculated to be of $k_{m,18}$=0.00042 and $k_{m,50}$=0.00084, respectively. For PNIPAM COOH 66k below the LCST, the diffusion is also slowed compared to non-functionalized NSiMs but not entirely stopped. Whereas above the LCST, the diffusion coefficient measured is significantly lower than the one of PNIPAM COOH 66k and non-functionalized NSiM. This is attributed to a less efficient conformational change of the PNIPAM brush layer from coil to globule. Indeed, the NH_2 terminated PNIPAM exhibits a significantly higher polydispersity index. A wide distribution of molecular weights will affect negatively the density of grafting [21–23], and thus the conformational change of the chains. In turn, this will impact the diffusion coefficient of molecules below and above the LCST through the modified membrane. In consequence, the thermo-response factor is significantly lower than *R* for the PNIPAM-COOH 66k. The results of the diffusion experiments of vitamin B12 are summarized in Table 5.2.

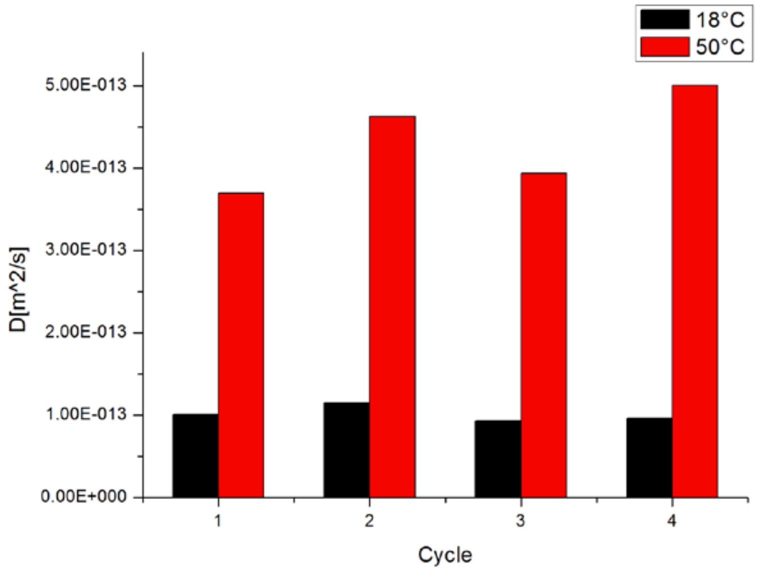

Figure 5.7 Reversible and reproducible thermo-responsive release characteristics of PNIPAM NH2 66k functionalized NSiM.

Table 5.2 Summary of diffusion experiments.

NSiM type	D_{18} 10^{-12} m²/s	D_{50} 10^{-12} m²/s	**R**	$k_{m,18}$ 10^{-3}	$k_{m,50}$ 10^{-3}
No NSiM – self diffusion (calculated)	238.40	511.73	2.15		
Virgin NSiM	0.25	1.11	4.44	1.05 ± 0.06	2.40 ± 0.14
PNIPAM COOH 66k funct. NSiM	0.15	1.14	8.46	0.63 ± 0.25	2.23 ± 0.55
PNIPAM NH_2 66k funct. NSiM	0.10	0.43	4.27	0.42 ± 0.04	0.84 ± 0.12

In view of the above results, the influence of the solute size on the diffusion through the modified membranes was studied extensively on PNIPAM-COOH 66k grafted NSiMs. FITC-dextrans of different molecular weights were diffused through a modified nanoporous membrane below (18°C) and above (50°C) the LCST. The hydrodynamic radii (Stoke radii r_s) given by the supplier (TdB Consultancy, Sweden) are considered herein as indicative of the size of the molecules (FITC-dextran 10k, 20k, 40k, and 70k have hydrodynamic radii of 2.4, 3.3, 4.5 and 6nm, respectively). Figure 5.8 shows the diffusion coefficients below and above the LCST as a function of the hydrodynamic radius of the molecule. The values are then compared with the corresponding diffusion coefficients obtained for vitamin B12 (r_s = 0.85 nm).

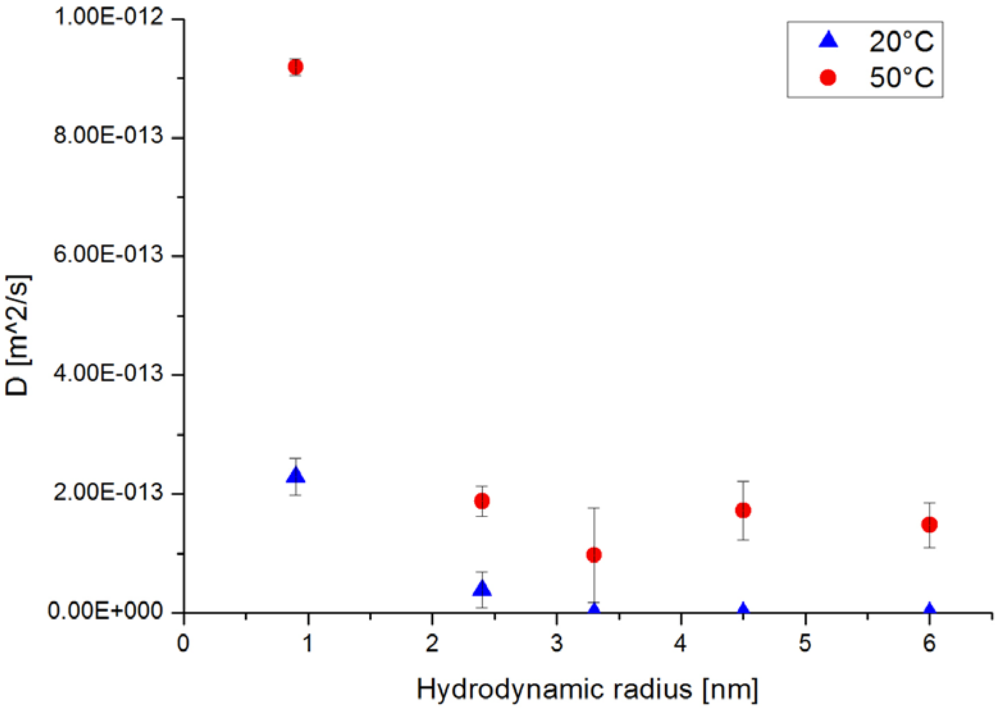

Figure 5.8 Measured diffusion coefficients of vitamin B12 and FITC-dextrans of various molecular weights as a function of their hydrodynamic radii across a PNIPAM-COOH 66k modified NSiM. The error bars are calculated for each data point from the error measured in blank samples on the instrument. A clear ON-OFF effect is observed for hydrodynamic radii larger than 2.4 nm. At 20°C, the diffusion from these molecules is effectively stopped, while at 50°C, all molecules diffuse through the PNIPAM-COOH 66k grafted NSiM.

From Figure 5.8, below the LCST (20°C), a clear cut-off is observed in the range of 2.4 to 3.3 nm (radii). Above the LCST (50°C), all molecules tested diffuse through the membrane (figure 5.9).

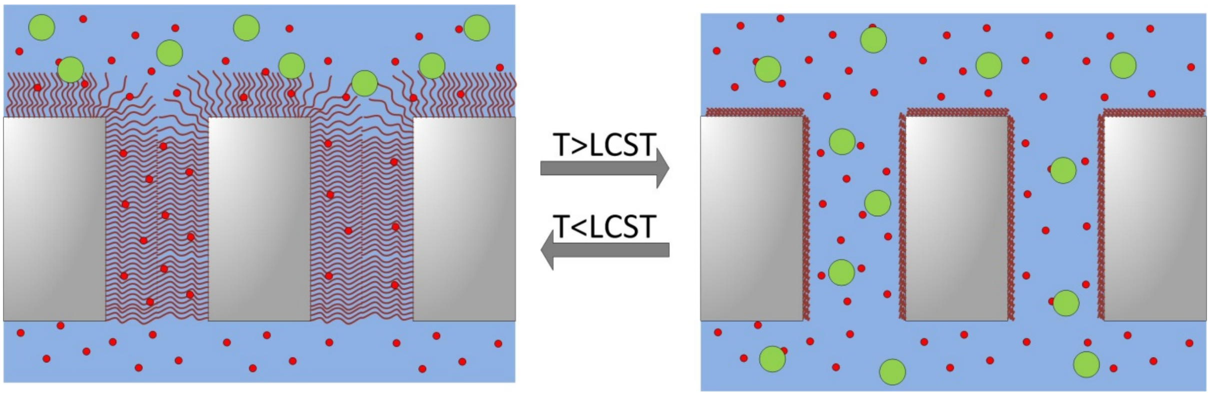

Figure 5.9 Schematic representation of PNIPAM modified nanopores with diffusion of all molecules above the LCST and diffusion of small molecules only below the LCST.

This cut-off is relevant for biomedical applications such as temperature-controlled drug delivery of pertinent analytes [24]. It might be possible to reduce this cut-off value by increasing the PNIPAM molecular weight. Indeed, grafting longer PNIPAM chains will increase the physical obstruction inside the nanopores and increase the path length of the solute. This latter can be considered for further study based on the nano-valve system described in this chapter.

5.3. Conclusions

In this chapter was discussed the molecular transport properties of both NSiMs with different mean pore diameters and PNIPAM grafted NSiMs (PNIPAM COOH 66k and NH_2 66k). The modified NSiMs were integrated into a specifically designed diffusion cell.

We demonstrated the ability to tune the molecular diffusion properties of the NSiMs by measuring the diffusion coefficient of fluorescein sodium molecules across NSiMs with different mean pore diameters obtained with Atomic Layer Deposition (ALD). The diffusion coefficient could be tuned almost by one order of magnitude, from $2x10^{-13}$ to $1.6x10^{-12}$ m^2/s for the smallest mean pore diameter (10 nm) and the largest mean pore diameter (90 nm), respectively.

Size-based separation experiments were also performed using NSiMs with a mean pore diameter of 10 nm and FITC-labelled dextrans molecules of different molecular weights with different hydrodynamic radii (from 1.4 to 4.5 nm). The diffusion of FITC-dextran 40k with a hydrodynamic radius of 4.5 nm close to the mean pore diameter of 10 nm of the NSiMs was almost completely hindered. This latter was verified by monitoring the transport rate of molecules across NSiMs and by calculating the ratio of the diffusion coefficient of the smallest molecule (fluorescein sodium) over FITC-dextran 40k being 3 fold larger than the ratio of the self-diffusion coefficients of the same molecules.

Finally, PNIPAM COOH 66k and NH_2 66k grafted NSiMs were used in diffusion experiments. The reversibility and reproducibility of the thermo-responsive behaviour were demonstrated by measuring the diffusion coefficient of vitamin B12 across different functionalized NSiMs at different temperature. A thermo-response factor as high as 8 has been measured for PNIPAM COOH 66k grafted NSiMs. Diffusion experiments with FITC-dextrans of different molecular weights demonstrated the temperature-controlled nano-valve behaviour of the PNIPAM COOH 66k functionalized NSiMs for all molecules above 3 nm in hydrodynamic radius. These results combined with the reversible behaviour of the modified membrane raise the possibility of using them as temperature controlled drug-release devices.

References

[1] K. Takamura, M. Koishi, T. Kondo, Studies on microcapsules, Kolloid-Zeitschrift Und Zeitschrift Für Polymere. 248 (1971) 929–933.

[2] P.-F. Li, X.-J. Ju, L.-Y. Chu, R. Xie, Thermo-Responsive Membranes with Cross-linked Poly(N-Isopropyl-acrylamide) Hydrogels inside Porous Substrates, Chemical Engineering & Technology. 29 (2006) 1333–1339.

[3] L.-Y. Chu, T. Niitsuma, T. Yamaguchi, S. Nakao, Thermoresponsive transport through porous membranes with grafted PNIPAM gates, AIChE Journal. 49 (2003) 896–909.

[4] Y. Shigeri, T. Kondo, Studies on Microcapsules. III) 1). Permeability of Polyurethane Microcapsule Membranes, Chemical & Pharmaceutical Bulletin. 17 (1969) 1073–1075.

[5] Y. Li, L. Chu, J. Zhu, H. Wang, S. Xia, W. Chen, Thermoresponsive Gating Characteristics of Poly(N-isopropylacrylamide)-Grafted Porous Poly(vinylidene fluoride) Membranes, Industrial & Engineering Chemistry Research. 43 (2004) 2643–2649.

[6] K. Kono, K. Kawakami, K. Morimoto, T. Takagishi, Effect of Hydrophobic Units on the pH-Responsive Release Property of Polyelectrolyte Complex Capsules, Journal of Applied Polymer Science. 72 (1999) 1763–1773.

[7] C.C. Striemer, T.R. Gaborski, J.L. McGrath, P.M. Fauchet, Charge- and size-based separation of macromolecules using ultrathin silicon membranes, Nature. 445 (2007) 749–753.

[8] J.R. Pappenheimer, E.M. Renkin, L.M. Borrero, Filtration, Diffusion and Molecular Sieving Through Peripheral Capillary membranes - A contribution theory to the pore theory of capillary permeability, American Journal of Physiology. 167 (1951) 13–46.

[9] R.E. Beck, J.S. Schultz, Hindered diffusion in microporous membranes with known pore geometry., Science. 170 (1970) 1302–1305.

[10] A.S. Iberall, A.M. Schindler, A kinetic theory, Near-Continuum model for membrane transport, Annals of Biomedical Engineering. 1 (1973) 489–497.

[11] H. Nikaido, E.Y. Rosenberg, Effect on solute size on diffusion rates through the transmembrane pores of the outer membrane of Escherichia coli., The Journal of General Physiology. 77 (1981) 121–135.

[12] C. Talmard, L. Guilloreau, Y. Coppel, H. Mazarguil, P. Faller, Amyloid-Beta Peptide Forms Monomeric Complexes With CuII and ZnII Prior to Aggregation, ChemBioChem. 8 (2007) Supporting Information.

[13] J.W. McBain, T.H. Liu, Diffusion of electrolytes, non-electrolytes and colloidal electrolytes, Journal of the American Chemical Society. 53 (1931) 59–74.

[14] R. Schmuhl, K. Keizer, A. van den Berg, J.E. ten Elshof, D.H. a Blank, Controlling the transport of cations through permselective mesoporous alumina layers by manipulation of electric field and ionic strength., Journal of Colloid and Interface Science. 273 (2004) 331–338.

[15] F. Montagne, N. Blondiaux, A. Bojko, R. Pugin, Molecular transport through nanoporous silicon nitride membranes produced from self-assembling block copolymers, Nanoscale. 4 (2012) 5880–5886.

[16] S. Prakash, M.B. Karacor, S. Banerjee, Surface modification in microsystems and nanosystems, Surface Science Reports. 64 (2009) 233–254.

[17] L. Chu, S. Park, T. Yamaguchi, S. Nakao, Preparation of thermo-responsive core-shell microcapsules with a porous membrane and poly (N-isopropylacrylamide) gates, Journal of Membrane Science. 192 (2001) 27–39.

[18] P.M. Kampmeyer, The Temperature Dependence of Viscosity for Water and Mercury, Journal of Applied Physics. 23 (1952) 99–102.

[19] J. Kestin, M. Sokolov, W.A. Wakeham, Viscosity of Liquid Water in the Range -8°C to 150°C, Journal of Physical and Chemical Reference Data. 7 (1978) 941–948.

[20] C.J. Seeton, Viscosity–temperature correlation for liquids, Tribology Letters. 22 (2006) 67–78.

[21] K.N. Plunkett, X. Zhu, J.S. Moore, D.E. Leckband, PNIPAM chain collapse depends on the molecular weight and grafting density., Langmuir. 22 (2006) 4259–4266.

[22] E. Bittrich, S. Burkert, M. Müller, K.-J. Eichhorn, M. Stamm, P. Uhlmann, Temperature-sensitive swelling of poly(N-isopropylacrylamide) brushes with low molecular weight and grafting density, Langmuir. 28 (2012) 3439–3448.

[23] H. Yim, M.S. Kent, S. Mendez, G.P. Lopez, S. Satija, Y. Seo, Effects of Grafting Density and Molecular Weight on the Temperature-Dependent Conformational Change of Poly(N -isopropylacrylamide) Grafted Chains in Water, Macromolecules. 39 (2006) 3420–3426.

[24] L.E. Bromberg, E.S. Ron, Temperature-responsive gels and thermogelling polymer matrices for protein and peptide delivery, Advanced Drug Delivery Reviews. 31 (1998) 197–221.

Chapter 6

Conclusion and Outlook

This thesis work aimed at fabricating functional and responsive nanoporous silicon nitride membranes that can be used as “smart” nano-valves for the controlled diffusion of molecules.

First a brief state of the art about the different types of nanoporous membranes and their fabrication methods was presented with detailed description of their specifications, advantages and disadvantages. From the information gathered and reviewed the choice of material and fabrication method was made. Because of its excellent mechanical and chemical stability, silicon nitride appeared as an obvious choice, allowing the fabrication of ultrathin nanoporous membranes with high mechanical strength and high throughput. In addition silicon nitride is compatible with the MEMS manufacturing technologies in clean room environment, and is well-known to be an excellent base chemistry for further functionalization with a wide variety of reactive groups. The fabrication method chosen involved a combination of block copolymer lithography and conventional microfabrication techniques. The nanopatterning of large scale surface (4 inches wafer) with diblock copolymer reverse micelles is an extremely low-cost technique allowing to generate a nanopattern in less than a minute. In addition the specifications of the nanoscale pattern (e.g. density, feature size, micelle interspace) can be tuned by varying several parameters such as the blocks molecular weights, the micellar concentration and the spin-coating speed during the deposition process.

In chapter 2 was described the full fabrication process flow of NSiMs at large-scale combining block copolymer lithography and conventional microfabrication techniques. Each fabrication step has been optimized in order to make this process robust and reliable. The mean diameter of the PS-P2VP block copolymer micelles used as templating structure reflects the mean diameter of the nanopores in the suspended low stress silicon nitride layer. The final nanoporous structure is obtained by performing a reliable pattern inversion of the micellar template into a metallic hard mask (lift-off) and pattern transfer into the underlying silicon nitride layer (RIE). The ability to tune the specifications of the starting micellar template has been demonstrated, therefore the ability to tune the porous structure parameters. One specific micellar system has been chosen and the nanopores in the final 200 nm thick suspended structure exhibit a narrow diameter and size distribution of 85 ± 15 nm and a nanopore density of 3.10^9 pores/cm^2. Standard photolithography was used to define the active areas of the nanoporous membranes, and square suspended structure with a side length as large as 2.5 mm has been achieved, exhibiting a total active area of 5.76 mm^2. Efforts were made in this fabrication process especially for the membrane release which is a high risk step impacting the final fabrication yield. If mass production is envisaged, several photolithographic mask could be prepared, each with a unique membrane size. This latter would add homogeneity in the fabrication process, especially for the DRIE of silicon (360 µm) for the membrane release. Indeed, apertures of different side length on the same wafer could present different etching depth. Also, several micellar systems exhibiting different mean feature size could be identified to potentially cover the full 10-100 nm range (typically mean feature size of 20, 50, 80, 100 nm) and used for the fabrication of nanoporous membranes.

Chapter 3 mostly focused on the final characterization of NSiMs in terms of nanopore opening and mechanical strength. First, three different techniques were used and compared to characterize the full opening of the nanopores. Atomic Force Microscopy (AFM) allowed determining the opening of the nanopores by scanning the front side and the backside and comparing the nanopore density per surface area measured. Scanning Transmission Electron Microscopy (STEM) and Transmission Electron Microscopy (TEM) allowed visualizing the full opening of the nanopore by collecting the transmitted electrons through the nanopores. All the techniques allowed measuring a mean pore diameter in good agreement with the mean micelle diameter of the starting micellar template. However, only AFM and TEM allowed characterizing precisely the nanopore profile which appeared to be vertical, confirming the reliability of the etching process used to create vertical nanopores. Second, the mechanical properties of porous and non-porous suspended membranes such as the Young's modulus and the residual stress were obtained using the bulge technique. The maximum pressure the membranes can withstand was also measured, and the increase of the mechanical strength of the suspended nanoporous layer has been demonstrated by reducing the square membrane side length and increasing the membrane thickness. However the values obtained for nanoporous membranes are effective values for the whole suspended structure, the influence of the non-porous suspended frame was not studied. Future work can be done in this direction by changing the width of the non-porous suspended frame and measure its influence on the overall mechanical strength. Buckling of ultrathin suspended square membrane has also been observed when fabricating nanoporous and non-porous super low stress silicon nitride membrane. Flattening of both membranes types was achieved by depositing a tensile-stressor overlayer of Al_2O_3 by ALD to reach an overall tensile stress of the composite structure superior to the minimum critical tensile stress necessary to avoid buckling.

In Chapter 4 was presented the surface modification of NSiMs in terms of pore size reduction using Atomic Layer Deposition (ALD) and by grafting thermo-responsive polymer poly(N-isopropylacrylamide) (PNIPAM). First, the pore size reduction and induced modification of the surface chemistry has been achieved by depositing in a conformal way Al_2O_3 by ALD. We observed the successful pore size reduction using TEM and characterized the resulting surface chemistry by X-ray Photoelectron Spectroscopy (XPS). The ability to tune the pore size after fabrication of NSiMs has therefore been demonstrated. However, efforts could be made to observe the modified nanopores in cross sectional view in order to confirm the conformal deposition of material along the sidewalls. Indeed, this latter would allow determining if the gas precursors used in the pore size reduction process successfully enter the nanopores depending on their size. Second, the successful grafting of different end functionalized PNIPAM chains using the grafting to in melt technique has been demonstrated. This grafting procedure is performed above the glass transition temperature of the polymer, allowing a better access of the polymer chains to the functional surface for covalent grafting. The successful grafting has been confirmed using XPS and by detecting the typical fingerprint of the amide groups composing the backbone of the PNIPAM chains. In addition, the characteristics of the grafted PNIPAM layers such as the grafting density, the theoretical chain length, and the distance between grafting sites were obtained from the ellipsometric measurement of the dry PNIPAM films. The brush layer conformation of the PNIPAM chains has been confirmed from these measured parameters. Future work could be done to develop a technique that will allow determining if PNIPAM chains were grafted inside the nanopores. This latter could be performed by grafting PNIPAM chains functionalized with fluorescent dyes onto NSiMs, and observation with high resolution confocal microscopy could be used to determine if PNIPAM chains are grafted along the nanopores sidewalls by scanning different focal planes to screen the whole thickness of the suspended membrane. However, nowadays the Z-resolution available is in the range of 500 nm, making this technique not suitable for ultrathin nanoporous membranes. It has been previously reported that TEM can be used to observe the grafting polymer, therefore a TEM cross sectional analysis of the PNIPAM functionalized NSiMs could be used to observe the grafting along the nanopores. Finally, the thermo-responsive behavior of the grafted PNIPAM brush layers has been confirmed by performing nano-indentation and AFM analysis in liquid environment. PNIPAM COOH 66k demonstrated the best ability to switch from a swollen to collapsed state because the successful morphological change operates when a good compromise is found between the grafting density and the length of the chains. All the PNIPAM grafted NSiMs (COOH 66k, NH_2 66k and NH_2 50k) were used in cell detachment experiments where only NSiMs functionalized with long chains (COOH 66k and NH_2 66k) were able to detach the cells from the surface when lowering the temperature below the Lower Critical Solution Temperature (LCST). From these experiments, the stronger conformal morphological change of the brush layer from swollen to collapsed state was observed for PNIPAM COOH 66k and NH_2 66k functionalized NSiMs. Regarding the experiments performed to observe the conformational morphological change of the PNIPAM brush layers from swollen to collapsed state upon temperature variation, efforts could be made to attenuate the electrostatic interactions when performing the nano-indentation by modifying the surface chemistry of the nanoindenter probe or by performing the experiment in a high ionic strength solution that will screen the long range electrostatic repulsions between the probe and the surface indented. Also, a wide variety of PNIPAM with different chain length could be grafted in the same conditions. This latter will allow identifying the influence of the polymer molecular weight on the grafting density using the grafting to in melt technique, and therefore identify the minimal conditions (grafting density, chain length) at which the conformational morphological change operates.

In the last chapter, NSiMS with different mean pore diameters and PNIPAM grafted NSiMs were integrated into a specifically designed polycarbonate microfluidic cell. This allowed characterizing the molecular transport properties of the different NSiMs. The ability to modify the diffusional properties of NSiMs by reducing the mean pore size has been demonstrated. The diffusion coefficient of fluorescein sodium molecules across NSiMs could be tuned by almost one order of magnitude from a mean pore diameter of 90 nm to a minimum pore diameter of 10 nm. Size-based separation experiments were also performed using NSiMs with a mean pore diameter of 10 nm and FITC-labelled dextrans molecules of different molecular weights. The diffusion of FITC-dextran 40k with a hydrodynamic radius of 4.5 nm close to the mean pore diameter of 10 nm of the NSiMs was almost completely hindered. Finally, PNIPAM COOH 66k and NH_2 66k grafted NSiMs were used in diffusion experiments. The reversibility and reproducibility of the thermo-responsive behaviour were demonstrated by measuring the diffusion coefficient of vitamin B12 across different functionalized NSiMs at different temperatures. A thermo-response factor as high as 8 has been measured for PNIPAM COOH 66k grafted NSiMs. Diffusion experiments with FITC-dextrans of different molecular weights demonstrated the temperature-controlled nano-valve behavior of the PNIPAM COOH 66k functionalized NSiMs for all molecules above 3 nm in hydrodynamic radius. Future work can be conducted to reduce the cut-off value of the “smart” nano-valves when the nanopores are supposedly closed. Indeed, small molecules still diffuse through the swollen PNIPAM brush layer. Therefore, the grafting of PNIPAM with a higher molecular weight would increase the physical obstruction inside the nanopores and increase the path length of the solute. Also, electrostatic interactions between the solute and the surface of the NSiMs do exist but were not considered in all the diffusion experiments. Performing these experiments with a high ionic strength solution would allow screening the long range interactions and reduce the Debye length by almost two orders of magnitude. Efforts could be made in future work to develop a new grafting chemistry allowing the covalent grafting of PNIPAM brush layers onto NSiMs processed with the pore size reduction technique which are presenting a different surface chemistry (Al_2O_3) from standard NSiMs (SiN).

The inconvenient controlled temperature set up used in all the diffusion experiment (water bath and heating plate) to observe the controlled diffusion of molecules through PNIPAM functionalized NSiMs needs to be improved. Typically, efforts could be made to develop a fully integrated system allowing the local heating of NSiMs. To do so, heating lines, typically made of platinum, could be evaporated on the surface of NSiMs. This would involve the modification of the fabrication process by adding a photolithographic and lift-off step to pattern the heating lines on the frontside of the wafer. Also, simulation using finite element method software would be necessary in order to determine the design properties of the heating lines, typically the width and thickness necessary to allow a sufficient local heating of the suspended membranes. Finally, a modification of the polycarbonate microfluidic cell would be necessary to integrate electrodes that would be in contact with the heating lines and would allow powering the whole device.

Recently, second generation filtration systems integrating NSiMs were designed and fabricated at CSEM. A 2 mL centrifugal tube (Appendix A.1) and a tangential flow filtration device (Appendix A.2) were used for small scale lab filtrations, such as size-based separations and sample concentration for diagnostics application. The promising preliminary results obtained when using these prototypes fluidic devices show that efforts should be pursued in integration to evaluate the full potential of NSiMs for bio- and med-tech applications.

Finally NSiMs can also be considered for sensing applications. Suitably modified thick membranes offer increased surface affinity area and enhanced output sensing signals, which make them increasingly attractive as biosensing platforms. Combined with various detection techniques, nanoporous membrane-based biosensors have advantages, including rapid response, high sensitivity, and reusability. For example, the Dutch company Pamgene incorporated nanoporous membranes in its kinase activity arrays [1]. Moreover, enhanced response times have been observed by controlling the transport of analytes through nanopores. The biosensing capabilities of the flow-through format have been proved through the detection of relevant biomarkers and viruses [2,3].

References

[1] Y. Wu, P. De Kievit, L. Vahlkamp, D. Pijnenburg, M. Smit, M. Dankers, et al., Quantitative assessment of a novel flow-through porous microarray for the rapid analysis of gene expression profiles, Nucleic Acids Res. 32 (2004) 1–7.

[2] M. Huang, B.C. Galarreta, A.E. Cetin, H. Altug, Actively transporting virus like analytes with optofluidics for rapid and ultrasensitive biodetection, Lab Chip. 13 (2013) 4841–4847.

[3] C. Escobedo, On-chip nanohole array based sensing : a review, Lab Chip. 13 (2013) 2445–2463.

Appendix

A.1 Centrifugal tube integrating NSiMs

Specifically designed polycarbonate tubes integrating NSiMs that can be inserted into standard commercially available centrifugal eppendorf were successfully fabricated. These devices can be used for small scale lab filtrations, such as size-based separations and sample concentration.

A similar device integrating pnc-Si nanoporous membranes has been reported and patented by Simpore, Inc. in 2011 (WO2011041671A1) and is commercially available. However, in contrast to our design these devices are fully integrated and cannot be disassembled. Being able to disassemble the whole device raise the possibility of reusing the integrated membrane and therefore reduce the costs for small scale lab filtration experiments.

Figure A.1.1 Standard commercially available 2 mL centrifugal tube in which a specifically designed tube integrating NSiMs and the solution of interest can be sled in.

The driving force allowing the transport of solute across NSiMs in such device is the centrifugal force. Nanoporous membranes have an inherent difficulty of passing a fluid from one side to another. As described by Simpore, Inc. in their patent, it requires an enormous amount of force for the fluid to navigate to the nanopore exit. Typically for nanopores with a diameter of 30 nm and a thickness of 15 nm, it would require a pressure of 100 atm to allow water to pass through the nanopores. This kind of enormous pressures cannot be supported by ultrathin suspended NSiMs, even with the great mechanical strength of silicon nitride. The patent from Simpore, Inc. describes a method to facilitate the fluid flow through nanoporous membranes by wetting the backside of the membranes to initiate the fluid flow. In our device, no pre-wetting chamber at the back side of the membrane was designed to initiate the fluid flow. Therefore, only microporous membranes fabricated using standard UV photolithography and that do not need any pre-wetting could be used with these centrifugal tubes for filtration experiments.

A.2 Tangential flow filtration device integrating NSiMs

In tangential flow filtration, the majority of the solute travels tangentially to the surface of the membrane rather than into the membrane (Figure A.2.1). Therefore the filtration process is slowed down but the tangential flow decreases the fouling of the nanoporous membrane by washing away the surface and applies less pressure onto the membrane.

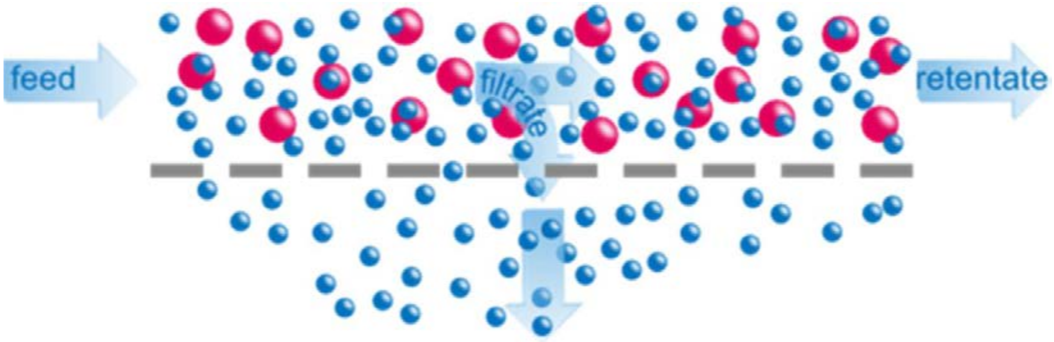

Figure A.2.1 Schematic representation of the tangential flow filtration process.

In order to increase the volume of solution to be filtrated and reduce the amount of force necessary to allow the transport of solute across the NSiMs, a tangential flow filtration system has been designed and fabricated at CSEM (Figure A.2.2 a)). This system including a turbisc micropump and a specifically designed fluidic cell integrating NSiMs with a backside pre-wetting chamber allowed the continuous filtration of solute with a volume from 2 to 100 mL (Figure A.2.2 b)). Preliminary results show that the filtrate flux through the membranes compares favorably to available data from commercially available systems. Microporous membranes (pore diameter 1µm) reached permeate flux of 1380 L/m^2/h (LMH) while nanoporous membranes (pore diameter 85nm) exhibited filtrate flux of 150 LMH. As a comparison, typical permeate flux for microfiltration using Pellicon (Millipore) devices are in the range of 10 to 100 LMH (source: http://www.millipore.com/catalogue/module/c613#0).

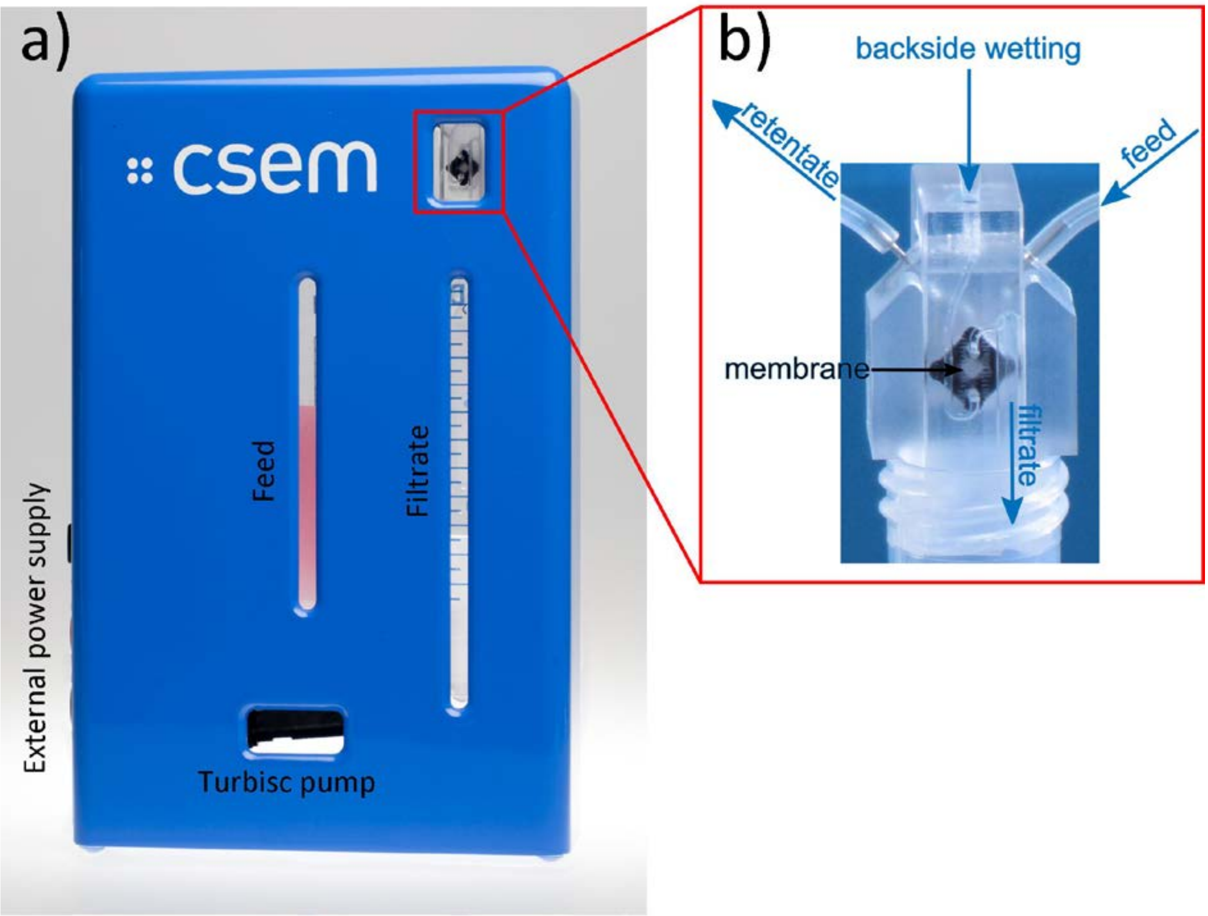

Figure A.2.2 Images of **a)** the whole tangential flow filtration device and **b)** zoom in on the cell integrating NSiMs with a pre-wetting chamber on the backside of the membrane facilitating the transport of the solute.

List of Publications, Scientific Reports and Conferences

Publication in peer reviewed journals

F. Montagne, N. Blondiaux, A. Bojko, R. Pugin, *Molecular transport through nanoporous silicon nitride membranes produced from self-assembling block copolymers*, Nanoscale 2012, 4, 5880-5886.

A. Bojko, G. Andreatta, F. Montagne, P. Renaud. R. Pugin, *Fabrication of thermo-responsive nano-valve by grafting-to in melt of poly(N-isopropylacrylamide) onto nanoporous silicon nitride membranes*, Journal of Membrane Science. (Submitted)

A. Bojko, M. Dadras, R. Pugin, *Unbuckling of low stress silicon nitride suspended thin films by deposition of tensile stressor overlayers of Al_2O_3 by Atomic Layer Deposition*, Thin Solid Films. (in preparation)

Technical and Scientific reports

A. Bojko, R. Pugin, *Fabrication of nanoporous silicon nitride membranes*, Confidential technical report own by CSEM SA, February 2014.

R. Pugin, G. Andreatta, S. Angeloni, A. Bojko, S. Ahmed, M. Dadras, M. Liley, A. Meister, F. Montagne, P. Niedermann, N. Schmid, *IPoSiM - Integrated porous silicon membranes*, CSEM SA scientific report 2013.

R. Pugin, S. Ahmed, G. Andreatta, S. Angeloni, A. Bojko, M. Dadras, D. Fengels, G. Franc, M. Liley, F. Montagne, P. Niedermann, N. Schmid, *IPoSiM - Integrated porous silicon membranes*, CSEM SA scientific report 2012.

F. Montagne, A. Bojko, H. Heinzelmann, R. Pugin, *Nanoporous Silicon Membranes as Filters and Sensors*, CSEM SA scientific report 2011.

Conferences & Poster presentations

G. Andreatta, S. Ahmed, S. Angeloni, A. Bojko, M. Dadras, R. Ischer, N. Marjanovic, F. Montagne, P. Niedermann, N. Schmid, R. Pugin, *IPoSiM - Integrated porous silicon membranes*, poster presentation at Multidisciplinary Integrated Project day at CSEM SA, December 2013, Neuchâtel, Switzerland.

A. Bojko, F. Montagne, R. Pugin, P. Renaud, *Molecular transport through nanoporous silicon nitride membranes produced from self-assembling block copolymers*, poster presentation at Nano-tera Annual Review Meeting, May 2013, Bern, Switzerland.

A. Bojko, F. Montagne, R. Pugin, P. Renaud, *Molecular transport through nanoporous silicon nitride membranes produced from self-assembling block copolymers*, poster presentation at CMi day, April 2013, Lausanne, Switzerland.

A. Bojko, F. Montagne, R. Pugin, *Molecular transport through nanoporous silicon nitride membranes produced from self-assembling block copolymers*, poster presentation at Multidisciplinary Integrated Project day at CSEM SA, December 2012, Neuchâtel, Switzerland.

A. Bojko, F. Montagne, R. Pugin, P. Renaud, *Molecular transport through nanoporous silicon nitride membranes produced from self-assembling block copolymers*, poster presentation at EDMI Research day, December 2012, Lausanne, Switzerland.

A. Bojko, F. Montagne, R. Pugin, P. Renaud, *Wafer-scale fabrication of functional and stimuli-responsive nanoporous silicon nitride membranes*, poster presentation at NAMIS autumn school, September 2012, Tokyo, Japan.

A. Bojko, F. Montagne, R. Pugin, P. Renaud, *Fabrication of ultrathin nanoporous silicon nitride membranes using self-assembling polymers*, talk given at 7th International Workshop on Nano-scale Spectroscopy and Nanotechnology, July 2012, Zürich, Switzerland.

A. Bojko, F. Montagne, R. Pugin, P. Renaud, *Fabrication of ultrathin nanoporous silicon nitride membranes using self-assembling polymers*, poster presentation at CMi day, April 2012, Lausanne, Switzerland.

Curriculum Vitae

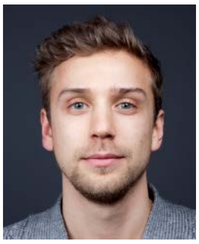

Personal details

Rue du Neubourg, 11 CH-2000 Neuchâtel
Phone : +41 78 748 98 22
Email : bojko.alex@gmail.com

Born in Reims, France 26/03/1987
Owner of driving license

Education

2010 - 2014 **Ph.D in Microsystems**
Ecole Polytechnique Fédérale de Lausanne (EPFL), Lausanne, Switzerland
Centre Suisse d'Electronique et de Microtechnique (CSEM), Neuchâtel, Switzerland

2006 - 2009 **Double M. Sc degree in Electronics and Microsystems engineering**
Ecole Polytechnique Universitaire de Montpellier, Montpellier, France
Politecnico di Torino, Turin, Italy

2004 - 2006 **Two years program In Physics and Engineering for entry examination to French engineering schools**
Lycée Franklin Roosevelt, Reims, France

July 2004 **Scientific Baccalauréat** (speciality: Engineering)
Lycée Franklin Roosevelt, Reims, France

Work Experience

May 2010 - February 2014 **Ph.D at CSEM**, Neuchâtel, Switzerland

This doctoral work was conducted in the frame of several challenging projects. Most of the work aimed at developing a new robust and reliable microfabrication process for the large scale manufacturing of silicon-based nanoporous membranes for biomedical applications. A large part was also dedicated to the design and planning of experiments, reporting and presentation of the results to the scientific community (conferences, seminars, publications, reporting).

March 2009 – January 2010 **Internship at EIA-FR**, Fribourg, Switzerland

Feasibility study of the fabrication of an ultrasonic data transmission device. This device is based on microfabricated resonant structures able to transmit data through the human body. Most of the work involved computer assisted simulation (COMSOL Multiphysics), design of experiments and reporting.

Skills

Scientific	Micro/Nanotechnology, Micro/Nanofabrication, Micro/Nanomecanics, Material science (semiconductors, metals, polymers), Micro/Nanoelectronics, Micro/Nanofluidics, Chemistry.
Technical	Micro/Nanofabrication tools (dry and wet etching, thin film deposition, photolithography), Optical and electronic microscopy (AFM, SEM, TEM, ellipsometry), Mechanical measurements (Indentation, profilometer, bulge testing), Chemical characterization (EDX, XPS).
Computer	Windows (Microsoft office), Mac OS, Image processing (ImageJ, WSxM), Data processing (Origin), Computer assisted design and simulation (Solid Works, COMSOL Multiphysics).
Languages	**French** – *mother tongue* **English** – *Technical and negotiations* **Italian** – *conversational* **Spanish** – *Fair comprehension*